UNIVERSITÉ DE STRASBOURG

Observatoire astronomique
de Strasbourg

Max-Planck-Institut für Astronomie Heidelberg
Max Planck Institute for Astronomy Heidelberg

Thesis to obtain the degree of doctor from the University of Strasbourg, in co–direction with the Max Planck Institute for Astronomy

Presented by

BENJAMIN P. M. LAEVENS

Finding and characterising the darkest galaxies in the Local Group with the Pan-STARRS 1 Survey

Public defence on 9 October 2015

Members of the jury:

Supervisor:	Mr. Hervé Wozniak, Astronomer, Observatoire astronomique de Strasbourg
Co–Supervisor:	Mr. Hans–Walter Rix, Professor, MPIA Heidelberg
External Rapporteur:	Mr. Michele Bellazzini, Director of research, INAF Bologna Astronomical Observatory
External Rapporteur:	Mr. Michael Irwin, Professor, IoA, University of Cambridge
External Examiner:	Ms. Eline Tolstoy, Professor, Kapteyn Astronomical Institute, University of Groningen
Internal Examiner:	Ms. Ariane Lançon, Professor, Observatoire astronomique de Strasbourg
Invited Member:	Mr. Nicolas Martin, chargé de recherche, Observatoire astronomique de Strasbourg

Discipline/Spécialité : Astrophysics

Contents

Acknowledgements

"All things are difficult before they are easy", Thomas Fuller, 1732

My three year PhD journey was by no means a sole undertaking. Many people significantly contributed, in their own way, to the work that I managed to achieve over the three years. These contributions may have been scientific, supportive or encouraging. It is to these people I owe many thanks, since without them, a PhD degree would not be within reach.

The most important person throughout my academic journey is without a shadow of a doubt Nicolas. You were always incredibly enthusiastic about the PhD and greatly encouraging as well. When there were very basic concepts that I did not understand or lagoons in my understanding, you always helped to explain these in a very normal manner and in such a way that I never felt stupid for asking the questions to start with. I have many fond memories of us working together. I will for example not forget that mad week in March 2014 and the great energy with which you still persisted to help me get the paper out, after we had been scooped with our first Milky Way discovery. This and countless other times such as teaching me to observe in Chile make me realise just how privileged I was to have you as a supervisor. I hope by the end of this three year adventure we can consider ourselves to be friends as well as future colleagues, should I have the opportunity to continue in science.

My next thanks go to Hans-Walter for supervising me in Heidelberg, where I ended up spending the majority of my time. Though very busy because of your many duties at the MPIA, you were always very interested in knowing the development of the thesis. You were at all times kind and patient and re–explaining things when I did not understand them. I thank you for always being able to place things in the bigger picture and to provide very helpful solutions at times when I got stuck. I also thank you for giving me the chance to go to many conferences and workshops around the world. Next, I wish to thank my collaborators for their great help, the most important of which are Eddie Schlafly and Branimir Sesar. Eddie, as our local MPIA Pan-STARRS man, was of enormous help when I got stuck with Pan-STARRS issues. Brani helped me a great deal with data reduction and many other general sciency problems. Finally I wish to thank other collaborators for their help along the way. These are people such as Michelle Collins, Édouard Bernard, Annette Ferguson, Rodrigo Ibata, Colin Slater, Eric Bell and Mark Norris. Next, I would like to thank the members of the jury for agreeing to referee my thesis: Ariane Lançon, Eline Tolstoy, Michele Bellazzini, Mike Irwin and Hervé Wozniak. Finally, I thank the University of Strasbourg for awarding me the IdEx grant, making my PhD research possible.

Behind all the scientific work there are of course a number of people that provide a lot of encouragement and support. They have been there unconditionally to support me come what may and I thank them for this. In first place, I thank all my family members: Mum, Tony, my sister Sarah *et papa également*. Thank you/*merci* for being my biggest supporters, since I was born. Without them, I wouldn't be where I am today. I also extend many thanks to my grandma and gramps, who have represented a lot more to me than 'just' grandparents over the years. Unfortunately my grandma is not around anymore, but I hope she would have been very proud. I also thank Mum and Tony for attentively reading and correcting this manuscript. I thank Aiara, who I met during my PhD, for making me incredibly happy, *obrigado! Ik bedank graag ook een aantal vrienden uit België voor hun interesse en steun gedurende deze drie jaren en ook voorgaande jaren, jullie weten wie jullie zijn!* Finally, these three years have been more than just work, there has also been meeting and making new friends. I will remember many happy moments with new friends: Paolo, Jakob, Richard, Simon, Hector, Miguel, Michael, Sasa and Ilya in Heidelberg.*Je remercie Jean–Baptiste, François et Jonathan, que j'ai rencontré à Strasbourg*.

Abstract

This thesis uses the Panoramic Survey Telescope and Rapid Response System 1 (Pan–STARRS 1, or PS1) Survey to find new Local Group satellites such as dwarf galaxies and globular clusters. Due to its 3π coverage, the survey allows for satellite searches in a search volume which has increased by 50–100%, relative to its predecessor: The Sloan Digital Sky Survey (SDSS). Therefore this survey is instrumental in helping resolve some key tensions that have become apparent between observation and theories. In the ΛCDM Model, the number of dark matter subhalos orbiting their host is on the order of hundreds and there is no preferred distribution of these dark matter halos. Observationally, the number density of dwarf galaxies is an order of magnitude lower and the dwarfs appear to lie in a plane, a claim which could never be fully substantiated due to previous surveys coinciding with the proposed plane (e.g. the SDSS). In light of these tensions, the objectives of this PhD thesis are two–fold. In a first phase, a search algorithm is developed to find new stellar substructure in the Milky Way or Local Group, inspired by techniques of past searches on the SDSS. Briefly, potential new satellites are detected by isolating old and metal–poor stars and convolving these with window filters tailored to the size of typical satellites. This technique takes into account the distance of the satellite, the background Milky Way contamination and the complex survey footprint. Five new Milky Way satellites are discovered using this search technique: two globular clusters called Laevens 1/Crater and Laevens 3, the first of which is the most distant cluster ever found in the MW and three satellites that straddle the globular cluster and dwarf galaxy classification: Triangulum II, Sagittarius II and Draco II. Though yielding five discoveries, this number is lower than the predictions of the ΛCDM models, assuming isotropy of the Milky Way satellites. This leads to the second aim of this thesis, namely quantifying the detection limits of the PS1 Survey. Dwarf galaxies of all sizes, magnitudes and distances are generated photometrically and spatially, while taking into account the survey completeness. These mock satellites are ingested into the data. The search algorithm is re–run on these new data. This leads to recovery rates that are broadly consistent with the SDSS searches, demonstrating that the search technique works efficiently. The detection efficiency maps over the entire PS1 sky can be used as a stepping–stone towards the quantification of the (an)isotropy of the Milky Way satellites' distribution. Using this information, the luminosity function of these satellites can be re–derived.

Résumé

Cette thèse utilise le relevé de donné du *Panoramic Survey Telescope and Rapid Response System 1 Survey* (Pan-STARRS 1, ou PS1) pour trouver de nouveaux satellites du Groupe Local: les galaxies naines et les amas globulaires. Puisque le relevé couvre les trois–quarts du ciel (3π), le volume de recherche pour trouver de nouveaux satellites est augmenté de 50 à 100% par rapport au grand relevé précédent: Le *Sloan Digital Sky Survey* (SDSS). Le relevé est donc important pour résoudre les tensions entre les observations et les modèles. Dans le modèle ΛCDM, il y a des centaines de petits halos en orbite autour de leur hôte et ceux–ci sont distribués de manière isotrope. Par contre, les observations que nous faisons montrent que le nombre de galaxies naines est un ordre de grandeur inférieur et qu'elles semblent être distribuées dans un plan, une affirmation qui, jusquà présent, n'a pas pu être complètement prouvée car les relevés précédents se trouvent dans des parties du ciel incluant le plan (par exemple le SDSS). Au vue de ces tensions, cette thèse a deux objectifs différents. Premièrement, un algorithme de détection est développé afin de trouver de nouveaux structures stellaires dans la Voie Lactée ou le Groupe Local. L'algorithme est inspiré de tentatives de recherches précédentes dans le SDSS. De nouveaux satellites potentiels sont identifiés en isolant d'étoiles vieilles et pauvres en métaux. Celles-ci sont convoluées avec des fonctions Gaussiennes, de taille d'un satellite typique. Cette méthode prend en compte la distance du satellite, la contamination due à la Voie Lactée et l'empreinte compliquée du relevé. Cinq nouveaux satellites sont découverts en utilisant la méthode décrite: deux amas globulaires du nom de Laevens 1/Crater et Laevens 3. Le premier est l'amas globulaire le plus lointain de la Voie Lactée. Les trois autres découvertes sont des satellites avec des charactéristiques intermédiaires entre les amas globulaires est les galaxies naines: Triangulum II, Sagittarius II et Draco II. Bien que cinq découvertes soient faites, le nombre de découvertes est inférieur à ce qu'on s'attendrait, en présumant une distribution isotrope dans le modèle ΛCDM. Ce résultat mène au deuxième objectif de la thèse, c'est à dire quantifier les limites de détections du relevé PS1. La photométrie et la distribution spatiale des galaxies naines de toutes tailles, luminosités et distances sont créées, tout en tenant compte du complétude du relevé. Ces galaxies artificielles sont insérées dans les données. L'algorithme de détection est appliqué aux nouvelles données. Les résultats sont cohérents avec ceux du SDSS, montrant que l'algorithme a une efficicacité élevée. Les cartes d'efficacité de détection du ciel complet peuvent être utilisées pour quantifier la distribution (an)isotrope des galaxies satellites de la Voie Lactée. En outre, ces informations peuvent mener a redériver la fonction de luminosité des satellites.

Chapter 1

Introduction

1.1 Galaxy formation in the ΛCDM model

The currently favoured cosmological model known as ΛCDM, describing the evolution and current structure of the Universe, consists of two main components: a cosmological constant (Λ) and Cold Dark Matter (CDM). The former represents the effects of what is known as dark energy, accounting for the expansion of space against the attracting force of gravity. The latter is a form of matter; cold because it moves slower than the speed of light and dark because it is unseen, therefore not emitting radiation or interacting heavily with it (Binney & Tremaine, 2008). This matter is invoked to explain numerous observations such as the dynamics of galaxies and the clustering of galaxies in the universe (Springel et al., 2005). All the 'visible' mass in the universe – alone – cannot account for the two aforementioned observations. Rotation curves of stars in galaxies are flat, i.e. with increasing radius the velocity of these stars is not decreasing as is expected from Newton's laws (Sellwood & Sanders, 1988). Similarly, the visible mass in the universe cannot explain why galaxies are clustered and attracted together in groups such as the Local Group of which the Milky Way (MW), Andromeda (M31) and numerous other smaller (dwarf) galaxies are its primary constituents. Therefore a large amount of matter must be present, but not visible to current telescopes, to account for these effects (Komatsu et al., 2009).

It is in this context that Local Group dwarf galaxies (DGs) have become a source of increasing interest. Such galaxies are the faintest, oldest and smallest galaxies known. These galaxies are the smallest scale on which dark matter (DM) manifests itself, containing so few baryons that the baryonic effect on the DM are not thought to be very important. These galaxies are therefore among the most heavily DM dominated objects in existence. In the ΛCDM model, where galaxies are born in DM halos, they are thought to be constituents that have contributed to the build up of larger galaxies such as the MW through a variety of merger (collisions) and accretion events onto their host. More specifically the DM collapses to form halos, which over time merge to produce larger halos. The gas which collapses to the centre of these halos and cools down is the key igniter of the birth of a galaxy (White & Rees, 1978). The current population of DGs are the ones that have survived these merger events. With observations of these galaxies we can infer the properties of some of the oldest constituents of the universe. Since stars are producers of chemical elements, observations of their chemical abundances provide constraints on how and when star formation happened and ceased.

Properties of these satellites such as their luminosity and size, along with their DM content, can give powerful constraints as to the range in parameters these 'survivor' satellites can take on and to what limit DM 'subhalos', in which DGs are born, can exist (Mateo, 1998; Grebel et al., 2003; Gilmore et al., 2007). For example, which properties determine that these satellites get accreted by their host galaxy? Which galaxies can survive interactions and to what extent? Which elements govern where these satellites lie in relation to their host?

Besides DGs, a second class of satellites exists. Globular clusters (GCs) are small concentrations of old and metal–poor stars residing in the halo of any galaxy, massive enough to host these satellites. Formation scenarios of these GCs are currently still unclear, though broadly speaking, these old satellites are thought to be formed as a part of their parent galaxy, with initial star formation turned off very soon after they come into existence. It is for this reason that they are not thought to be part of dark–matter subhaloes of their own. In fact they are shown to be baryonic systems, with most of their visible mass amounting to their total mass. Their shallow potential well is responsible for the failure to retain gas, which would lead to subsequent generations of stars. These systems therefore, in general, do not show metallicity spreads. Their in–situ formation, would explain their preferential locations in the inner parts of the Galaxy ($< 50\,\mathrm{kpc}$). The tight gravity which binds these objects explains their smaller size or half–light radii (van den Bergh, 2008) as well as their spherical or 'globular' shape. In the same formation scenarios, the GCs which are observed in the outer parts of the MW's halo ($> 50\,\mathrm{kpc}$) are thought to be the remnants of more massive DGs accreted onto the MW, i.e. formed ex–situ.

Although ΛCDM has been largely successful at reproducing the universe in its current structure, and on a large scale, accounting for the dynamics of galaxies and the clustering of galaxies *inter alia* (Spergel et al., 2003; Komatsu et al., 2011), it shows mismatches at the smallest scale, that of the DG scale. Three problems have become apparent with the model in the wake of observations that are made in the Local Group and the MW in particular. Firstly ΛCDM does not indicate any preference for how these satellites should be distributed around their larger host galaxy (Starkenburg et al., 2013). Instead of an isotropic distribution, however, a clustering of these satellites in a plane is currently observed and proposed (Lynden-Bell, 1976; Pawlowski et al., 2012; Ibata et al., 2013). Secondly, the cosmological simulations indicate that the number density of this population of surviving satellites today should be in the order of hundreds. Current observations point to the number density of satellites being an order of magnitude lower than the predicted number with the MW and M31 containing around 70 satellites in total (Klypin et al., 1999). Finally, the readily accepted distinction between GCs and DGs has become tenuous (Gilmore et al., 2007). Though not directly linked to the outcomes or results of the ΛCDM model, these distinctions in general stem from a broader understanding of galaxy formation and the roles within which smaller constituents play.

In the continuation of this introductory section I will give an overview of the current state of the field of DGs and to a lesser extent GCs. In Section 1.2, I give an historical overview of the field, detailing discoveries and how the field has grown to its present form. In Section 1.3, I outline the spectroscopic follow–up campaigns that have inevitably followed as a result of new DG discoveries. This section will naturally lead to Section 1.4 which will elaborate and expand on the three aforementioned tensions in galaxy formation models. In Section 1.5, I give an overview of the Panoramic Survey Telescope and Rapid Response System 1

(Pan-STARRS 1, or PS1) Survey, which was used for the endeavours of this PhD thesis. Finally, in Section 1.6, I will outline the structure and objectives of the thesis.

1.2 An historical overview of the search for stellar substructure in the Milky Way

1.2.1 From the Magellanic Clouds to Sagittarius: a brief history

We have been aware, for over 1000 years of the first two and largest satellite galaxies of the MW. Visible to the naked eye, and appearing like two faint clouds of the night sky, these satellites held a variety of names until the names of the Small and Large Magellanic Clouds were universally accepted, named after the Portuguese explorer Magellan, whose crew (re-)discovered the clouds on the first trip around the world in the sixteenth century. It took until the twentieth century for the next few satellites to be discovered. This occurred in 1938 when Shapley (1938a) discovered the Sculptor DG on photographic plates taken at the Boyden Observatory in South Africa. Soon thereafter he noted the discovery of a second dwarf this time in the constellation of Fornax (Shapley, 1938b). The author mused about the possiblity of other such systems existing in the Local Group. This reflection became reality with the discoveries of four more 'Sculptor-type' systems: Leo I, Leo II (Harrington & Wilson, 1950), Draco and Ursa Minor (Wilson, 1955), from photographic plates at the Palomar Observatory. Cannon et al. (1977) and Irwin et al. (1990) discovered Carina and Sextans respectively, on UK Schmidt plates, where the latter was discovered using an automated scanning system of photographic plates. This brought the total tally to ten DGs, with the last eight now commonly known as 'classical' DGs.

The next discovery was unique because it was serendipitous and found through spectroscopic means, rather than imaging. Ibata et al. (1994) discovered the Sagittarius dwarf when analysing velocities of stars in the MW's bulge. In so doing they noticed a velocity offset of a subsample of stars in colour-velocity space, inconsistent with the bulge stars they were observing. Subsequent papers found that this DG was in fact embedded in a stream, with tails over the whole sky (Mateo et al., 1996; Ibata et al., 1997; Majewski et al., 2003). These observations have since become interesting as valuable information to constrain the MW's potential (Law & Majewski, 2010; Peñarrubia et al., 2010a). Besides this, the discovery of Sagittarius and its stream was the first direct evidence of a merger event between a smaller galaxy and its larger host. This changed the prevalent view that the MW was a stable, static, confined system, that had finished evolving billions of years ago, moreover it showed the MW itself is still undergoing change as it accretes stars from nearby neighbours. This discovery was significant in an age where consensus was growing towards the ΛCDM model as a fully contained theory describing the Universe from the large scale to the small scale. Such models were showing that merger events were common and that many more DM subhalos, the birth places of DGs, and therefore a population of old, metal–poor DGs should be present around the MW, thus far undetected (Bullock et al., 2000, 2001).

1.2.2 The Sloan Digital Sky Survey: the first generation of large sky surveys

To resolve these predicted faint galaxies, new and improved means were necessary. Photographic plates allow DGs down to $\mu \sim 25.5$ mag arcsec^{-2} to be resolved (Whiting et al., 2007). With the advent of large CCD sky surveys, covering large swathes of the sky, came the possibility of searching for these faint metal-poor populations down to fainter luminosities. To this end, new techniques were developed to find resolvable stellar over densities which, whilst appearing invisible on the images, could be identified using colour and magnitude information[1]. Willman et al. (2002) undertook the first such attempt to search for new DGs, resulting in the discovery of a new satellite in the constellation of Ursa Major: SDSS J1049+5103 (Willman et al., 2005a). The title of the paper: "A New MW companion: unusual globular cluster or extreme dwarf satellite", compactly summarised the predicament which Willman et al. (2005a) faced. Willman 1 – as it was renamed – sits in no-man's land between the smaller, compact GCs and the larger, extended DGs. This discovery reinforced a tension that had already been growing at the time, namely the distinction between GCs and DGs; the decade preceding the discovery of Willman 1 had showed that some systems did not neatly fit in either category. Though classified as a GC, ω Cen for example shows signs of a metallicity spread, compatible with DGs (Ashman & Zepf, 1998), whereas objects such as Palomar 14, display central star densities also similar to DGs (Harris, 1996). The discovery of Willman 1 was quickly followed by Willman et al. (2005b) quantifying the discovery of Ursa Major I.

Soon thereafter other discoveries emerged from the Sloan Digital Sky Survey (SDSS). The "field of streams" images (Belokurov et al., 2006a), which binned the SDSS data in magnitude slices, revealed three more typical and obvious DGs: Canes Venatici I, Ursa Major II and Boötes I (Zucker et al., 2006b,a; Belokurov et al., 2006b). Belokurov et al. (2007) announced the discovery of a further five satellites: Hercules, Coma Berenices, Leo IV, Canes Venatici II and Segue 1. In contrast to previous discoveries, these satellites were followed up to supplement the SDSS photometry. Segue 1 – at the time thought to be a GC – was the second object to be found in what would later be coined the "valley of ambiguity", which is the region of r_h vs. M_V space that straddles the 'classical' boundaries between dwarfs and globulars (Gilmore et al., 2007), thus showing many similarities with Willman 1. Figure 1.1 shows where the MW GCs and DGs lie in that parameter space. All the satellites fainter than $M_V \sim -3$ and in the $10\,\mathrm{pc} < r_h < 100\,\mathrm{pc}$ range blur together, effectively creating a bridge between GCs and DGs.

The discoveries of Leo T, Boötes II, Boötes III, Pisces II, Segue 2 and Leo V brought the total tally to 27 MW satellites (Irwin et al., 2007; Walsh et al., 2007; Grillmair, 2009; Belokurov et al., 2009, 2010). Many of the new satellites brought surprises. Segue 2 and Boötes II further increased the number of objects in the valley of ambiguity. The discovery of Hercules, which is the second most distorted and elongated MW satellite discovered to date, has been the subject of many studies, precisely because of its morphology (Coleman et al., 2007; Martin & Jin, 2010; Deason et al., 2012; Roderick et al., 2015). Leo T, with its higher metallicity $[\mathrm{Fe/H}] = -1.6$ and distance$\sim 420\,\mathrm{kpc}$, revealed an isolated DG at the very outskirts of the MW, but with many indicators of recent star formation, because its isolation allowed it to retain its gas to do so. Subsequent measurements showed this to be the case (Weisz et al., 2012). Finally, Leo V, just $\sim 20\,\mathrm{pc}$ from its brother Leo IV, has prompted scenarios to be explored that they are in fact companions, with a bridge of stars connecting them (de Jong et al., 2010). These and

---

[1] This technique will be expanded upon in Chapter 2.

subsequent discoveries are often commonly referred to as ‘ultrafaint’ dwarfs[2].

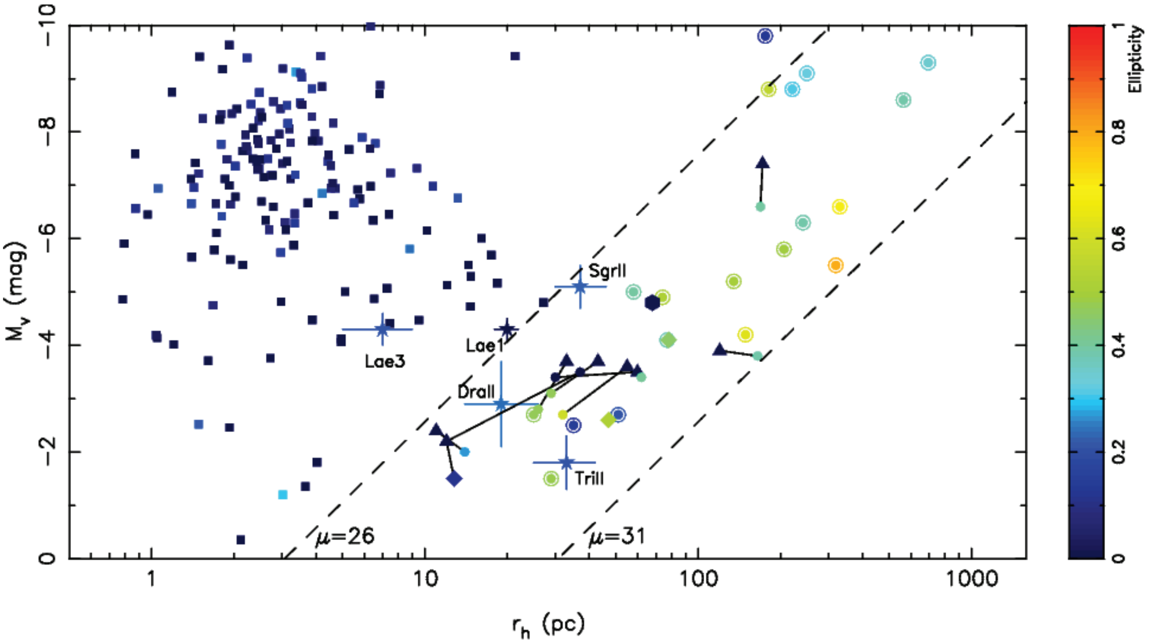

Figure 1.1 - Distribution of MW satellites in the size-luminosity plane, colour-coded by their ellipticity. Squares represent GCs from the Harris (2010) catalogue, supplemented by the more recent discoveries of Segue 3 (Belokurov et al., 2010), Muñoz 1 (Muñoz et al., 2012), and Balbinot 1 (Balbinot et al., 2013). MW confirmed DGs are shown as circled dots, with their properties taken from McConnachie (2012). The co-discoveries by Bechtol et al. (2015) and Koposov et al. (2015) are shown as triangles and filled circles respectively, with the co-discoveries linked to each other by a black solid line reflecting the two groups' different measurements. The Kim et al. (2015a), Kim et al. (2015b), and Kim & Jerjen (2015) satellites are shown as diamonds. Hydra II, discovered in SMASH, is shown by a hexagon. Finally, the five PS1 discoveries (Lae 1, Tri II, Sgr II, Dra II, and Lae 3) are shown as stars.

1.2.3 A second generation of sky surveys arrives: DES, PS1, Atlas, SMASH

After the SDSS discoveries, a period of tranquility followed as second generation surveys were being prepared. Such surveys are Pan-STARRS 1 (Chambers, K. et al. in prep.), the Dark Energy Survey (DES; The Dark Energy Survey Collaboration (2005), VST Atlas (Shanks et al., 2013), and Survey of Magellanic Stellar History (SMASH; Nidever D. et al. in prep.). The starting shot for this second generation of survey discoveries came with the co–discovery of the stellar system PSO J174.0675–10.8774, also known as Crater or Laevens 1, found concomitantly in the PS1 and VST Atlas survey (Laevens et al., 2014; Belokurov et al., 2014)[3], and probably the most distant GC of the MW. Within four weeks of each other, the discoveries

---

[2] The distinction between ‘classical’ and ‘ultrafaint’; DGs stems from a combination of date of discovery and therefore means of discovery e.g. plates versus CCDs, as well as from the differences in observed magnitudes. Although SDSS discoveries are simply the smaller, fainter and more metal–poor counterparts of their ‘classical’ siblings, this distinction has stuck. This means that, confusingly, a satellite such as CVn I is an ultrafaint, though arguably also displaying many similarities to its ‘classical’ counterparts.

[3] See Chapters 3 and 4 of this thesis.

of some 12 new satellites were announced, many of which were new DGs or Segue 1–like satellites (Bechtol et al., 2015; Koposov et al., 2015; Laevens et al., 2015b; Martin et al., 2015; Kim et al., 2015a). A large fraction of these satellites was found in the DES, whose current footprint observes some $\sim$ 5000 degrees^2, in the vicinity of the Magellanic Clouds. Though the footprint is reasonably small in size (when compared to large sky surveys such as the SDSS or PS1), the survey reaches unprecedented depths for MW satellite searches, therefore yielding many new satellites. This is possible due to the survey being conducted with a 4m telescope using DECam on the 4m Blanco telescope at Cerro Tololo, Chile. We can therefore expect this survey to yield many more discoveries as more years of data are accumulated.

Three of the nine new satellites are unambiguous DGs: Grus I, Tucana II and Eridanus II, the last of which shows many similarities to Leo T (Irwin et al., 2007), due to its similar distance and magnitude. Colour Magnitude Diagram (CMD) features of this DG hint at the possible presence of some blue–loop stars, indicative of recent star formation. The satellite is further interesting as Koposov et al. (2015) cautiously point out the presence of fuzzy blobs on the images, which could be GCs associated to Eridanus II, making it the faintest satellite known to contain these star clusters. Deeper imaging and spectroscopy of Eridanus II's central regions will be much sought after to confirm the blue–loop stars and the presence of GCs. Four of the six other satellites are typical Segue–1 like satellites in the $-3.4 < M_V < -2.7$ range, with sizes of $26\,\text{pc} < r_h < 32\,\text{pc}$, but out at further distances relative to the SDSS discoveries: $30\,\text{kpc} < d < 114\,\text{kpc}$. These satellites are Reticulum II, Horologium I, Pictoris I and Phoenix II, the first of which bears all the hallmarks of Segue 1, with all of its properties being very similar. The final two satellites are probable GCs, one of which was already discovered as Kim 2 (Kim et al., 2015b) and Eridanus III. Koposov et al. (2015) point out that these satellites are unlikely to be clustered around the LMC and SMC through isotropic means, possibly hinting at these satellites being associated to the clouds.

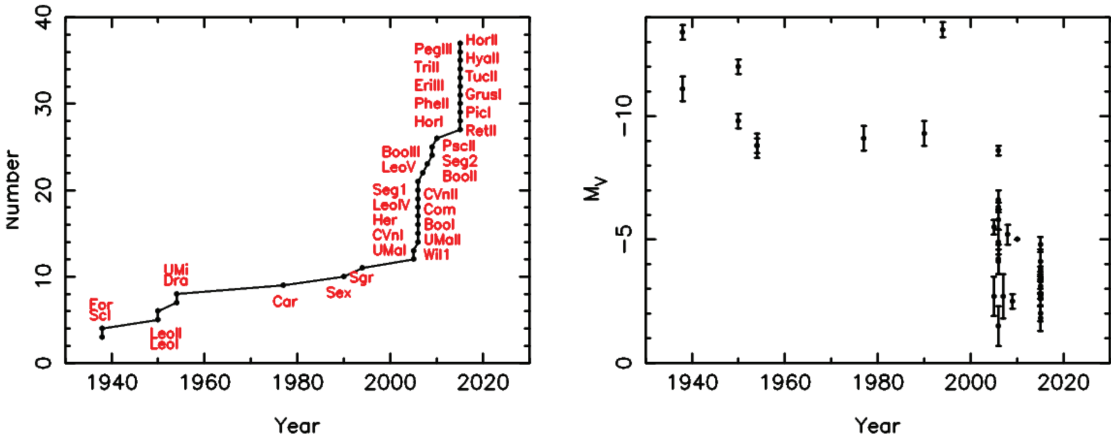

Figure 1.2 - *L*eft: The number of satellites as a function of discovery data. The number of galaxies, shoots up with the age of large CCD surveys, going from 11, pre-2005 to ~37 as of this year. *R*ight: M_V of satellites as a function of the year they were found. The explosion of satellites in the SDSS and DES, coincides with many new fainter satellites.

Other survey discoveries have included those of Triangulum II[4] (Laevens et al., 2015b),

---

[4] Subject of this thesis in Chapters 3 and 5.

another Segue 1–like object. Kim et al. (2015a) discovered Pegasus III in the latest SDSS DR 10 release, with properties such as distance, size and magnitude very similar to Pisces II with a possible physical association such as the Leo IV and Leo V pair (Belokurov et al., 2008). Finally the last two sets of discoveries to date are Horologium II (Kim & Jerjen, 2015) in DES and two more ambiguous satellites in the constellations of Draco and Sagittarius[5], whose current classification is difficult, as they straddle the GC–DG regimes (Laevens et al., 2015a). Sagittarius II, with a magnitude at $M_V \sim -5$, is an interesting object as it would either be the most extended GC of the MW or the most compact DG known in its magnitude range. Figure 1.2 shows the discovery of the MW DGs and their corresponding magnitude as a function of time, clearly showing the explosion of new discoveries with the age of large sky surveys, allowing larger surface brightness ranges to be explored. The current census of MW DGs sits at $\sim 35 - 40$.

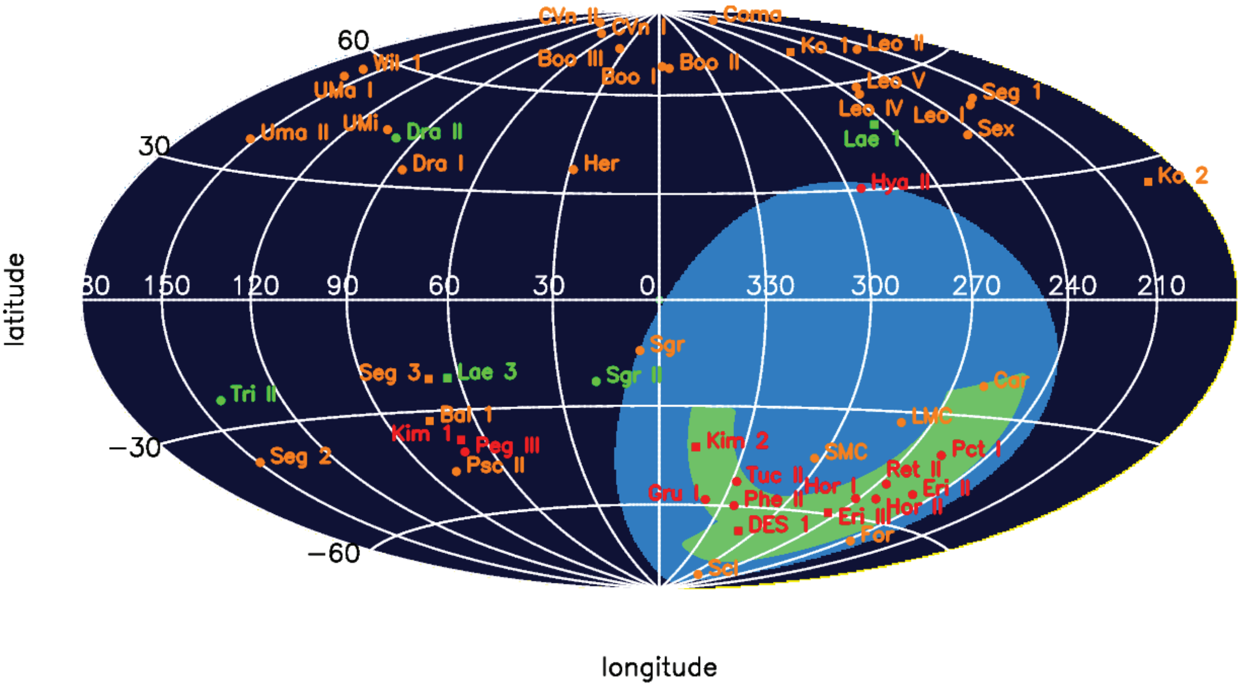

Figure 1.3 - Longitude versus latitude of MW satellites. Colours denote period of discovery, whereas symbols reflect types of satellite: circles for DGs, squares for GCs. Orange satellites are SDSS satellite discoveries until ∼2012. These are the ∼ 16 DGs and the 4 GCs (Willman et al., 2005a,b; Zucker et al., 2006b; Belokurov et al., 2006b; Zucker et al., 2006a; Belokurov et al., 2007; Walsh et al., 2007; Belokurov et al., 2008; Koposov et al., 2007; Belokurov et al., 2009, 2010; Balbinot et al., 2013). Red denotes any satellite that has been found in the last year (barring PS1 discoveries). These are mostly satellites found in the DES, but also in the SDSS and SMASH (Bechtol et al., 2015; Koposov et al., 2015; Martin et al., 2015; Kim et al., 2015b,a; Kim & Jerjen, 2015). Green denotes the PS1 discoveries and subject of this thesis (Laevens et al., 2014, 2015b,a). The dark blue represents the PS1 footprint, whereas the light green shows a rough view of the DES footprint.

The field of GCs has recently seen a small revival as new parts of the sky are being probed. Such discoveries of mainly low luminosity GCs show that the MW GC population is still far

---

[5] See Chapters 3 and 6.

from being complete. Since the SDSS discoveries of four GCs, all of which are faint, small and in the inner parts of the Galaxy: Koposov 1 and 2, Segue 3, Balbinot 1 (Koposov et al., 2007; Belokurov et al., 2010; Balbinot et al., 2013), as well as Muñoz 1 from deep MegaCam imaging (Muñoz et al., 2012), the outer reaches of the halo appear to be more populated with GCs. The last searches which revealed distant MW GCs date back to the Palomar searches (Arp & van den Bergh, 1960) and the discovery of AM–1 at $\sim 125\,\mathrm{kpc}$ (Madore & Arp, 1979). New discoveries have included the aforementioned system PSO J174.0675–10.8774, as well as Kim 2, Eridanus III (Kim et al., 2015b; Bechtol et al., 2015; Koposov et al., 2015), Laevens 3 (Laevens et al., 2015a) and DES 1 (Luque et al., 2015), doubling the spatial outer halo cluster population. This is not surprising as discoveries in M31 similarly suggest that the potential of finding new GCs could be higher than initially thought as a collection of new extended outer halo clusters are also found there (Huxor et al., 2005; Mackey et al., 2013).

Figure 1.3 shows the census of MW satellites on the sky. These include all the 'classical' and SDSS satellites (dwarfs and globulars) and all other objects found since 2014 in PS1, DES and SMASH. The SDSS satellites (orange) are mostly concentrated in the North where a large number of the original searches were conducted, with some satellites in the South from the Segue stripes. All recent discoveries (except PS1) since 2014 are given in red. Many of these are from the DES, which is now correcting for the historic North–South imbalance of faint satellites. PS1 discoveries are given in green, with three out of the five discovered at low latitude, where SDSS has no coverage. The lack of satellites near the disc is a direct result of the higher number density of stars which lie there.

1.3 Campaigns of further satellite characterisation

Campaigns to further characterise satellites are nearly as old as the photometric or imaging campaigns themselves. While imaging can provide a first general indicator of a system's properties such as its size, distance, magnitude, it does not, in general, answer the more fundamental and ultimately most interesting aspects of the system. To conclusively place objects in the bigger context, additional spectroscopy is necessary to ascertain the DM content and the metallicities, both of which provide valuable insights into the nature of the system, the star formation histories *inter alia*. In this section of the introduction, I will give an overview of the spectroscopic campaigns which have naturally followed. Towards the end of this section, I will expand a little more on the systems that lie in the "valley of ambiguity" (Gilmore et al., 2007) and how spectroscopy is currently shaping this field and what can be expected in the future.

Before exploring spectroscopy, it is worth recounting the first steps taken in the field, as their results, though over fifty years old, remain largely valid today. Hodge (1961a,b, 1962, 1963, 1964) undertook the first studies of the number density of stars as a function of radius. This approach was successful at correctly identifying two key features of DGs. By counting stars on the photographic plates, he was able to draw lines of constant number density of stars as a function of radius. From this he concluded that the six DGs he was measuring at the time (Sculptor, Fornax, Leo I, Leo II, Ursa Minor and Draco) were flattened and that the number density of stars could not be successfully reproduced with profiles such as the de Vaucouleurs profile (de Vaucouleurs, 1948), common at the time for describing other galaxies.

Instead Hodge noted that the stellar profiles were better described by a King model (King, 1962), which accounted for a steeper drop–off of stars at the outskirts of the galaxy. Irwin & Hatzidimitriou (1995) used the automated scanning systems, previously described, to repeat Hodge's work including all eight 'classical' dwarfs and refined these results.

Aaronson (1983) was the first study to measure a velocity dispersion for a dwarf spheroidal. Using spectra from three carbon stars, the author calculated the line–of–sight velocity, which in turn yielded a velocity dispersion of 6.5 kms^{-1} for Draco. From dynamical arguments and the virial theorem, it was concluded that Draco contained DM, which had already been predicted by Faber & Lin (1983), who used a relation between the MW's mass, and the dwarf's distance, mass and orbital eccentricity, to show that the total mass of the then known DGs was larger than the luminous mass. The 1980's saw further measurements of velocity dispersions of Sculptor, Fornax, Leo I, Leo II, Draco and Ursa Minor all of which consistently showed velocity dispersion measurements of 6–10 kms^{-1} (Seitzer & Frogel, 1985; Suntzeff et al., 1986; Aaronson & Olszewski, 1987). Unfortunately, these samples suffered from small–number statistics and it was not until the 1990's when larger samples were acquired, that the initial measurements were largely confirmed (Olszewski et al., 1995; Armandroff et al., 1995). Mateo et al. (1993) noticed with their velocity dispersion measurements – and therefore mass–to–light ratios – of stars in Fornax and Carina a scaling relation. They noted that mass–to–light ratios were linked to luminosity, i.e. the fainter the systems, the more heavily DM dominated it is. At the turn of the century, samples into their hundreds continued to be collected for the bright DGs, e.g. Tolstoy et al. (2004); Battaglia et al. (2006, 2011) for Sculptor, Fornax and Sextans, but see also Bellazzini et al. (2001); Walker et al. (2007, 2009). These studies revealed that the DGs contained multiple stellar populations.

With the discoveries of the fainter SDSS DGs, the spectroscopic efforts continued. Kleyna et al. (2005), with a small sample of 5 stars, provided the first velocity dispersion for Ursa Major I, yielding $\sigma > 6.5$ kms^{-1} and M/L=500. Muñoz et al. (2006) soon thereafter found a similar velocity dispersion for Bootes I, but owing to its larger magnitude revealed a smaller M/L=130, as expected from the scaling relation (Mateo et al., 1993). These two follow-up studies quickly revealed the real challenge facing spectroscopists. While the 'classical' dwarfs have red giant branch stars in their multitudes, the SDSS galaxies have far fewer of these stars. In very extreme cases such as Segue 1, which has just six or seven red giant brach stars, this is further compounded. In its case as well as for many other faint satellites, stars further down on the main–sequence and the turn–off need to be targeted and these are naturally a lot fainter. Therefore with current means, only the best instruments on some of the largest telescopes such as DEIMOS on Keck, have some hope of shedding light on these systems. In fact Ibata et al. (2006) and Martin et al. (2007) measured the velocity dispersions and mass–to–light ratios of Canes Venatici I, Boötes I, Ursa Major I and II and Willman 1. In all cases the satellites were confirmed to have $\sigma > 3\mathrm{kms}^{-1}$ and to be heavily dark–matter dominated. Ibata et al. (2006) showed distinct kinematic populations in their study of CVn I, echoing some of the previous results of the 'classical' DGs. Simon & Geha (2007) found similar results for their analysis, which also extended to stellar systems such as Canes Venatici II, Coma Berenices, Leo IV, Leo T and Hercules.

More recently it has been shown that the velocity dispersion measurements are not so robust as was initially thought. Second epoch observations of some of the DGs, notably Segue 1, Bootes I and Hercules have revealed discrepancies with the original values. Simon et al. (2011) showed when re–measuring the velocities of Geha et al. (2009) that one of the red giant brach stars was displaying variable velocity. Though it did not impact the overall conclusion of that particular paper, which concluded that Segue 1 has $\sigma = 3.7^{+1.4}_{-1.1}$ kms^{-1}, McConnachie & Côté (2010) noted that if you start from the assumption of a purely stellar system – and therefore no DM –, then the impact of binary stars can inflate the velocity dispersion to $\sim$ 4kms^{-1}, i.e. of the order of the measurements for Segue 1. Other re–measurements of satellites' velocity dispersions were conducted, notably for Bootes I (Koposov et al., 2011). The authors revised the velocity dispersion of Boötes I down from $\sigma = 6.5^{+2.0}_{-1.4}$ kms^{-1} (Martin et al., 2007) to $\sigma = 4.6^{+0.8}_{-0.6}$ kms^{-1} assuming one stellar component. The authors in fact favour two populations with cold and warm components. While the discrepancy can be explained away due to different methods followed – Koposov et al. (2011) used a technique to account for binary stars – this remains worrisome nonetheless. At this point it is worth pointing out that in more general terms some of the assumptions that go into kinematic analyses to start with could be fundamentally flawed. Five assumptions are employed, which – as Walker (2013) points out – are all flawed on some level and formulae that are commonly used to derive the DM contents such as those calculated by Illingworth (1976) and Richstone & Tremaine (1986), all stem from these assumptions. They are the following: (i) the system is in dynamical equilibrium and (ii) spherically symmetric, (iii) the system's velocities are isotropic, i.e. equal in three dimensions, (iv) the system is composed of a single stellar component and (v) mass follows light. While the first four are shown to probably not impact results greatly, the last assumption is less clear.

1.4 Tensions between models and observations

1.4.1 Missing satellite problem

"Where are the missing galactic satellites?", was one of two papers (Klypin et al., 1999) – the other is Moore et al. (1999) – to lay bare the discrepancy between the number of observed DGs and the number of DM subhalos, outputted from simulations, now commonly referrred to as "the missing satellite problem". Cosmological simulations predict on the order of $\sim$500 DM subhalos (Bullock et al., 2010), whereas currently some 40 satellites are known (see figure 1.4 for a visual representation of the output of such a simulation by O. Gnedin). As a result, much time has been devoted to either proposing mechanisms to account for the differences or highlighting that we may not be in a position to accurately compare observations with simulations. Let us start with the first. There have been broadly two approaches to this problem. Modifications are introduced that leave the number of subhalos unaltered, but instead explain why just a fraction of the DM halos are populated with stars. The other approach is to actually reduce the number of subhalos to be in broader agreement with the number of observed satellites. Within the first approach, there are then two further subcategories: some groups compare the luminosity of satellites with the present–day mass of the subhalos e.g. Peñarrubia et al. (2008) and others which assume that only the largest halos, defined at time of re–ionisation, contain the DGs (e.g. Koposov et al. 2009; Macciò et al. 2010).

Several studies have shown that fine–tuning the initial set–up of the simulations can go a long way to explaining the observed properties of the current day satellites (Koposov et al., 2009;

Macciò et al., 2010). In such scenarios, the star formation is not 'turned on' in most of the DM subhalos due to a variety of mechanisms. These are photo–ionisation, supernova feedback, tidal stripping and/or the interplay between all these elements. Photo–ionisation can halt star formation for hotter DM halos, because it makes these halos inefficient at accreting gas. This in turn is responsible for slowing down the supply of baryons, necessary for star formation to exist. Similarly the ejection of reheated cold gas by supernovae can starve halos of the gas necessary to initiate star formation. Finally tidal stripping due to interactions with the parent galaxy can reduce the number of sub halos which exist. Koposov et al. (2009) and Macciò et al. (2010) generally point out that these parameters are so potentially significant that the outcomes can vary quite drastically.

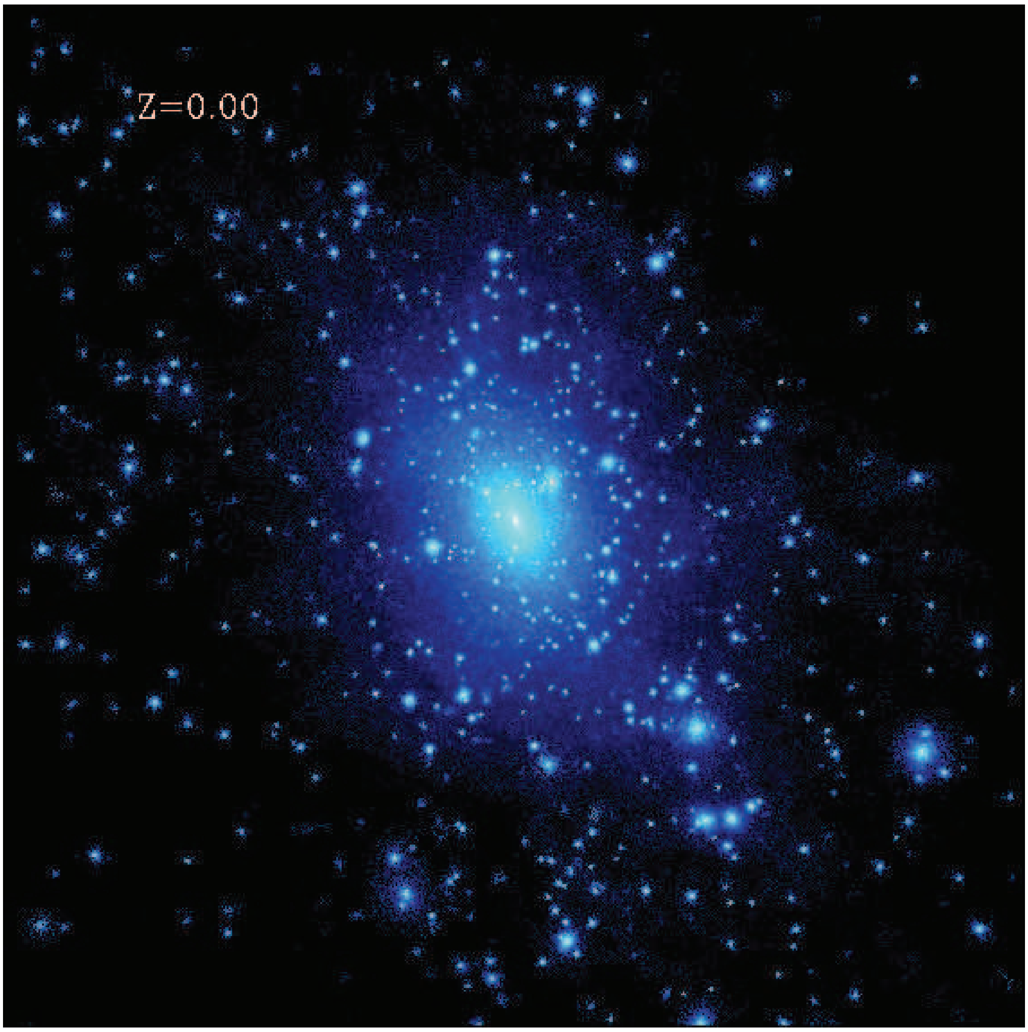

Figure 1.4 - Cosmological simulation demonstrating the appearance of the MW and its surroundings at the present day (z=0). All the blue dots represent little halos around a host halo to be compared with the MW and its satellite distribution. The distribution of these halos is isotropic and in the order of several hundreds (Image Credit: O. Gnedin).

Nevertheless there are still many problems with these solutions. Boylan-Kolchin et al. (2012), building on their work of Boylan-Kolchin et al. (2011), point out that the masses of the most massive subhalos is in conflict with the masses of the present–day ‘classical’ DGs: the “too big to fail” problem. The abundance–matching techniques (Moster et al., 2010) therefore seem to work inadequately, when extrapolated at the faint end, to explain these discrepancies. This could be due to other factors in the simulations. Many simulations ignore the presence of the MW or host galaxy’s disc. Some papers have shown that the presence of a disc could go a long way to explaining the depletion of many satellites, among them the most massive ones e.g. Peñarrubia et al. (2010b). More specificially the presence of the disc is expected to induce tidal destruction of the satellites, especially if the density profiles are cored (Peñarrubia et al., 2010b), and not cusped as simulations predict. This discrepancy can also be resolved, however, if the DM is pushed away from the centres (cored) and pushed to the outskirts through the supernovae feedback previously mentioned (Pontzen & Governato, 2012). This would result in the cored profiles that would get so easily disrupted by the disc. Caveats to these solutions are that the energy required in feedback to produce the cored profiles could be too high (Garrison-Kimmel et al., 2013).

The last few paragraphs have shown that whenever solutions are shown for a problem, other problems or caveats arise. Part of the answer to the discrepancies may lie in earlier mentioned information, namely that we are not in a position to compare simulations and observations. Current simulations probably do not have enough of a resolving scale to make accurate enough predictions about the satellite distribution, and the underlying assumptions are too great. The inclusion of baryons (Zolotov et al., 2012) in simulations, often not entirely accounted for, will almost certainly yield different outputs (as we saw for example with the inclusion of the disc). Observationally, there are many factors that come into play which in fact would not rule out simulations’ predictions. The mass of the MW is not accurately constrained with ranges of a factor of 3 (Watkins et al., 2010). The mass of the host galaxy is inextricably linked to the masses of the subhalos. Secondly, it is also unclear whether the plethora of satellites do exist. For example, it was shown that for the SDSS, satellites *à la* Segue 1, can only comfortably be found out to $40 - 50$ kpc (Koposov et al., 2009). Tollerud et al. (2008), Bullock et al. (2010) and Hargis et al. (2014) have shown that several hundreds of these faint satellites can populate the MW halo. In fact, the discoveries in the DES have gone a long way to showing that if we had such a deep survey over the entire sky – or even deeper than that – we would probably find these satellites in their multitudes. The Large Synoptic Survey Telescope (LSST) will probably be the next survey to shed light on this problem. Finally, our position in space is awkward. We sit in the MW and have a difficult time finding such satellites near the disc or bulge, which could be obscuring our view. For example, it was recently shown that strong evidence points to the existence of one such DG in this area, but has been as of yet, too difficult to robustly confirm (Chakrabarti et al., 2015).

1.4.2 The plane of satellites

As already touched upon in Section 1.1, the orientation and distribution of satellites has been a source of scientific debate in the age of ΛCDM. In the hierarchical merging scenarios that the theory prescribes, no preferential alignment is found for the DGs (Wang et al., 2013). Lynden-Bell (1976) and Kunkel & Demers (1976) were the first to point out the preferential orientation of satellites around the MW. They observed the proximity of the then–known dwarfs relative to the orbital plane of the Magellanic Clouds and Stream. In the former paper the hypothesis was proposed that a larger Magellanic Galaxy has existed, that was destroyed by tidal interactions with the MW and resulted in two large components (the clouds) and smaller bits (the other DGs). Kroupa et al. (2005) was the first real paper to mount an offensive against the ΛCDM model. The authors argued that the polar alignment of the eleven known MW satellites – disc of satellites (DoS) – conflicted with the distribution of DM subhalos, expected from ΛCDM. They note that the preferential alignment of satellites is incredibly rare and that, in an universe dominated by DM, the effects of organised accretion should have been 'forgotten' by the satellites as they relax into their orbits and positions around the MW. Their work builds on previous work by Kroupa (1997) which showed that DGs, with properties of the 11 'classical' DGs can be successfully reproduced by dark–matter free stellar systems that form as tidal DGs out of galaxy merger events. The paper sparked the debate between proponents and opponents of the model since then. Zentner et al. (2005) showed with their initial set–up which included filamentary accretion that anisotropic distribution of satellites could in fact be commonly reproduced, or put differently that the chance of drawing an isotropic distribution was smaller than 10^{-4}. Libeskind et al. (2005) similarly showed that such scenarios could also be reproduced if fine–tuning the initial set–up (but see also Libeskind et al. 2009; Wang et al. 2013).

With the discovery of the SDSS satellites, proponents of the plane of satellites have pointed out that many of the new discoveries lie in the polar plane (Kroupa et al., 2010). Pawlowski et al. (2012) re–dub the DoS, with the Vast Polar Structure (VPOS) as they extend the analysis from Kroupa et al. (2005) and Kroupa et al. (2010) to include all the latest SDSS discoveries as well as streams and young outer halo GCs (Mackey & van den Bergh, 2005), thought to have originated in DGs that were accreted onto the MW (Dotter et al., 2011). Similar to Pawlowski et al. (2011) and previous works, this study builds on the notion that the satellites all align in a plane as a result of a very early merger event, with galaxies forming from the tidal debris. Pawlowski et al. (2012) conclude that the young outer halo GCs align well with the VPOS and that 7 out of the 14 streams they consider, though Belokurov (2013) points out that while it appears that half of these streams align, in terms of mass, the 7 streams are quite small relative to the total mass. The authors conclude the probability of the orientation they measure to be very low ($< 0.3\%$) when assuming isotropy to start with. Pawlowski et al. (2015) re–worked the analysis taking into account the new discoveries from PS1, DES, SDSS and SMASH and concluded that their results were largely unchanged by the inclusion of some 12+ new satellites.

While the VPOS is an idea, greatly growing in relevance, there are several caveats which should be pointed out. Firstly, it is not necessarily surprising that a polar alignment is found, since the two most productive surveys in terms of satellite discoveries: SDSS and DES actually lie in regions that coincide with the extensions of the original 11 satellite plane. The initial SDSS coverage is centred on the Northern Galactic Cap, while the DES largely sits near the Magellanic Clouds. However, two more additional caveats to those would be that, the SDSS failed to find new DGs that were bright, distant and far away from the plane, while Pawlowski et al. (2015) show that the probability of the satellites being found in the areas they were found in the DES is also low in probability if assuming isotropy. Another admonition to this plane hypothesis is the fact that just a handful of the data points drive the fit to start with. For example, objects such as Segue 1, Triangulum II, but also Ursa Major II are so close to the MW centre that they are nearly negligible in the analysis since any plane through the MW centre would include them.

Figure 1.5 shows the VPOS by Pawlowski et al. (2015) face–on and edge–on with the latest census of satellites. The plane of satellites was recently extended to M31. Ibata et al. (2013) showed that 50% of DGs lie in a spatial as well as orbital plane (with the exception of one DG, which counter–rotates in the opposite direction).

It is exactly for these reasons that the PS1 survey is so crucial, since for the first time a survey will be able to probe three quarters of the sky down to uniform precision and depth, allowing for a robust statement to be made about (an)isotropy of the MW satellites. This has been one of the later aims of this PhD thesis. For more information on this, see Chapter 7.

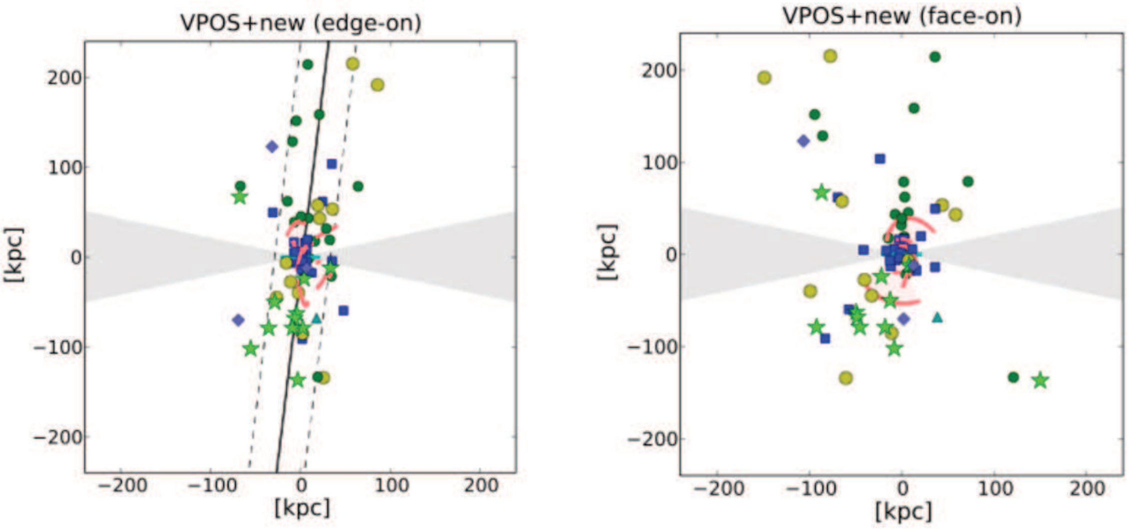

Figure 1.5 - Plot of the VPOS taken from Pawlowski et al. (2015). The left hand side shows the plane edge–on, i.e. such that the thickness is minimised. The right hand side shows the plane face–on, i.e. rotated by 90 degrees relative to the left side. The yellow dots are the 'classical' DGs. Fainter satellites are shown by the green dots and young halo clusters by the blue squares. Finally lighter blue diamonds represent recently confirmed GCs: Laevens 1/Crater and Kim 2.

1.4.3 Star clusters, dwarf galaxies and ... the weird bits in between

Throughout this introduction, recurring statements have been made about either the discovery of ambiguous objects, straddling the no–man's land region between clusters and dwarfs in the size–luminosity plane or the inconclusive measurements regarding their DM content because of the effect of binaries and foreground contaminants. These observations have prompted people to re–assess the definition of a galaxy (Tolstoy et al., 2009). Willman & Strader (2012) give a brief overview of what has constituted a galaxy in the past and converge on the following definitions of a galaxy:

"A galaxy is a gravitationally bound collection of stars, whose properties cannot be explained by a combination of baryons and Newton's laws of gravity."

This definition is elegant and clear because it has the benefit of allowing for different interpretations of the cosmological model. In any DM model, this definition simply means that DM must be invoked, whereas for other theories that reject DM, such as Modified Newtonian Dynamics (Milgrom, 1983) the statement still holds, that Newton's cannot offer a comprehensive explanation. In view of this definition, and with the current data at hand, the likes of Segue 1 and Willman 1 clearly fall into the category of galaxy, though the caveats of binaries and foreground contaminants influencing the results should be reiterated. Recent work has tried to explain the origin of these satellites. Deason et al. (2014) for example draw attention to the notion of "satellites of satellites". In the ΛCDM model, these sub–sub halos are the accompanying smaller constituent of more massive satellites or the remnants of destroyed satellites. As of yet, little work has been done regarding these sub–sub halos. For example it is not known whether these halos would turn on star formation or are in fact completely dark. It is also unclear how many of these types of halos would have survived until the present day and therefore how their number equates to the number of sub–halos. The apparent connection of three of the four 'transition' systems from the SDSS: Willman 1, Segue 1 and Segue 2, as well as the more recently discovered Triangulum II, with streams seem to bring support to this idea. While entirely speculative in the case of Triangulum II, which sits in the general region of the Triangulum–Andromeda structure (Laevens et al., 2015b), cases have been made for and against satellite–stream associations. Belokurov et al. (2009); Deason et al. (2014); Newberg et al. (2010); Koch et al. (2009) have shown associations between Segue 1 and Bootes II and the Orphan Stream and Sagittarius Stream respectively, though other authors have shown the contrary with different abundance patterns between the stream and satellites (Vargas et al., 2013; Casey et al., 2014; Koch & Rich, 2014). Finally, on a sidenote, it should be noted that the idea of satellites of satellites has already been mentioned earlier, but not by that explicit name when briefly drawing on the associations between Leo IV and Leo V, and even possibly Pisces II and Pegasus III. Exploring the sub–sub halo models and investigating stream associations can help to place these objects in the context of galaxy formation.

It is worth noting that indirect detection of DM particle self–annihilation in objects such as Segue 1, Segue 2, Willman 1, Reticulum II, Triangulum II and maybe even Draco II[6] would probably be the best chance yet of resolutely classifying these satellites as galaxies or remnants thereof. A whole subbranch of astronomy and particle physics sets out to use the satellites to (indirectly) detect DM. These six objects are among some of the highest chances of detecting DM particles because of their presumed high mass–to–light ratios as well as their proximity ($< 40\,\mathrm{kpc}$). In fact these objects and the general number density of satellites in general, are used to put constraints on the types and masses of DM particles (Tremaine & Gunn, 1979). An indirect detection could consist of high–energy photons as a result of DM self–annihilation (Gunn et al., 1978) or particle decay (Kusenko, 2006). Surveys are currently being conducted with γ–ray telescopes (Abdo et al., 2010) and Cherenkov telescopes (Pieri et al., 2009). Bonnivard et al. (2015) have shown Reticulum II to have a J–factor which is among the highest ever found for a MW DG. The J–factor quantifies the sensitivity of the object to a DM detection, i.e. the higher this factor the better. Geringer-Sameth et al. (2015) reported the indirect detection of gamma–ray emission from Reticulum II, hinting at the presence of DM, whereas Drlica-Wagner et al. (2015) report the detection to be low significance. Needless to say that this will be an interesting branch of astronomy to watch out for as these measurements increase in precision.

---

[6] If follow–up points more toward a Segue–1 look–a–like.

1.5 The Pan-STARRS 1 3π survey

In this section of the introduction, a little background information will be provided about the PS1 survey, since this survey has been the main resource throughout the PhD to conduct the search for stellar substructure. In the two following subsections I will outline the survey specifics and give a short overview of some of the interesting, high–impact science to already emerge from the data, while data have only been accessible to the collaboration.

1.5.1 Survey specifics

PS1 first saw light in June 2006. The 1.8m telescope is located on Haleakala, Maui, Hawaii and has observed all the visible night sky ($\delta > -30°$). The survey is panoramic since it observes 3/4 of the sky (hence '3π'). Its rapid response consists of its capability of rapidly detecting an interesting astronomical event, such as a killer asteroid approaching. The telescope has a 1.4 Giga pixel camera and a field of view of 3 degrees, equivalent to six times the width of the full moon. The PS1 survey observed the night sky for a total of 3.5 years gathering up to 4 exposures per year in each of the 5 optical filters ($g_{\mathrm{P1}}r_{\mathrm{P1}}i_{\mathrm{P1}}z_{\mathrm{P1}}y_{\mathrm{P1}}$; Tonry et al. 2012), contrary to the SDSS. These filters are very similar to the SDSS filters, with the transformation between the SDSS and PS1 filters given by Tonry et al. (2012). Four out of the five filters correspond to SDSS's filters, with the SDSS's blue 'u' filter, replaced by an infra–red 'y' filter. Once the individual frames have been taken at the summit, they get downloaded and processed through the Image Processing Pipeline (Magnier, 2006, 2007; Magnier et al., 2008). Figure 1.6 shows the spatial coverage of the SDSS data (green). All of this coverage, combined with the dark blue coverage is the full spatial extent of PS1. The light blue corresponds to the $\delta < -30°$ region where PS1 does not observe.

In this section, I will give a brief technical outline of the various PS1 data versions that have circulated within the internal PS1 collaboration. Though these details are a little dry and not of much relevance to someone interested in the final data product, an overview of this is necessary to understand the way that the PhD thesis has evolved and been impacted by the various data releases as they have become available. These releases or processing versions (PV) to the PS1 collaboration have happened in three main phases. Each processing version has had a single epoch data release, containing time averaged photometric measurements of PS1 sources and a stacked catalogue, containing the stacked photometric measurements of those sources. The single epoch data of PV1 was released in mid–2012, with the stacked PV1 photometry available mid-2013. PV1 contained some 223 000 exposures over the whole sky. The second processing version became available in September–October 2014, containing a $\sim 25\%$ increase in exposures relative to PV1 (280 000) and pipeline improvements, and cleared a lot of artefacts in the data. Finally, in July 2015, the stacked PV3 catalogue became available with the total number of exposures of the whole survey containing some 375 000 exposures. Table 1.1 shows the depths of the PV2 data in relation to the SDSS depths. These values are taken from Metcalfe et al. (2013).

The start of my PhD in October 2012, coincided with the PV1 single epoch data release of that same year. As and when the subsequent data versions, as detailed in the previous paragraph, became available, the search algorithm for Local Group stellar substructure, which is detailed

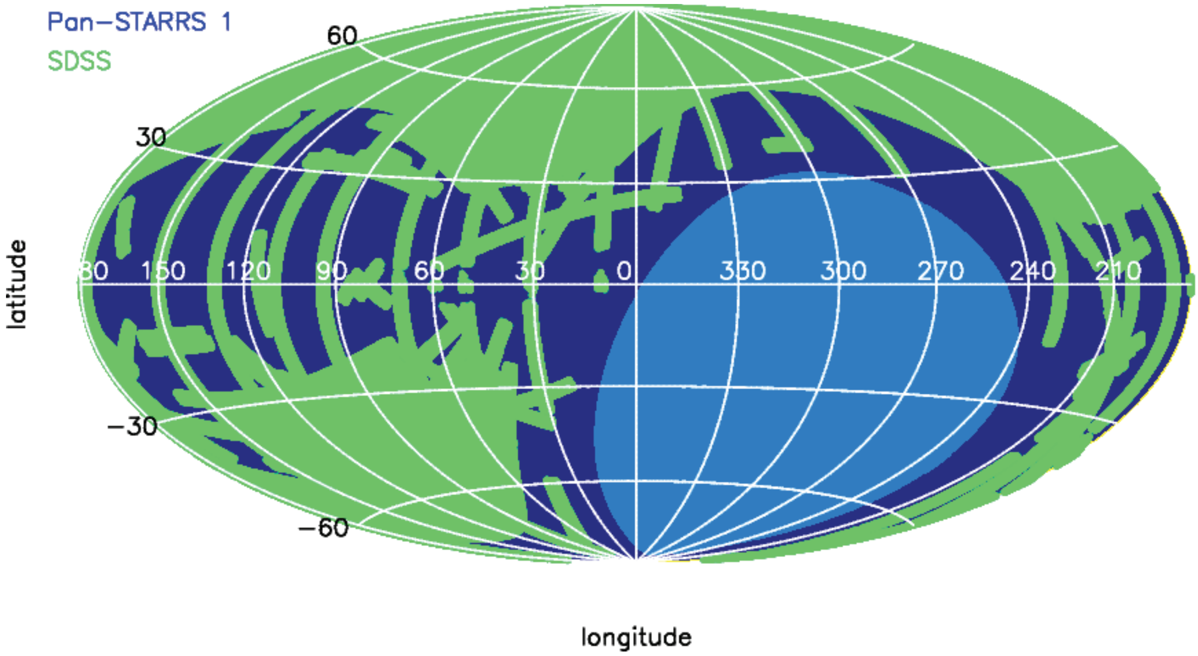

Figure 1.6 - The survey footprints of the SDSS (green) and PS1 (dark blue) in galactic co–ordinates. Light blue shows the area where neither SDSS or PS1 observe i.e. $\delta < -30°$. As can be seen PS1 contains just under double the coverage of the SDSS, making it a prime resource for the search of stellar substructure.

in Chapter 2, was repeated on the latest data set. While the PS1 single epoch data has been sublimely calibrated and contains exquisite photometry, this has not been the case for the stacked catalogues. The photometry for these catalogues was obtained by performing psf photometry on the co-added images. Since conditions varied over the course of the survey and thus when the exposures were taken, the best fitting psf for each source in each exposure changes as a function of time. In other words, differing psfs for each exposure were stacked one on top of the other. Photometry was then performed on these images. Ideally, we would have liked "forced photometry" where source detection is performed on the co–added image, but the positions are then subsequently used to perform photometry on the individual exposures. Finally the exposures and measurements are stacked, yielding good quality forced photometry. Consequently the photometry used through out the thesis has suffered from some photometric scatter of 0.1–0.2 magnitudes for 10–20% of the sources, particularly at the faint end where the effect of performing photometry on the co-added image, rather than the single images is the worst. For the purposes of Local Group satellite searches, the faint stars are very important as will be seen in the next chapter. The PV3 photometry has been available since mid-July, though unfortunately still not containing the forced photometry. To date, the search algorithm was performed on the PV1 (single epoch and stacks) and PV2 (stacks) data sets. The ultimate goal will be to perform the search on the final PV3 catalogues.

Table 1.1 - Depths for PS1, SDSS and SDSS 82.

Band	PS1 (50%)	PS1	SDSS DR8	SDSS S82
g	23.4	23.0	22.8	24.2
r	23.4	22.8	22.2	23.6
i	23.2	22.5	21.6	23.1
z	22.4	21.7	20.3	21.8
y	21.3	20.8	–	–

1.5.2 PS1 Local Group scientific output

The Key Project 5 of the PS1 collaboration, entitled "Structure of the MW and Local Group", has seen many other related MW science outcomes, with undoubtedly many more to follow. A few publications about stellar streams have resulted from the survey. These are for example the discovery of a new stream near the galactic bulge in the constellation of Ophiucius (Bernard et al., 2014a; Sesar et al., 2015). Other work conducted has led to a panoramic view of the bifurcation of the Sagittarius stream, especially interesting for its extension to the Southern galactic hemisphere (Slater et al., 2013). Slater et al. (2014) presents a panoptic view of the Monoceros ring and compares this to mock observations of simulations aimed at explaining the origins of Monoceros. One of the most interesting science results to result from PS1 is the 3–D dust maps, e.g. Schlafly et al. (2014a); Green et al. (2014, 2015), which in turn have allowed distances to be estimated to molecular clouds (Schlafly et al., 2014b, 2015). The coverage of the MW's disc, not observed by the SDSS, has allowed similar searches as ours for substructure in the form of open clusters, e.g. Lin et al. (2015). On a more theoretical note, Bernard et al. (2014b) derived fiducial sequences of 13 Galactic GCs and 3 open clusters using the PS1 photometry. Finally, PS1 as a time–domain survey is proving to be very valuable for variability studies, such as classifying and searching for variable stars such as RR Lyrae and cepheid stars (Hernitschek et al. in prep.).

1.6 The objectives of the thesis

Many of the objectives of this thesis can be seen in the context of the current challenges to the ΛCDM model. We saw in the previous sections of the introduction that the idea of a plane of satellites has been winning terrain, while suffering from the drawback that this plane currently looks plausible because most of the area probed around the MW, actually coincides with that plane to start with. The PS1 Survey with its three quarter sky coverage is the first survey that can make any quantative statement on this anistropy. The thesis has therefore consisted of two main objectives. The first was to search for new MW (or Local Group) satellites. The second aim has been to assess the recovery rate of simulated MW satellites, from which (an)istropy can be quantified. The second objective is a work in progress for which this thesis is a snapshot, such that a definite quantification of the (an)isotropy will soon be performed from the final data set (PV3).

In Chapter 2, I develop the search algorithm for stellar over densities on the PS1 survey. Here, I delve a little more into the PS1 specifics that influence the search algorithm's development.

I then proceed to develop the search algorithm along with a detailed mathematical explanation. Finally, I compare the efficiency of my search algorithm to other surveys such as the SDSS.

Chapter 3 describes the satellite discoveries that resulted from the search algorithm. This chapter provides further background information for the following three chapters.

Chapters 4, 5 and 6 contain the three papers that have resulted from my PhD work detailing the discovery and characterisation of five new MW satellites. The first two papers are published and the last one has just been accepted for publication.

In Chapter 7, the PS1 detections limits will be quantified. More specifically, this chapter aims to address what the recoverability is of MW satellites of different properties, if they are simulated and injected into the PS1 data.

Finally, Chapter 8 concludes with a summary of the thesis work. Here, I will also outline the next important steps that need to be undertaken to conclude any further PS1 work as well as providing a perspective of the field in general.

Chapter 2

An Automated Search for Local Group satellites with PS1 3π

At the turn of the century, with the advent of large CCD Sky Surveys such as the Sloan Digital Sky Survey (SDSS; York et al. 2000), innovative and different techniques were developed to find new, faint, stellar systems over large swathes of the sky. As already touched upon in the Introduction, pre-SDSS searches were limited to the photographic plates, which could only resolve bright DGs down to a surface brightness cut-off limit of $\mu \sim 25.5$ mag arcsec^{-2}(Whiting et al., 2007). Essentially, scanning lots of new CCD images would not work for two mains reasons. Firstly the data are too large to do this effectively, but more importantly DGs are just too faint to be visible on CCD images. The different techniques are all a variation on a theme, but rely on using an automated algorithm to search for spatial, stellar over densities corresponding to old, metal-poor populations in colour-magnitude space. Such techniques were first successfully applied on the SDSS (Koposov et al., 2008; Walsh et al., 2009) and led to the discovery of some $\sim$ 16 new DGs e.g. (Willman et al., 2005a,b; Belokurov et al., 2006b; Zucker et al., 2006b,a; Belokurov et al., 2007; Walsh et al., 2007; Belokurov et al., 2010). In this chapter I outline the technique that was developed specifically to the PS1 Survey, taking into account the survey specifics. Specifically, in section 2.1, a more detailed, yet compact overview of the technique is given. In section 2.2, a little detour is taken and the reader is provided with a broader understanding of some of the PS1 specific issues, such as star–galaxy separation, spatial inhomogeneity of the survey, amongst others that are important to know, since they influence the development of the search technique. Equipped with this information, the search algorithm along with a mathematical explanation are provided in Section 2.3. Finally, in sections 2.4 and 2.5 the interpretation of the algorithm output is explained as well as the efficiency of the technique compared to the SDSS searches.

2.1 Outline of the search algorithm

In this section, the reader is provided with the general concepts of the search algorithm, which is explained more in-depth in the subsequent sections of this chapter. The nature of DGs has already been established in the introduction: they are amongst the oldest and most-metal poor galaxies in the Universe. Since metal-poor and old stars are therefore the primary constituents of these galaxies, a sensible first step would be to isolate these types of stars in the PS1 data with information from theoretical stellar evolutionary tracks, i.e. isochrones. The next aspect which can be accounted for is the distance at which such a galaxy may lie: such galaxies can lie within the vicinity of the Milky Way (MW) or M31, the two galaxies the PS1 survey can probe in detail. Similarly the PS1 survey would be able to find isolated DGs in the Local Group as well. Previous discoveries of DGs show which ranges of distances within which these galaxies can occur. The distance is therefore taken into account by shifting the isochrones to several distance-moduli or distance bins such that the stars that lie on these evolutionary tracks at those corresponding distances may be isolated. Finally, the typical DG sizes can be accounted for by convolving the distribution of isolated stars with Gaussian (window) functions that are specifically tailored to the size of these galaxies, whilst subtracting out a convolution of the star density with far larger Gaussians to account for the slowly varying galactic background. This produces maps of over and under densities, which can be converted into significance maps. Accounting for background galaxy (cluster) contaminants, known objects in the Local Group and bright foregound stars, a list of significant detections can be determined, at which positions the Colour–Magnitude Diagram (CMD) and spatial distribution features can be investigated and studied more closely. In this analysis, the complex survey footprint is taken into account: some regions of the survey will have been better observed than others due to better weather conditions. Conversely some parts of the sky may have gaps or holes due to bad weather or chip gaps. These effects as well as developing the search algorithm on manageable sizes of data are taken into account in the search algorithm. These various steps are explored in the next sections of this chapter.

2.2 Pan-STARRS 1 specific issues

Before delving into the specifics of the search algorithm, I present here some of the specifics of the PS1 survey that influence the way the search algorithm is constructed and performed. In this section I will expand on the concepts briefly mentioned in the previous section relating to the application of the search algorithm on manageable sizes, the spatial completeness of the survey and finally star–galaxy separation.

2.2.1 Application of search algorithm to manageable data size

The size of the PS1 data for a single processing version containing all information related to the stacked data is 2 pettabytes or in other words: gigantic. Clearly, running a blind automated search over the whole sky will not work as the computer will probably be unable to handle the amount of data. It is therefore necessary to run the search algorithm on manageable sizes of data that are less memory intensive. To do this, a similar approach to Koposov et al. (2008) is adopted. After downloading the PS1 data, the PS1 sky is divided into smaller, separate patches on which the search algorithm is run. To avoid projection effects, galactic co-ordinates are converted into local tangentially projected co-ordinates. This is also elegant since – by construction – these patches end up being squares and therefore are symmetric. Though the size of the tangentially projected square is somewhat arbitrary, the following factors come into play: such squares of data should not be too large, for the computational issues already stated, but also to avoid distortion effects due to the tangential projection (Koposov et al., 2008). Similarly the patches should not be too small such that the search algorithm does not result in becoming an unmanageable process with many subfiles to manage. Therefore a size of 40 by 40 degrees^2, or 1600 degrees^2 was converged upon.

The tangential projection is performed by defining a projection point – in longitude and latitude – through which all other longitude and latitude positions are projected and relative to which all other longitude and latitude positions are defined. In the new tangential system, the projection point is centred at $(\chi,\ \eta) = (0°,\ 0°)$. If, for example, a centre is chosen at: $(l,\ b) = (30°,\ 35°)$, then in the new tangential co-ordinate system, χ and η, the galactic co-ordinates will correspond to $(\chi,\ \eta) = (0°,\ 0°)$. For a star at $l < 30°$, the star will be at $\chi < 0°$. Since the sizes of the patches are 1600 degrees^2, each galactic co-ordinate projected through the centre is only kept in the patch if it satisfies the patch size criteria, i.e. $-20° < \chi < 20°$ and $-20° < \eta < 20°$. At lower latitudes such a tangential projection will closely correspond between the galactic and tangential co-ordinate system e.g. in the previous example $l = 10°$ will more or less correspond to $\chi \sim -20°$. At higher latitudes, these effects become more noticeable as space gets squeezed into the ellipsoidal shape of the galactic coordinate system. Here, for example if projecting through the point $(l,\ b) = (210°,\ 70°)$, the spatial extent in galactic co-ordinates will be much larger than indicated by the 1600 degrees^2 extent in tangential co-ordinates.

Now that we know the best way to manage the data with the tangential projection, the last thing left to do is to define a set of longitude and latitude centres through which to project the data. To enable this, a sensible range of longitude and latitude centres should be decided upon, which take into account the Galaxy's morphology. Clearly, it is preferable to run the search algorithm in a way that avoids large chunks of the MW's disc and bulge as the density and number of stars is overwhelmingly high here. Even trying to find an $M_V = -6$ DG here would be extremely difficult, if not impossible. Another factor to consider is the effect of dust at very low latitudes, which will heavily extinct some regions. Motivated by this, an initial decision was taken to avoid regions at $|b| < 15°$. Avoiding these low latitudes, leaves 75°, North and South for the search. Since the patches are 40 by 40 degrees^2 in size, sensible latitude centres on which to run the algorithm are therefore $b = \pm 35°$ and $b = \pm 70°$. This means that the lower latitude patches roughly stretch in the following range: $\pm 15° < b < \pm 55°$. Conversely the high latitude patches cover approximately the following: $\pm 50° < b < \pm 90°$. This prescription allows for a five degree overlap between low and high latitude patches, to avoid any potential new satellites sitting on the boundary between two patches. Having defined the latitude centres, the longitude centres need to be determined. Again, to avoid satellite candidates sitting in regions that sit on the boundary between two patches, each patch overlaps with the adjacent patch. The amount of overlap is latitude dependent because of the projection effects previously mentioned. At low latitude: $b = \pm 35°$, patches are offset by 30° allowing for an approximate 10° overlap. At higher latitudes, an offset of 60° is sufficient to have overlap between the patches. The explanation in this last paragraph translates to the following longitude and latitude centres:

$l = 0°, 30°...330°$ for $b = 35°$
$l = 30°, 60°...240°$ for $b = -35°$
$l = 30°, 90°...330°$ for $b = 70°$
$l = 30°, 90°...270°$ for $b = -70°$

For projections at $b = -35°$ and $b = -70°$, no more patches are generated for longitudes higher than $l = 240^\circ$ and $l = 270^\circ$ respectively as this corresponds to the $\delta = -30^\circ$ limit where PS1 stops observing. This patch configuration was adopted for the PV1 single epoch and stacked data. Even taking into account the concerns raised earlier about dust and high star density at low latitudes, the patch configuration was extended for the PV2 search the configuration to include 10 more degrees of PS1 data at lower latitudes: ($|b| > \pm 5^\circ$. The following patches were run in PV2 as well, though this time 20 by 40 degrees^2, to avoid a three quarter overlap with patches at $b \pm 35^\circ$:

$l = 0^\circ, 30^\circ, 60^\circ ... 240^\circ$ for $b = 25^\circ$
$l = 0^\circ, 30^\circ, 60^\circ ... 240^\circ$ for $b = -25^\circ$

Figure 2.1 shows the patches the search algorithm was run on in galactic co-ordinates with the PS1 footprint included as well (blue). There is no significance in the different colours of these patches, except to show more clearly the extent of the different patches and how they overlap, for example, at different latitudes. Some of the patches are omitted from the plot to avoid cluttering it too much. More details about this can be found in the caption.

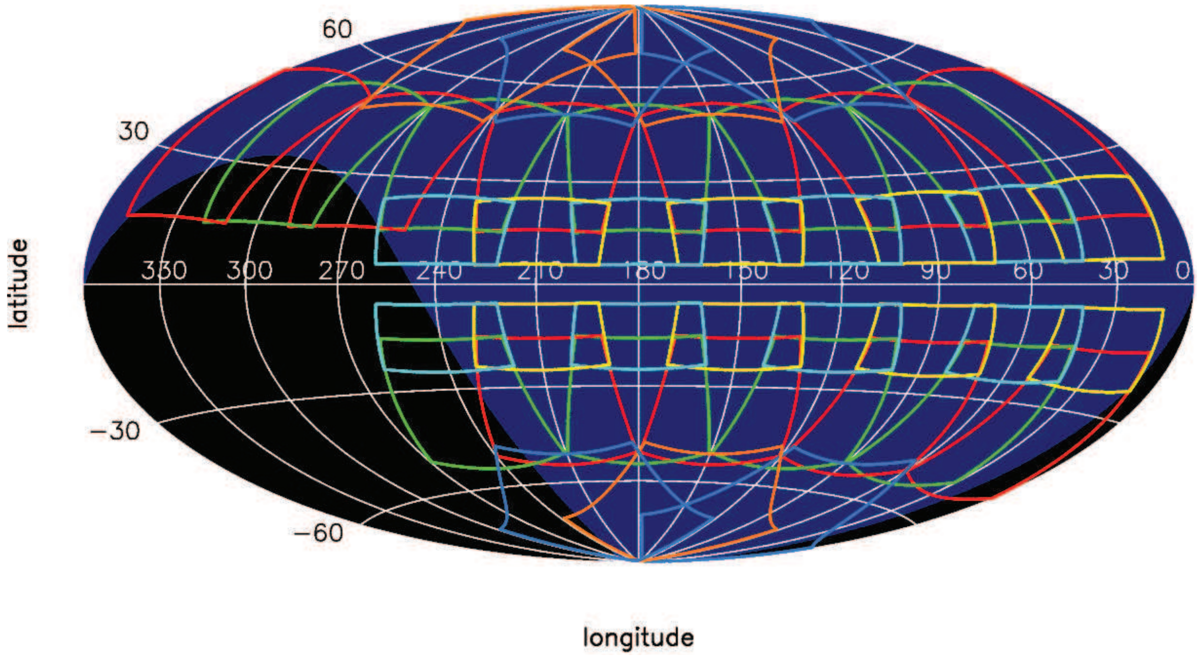

Figure 2.1 - Longitude versus latitude for the whole sky, containing the PS1 footprint (dark blue). The various squares represent the 1600 degrees^2 patches, on which to run the algorithm. A combination of colours is used to represent the different latitudes at which the patches are situated, with cyan and yellow representing patches centred on $b = \pm 25^\circ$, red and green represent $b = \pm 25^\circ$ and finally, orange and intermediate blue show the patches at $b = \pm 70^\circ$. The choice of two colours per latitude is to make the overlap between patches more easily visible. To avoid cluttering the plot, the patches centred at $(l,\ b) = (0^\circ,\ \pm 25^\circ)$, $(l,\ b) = (0^\circ,\ \pm 35^\circ)$, $(l,\ b) = (30^\circ,\ \pm 70^\circ)$, $(l,\ b) = (270^\circ,\ \pm 70^\circ)$, $(l,\ b) = (330^\circ,\ 70^\circ)$ are omitted. For complete list of the patches, please see the list of patches in section 2.2.1

2.2.2 Star–galaxy separation

The next PS1 specific issue to consider is star–galaxy separation. Though the search algorithm searches for new DGs, background galaxies or galaxy clusters which may lie further away can have magnitudes and colours which are similar to constituent stars of DGs, especially at the faint end[1]. The search algorithm will have maximal performance under the assumption that stars and galaxies can be separated successfully. So how can it be known if a source is a star or a galaxy? The first obvious answer is whether a source is point-like or extended. To assess whether or not this is the case, one can look at point spread function (psf) magnitudes and aperture (ap) magnitudes. The former determines the magnitude by fitting a psf to the source, whereas the latter determines the magnitude by placing a fixed aperture around the source. If the difference between these magnitudes is minimal, we know that the psf and ap are performing well in containing most of the flux. If there is a discrepancy between them, then the psf is not accounting for all the flux of an extended source and we are in the presence of a galaxy. At the bright end, using the difference between psf and ap magnitudes typically works well to determine which type of object a source is, since these objects are well resolved. At the faint end, where things become unresolved, these clear boundaries become blurred and a psf–ap cut will not be ideal.

My approach in dealing with this problem has varied over the course of the PhD. For the PV1 single epoch data, I used a probabilistic approach, where a star or galaxy was assigned a number between zero and one, where zero corresponds to a galaxy and one to a star. My supervisor, Nicolas Martin derived this probabilistic approach by using the Pan Andromeda Archaeological Survey (PAndAS; Ibata et al. 2007; McConnachie et al. 2008) around M31 as the ground truth. The PAndAS coverage coincides completely with the PS1 coverage, but is at least two magnitudes deeper than PS1, making the survey a valuable tool in assessing the star–galaxy separation problem. At fainter magnitudes in PS1, he used the information from the better resolved data in PAndAS where a clear distinction between stars and galaxies can be comfortably made. The model he used to determine these probabilities is the following:

$$P_i = \frac{\eta A_{star} m^{b_{star}} G(\Delta m, \mu_{star}, \sigma_{star}) + (1-\eta) A_{gal} m^{b_{gal}} G(\Delta m, \mu_{gal}, \sigma_{gal})}{1 + \exp\frac{\mathrm{mag} - mag_0}{\rho}} \tag{2.1}$$

where m and Δm refer to the location of the star in the psf, psf-ap plane in one band, where $A_{star/gal} m^{b_{star/gal}}$ are information related to the luminosity function. The denominator models the spatial completeness of that particular part of the PS1 sky, where m_{lim} is the place where photometric errors are 0.1 and where ρ parametrises the rapidity of the transition between complete and incomplete data. Finally η is the stellar fraction, with $1 - \eta$ correspondingly showing the galaxy fraction. Evaluating the likelihood of this model given the data, delivers a probability of a source being a star or a galaxy. Please note that I was not instrumental in the above analysis as this was conducted prior to my PhD starting. I simply received a list of these probabilities at the beginning of my PhD.

For PV1 and PV2 stacked data, a less sophisticated approach was used. Unfortunately, the derivation of these probabilities was not possible for the stacked data, due to the lack of forced

---

[1] Remember that the search algorithm relies on isolating spatial over densities of stars that are old am metal–poor in the CMD, using isochrones.

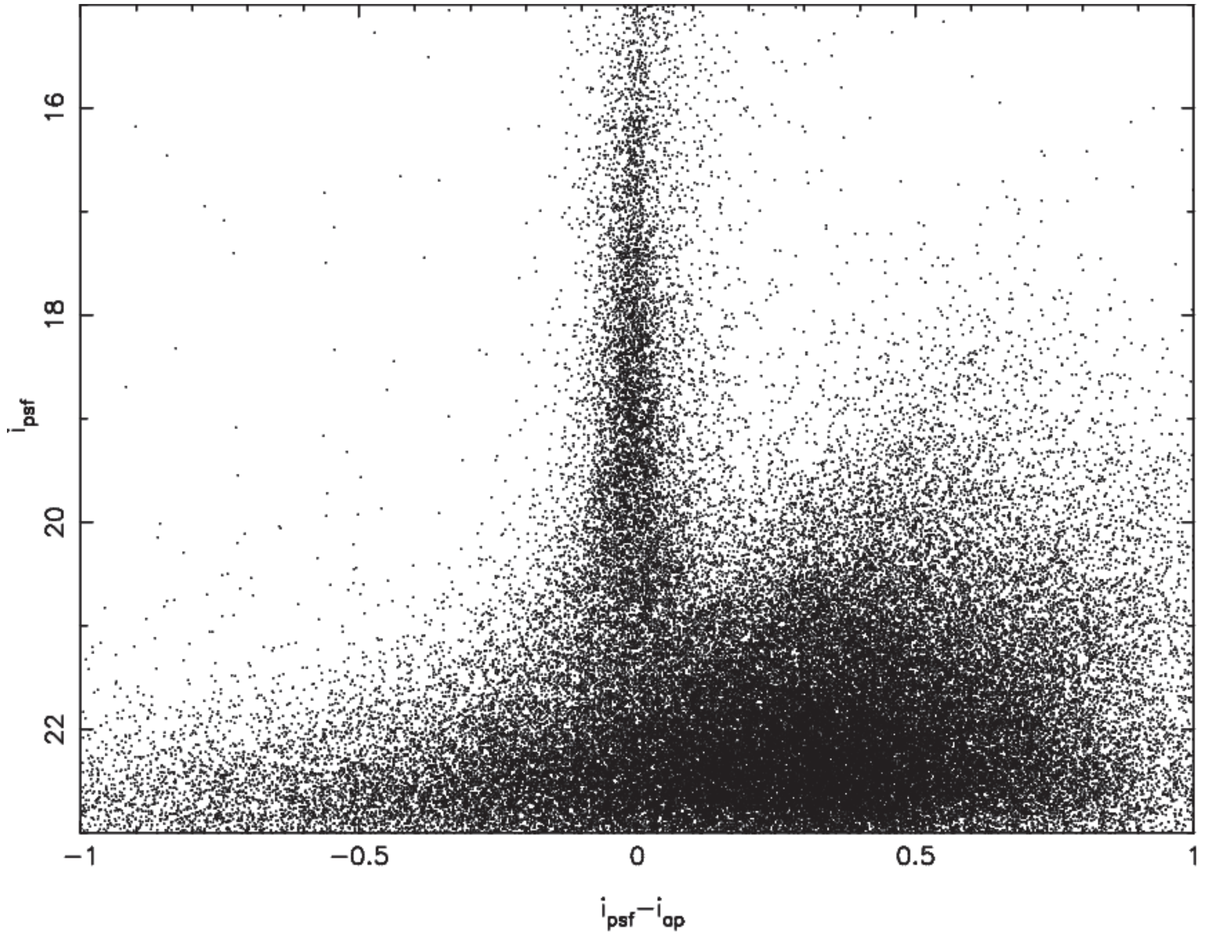

Figure 2.2 - $i_{psf} - i_{ap}$ vs. i_{psf} for $\sim$ 120 000 sources in the $60^\circ < b < 90^\circ$, $0^\circ < l < 360^\circ$ range. At bright magnitudes $15 \lesssim i \lesssim 20$ stars sit very clearly around 0. For sources fainter than i$\sim$20, things start to get increasingly difficult as stars and galaxies merge into one large blob at the faint end. The PS1 flag, which was used to identify stars, takes this variation of $psf - ap$ as a function of magnitude into account, when it isolates stars, i.e. at the bright end, it has stricter limits in $psf - ap$ of what is deemed a star, whereas at the faint end, there is a lot more leeway. The conservative $psf - ap < 0.3$ cut that was used to isolate galaxies, does a reasonable job of isolating galaxies, but also with some contamination from stars.

psf photometry in either data versions[2]. An initial experimentation with a simple psf-ap magnitude cut of 0.15, 0.2 and 0.3 was conducted to see what impact it would have on our search algorithm results. This approach was found to be unsatisfactory since it did not do a good job of weeding out background galaxies and galaxy clusters at the faint end in the stellar samples. For reasons we shall see later, it will be desirable to construct a map containing galaxies too[3]. Stellar and galaxies samples were constructed with two separate approaches. The PS1 stellaricity index was used to find stars. This stellaricity index is a smarter psf-ap cut, which changes as a function of magnitude amongst others. The stellaricity index did a far better job of containing stars than any experimentation with a psf-ap cut. A galaxies' map was constructed using a conservative psf-ap magnitude cut of 0.3, to make sure that not too many stars would be classified as galaxies.

---

[2] the issues relating to the forced photometry were already addressed in section 1.5.

[3] This will be used as a means of cross-referencing significant detections outputted by the search algorithm in the stellar maps with significant detections in the galaxies' maps.

Figure 2.2 shows $i_{psf} - i_{ap}$ as a function of i_{psf} for $\sim$ 120000 stars and galaxies near the Northern galactic cap. If we now return to equation 2.1, it can be seen why this approach for PV1 and PV2 stacks is less sophisticated. The probability in equation 2.1 reduces to two probabilities: 1 for a star and 0 for a galaxy, whereas the single epoch data allowed for this number to vary between 0 and 1. Figure 2.3 shows the result of querying the PS1 database for stars (left) and galaxies (right) for a 1600 degrees^2 patch. This patch is centred on $(l,\ b) = (30°,\ 70°)$ and fully coincides with the SDSS coverage. This plot is colour-coded by number of stars per pixel for stars and galaxies of $15 < i < 23$. The map on the left clearly shows the distribution and variation of sources over the sky that one would expect from a stellar map, whereas the galaxies' map displays a more filamentary structure.

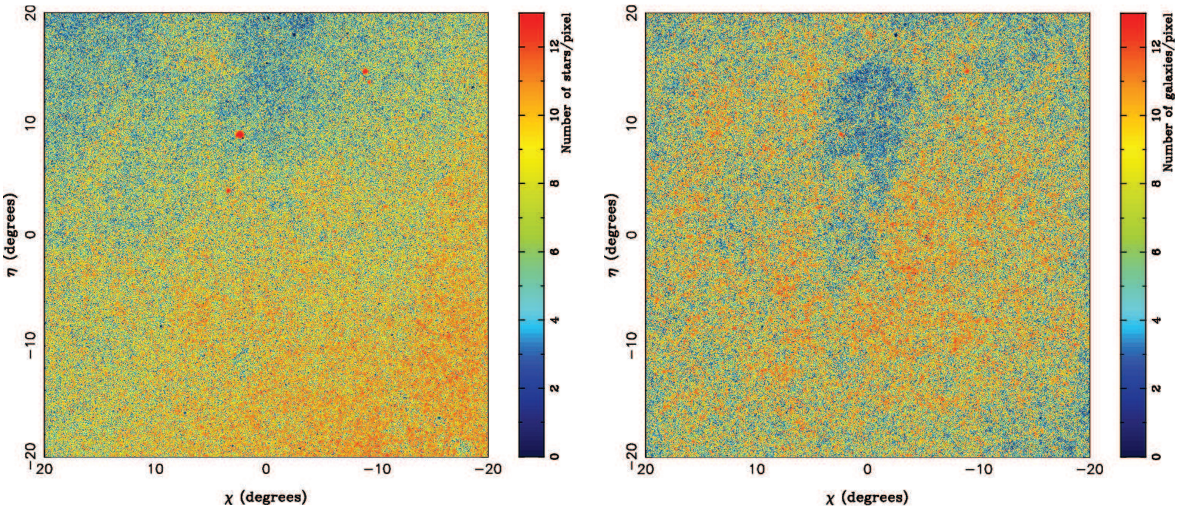

Figure 2.3 - Stellar map (left) and galaxies' map (right) for a PS1 1600 degrees^2 patch, centred on $(l,\ b) = (30°,\ 70°)$ also observed by the SDSS. This plot is colour-coded by the number of stars per pixel for stars or galaxies of $15 < i < 23$. The map on the left clearly shows the distribution and variation of sources over the sky that one would expect from a stellar map, whereas the galaxies' map displays a more filamentary structure. In both maps the effects of shallower data and holes can be seen. For example in the galaxies' map at $(\chi,\ \eta) = (0°,\ 10°)$, the data look a lot shallower than at $(\chi,\ \eta) = (-10°, -10°)$.

2.2.3 Dust

Having outlined a methodology by which stars and galaxies can be retrieved, the next step is to construct patches of 1600 degrees^2 for a stellar sample and a galaxies sample. To do this, the PS1 database is queried using the star–galaxy separation as already described in section 2.2.2. Before tangentially projecting the stars through the various centres to get the relevant patches, as described in sections 2.2.1, the stars need to be de-reddened to take into account the effects of dust. To do this, the dust maps from Schlegel et al. (1998), adopting the extinction coefficients of Schlafly & Finkbeiner (2011) are used. These coefficients are $A_g = 3.172$, $A_r = 2.271$ and $A_i = 1.682$. A panoramic view of the dust, colour-coded by $E(B-V)$ can be seen in Figure 2.4.

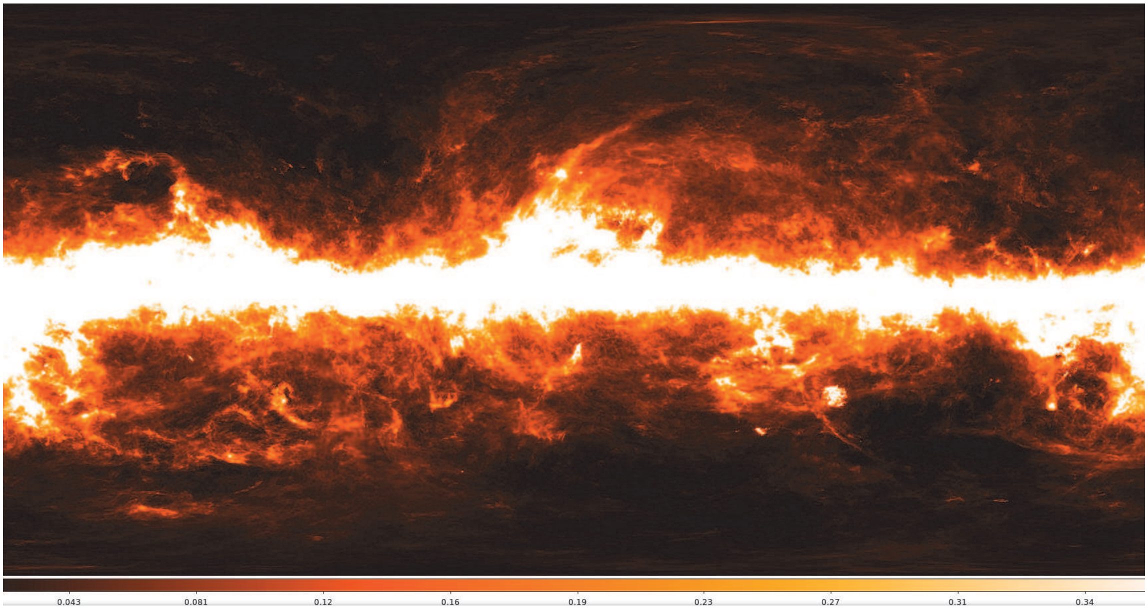

Figure 2.4 - A panoramic view of the Schlegel et al. (1998) dust maps, colour-coded by $E(B-V)$. These values along with the extinction values from Schlafly & Finkbeiner (2011) are used to de-redden the magnitudes.

2.2.4 Spatial completeness

Throughout this PhD thesis, the PS1 survey has been gathering and stacking ever more data, reflected by the different processing versions (PV1, 2 and 3) that have been released to the internal collaboration over the years. This means that the spatial inhomogeneity has varied over the course of these processing versions and has decreased with later PVs. For reasons that will become more apparent in the next section (2.3), the completeness of the survey needs to be quantified as the convolution search algorithm will be impacted by and depend on it. To resolve the spatial footprint of the survey on a sufficiently fine grid, the PS1 sky is pixelised in 0.5×0.5 arcmin^2 pixels for each band of interest. For a specific band, the star that lies closest to the centre of the pixel is determined. That same star is then identified in the other four PS1 bands. If an observation of that star exists in at least two other PS1 bands (other than the band it was originally found in), the pixel is deemed ‘complete’ and assigned a value of 1. If the criterion is not satisfied, the pixel is deemed ‘incomplete’ and given a null-value. A value of -1 is assigned to pixels that are too extincted by dust: $E(B-V) > 0.555$ (Majewski et al., 2003). Though the physical origin of 0 and -1 are different, they correspond to the same situation, namely a lack of data for the particular pixel in the sky. Hence -1 is actually re-assigned to 0. This approach effectively boils down to observing the star in three different bands, from which (in)completeness is determined. This process is done repeatedly for every single pixel over the whole sky and for each band.

This approach was developed by Nicolas Martin prior to the start of my PhD. I used this approach to construct completeness maps of the whole PS1 sky. Figure 2.5 shows a comparison of the completeness in the PV1 single epoch data and the PV2 stacked data, where blue indicates a complete pixel (1), green displays incomplete pixels (0) and -1 should be dust extincted pixels (not present here since this patch is at high latitude in the halo). The data coverage improvement as a function of time can be clearly seen, with the PV1 single epoch data containing a lot more holes than the PV2 stacked coverage, which is essentially complete for this part of the sky. These are the same patches as in Figure 2.3, i.e. centred on $(l, b) = (30°, 70°)$.

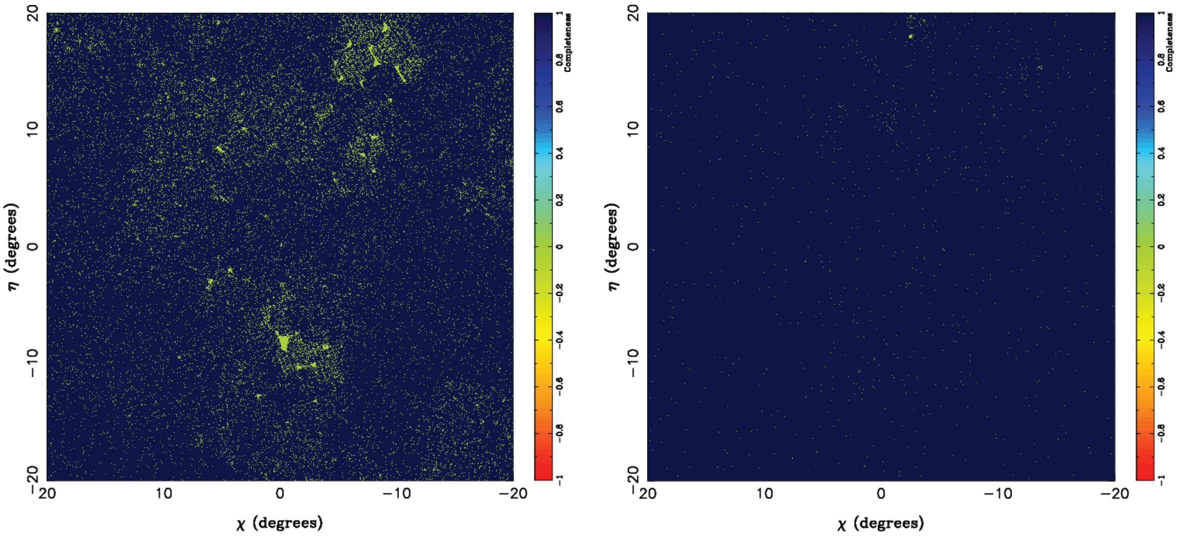

Figure 2.5 - Completeness pixels of the PV1 single epoch data (left) vs. the PV2 stacked data (right), where blue indicates complete pixels (1), green displays incomplete pixels (0) and -1 should be dust extincted pixels (not present here since this patch is at high latitude in the halo). The right hand side panel is more complete since it contains more data (PV2), whereas the PV1 single epoch data still contains quite a few holes. These two patches correspond to the same coverage as Figure 2.3.

2.3 Satellite search algorithm in Pan-STARRS 1 3π

In this section, I will develop the tools and the various aspects that come into play for the search algorithm. Before constructing a search algorithm, it is useful to consider which part of the 4-D parameter space, e.g. metallicity, age, size and distance are worthy exploring. Which values of this 4-D space are typical DGs most probable to take on? How can that information be used to tailor the search algorithm such that its efficiency is maximised? In a Bayesian approach, this would come down to constructing sensible priors, which are used to conduct the search. The best way to do this is to use the information of the SDSS discoveries to constrain the right parts of parameter space. In Section 2.3.1, I will look into how information from isochrones representing typical DG ages and metallicities can be used to isolate the most likely DG stars. In the ensuing Section 2.3.2, the distance at which these satellites may lie will be folded in. Finally, in Section 2.3.3, the mathematics of the convolution search algorithm are detailed, which also take into account the final dimension of the 4-D parameter space, which is the typical size of the DG.

2.3.1 Age and metallicity: tool to isolate potential dwarf galaxy stars

Since DGs are some of the oldest galaxies known, whose star formation is thought to be shut down early on in the Universe, a sensible assumption is that DG member stars are metal-poor and old (Brown et al., 2012). In terms of photometry, this assumption very broadly translates into blue stars in the CMD. To understand this better it is useful to consider the stellar evolutionary features of two known DGs found in the SDSS as a talk-through example.

Figure 2.6 shows the CMDs of the faintest SDSS DG Segue 1 ($M_V = -1.5$) and the third brightest DG Boötes I ($M_V = -6.3$) in the left and right panels respectively. In each case the stars are shown within one half-light radius of their centres, adopting the favoured structural parameters (Martin et al., 2008).

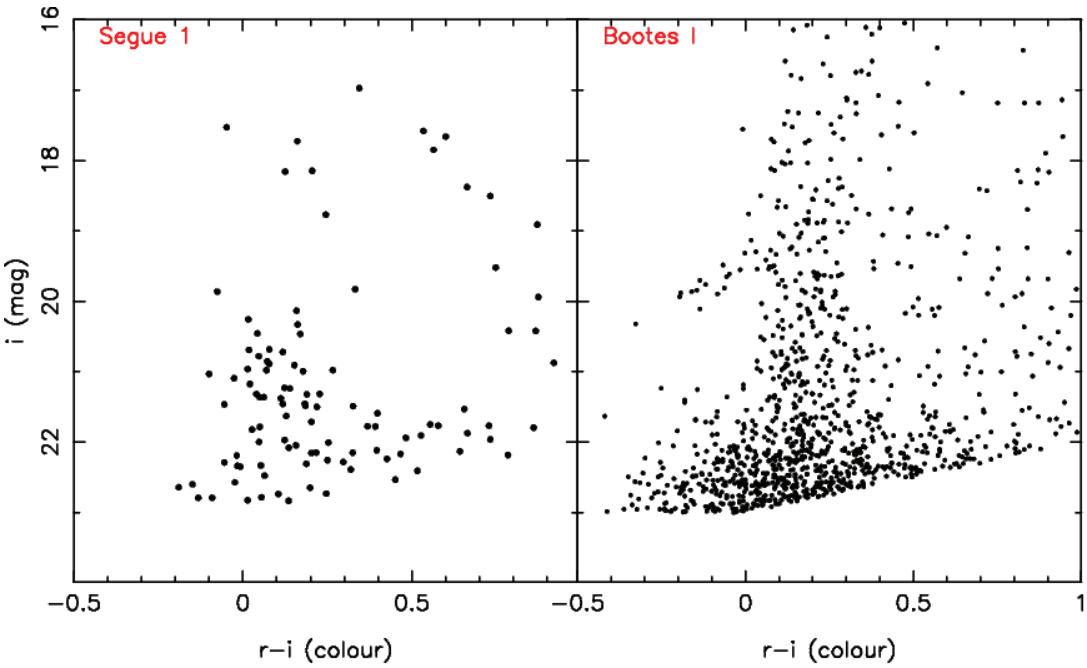

Figure 2.6 - CMD for two DGs found in the SDSS: Segue 1 ($M_V = -1.5$) and Boötes I ($M_V = 6.3$). The panels on the left and right show all blue stars ($r - i < 1.0$) within two half-light radii of the centre of the two satellites. The stellar evolutionary features of Boötes I are very clear, with a main-sequence turn-off, pronounced horizontal branch and tip of the red giant branch. In the case of Segue 1, the features are a lot less pronounced and show just a mild over density of blue stars.

If we consider Boötes I, we can clearly see a pronounced horizontal branch at $i \sim 19.5 - 20$, with a red giant branch extending up from $i \sim 19$ to $i \sim 16$ for $0.1 < r - i < 0.4$. If we go fainter than the blue horizontal branch, we can also see the giant branch continue down towards the main sequence turn-off which disappears into a smudge of stars at the edge of the detection limit. While Boötes I is visible as a spatial over density in the SDSS data, even without making a colour-cut to isolate blue stars, say $-2.0 < r - i < 1.0$, this is a lot less obvious for a satellite such as Segue 1. Let us re-consider the figure. In this example, the only really obvious feature is a main-sequence extending from $i \sim 22$ up to $i \sim 20$. There are very few stars that would constitute red giant branch stars or horizontal branch stars. In this case, one relies on finding an over density corresponding to some $\sim 30 - 40$ blue main-sequence stars relative to a neighbouring field region. The plots therefore highlight the varying luminosities these satellites can have and how (un)obvious these stellar evolutionary features can be.

A first obvious thing that can be done to select potential blue, metal-poor satellite stars is to just apply a simple colour-cut. (Koposov et al., 2007) adopted this approach to quantify the detectability of the SDSS satellites [4]. Although this method will yield the detection of both

---

[4] Note that at the beginning of the PhD such a colour-box was applied to the PV1 single epoch data.

objects (on deep enough data), a list of possible satellite detections based on a colour-box cut will include many blue stars that may not show any coherent stellar evolutionary tracks pertaining to a satellite. It is for these reasons a more refined approach was adopted that followed the Walsh et al. (2009) efforts [5]. Here, stars are isolated making use of the stellar tracks or isochrones, which correspond to two of the 4-D parameter space: metallicity and age. Taking a representative sample of isochrones in age and metallicity of DGs, an area in colour–magnitude space, for a fixed distance, can be defined where a star is deemed a likely DG star candidate. Effectively what this comes down to is assigning a probability of one or zero to a PS1 star. If the star lies in a part of colour–magnitude space that coincides with the isochrone(s) location, then the star is of interest and assigned a probability of one. If this criterion is not fulfilled, a star is discarded with a zero probability.

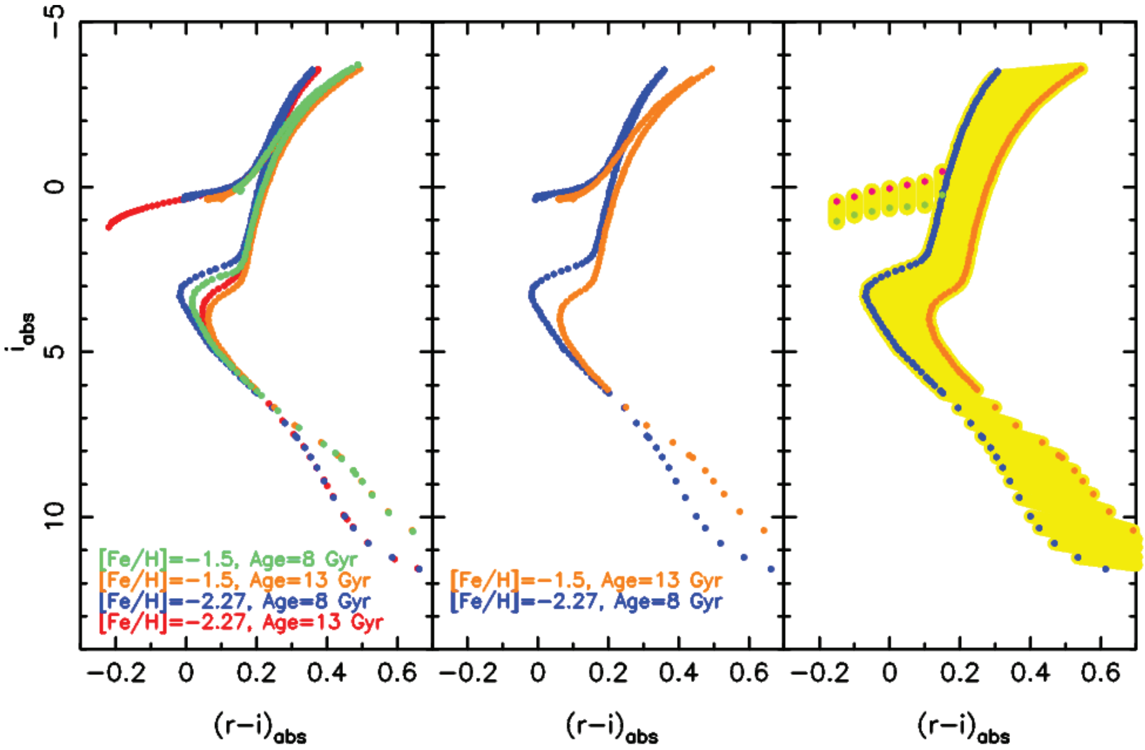

Figure 2.7 - *Left:* Four sets of isochrones, corresponding to [Fe/H] = −1.5, t = 8 Gyrs (green), [Fe/H] = −1.5, t = 13 Gyrs (orange), [Fe/H] = −2.27, t = 8 Gyrs (blue), [Fe/H] = −2.27, t = 13 Gyrs (red). *Middle:* The reddest ([Fe/H] = −1.5, t = 13 Gyrs; orange) and bluest ([Fe/H] = −2.27, t = 8 Gyrs; blue) isochrone are selected. *Right:* The two isochrones are shifted redward and blueward by $r - i = 0.05$ to allow for more stars within the isochrone contour. A horizontal branch is constructed, allowing for fainter and brighter stars than the limits given by the isochrones. Yellow indicates the contour within which stars can lie.

At this point we need to go into the details of how the isochrone information is used. Following Walsh et al. (2009), an upper and lower limit in age and metallicity can be defined in colour–magnitude space, which encapsulate all the likely ages and metallicities of SDSS–type DGs can have: [Fe/H] = −2.27, t = 8 Gyr and [Fe/H] = −1.5, t = 13 Gyr. For this purpose, PARSEC[6] isochrones (Bressan et al., 2012) were chosen and downloaded. The four possible isochrone combinations can be seen in the left hand side panel of Figure 2.7. It can be seen that

---

[5] As of PV1 stacked data and thereon, this approach was adopted.

[6] http://stev.oapd.inaf.it/cgi-bin/cmd

the bluest and reddest isochrone are those corresponding to [Fe/H] $= -2.27$, $t = 8$ Gyr and [Fe/H] $= -1.5$, $t = 13$ Gyr. These two isochrones are chosen as the outer limits of isochrone contours (middle panel). The red and blue isochrone are offset by 0.05 in $r - i$ redward and blueward respectively, to allow for more stars in the isochrone contour (right panel). The horizontal branch is omitted and re-constructed, allowing for a broader upper and lower boundary in magnitude to encompass more stars (right panel). The horizontal branch is a little redward (to $r - i \sim -0.15$) than the bluest PARSEC horizontal branch ([Fe/H] $= -2.27$, $t = 13$ Gyr).

2.3.2 Folding in the satellite's distance

In the last Section, we saw how old and metal-poor stars can be isolated; however, this did not take into account the distance at which the DGs lie. In fact, we were dealing with absolute magnitudes and not apparent magnitudes, but this can be easily resolved using the distance-modulus equation [7]. For example an horizontal branch ($M_i \sim 0$ for $-0.2 < (M_r - M_i) < 0.1$) of a DG at a distance of 25 kpc or $\mu = 17$ has an horizontal branch at $m_i \sim 17$, whereas a DG out at 100 kpc, will have this horizontal branch at a fainter magnitude ($m_i \sim 20$). This brings us to the third dimension which is the distance. From the SDSS satellites, we have an idea of what the typical distances of these satellites are. The nearest SDSS MW satellite Segue 1, lies at a distance of 23 kpc, while Leo T, the furthest MW satellite lies at 417 kpc (Irwin et al., 2007). The PS1 survey's satellite galaxy mining possibilities are not just confined to the MW: with a limiting magnitude of $i \sim 22.5$ (in PV2), a red giant branch spanning $M_i \sim -3$ to $M_i \sim 0$ corresponds to $i \sim 21.0 - 24.0$ at the distance of M31. Therefore the potential of finding satellites in PS1 is limited to and just beyond the distance of M31. Following the same argument, a bright Local Group DG anywhere up until the distance of M31 could also be resolved. Such a satellite was found for instance very recently in the DES survey with the discovery of Eridanus II at a distance of ~ 380 kpc (Bechtol et al., 2015; Koposov et al., 2015).

The possible distances at which Local Group satellites can lie at can be accounted for by cycling through various distance intervals. To do this, the isochrones can be shifted to the required distances using the distance-modulus equation. At any given distance, the stars that lie within the isochrone contour or mask can be isolated. However, since no magnitude measurement has zero-uncertainty and uncertainties increase with fainter magnitudes, the shape of the isochrone mask needs to be widened. To account for this, the average uncertainty in colour is calculated and widened by that amount for a given magnitude bin. More specifically, the isochrones are splined and defined at 0.1 magnitude intervals. For that magnitude interval, the average colour uncertainty is calculated for all stars that lie within $-2.0 < r - i < 1.0$ for a given patch (1600 degrees^2) on which the search algorithm will run. The reason for having a patch specific widening of the isochrone is to avoid widening the isochrones by an arbitrary amount uniformly over the whole sky, which probably does not account for the average uncertainty depending on location (high lattitude or low lattitude) or regions of patchy coverage versus deep coverage areas. To summarise, the isochrones are widened in colour with a magnitude and patch-dependency factors.

Accounting for distance, I cycle through distances in 0.5 distance-modulus steps starting at a distance-modulus of 17.0 and continuing all the way to distances just beyond M31 at a

---

[7] $\mu = m - M = 5\,log_{10}(d) - 5$

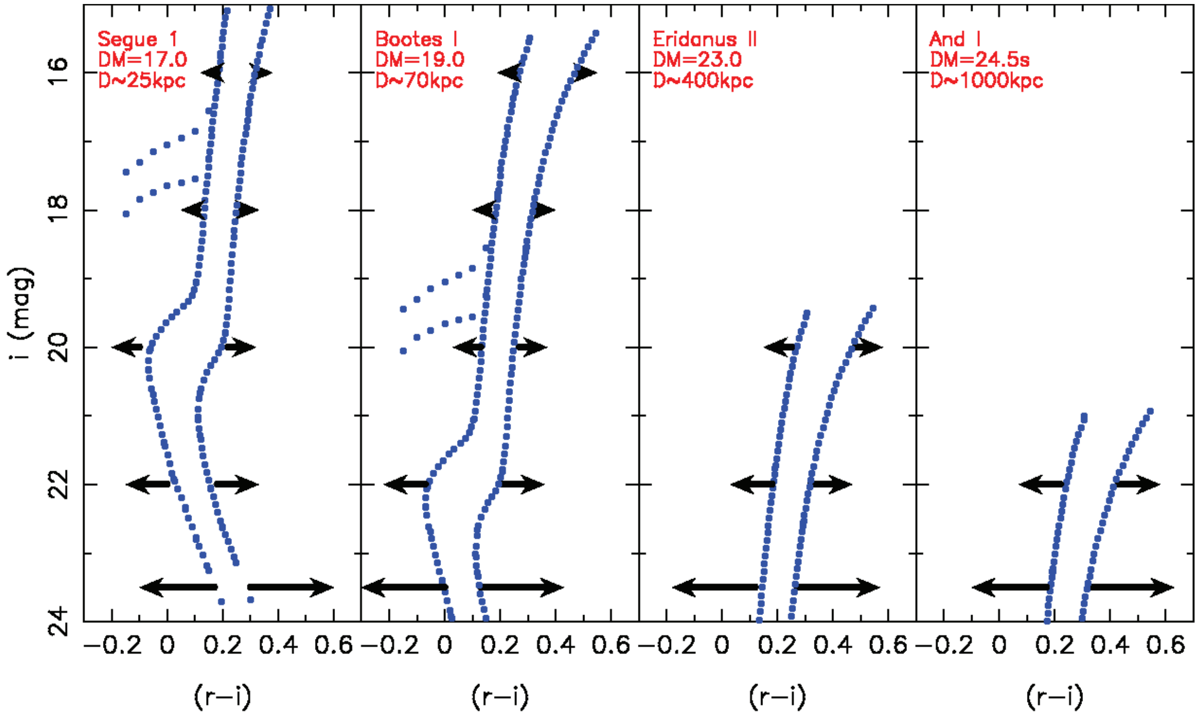

Figure 2.8 - Four sets of isochrones defining the contours within which stars can lie. The length of the arrows indicate the typical width by which the isochrones are widened for a given 1600 degree^2 patch. The distances of these four isochrones correspond roughly to the distances of four known DGs: Segue 1 (25 kpc), Boötes I (70 kpc), Eridanus II (400 kpc) and Andromeda I (1000 kpc)

distance-modulus of 24.5. This means that 16 different distance bins are explored. To give an idea as to which stellar evolutionary features are situated where in colour-magnitude space, Figure 2.8 shows four sets of isochrones shifted to different distances, indicating a hypothetical but realistic shift (black arrows) of the mask to account for the photometric uncertainties. The four panels correspond to distance-moduli of 17.0 (25 kpc), 19.0 (70 kpc), 23.0 (400 kpc) and 24.5 (1000 kpc) which broadly correspond to distances of Segue 1, Boötes I, Eridanus II and Andromeda I. The elegance of using isochrones is demonstrated here: since photometry is more precise at brighter magnitudes, at closer distances, individual features such as the tip of a red giant branch, the horizontal branch and possibly the main-sequence turn off should be visible for different distance-moduli (e.g. Segue 1 vs. Boötes I). At distances above 200 kpc, these features become less important to detect since the photometric uncertainties start to dominate. For example at a distance-modulus of 21.0-22.0, the horizontal branch will not be clearly visible within the isochrone as the colour uncertainties become too large and everything becomes one big smudge. At larger distances the use of isochrones becomes less effective as the isochrone mask tends more to a colour box cut.

Figure 2.9 shows the effect of using an isochrone mask to resolve the different stellar evolutionary features associated to Boötes I. The top panel shows the 1600 degree^2 patch centred on $(l, b) = (30°, 70°)$, containing Boötes I (red circle). This patch contains all the stars that were isolated in that part of the PS1 sky using the isochrone mask, shifted to the distance closest to Boötes I ($\mu = 19$), which are the stars (black) in the bottom panel. The isochrone mask (red), widened for the colour uncertainty can also be seen on the bottom panel. Boötes I's stars within 1 half-light radius are overplotted in light blue. Clearly, a large fraction of Boötes I's

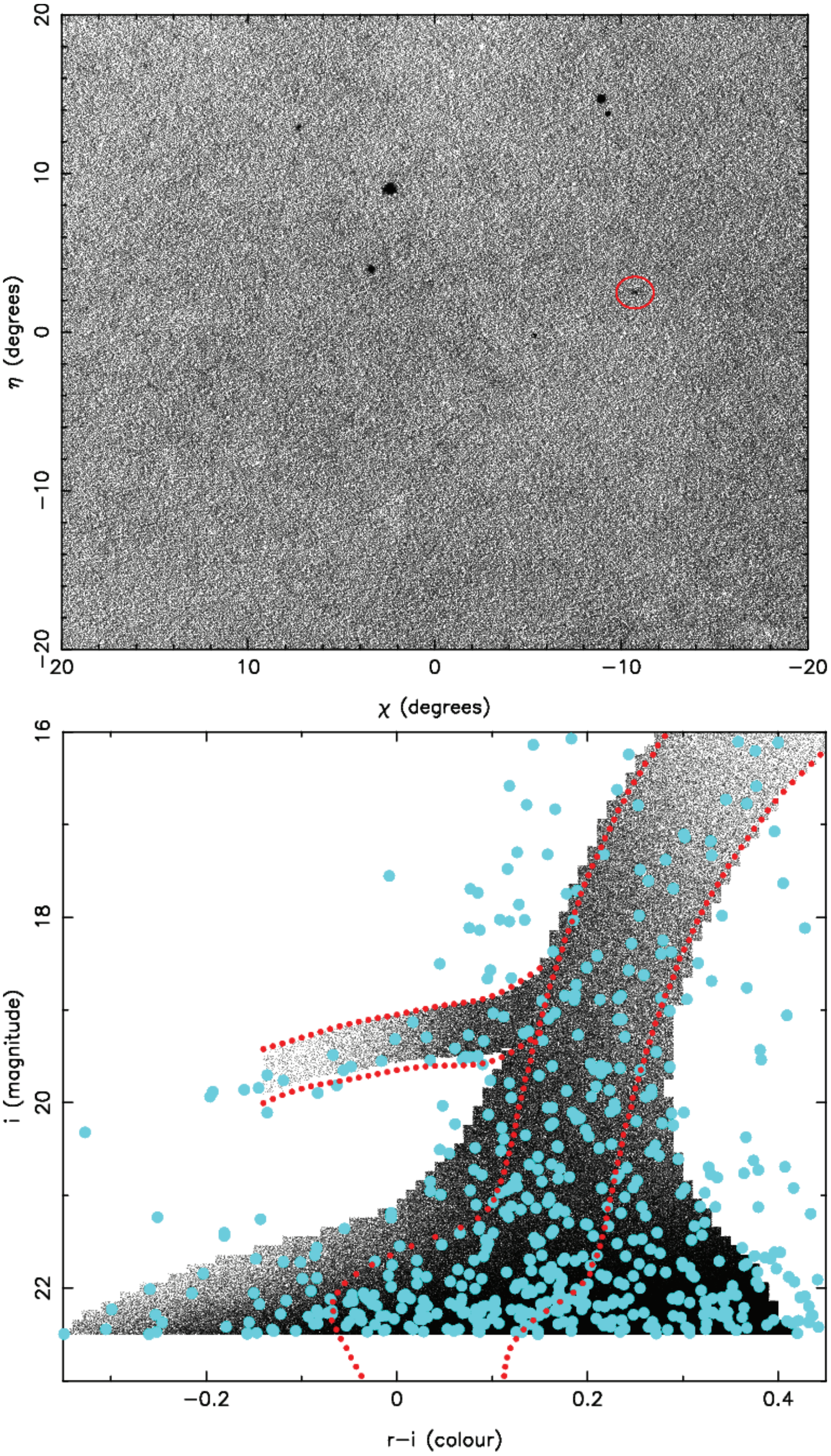

Figure 2.9 - Spatial distribution of the subset of stars that are selected as metal-poor blue stars (top), corresponding to all the stars (black) in the isochrone on the bottom panel. The red circle corresponds to the location of Boötes I, which displays a spatial over density. The light blue stars in the bottom panel show Boötes I's stars within 1 half-light radius. Clearly, many of Bootes I's stars ($\mu = 19.1$) are best picked up by the isochrone contour shifted to $\mu = 19.0$

stars are picked up by the mask, highlighting the power of using the isochrone mask. It must be noted that this example is somewhat contrived since this satellite is the third brightest one found in the SDSS (After Canes Venatici I and Hercules) and therefore is a rather obvious detection. With a colour-box approach such as Koposov et al. (2007) this detection would have made it to the top of a list of significant detections as well. The power of the isochrone will be far more readily visible in the faint regime where in some cases just an over density of some twenty to forty stars needs to be found.

2.3.3 The search algorithm explained

Having accounted for the typical population of stars a DG has and the distances at which they may lie, the final factor to consider is the DG's size on the sky. From previous searches such as the SDSS search, the typical sizes of such MW DGs are known. Amongst the SDSS discoveries, the smallest satellite (on the sky) was Pisces II with a size of 1.1′, whereas the largest one Ursa Major II has a 16′ size. It is therefore clear that these satellites can take on a variety of sizes, which is a direct consequence of the physical size/distance ratio these satellites have (Brasseur et al., 2011). Following the Koposov et al. (2007) prescription, over densities are detected using the 'difference of gaussians' method. The idea behind this method is to estimate the stellar density at specific locations with different resolving scales. This is achieved by calculating the local density of stars at any given point in the PS1 data and subtracting the local background stars at that same point. The signal and the background are the results of the same operation but with different resolving scales. The resolving scales here are the sizes of the over densities being searched for locally. Here, the resolving scale of the local signal corresponds to the size of a satellite galaxy. The local background is resolved at far larger scales as it needs to account for the slowly varying galactic background relative to the quickly fluctuating signal. It is this operation, detailed further in the following paragraphs, which will be performed repeatedly for each distance bin on a given patch.

2.3.3.1 The signal and the background

Let us now explore the mathematics and the tools necessary to do this. We can represent the distribution of stars (which are the ones that were isolated for a given distance using the isochrone mask) as a set of Dirac Delta Functions, which from its properties, is only defined at the positions of the stars themselves.

$$I(x,y) = \Sigma_i \delta(x - x_i, y - y_i) \tag{2.2}$$

To resolve the different spatial scales, the distribution of stars (Dirac Delta Functions) are convolved with a 2-D Gaussian of some size σ, which is the resolving scale:

$$L(x,y,\sigma) = I(x,y) * g(x,y,\sigma) \tag{2.3}$$

where:

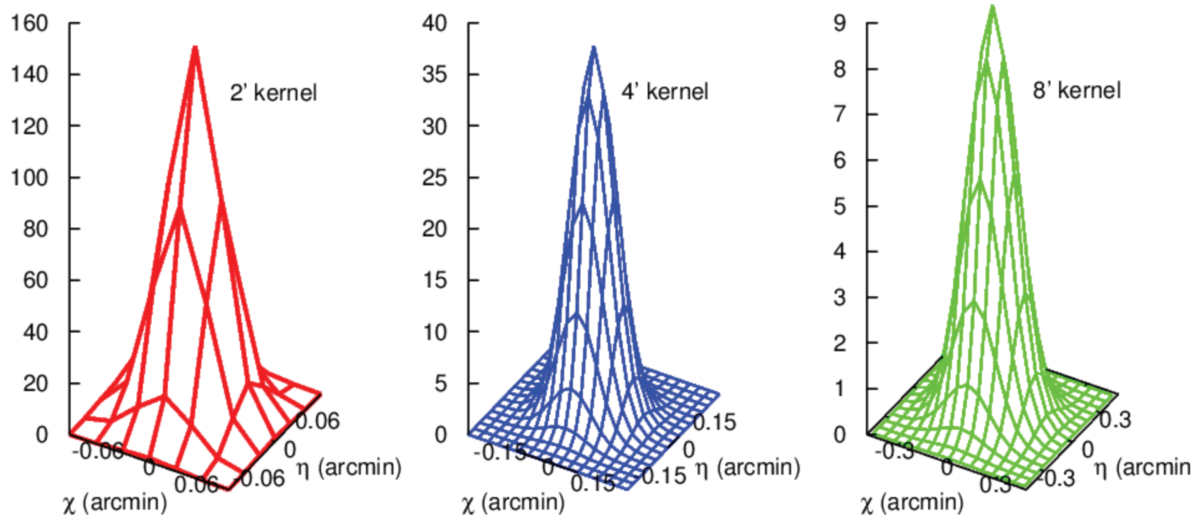

Figure 2.10 - The three Gaussian 'signal' filters used in the convolution search. The dispersion sizes of these kernels are: 2′ (left), 4′ (middle) and 8′ (right).

$$g(x,y) = \frac{1}{2\pi\sigma^2}\exp\left(\frac{x^2+y^2}{2\sigma^2}\right) \tag{2.4}$$

resulting in a function evaluating the number density of stars at the positions of the stars, given the Gaussian function of size σ. Here it is assumed that a round, symmetric Gaussian with $\sigma_x = \sigma_y = \sigma$ represents the over density's size symmetricaly in both dimensions[8]. The Dirac Delta Function's sifting properties are such that the evaluation of the density of stars at some position is the evaluation of the Gaussian at the Dirac Delta Function's position. This results in:

$$g(x,y) * \delta(x-x', y-y') = \frac{1}{2\pi\sigma^2}\exp\frac{[(x-x')^2+(y-y')^2]}{2\sigma^2} \tag{2.5}$$

Or in words: this operation is the evaluation of the density at some given point (x,y) given the number density of stars within the influence of the Gaussian and the weight those stars have on the Gaussian function. To produce the differential image map which is the difference between the two convolutions at different scales, each representing the signal (σ_1) and the background (σ_2), the following expression is obtained:

$$\Delta L = L(x,y,\sigma_1) - L(x,y,\sigma_2) \tag{2.6}$$

This operation results in local 'over dense' and 'under dense' counts at positions where either the signal or background were maximised respectively. To evaluate this expression, the 1600

---

[8] In reality, a dwarf is rarely spherical, but this approximation works well enough as demonstrated by the SDSS searches (Koposov et al., 2008).

degrees^2 patch is pixelised with 2 × 2 arcmin^2 pixels. This means that for a 40 × 40 degree^2 patch, some 1200 × 1200 pixels are evaluated, i.e. 1440000 pixels. At each given pixel a Gaussian is placed and the contribution each star's distance has relative to the central pixel is evaluated. All these contributions are summed up which give the value for that pixel. This is done twice – as already mentioned – for the signal and the background, with the final pixel counts being the difference of the signal and the background.

Therefore the evaluation of the over/under-density of pixel (x_i, y_j) can be reformulated as follows:

$$\Delta L(x_i, y_j) = \sum_{k=1}^{N_{*all}} \sum_{l=1}^{N_{*all}} g(x_i - x_k, y_j - y_l, \sigma_1) - \sum_{k=1}^{N_{*all}} \sum_{l=1}^{N_{*all}} g(x_i - x_k, y_j - y_l, \sigma_2) \tag{2.7}$$

where the counts for a given pixel (x_i, y_j) is determined by calculating the distance between each star's position (x_k, y_l) and the evaluated pixel (x_i, y_j) and summing the contribution the Gaussian has at that distance from the pixel (x_i, y_j). This expression is computationally expensive since it relies on calculating the weight that each star's distance will have relative to the central pixel for which the Gaussian is being evaluated. This problem can be simplified, by binning the stars into the 2 × 2 arcmin^2 pixels that were mentioned earlier. Instead, one can evaluate the central pixel (x_i, y_j), by simply assessing the number of stars per pixel and multiplying this by the distance of the pixel relative to the central pixel. By binning the stars into their corresponding pixels, the computational time is reduced by the ratio of the number of stars to pixels per bin. The calculation can be further constrained to evaluating contributions which are non-negligible, i.e. just to a certain distance away from the central pixel after which point the contribution is very close to zero. Therefore the summation can be simplified to now run over all pixels (rather than stars) and within $\pm 4\sigma$. The equation now becomes:

$$\Delta L(x_i, y_j) = \sum_{k=-4\sigma}^{k=4\sigma} \sum_{l=-4\sigma}^{l=4\sigma} g(x_i - x_k, y_j - y_l, \sigma_1) d(x_k, y_l) - \sum_{k=-4\sigma}^{k=4\sigma} \sum_{l=-4\sigma}^{l=4\sigma} g(x_i - x_k, y_j - y_l, \sigma_2) d(x_k, y_l) \tag{2.8}$$

where now x_k and y_l represent pixels and not stars and $d(x_k, y_l)$ represent the star counts per pixel.

Up until now, the mathematics have been developed, without really connecting this much to something more intuitive or physical. It was previously stated that the signal should represent the size of the satellite, whereas the background should represent the slowly varying background. Previous SDSS quantifications of DG detectabilities such as the Koposov et al. (2008) paper experimented with 2′, 4′ and 8′ kernel for the 'signal' and found this worked well to retrieve all the SDSS satellites. Koposov et al. (2008) subtracted background convolutions with kernels, sized 1 degree. While adopting Koposov et al. (2008) signal values; smaller background kernes values were chosen in the interest of minimising computational time. Nevertheless the sizes were chosen to be large enough such that the effect of the background kernel is clearly noticeable relative to the signal kernel.

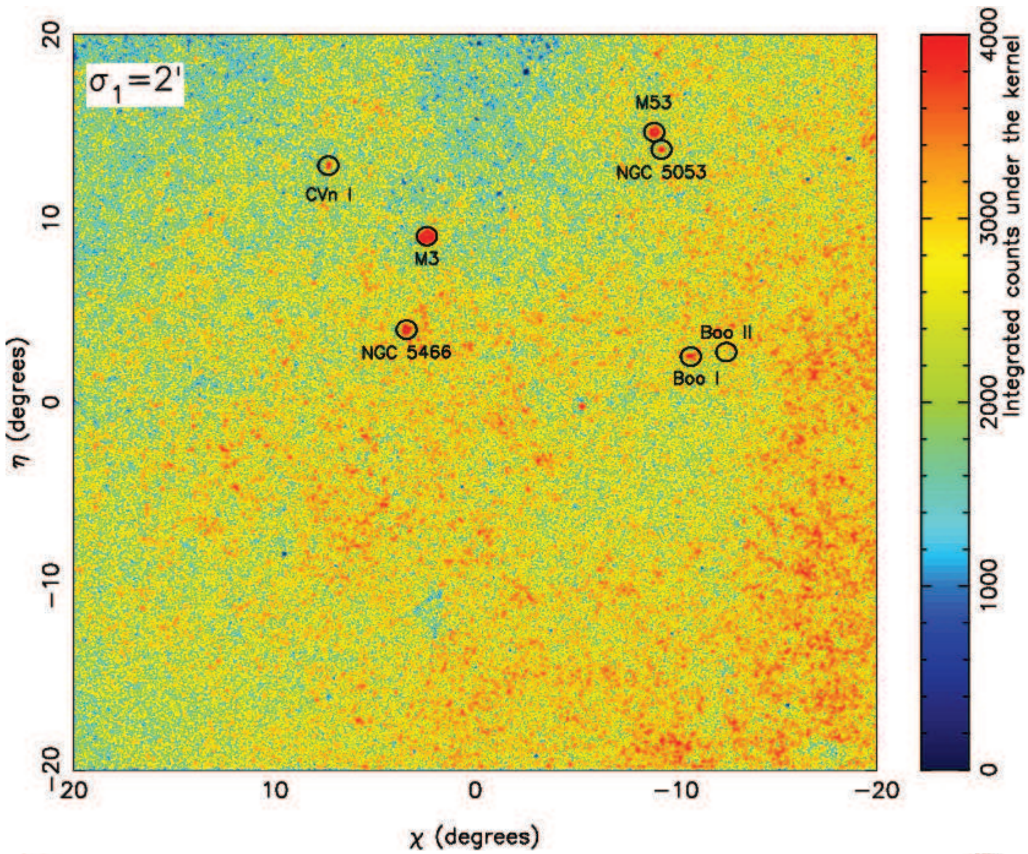
σ$_1$=2'
M53
NGC 5053
CVn I
M3
NGC 5466
Boo II
Boo I
η (degrees)
χ (degrees)
20
10
0
−10
−20
Integrated counts under the kernel
0
1000
2000
3000
4000

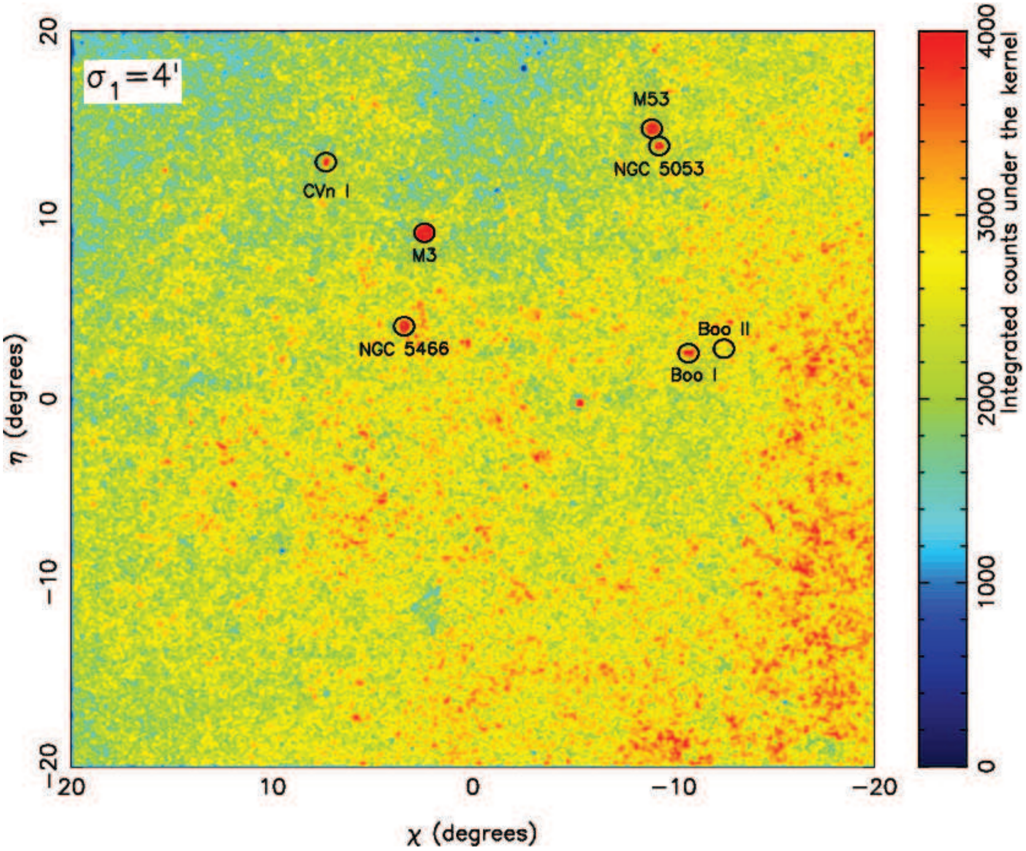
σ$_1$=4'
M53
NGC 5053
CVn I
M3
NGC 5466
Boo II
Boo I
η (degrees)
χ (degrees)
20
10
0
−10
−20
Integrated counts under the kernel
0
1000
2000
3000
4000

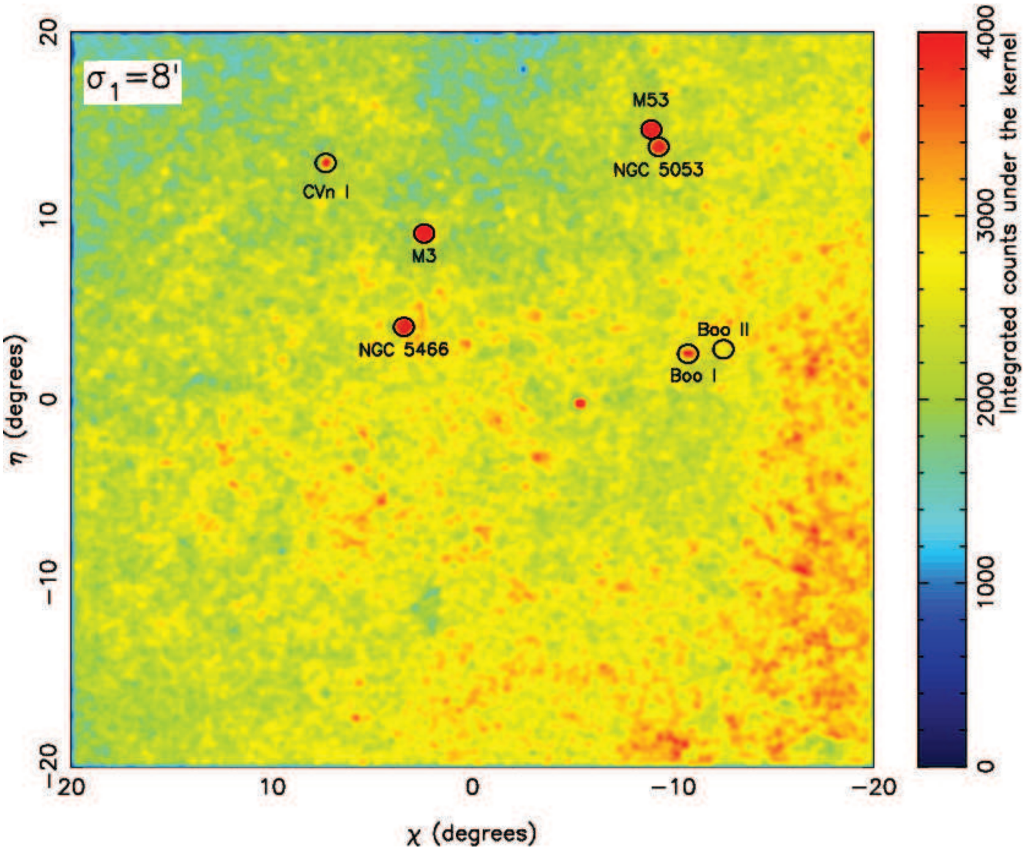

Figure 2.11 - Signal convolutions for the three different kernel sizes: 2′ (top), 4′ (middle) and 8′ (bottom). This is the usual patch centred on $(l,\ b)\ =\ (30^{\circ},\ 70^{\circ})$, containing 3 known MW DGs: Boötes I and II and Canes Venatici I as well as four MW GCs: M53, M3, NGC 5053, NGC 5466. The three different plots illustrate the power of the different resolving scales. The 2′ kernel is a lot more sensitive to the very small scale, showing many more localised peaks, the 8′ kernel on the other hand picks up the far larger scales. Those areas that were picking up little localised over dense blobs in the 2′ map, mostly disappear in the 8′ map (look at Böotes II in the three different maps). The 4′ map lies somewhere in between the two other maps, picking up some of the smaller structure, while also convincingly picking up the larger objects in this field.

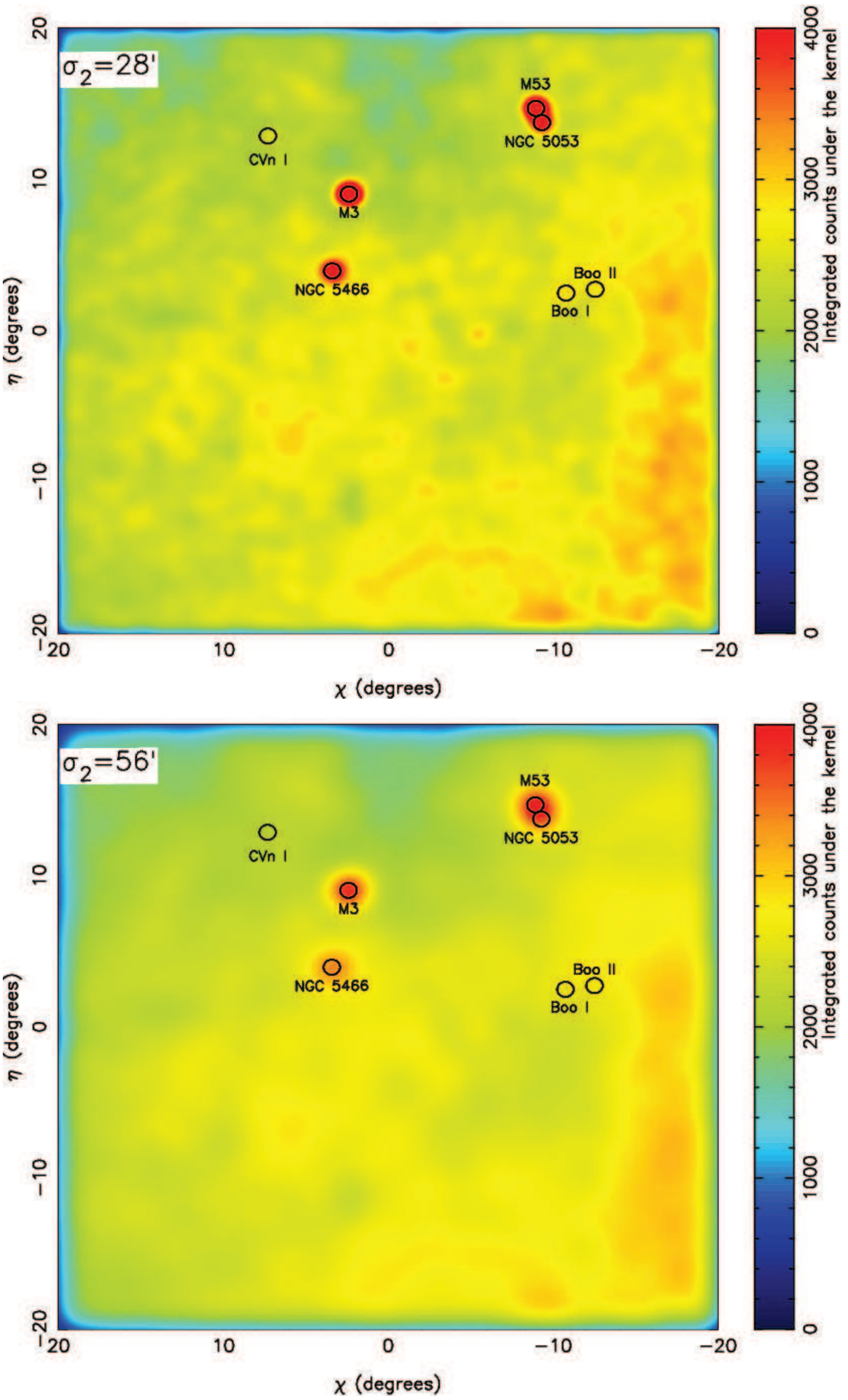

Figure 2.12 - The result of the background convolutions can be seen here for 28′ (top) and 56′ (bottom). The former gets subtracted from the 2′ and 4′ maps whereas the latter is subtracted from the 8′ map. The image here looks a lot coarser, due to the larger kernel sizes. The large GCs are still being picked up, but their counts are lower at the centre than for the signal.

Table 2.1 - Kernel and Resolution Properties for convolution search algorithm

	PV1		PV2		
Kernel signal (′)	4	8	2	4	8
Kernel background (′)	28	56	28	28	56
Pixel resolution (′)	2	2	0.5	2	2

Table 2.1 shows the different kernels that were used over the course of the PhD. The only difference between PV1 and PV2 was the addition of the 2′ kernel. A 2′ kernel was avoided until PV2, because of the finer pixel resolution necessary to evaluate the convolutions. We saw in this chapter that a 2×2 arcmin^2 pixel resolution was used for the evaluation of the convolution. This is true for 4′ and 8′ kernels, but turns out to be a bad idea In the case of the 2′ kernel because the dispersion of the Gaussian is the size of the pixel resolution. This means that if a Gaussian were placed at a given pixel, the next pixel along would see its stellar contribution severely reduced, since the Gaussian's value will already be small at this adjacent pixel. Indeed, convolutions were run precisely to see the effects of this and showed that running the 2′ kernels on 2′ resolution would not work as this created very noisy maps. Instead a 0.5×0.5 arcmin^2 resolution was used. Consequently one such pixel is $1/16^{th}$ the size of a regular 2′ pixel, therefore slowing the convolution code down by a factor of 16. The graphical representation of the two different convolutions (signal and background) can be seen in Figures 2.11 and 2.12.

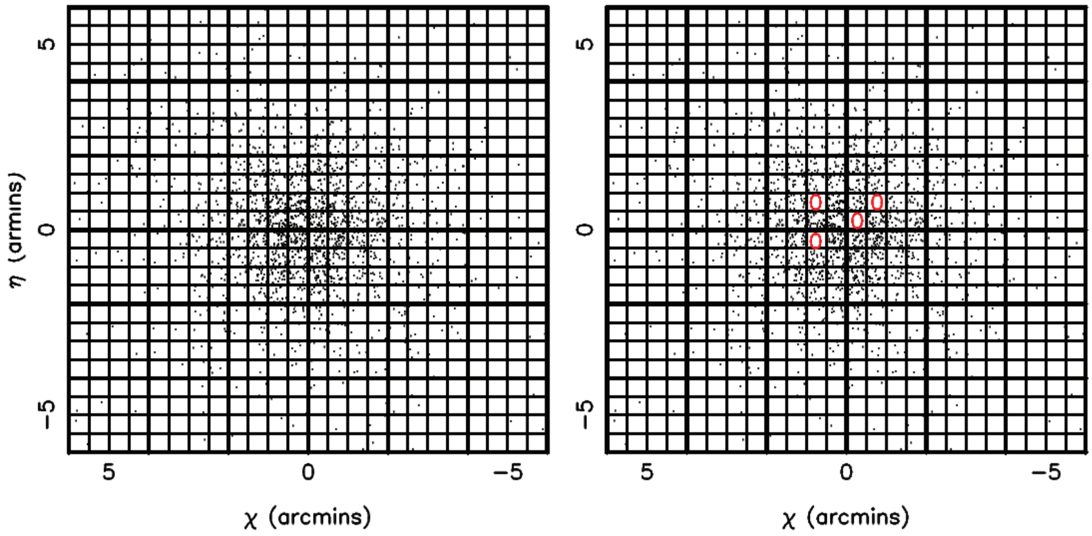

Figure 2.13 - A simulated galaxy with the grid on which the convolution calculation is done is superimposed. The larger grid (thick lines), corresponds to the resolution scale of the convolution with the signal or the background (for 4′ and 8′ kernels) only. The finer grid, shows the resolution of the completeness calculation. On the left, all the small pixels are complete, whereas on the right side, four pixels (marked with '0') are incomplete. When the convolution is performed here, the hole will be accounted for by boosting the signal or the background.

2.3.3.2 Folding in the completeness

We saw in section 2.2.4 that maps are generated quantifying the completeness of a pixel on a 0.5×0.5 arcmin^2 resolution, where a pixel is either complete (=1) or is incomplete (=0). The above formulation of the 'difference of Gaussians' equation would work if the data were complete, i.e. each pixel=1, over the whole sky. We have already seen that this is not the case. Let us consider the contrived situation in Figure 2.13 containing a mock galaxy in both panels. The left panel represents complete data coverage over the whole extent of the galaxy (all pixels are 1). In the right panel, 4 of the pixels are incomplete (0) and contain no data. These two panels show two resolution sizes (2′ resolution – big pixels – and 0.5′ resolution – small pixels). Assume here that a 4′ signal kernel is run and therefore using a 2′ resolution scale, then the large pixel centred at $(\chi,\ \eta) = (1.0°,\ -1.0°)$, will look to its neighbouring pixels and assess the density of stars in each of the large pixels and multiply this by the distance from the central pixel to sum up all the contributions of neighbouring pixels. If the convolution code were run on the right hand side grid, assuming that the data were complete, then for those small pixels that are zero, the counts will be lowered because the density of stars is lower due to the empty pixels. In this section I will explain how this can be taken into account by normalising the counts in each large pixel by a completeness-corrected factor, which boosts the counts by the ratio of the total number of small pixels (16 small pixels for every large pixel) to the number of complete small pixels[9]. Returning to the example in Figure 2.13, this would mean that at pixel $(\chi,\ \eta) = (-1.0°,\ 1.0°)$, the counts are normalised by a factor proportional to 14/16 since two of the sixteen pixels are incomplete.

What was described in words, translates – mathematically – into calculating a Gaussian integral over all space for each pixel on the 0.5×0.5 arcmin^2 resolution scale. This integral is the following:

$$\int_{-\infty}^{\infty} \int_{-\infty}^{\infty} \frac{1}{2\pi\sigma^2} \exp\frac{[x^2 + y^2]}{2\sigma^2} dxdy = 1 \tag{2.9}$$

If this equation is multiplied by some constant function, c(x,y), always defined to be one, the integral does not change but becomes:

$$\int_{-\infty}^{\infty} \int_{-\infty}^{\infty} c(x,y) \frac{1}{2\pi\sigma^2} \exp\frac{[x^2 + y^2]}{2\sigma^2} dxdy = 1 \tag{2.10}$$

Hence in areas with perfect coverage this equals one. In incomplete areas, this will equal a value smaller than one. This means that when dividing the original pixel count by the completeness factor, the counts will be artificially boosted to reflect the lack of data in those areas. Once again, the further simplifying assumption of all space equating to pixels within $\pm 4\sigma$ can be applied, which results in:

---

[9] For the 2′ kernel, the resolution grid for the counts and the completeness are the same and therefore the counts are simply boosted on a one to one pixel level.

$$\int_{-4\sigma}^{4\sigma}\int_{-4\sigma}^{4\sigma} c(x,y)\frac{1}{2\pi\sigma^2}\exp\frac{[x^2+y^2]}{2\sigma^2}dxdy = 1 \tag{2.11}$$

The integral can be re-written into a summation, which does the following: for each pixel, count all the contributions of the pixels (values of 1 and 0) 4σ away multiplied by the evaluation of the Gaussian at those points. This convolution is identical to the signal or background convolution, where, instead of binned stars, zeroes and ones are multiplied by the Gaussian. The summation is the following:

$$CF(x_i, y_j, \sigma) = \sum_{k=-4\sigma}^{k=4\sigma}\sum_{l=-4\sigma}^{l=4\sigma} g(x_i - x_k, y_j - y_l, \sigma)c(x_k, y_l) \tag{2.12}$$

Combining equation 2.8 and equation 2.12, the equation that is evaluated can be seen below. This is the most important equation from the thesis.

$$\Delta L(x_i, y_j) = \frac{\sum_{k=-4\sigma}^{k=4\sigma}\sum_{l=-4\sigma}^{l=4\sigma} g(x_i - x_k, y_j - y_l, \sigma_1)d(x_k, y_l)}{\sum_{k=-4\sigma}^{k=4\sigma}\sum_{l=-4\sigma}^{l=4\sigma} g(x_i - x_k, y_j - y_l, \sigma_1)c(x_k, y_l)dx_i dy_j} - \frac{\sum_{k=-4\sigma}^{k=4\sigma}\sum_{l=-4\sigma}^{l=4\sigma} g(x_i - x_k, y_j - y_l, \sigma_2)d(x_k, y_l)}{\sum_{k=-4\sigma}^{k=4\sigma}\sum_{l=-4\sigma}^{l=4\sigma} g(x_i - x_k, y_j - y_l, \sigma_2)c(x_k, y_l)dx_i dy_j} \tag{2.13}$$

Figure 2.14 is the graphical representation of the completeness corrected normalisation factor (denominator from equation 2.13) for the signal and background, whereas Figure 2.15 shows the effect of normalising the signal and the background by the normalisation factors. These plots are shown for 4′ (signal) and 28′ (background) only. Finally, Figure 2.16 shows the effect of subtracting the normalised background from the normalised signal, i.e. the differential density image maps. This is effectively the evaluation of equation 2.13 in its totality. Please see the figure captions for more explanation. Please bear in mind that thoughout this explanation, these plots have been shown for a randomly chosen distance-modulus of 20.0. In reality these plots are just $1/16^{th}$ of the totality, as they exist also for all the other distance modulus bins. We shall see in the next section how all these different maps will be combined into statistical significance.

2.4 Detection significance

At this point, a large amount of work has been done, since now differential density image maps can be produced for the whole sky; however, these maps alone are not enough. From the previous section, we know that those places of interest are the regions which are over dense, but it is not possible to simply make an arbitrary cut in the integrated counts under the kernel in these maps, since they do not contain statistical information. For example, an over density of 700 of integrated counts under the kernel in patch A, will not mean the same

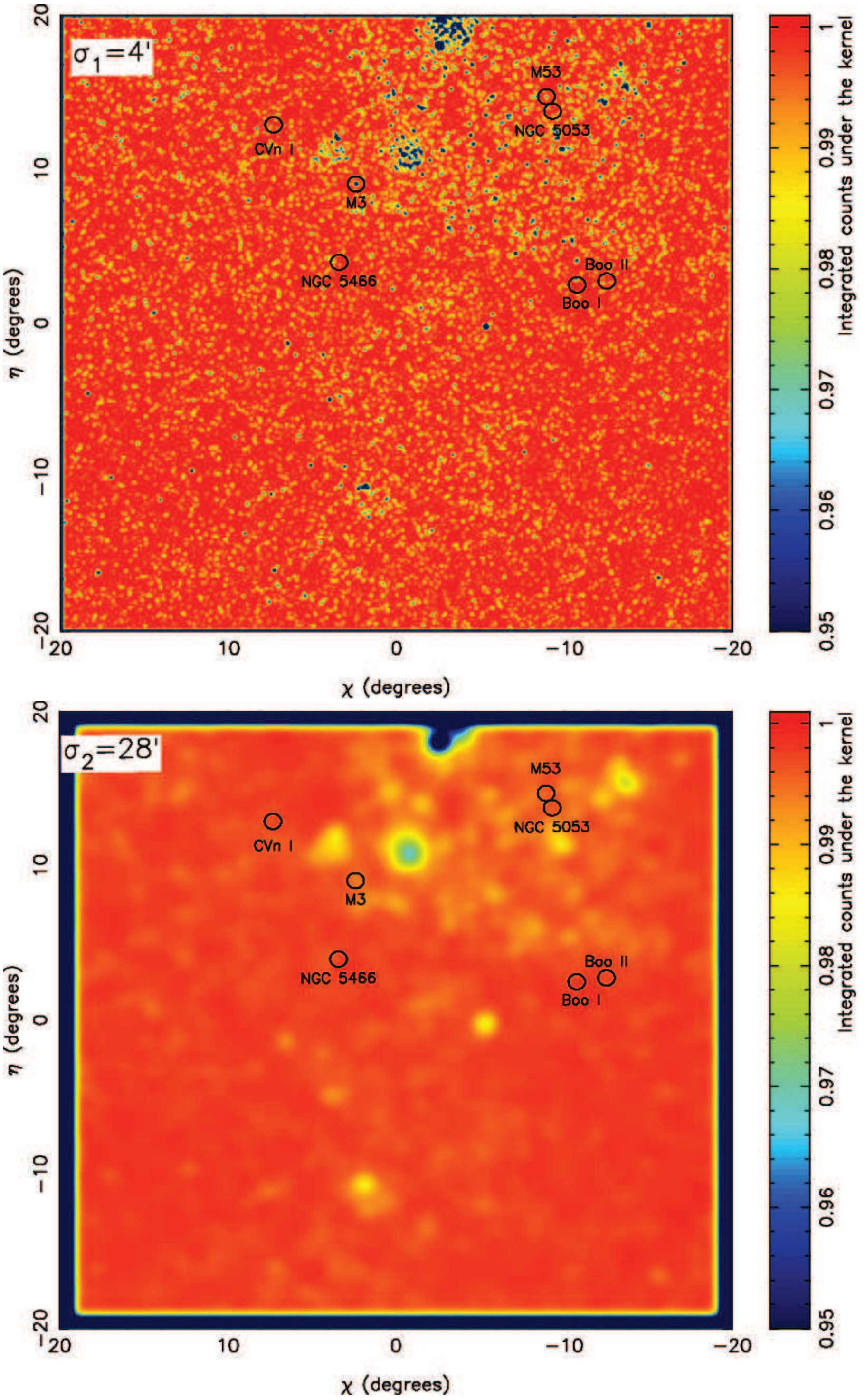

Figure 2.14 - The graphical representation of convolving the completeness counts with a Gaussian of 4′ (signal) and 28′ (background) on the top and bottom respectively. The colour-bar ranges from 0.95 to 1.0, highlighting how the completeness varies as a function of position. Note for example that M3 (GC) is incomplete right at the centre, which is due to crowding, causing there to be no data right at the centre. Hence for this object the counts will have been boosted as was explained using Figure 2.13 and equation 2.13.

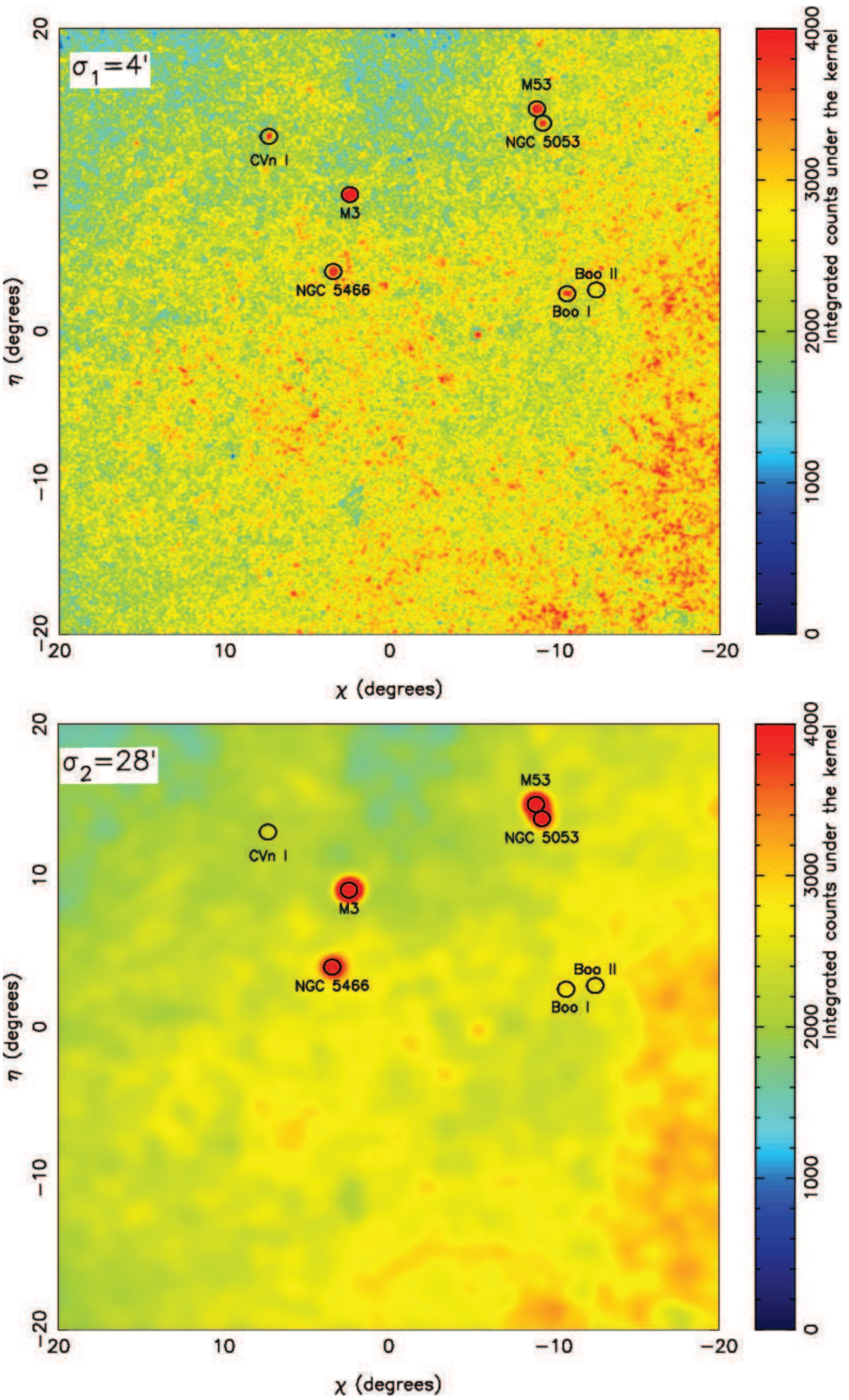

Figure 2.15 - These two panels are as a result of normalising the signal and the background from Figures 2.11 and 2.12 by the counts in the two panels from Figure 2.14. One can see that the counts are slightly boosted relative to Figures 2.11 and 2.12 (both sets of figures are on the same colour–scale making direct comparison possible).

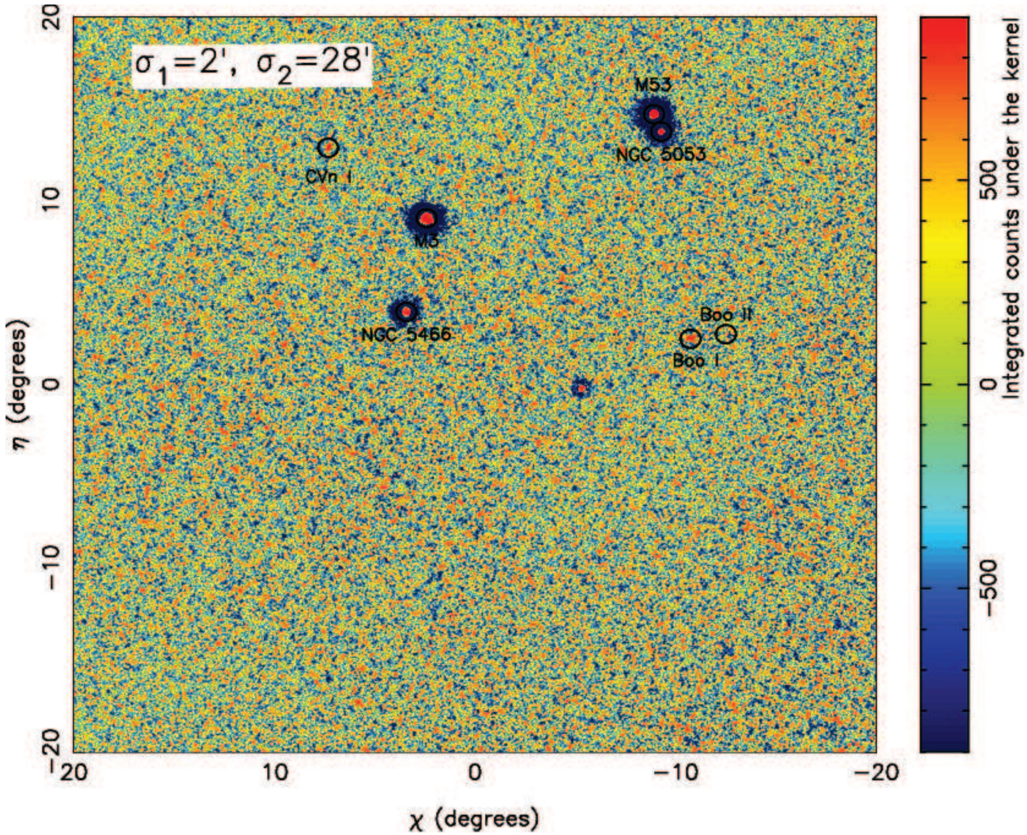
σ₁=2', σ₂=28'
M53
NGC 5053
CVn I
M3
NGC 5466
Boo II
Boo I
η (degrees)
χ (degrees)
20
10
0
−10
−20
Integrated counts under the kernel
500
0
−500

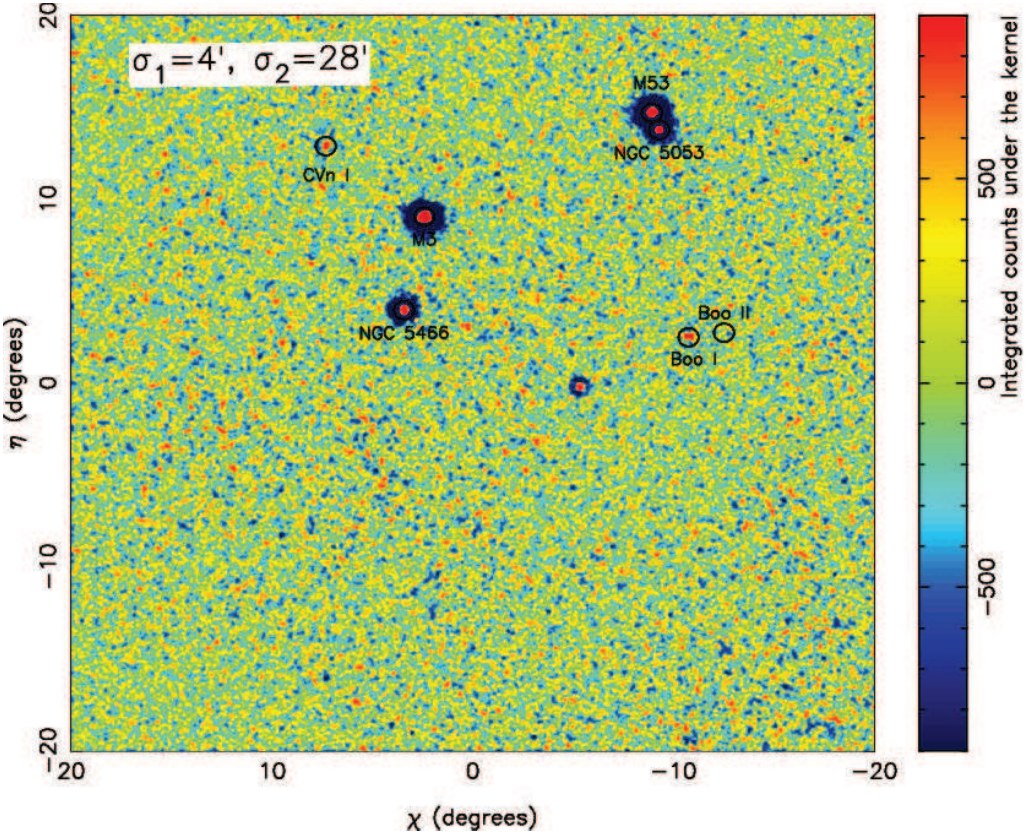
σ₁=4', σ₂=28'
M53
NGC 5053
CVn I
M3
NGC 5466
Boo II
Boo I
η (degrees)
χ (degrees)
20
10
0
−10
−20
Integrated counts under the kernel
500
0
−500

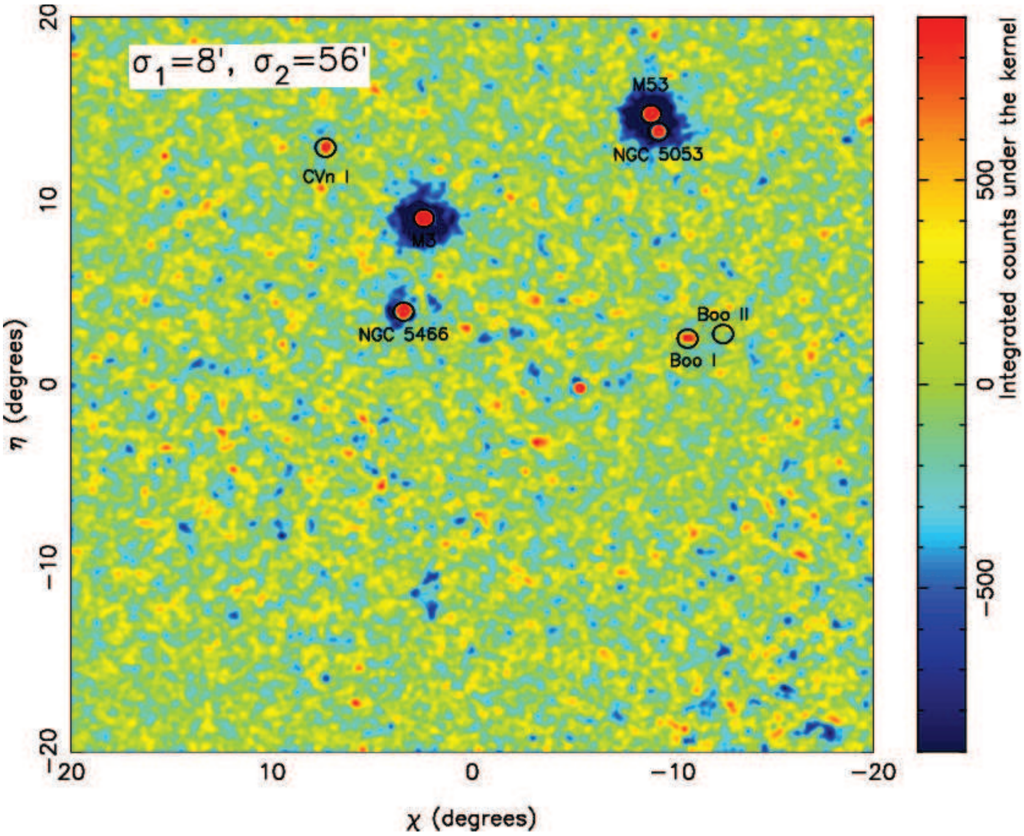

Figure 2.16 - The final differential density image maps after doing the following steps: 1) convolve stellar density with signal Gaussian, 2) divide counts of signal convolution by completeness convolution, 3) repeat 1) and 2) for the background, 4) Subtract the background from the signal. Here, the maps are shown again for 2′, 4′ and 8′. Once again the difference in resolving scales can be clearly seen between the different maps. The troughs around the over dense objects (the 4 GCs) are due to the background kernels still being a good fit for these large clusters' sizes. Therefore the result of subtracting the background from the signal for these satellites, causes large negative tails or negative integrated counts. Two out of the three MW satellites (Boötes I and CVn I) appear very convincingly in these final maps. Boötes II does not show up well at all, but this is unsurprising since it is the lowest surface brightness satellite (along with UMa II) found in the SDSS. The other GCs are picked up very convincingly (which you would expect since they are visible on photographic plates).

as the integrated counts of the same number in some other patch B. If 700 counts in patch A are at $b = 10^\circ$, this is not equivalent to 700 counts at $b = 85^\circ$ in patch B. The detection at high latitude would be rarer because the number density of stars is lower here. At regions closer to the disc, there should be more detections above 700 counts, due to the sheer number of stars at lower latitudes. In this example, the 700 counts in patch B is more significant that in patch A. Also, the coverage and depths of the patches can vary by one magnitude. For example in patch C there could be 10 or more detections above 700 counts, whereas in patch D, this could be 2 because of varying depths. A further complication arises: for any given patch there are 48 different maps, corresponding to 16 different distance–moduli for three different kernels. In other words: there is simply too much information in all these separate maps to realistically analyse. In the following section we will see how the conversion from 48 differential density image maps per patch into one statistical significance map per patch will be achieved.

2.4.1 Short mathematical approach

The significance of a detection is computed by dividing the number of integrated counts by the local variance of the counts. ‘Local’ denotes pixels that lie within the vicinity, within a radius of 1 degree, of the pixel for which the significance is being calculated. There is a slight subtlety, in that the inner half degree region, of the one degree annulus is not considered in the variance calculation. This is done to avoid being heavily biased by a booming detection in this region which will fan out a considerable amount of area. Therefore for a given pixel, the standard deviation is determined between half a degree annulus to a degree annulus away according to the following equation:

$$s(x_i, y_j)^2 = < \left[\Sigma_{k=a}^{k=b}\Sigma_{l=a}^{l=b} S(x_k, y_l)\right]^2 > - \left[< \Sigma_{k=a}^{k=b}\Sigma_{l=a}^{l=b} S(x_k, y_l) > \right]^2 \tag{2.14}$$

where S is the integrated counts under the kernel (the differential density counts). The statistical significance is then evaluated by dividing the counts by the square root of the standard deviation which is the variance:

$$S/N(x_i, y_j) = \frac{\Delta L(x_i, y_j)}{s(x_i, y_j)} \tag{2.15}$$

The results of these calculations can be seen in Figure 2.17, which shows the differential density counts (top), the noise or variance (middle) and the signal to noise (S/N) – the result of dividing one by the other (bottom). This is once again shown for the usual patch: $(l,\ b) = (30^\circ,\ 70^\circ)$ containing some of the SDSS satellites and for the same distance–modulus as all previous plots ($\mu = 20$). In the S/N map of this figure, it is clear that some blobs in the differential density map disappear since they turn out not to be very significant relative to the neighbouring regions. Reassuringly, the GCs and the SDSS DGs (except Boötes II) turn out as the most significant detections of this particular patch.

2.4.2 Combining statistical information for a given patch

Though the statistical significance can now be determined, there is still far too much information for realistic analysis. For each patch there are 48 different maps and files containing

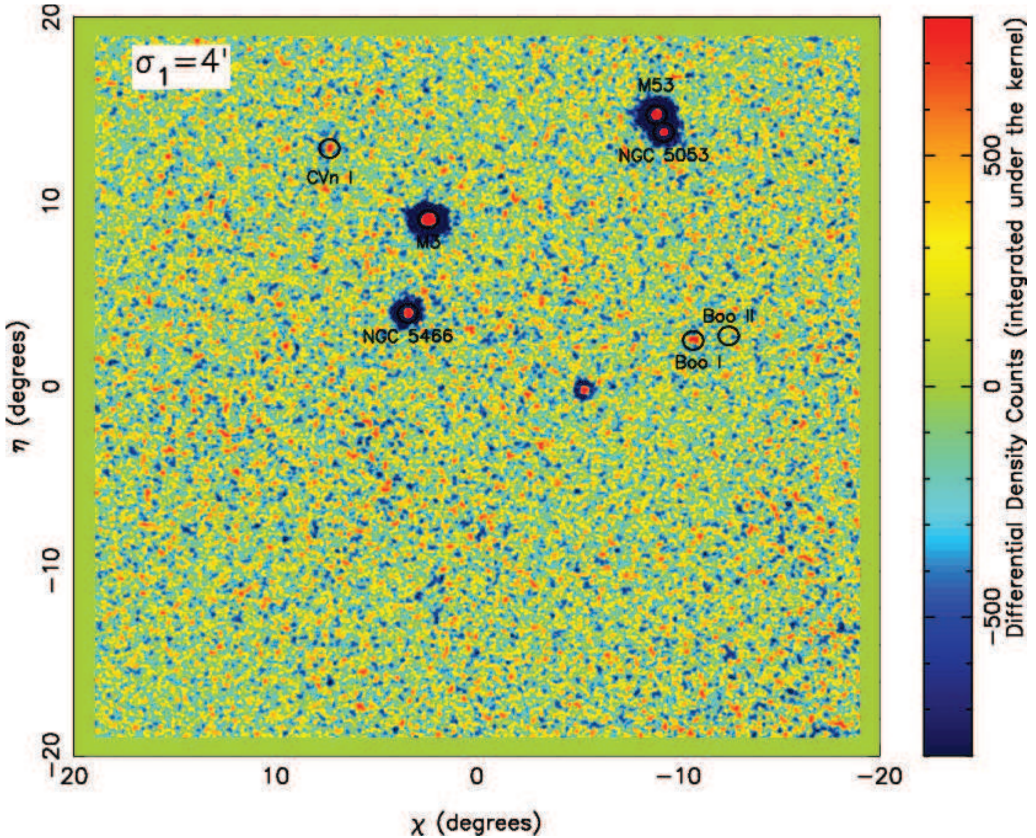
σ1=4'
M53
NGC 5053
CVn I
M3
NGC 5466
Boo II
Boo I
η (degrees)
χ (degrees)
20
10
0
−10
−20
Differential Density Counts (integrated under the kernel)
500
0
−500

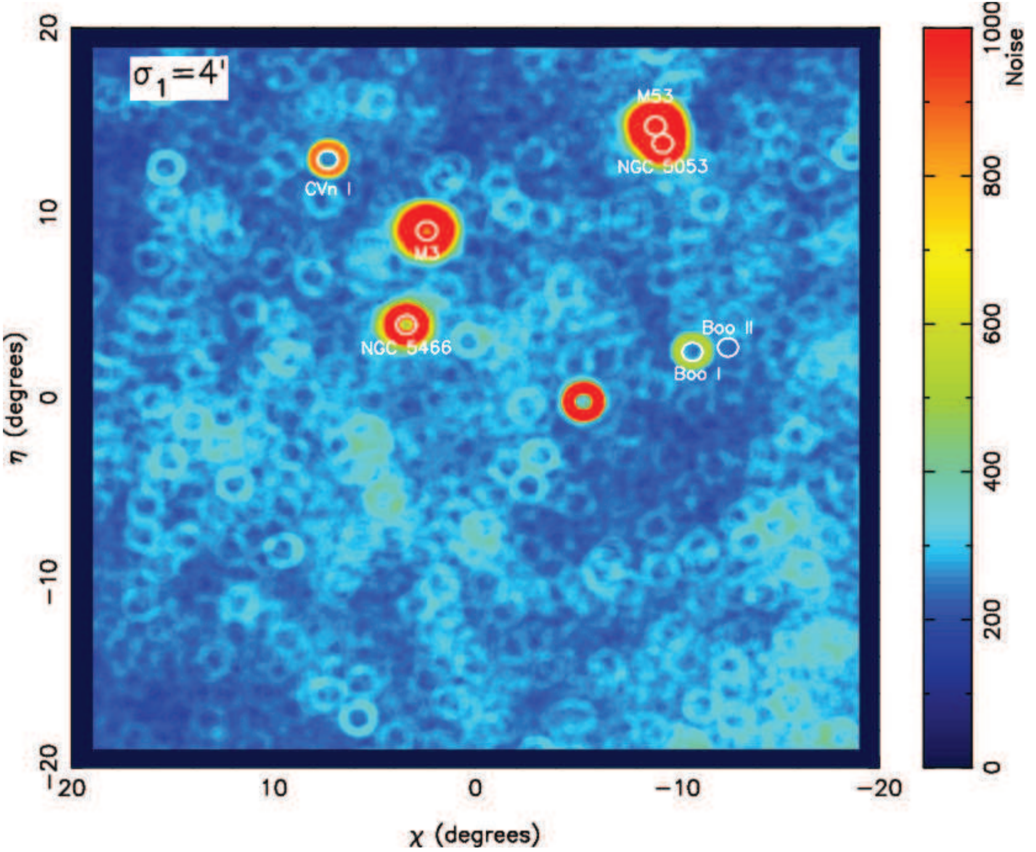
σ1=4'
M53
NGC 5053
CVn I
M3
NGC 5466
Boo II
Boo I
η (degrees)
χ (degrees)
20
10
0
−10
−20
Noise
1000
800
600
400
200
0

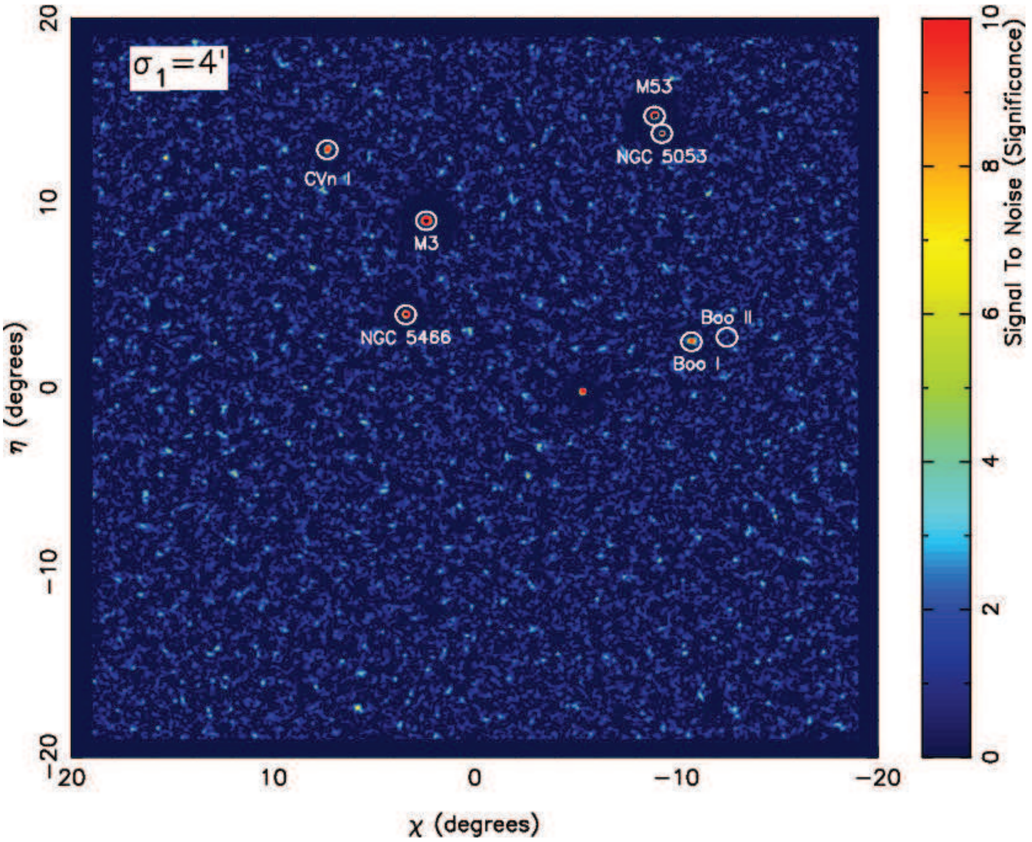

Figure 2.17 - *Top:* differential density image map for the 4′ kernel (in fact the same plot as middle panel of Figure 2.16) *Middle:* The calculation of the variance or noise. The plot shows the annuli that calculate the local variance for some given points with annuli 1 degree in size (the inner half degree is discounted). *Bottom:* The S/N or the result of dividing the top panel by the middle panel. As can been, some of the bobs from the differential density image map disappear as they turn out not to be significant relative to the neighbouring regions. Fortunately, the 4 MW GCs as well as 2/3 SDSS DGs turn out to be among the most significant points in the patch.

information. Therefore a way of combining the information into a 'Master Significance' map for each individual patch is necessary. To achieve a 'maximum' significance map we proceed as follows: for each pixel, I cycle through the maps corresponding to the different kernels and distance-moduli and determine the kernel and distance-modulus map for which the S/N is maximised.

Several complications arise when doing this: Firstly, the 4′ and 8′ maps have a pixel resolution of 2′, whereas the 2′ maps have a 0.5′ resolution. This means that for each pixel in the 4′ and 8′ maps, there are 16 pixels in the 2′ maps. The second issue is a universal statement about S/N over one patch for every kernel and distance-modulus and indeed over the whole PS1 sky itself. The distribution of significance counts for a 2′, 4′ and 8′ maps are not the same, with a non–zero median, but offset to the positive depending on the kernel size that was used. The differences in distribution of counts arise due to the smaller pixel resolution that was used for the 2′ map, which makes the data a lot more noisy. The following steps are undertaken to solve these two issues:

- For a patch A, re-scale map of kernel k_i and dm_j, using m (median) and σ (sigma) of the counts, i.e. for a S/N count, re-scale according to:
  $SN_i = \frac{SN_i - m}{\sigma}$
- Coarse the 2′ kernel maps from a 0.5′ to 2′ resolution, by taking the maximum-value pixel from the 16 pixels and assign that pixel to be the 'new' pixel on a 2′ resolution;
- For a specific kernel, stack all the distance-modulus maps: this gives a 'Master Significance' map per kernel;
- Re-scale the counts of the kernel-dependent 'Master Significance' maps, using the formula in bullet point 1;
- Stack the three kernel-dependent 'Master Significance' maps;
- Re-scale the counts again.

This approach is adopted over the entire PS1 sky, allowing for a universal S/N value. We now have a 'Master Significance' map for each patch for the whole survey, with a S/N which is consistent over the whole sky. Figure 2.18 shows the re–normalised 'Master Significance' maps for the different kernel sizes: 2 ′ (panel 1), 4′ (panel 2), 8′ (panel 3) and the final stacked map, containing information from 48 different maps: 3 kernels and 16 distance–moduli (panel 4).

2.4.3 A brief aside: galaxies' map

Up until now, we have only considered the search algorithm (2.3) and the significance calculation (2.4) on the stellar map, which was illustrated with various plots throughout those two sections. Remember that in section 2.2.2 we saw that two maps were extracted from the PS1 database, the second of which is a galaxies' map. The explanation detailed so far is not

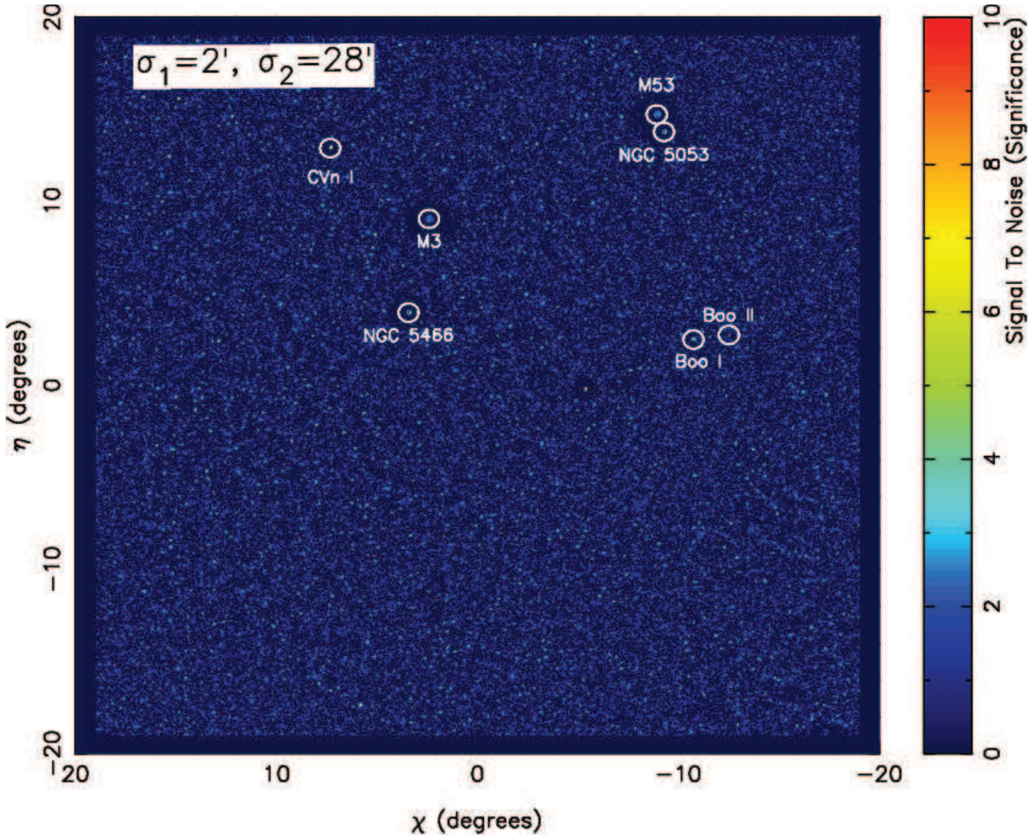
σ_1=2', σ_2=28'
M53
NGC 5053
CVn I
M3
NGC 5466
Boo II
Boo I
η (degrees)
χ (degrees)
Signal To Noise (Significance)
20
10
0
−10
−20
0
2
4
6
8
10

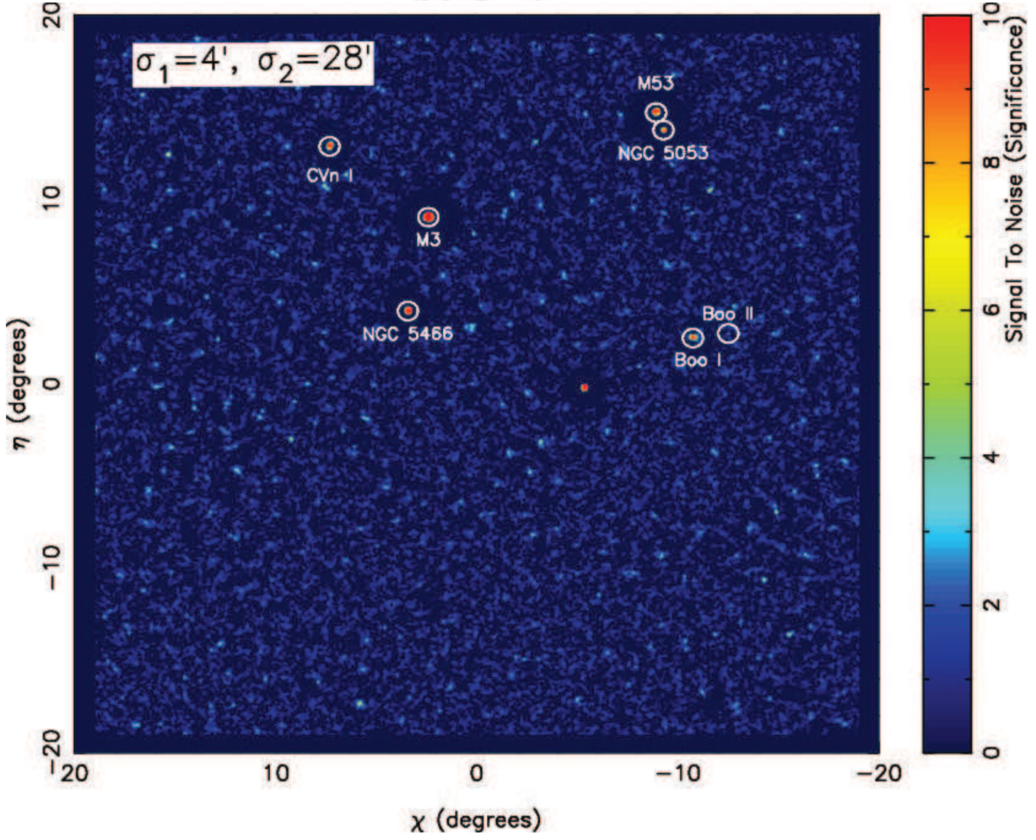
σ_1=4', σ_2=28'
M53
NGC 5053
CVn I
M3
NGC 5466
Boo II
Boo I
η (degrees)
χ (degrees)
Signal To Noise (Significance)
20
10
0
−10
−20
0
2
4
6
8
10

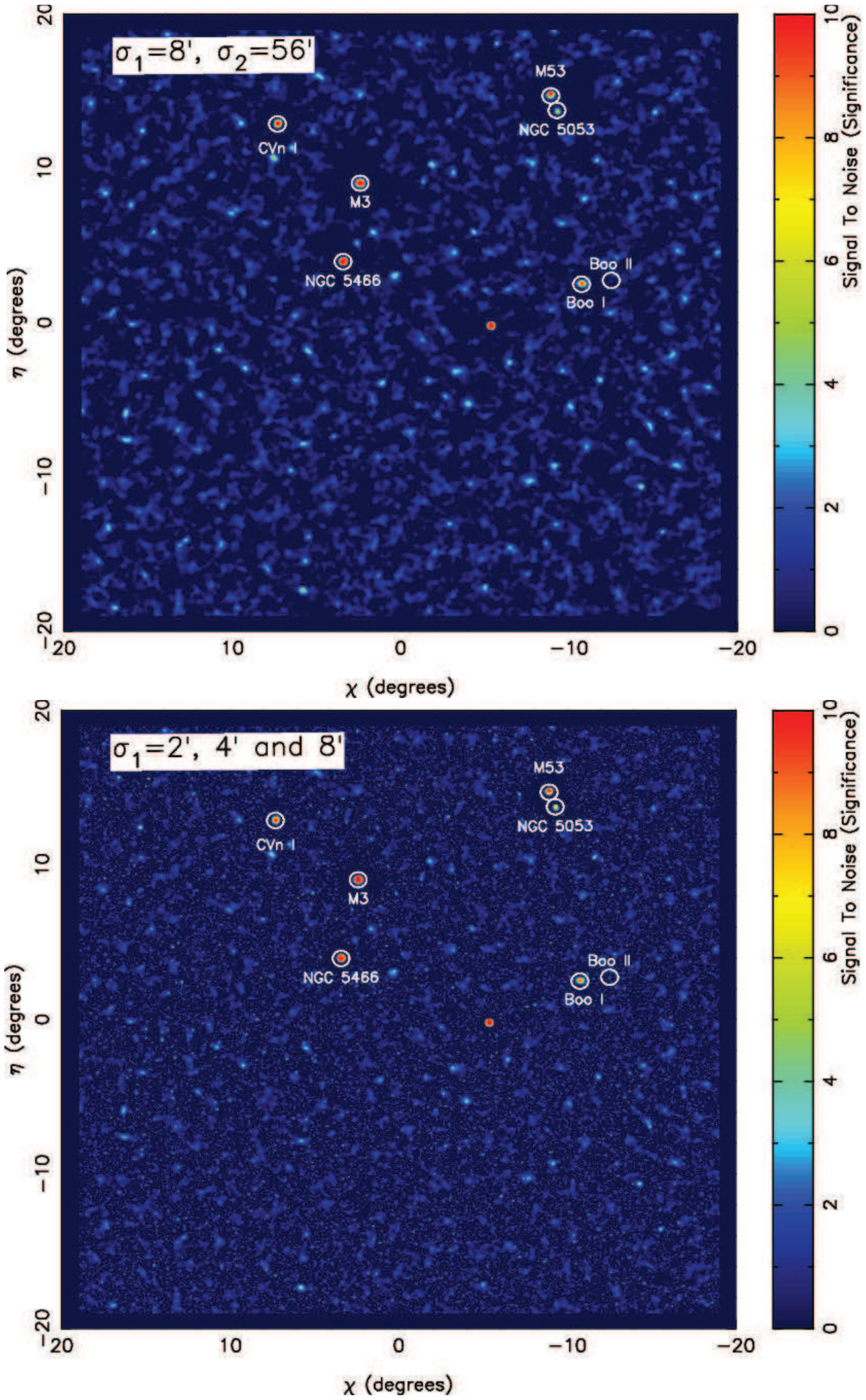

Figure 2.18 - Three panels showing the result of stacking all the distance-moduli for a given patch for a given kernel size: 2′ (first panel), 4′ (second panel), 8′ (third panel) and requiring the maximum pixel value. The final panel shows the result of stacking all the distance-moduli and three kernels. In each of the four plots, these significance maps have been rescaled using σ and m as described in section 2.4.2.

performed once, but twice, i.e. also on a map containing galaxies[10]. The purpose of this is to cross–reference between the two maps to weed out false positives or contaminants in the stellar map such as background galaxies or galaxy clusters, which show up as significant over densities. To understand this a little better, let us return to our usual patch and consider Figure 2.19. In this figure, you can see dearths in S/N for many of the MW satellites, such as CVn I or Bootes I, confirming them to be stellar systems, while not cross–referencing with background galaxies or galaxy clusters. If we now consider 'Alf Boo 5' in the galaxies' map and the stellar map of Figure 2.18, it can be seen that the location of this object is consistent with a peak in both maps. This object is not interesting as its high S/N in the galaxies' map shows it is a contaminant in the stellar map. Using certain criteria (which we will see in the next section), a reduced list of significant detections may be constructed by cross–referencing with contaminants.

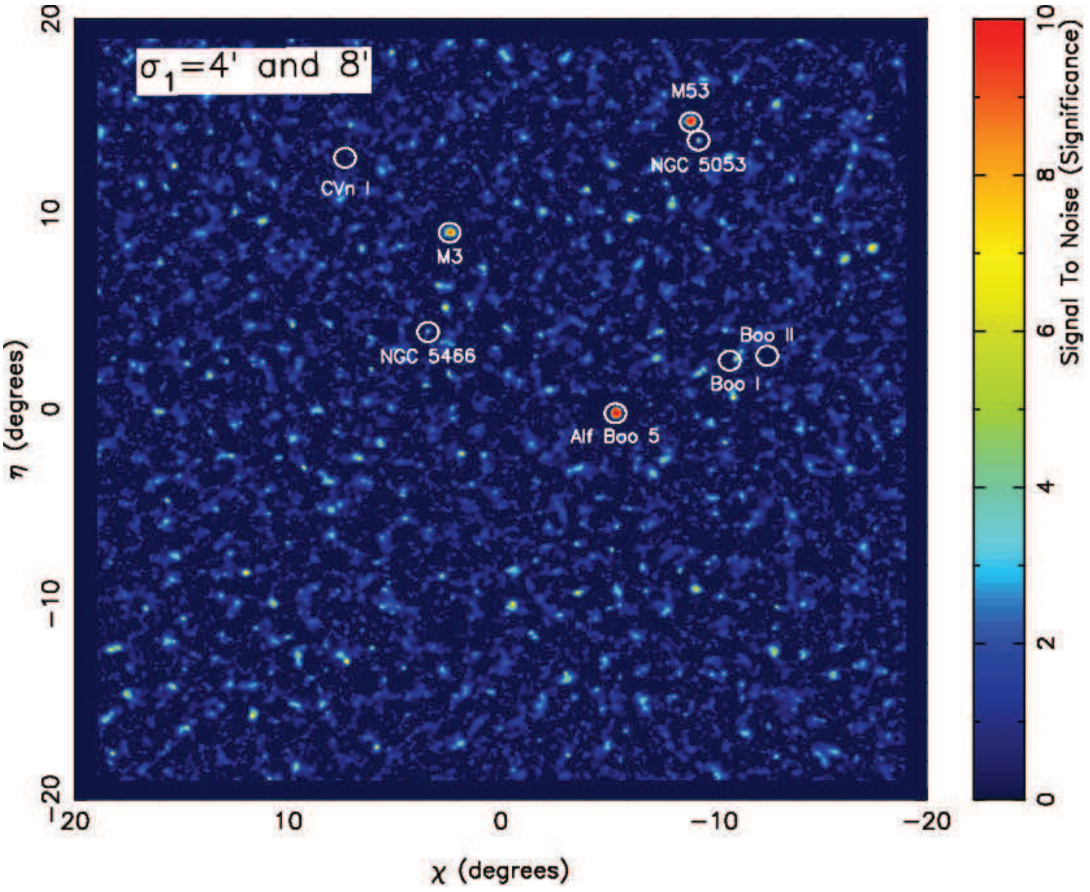

Figure 2.19 - Stacked (4′ and 8′) S/N map for galaxies' sample. Many of the MW satellites show up as insignificant detections in the galaxies' map confirming them to be real stellar systems. Some of the MW GCs also show up as significant detections in the galaxies' map. This because they are so bright that the star–galaxy separation breaks down and also starts classifying some of the sources here as galaxies. 'Alf Boo 5' shows up significantly in the galaxies' map and the stellar map in Figure 2.18, confirming that it is a contaminant in the stellar map and should be excluded.

---

[10] There is a slight difference between the stellar map and the galaxies' map. While the stellar map has all three kernels stacked on top of one another, we will see in section 2.5 that only 4′ and 8′ will be stacked on top of each other for the galaxies' map.

2.5 Search algorithm efficiency: PS1 vs. SDSS

The whole search algorithm has now been explained and developed. The next logical step is to ascertain whether the algorithm works. Luckily, there are a number of known MW satellites, with which it is possible to compare because the total SDSS footprint is also in PS1. These systems span: $-8 < M_V < -1$ and $26 < \mu < 29$. Such a comparison is useful for a variety of reasons. Not only is it a useful diagnostic to determine the algorithm efficiency, it also gives a clear indication of a good threshold at which to cut the data, such that significant detections can be investigated. Taking into account the surface brightness of the sample of SDSS satellites and the intermediate nature of the PS1 PV2 data[11], the stellar significance of these satellites can be used to infer a realistic and sensible cut, above which candidate detections are deemed 'significant' and worthy of investigation. Once such a threshold is determined, the significance of the SDSS satellites in the galaxies' map may be investigated. This in turn will determine how well star–galaxy separation is working and to what extent a cut can be made on the galaxies' map to allow us to eliminate false contaminants such as background galaxies or galaxy clusters, GC systems associated with background systems, all of which can masquerade, photometrically–speaking, as objects of interest in this search. The point of this is to strike a balance between eliminating false contaminants, but not having such a sharp cut that one or more of the SDSS satellites would be eliminated due to galaxies' counts.

Table 2.2 - S/N for stellar and galaxies' map for the SDSS MW satellites

Satellite	SN_{Stars}	SN_{Gals}	Satellite	SN_{Stars}	SN_{Gals}
Leo I	97.5	27.1	Pisces II	6.7	-0.5
Leo II	89.6	11.5	Ursa Major II	6.4	2.0
Draco	47.7	5.8	Canes Venatici II	6.2	-1.2
Canes Venatici I	31.2	0.0	Segue 2	4.9	0.5
Ursa Minor	27.3	3.1	Ursa Major I	4.7	0.8
Bootes I	11.6	-0.1	Leo V	4.1	0.9
Sextans	11.2	0.1	Hercules	3.9	0.4
Willman 1	10.6	0.5	Pegasus III	3.7	-0.2
Coma Berenices	8.6	2.7	Bootes II	3.4	-0.8
Segue 1	7.3	-0.7	Leo IV	1.7	-0.1

2.5.1 Recovery rate of the SDSS satellites

The S/N for each satellite is determined by finding the hottest (or highest) S/N pixel near its co-ordinates in the stellar map and finding the corresponding pixel in the galaxies' map. These values are listed in Table 2.2 for all the MW satellites. All the 'classical' DGs, observable in PS1 are found with very high S/N (Leo I, Leo II, Draco, Ursa Minor and Sextans; $SN > 11\sigma$). The more interesting satellites are the SDSS ones, because these are the type of faint satellites that are being searched for in PS1, since anything brighter should have already been found on the photographic plates. The four first 'obvious' satellites found in the SDSS were Willman 1 (Willman et al., 2005a), Canes Venatici I (Zucker et al., 2006b), Boötes I (Belokurov et al.,

---

[11] There is a lack of forced photometry and PV2 is not the final depth of the survey.

2006b) and Ursa Major II (Zucker et al., 2006a). Three out of four of these (Canes Venatici I, Boötes I and Willman 1) are the top three SDSS satellites retrieved in this PS1 search, wholly consistent with the sequence of discovery. The other SDSS satellites were mostly confirmed at telescopes before the papers were published. This was the case for Ursa Major I (Willman et al., 2005b), Coma Berenices, Leo IV, Canes Venatici II, Segue 1 and Hercules (Belokurov et al., 2007), Boötes II (Walsh et al., 2007), Leo V (Belokurov et al., 2008), Segue 2 (Belokurov et al., 2009), Pisces II (Belokurov et al., 2010) and Pegasus III (Kim et al., 2015a). This is also consistent with the lower, but still very convincing S/N values that these satellites have in PS1. Coma Berenices, Segue 1, Pisces II, Ursa Major II and Canes Venatici II are convincingly detected with $S/N > 6\sigma$. Two satellites are found at $S/N > 4.5\sigma$ (Segue 2 and Ursa Major II), also a reasonable result. The other five SDSS satellites are discovered with very low S/N ($1.7\sigma < S/N < 4.1\sigma$). Significance maps in both the stellar and galaxies' maps, centred on the satellites are shown in Figure 2.20. The CMDs within 2 half-light radii (using the structural parameters in McConnachie (2012)) are shown in Figure 2.21. Spatial distribution of blue stars ($r - i < 1.0$) in a field centred on the satellites is shown in figure 2.22.

2.5.1.1 A closer inspection: Hercules, Boötes II, Leo IV and Leo V

It is worth spending some time understanding why some of the SDSS satellites do not yield high S/N values. The only real surprise amongst these is Hercules, which was the second brightest satellite found ($M_V = -6.6$, $\mu = 28.3$[12] , $r_h = 8.6$, $\epsilon = 0.68$; McConnachie 2012). The other four satellites are either faint (Boötes II) or distant making identification difficult due to photometric uncertainties at the faint end (Leo IV, Leo V and Pegasus III). In fact, I argue that Pegasus III should not be considered in this list, since it is a more recent satellite discovery of the latest SDSS DR and therefore benefits from wider coverage and better photometry.

Of all the SDSS satellites, Hercules is the second most distorted. A first reason why it may not be picked up is the round kernel that is being used. That seems unlikely since previous SDSS satellite detection efficiency papers such as Koposov et al. (2008) succesfully retrieve Hercules. In addition to this, Ursa Major is more distorted, and is found with higher S/N. Therefore neglecting this, another explorable avenue is the photometry in the vicinity of Hercules. In Figure 2.23 a spatial distribution (top left) of all blue stars can be seen (using a colour-box cut of $-2.0 < r - i < 1.0$). From this cut, it is clear that there is a spatial over density there. The photometry of the stars within 1 half–light radius paints a different picture: just a portion of these stars lie on the isochrone mask (distance–modulus=20.5) which is closest to Hercules' distance-modulus (20.6). There are many other red fainter stars and brighter bluer stars not represented by the mask. Nevertheless, the main features of Hercules are apparent, with its horizontal branch being the most pronounced, and in fact not fully contained by the isochrone mask [13]. If selecting all the stars that lie on the isochrone mask, then less than 50 % of stars are retained. The stars that correspond to this mask produces the spatial distribution of stars in the bottom left panel of figure 2.23. Here, a large portion of the over density has disappeared. An over density is still present, but less apparent relative to the neighbouring regions. This means that when the significance is being computed Hercules is not found to be highly significant because the counts near Hercules are not much higher than the local variance (see

---

[12] Note that here surface brightness and not distance–modulus is meant.

[13] The CMD mask will need to be re-evaluated for the PV3 detection run, possibly extending the horizontal branch to bluer ranges.

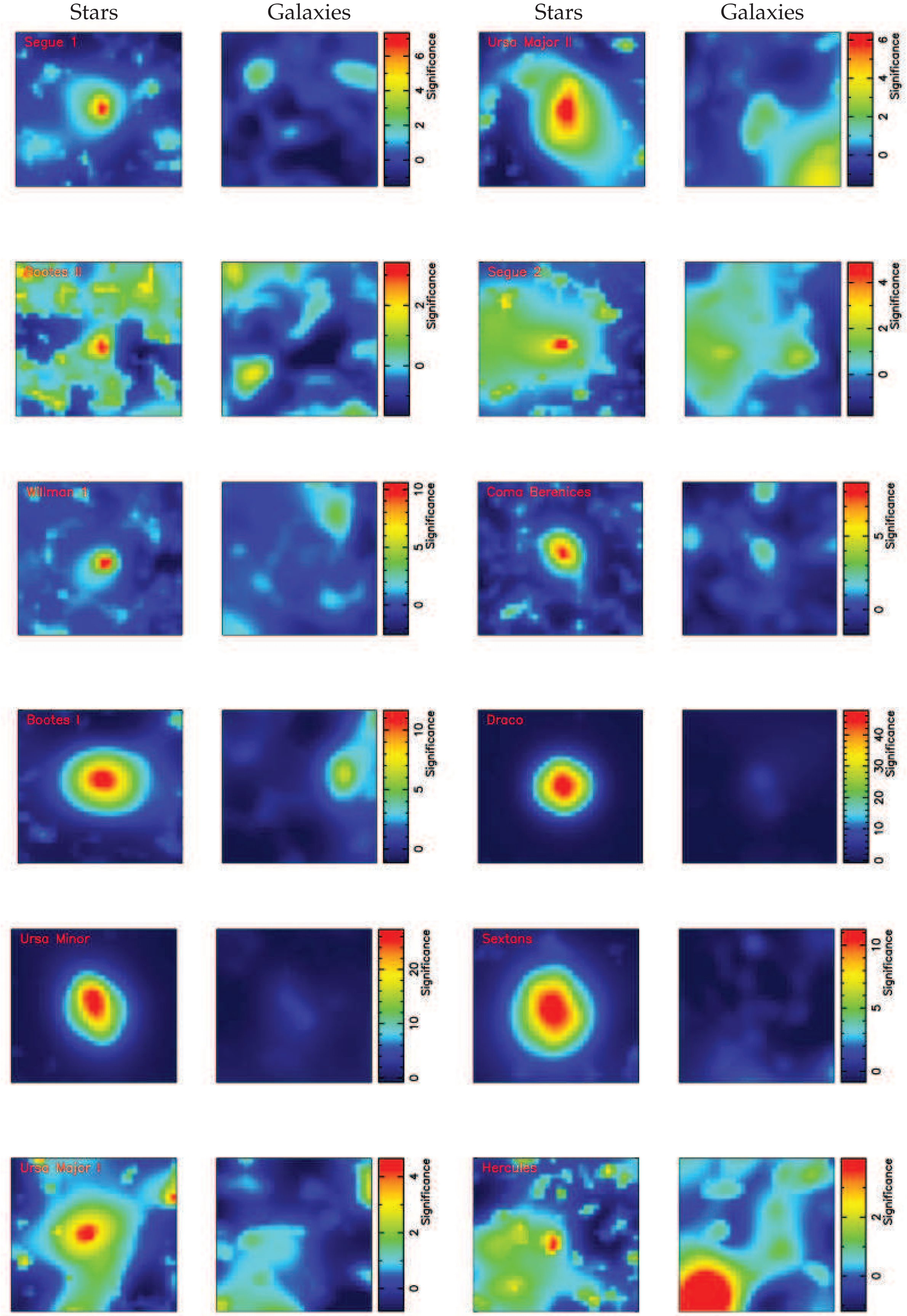
Stars
Galaxies
Stars
Galaxies
Segue 1
Significance
0
2
4
6
Ursa Major II
Significance
0
2
4
6
Bootes II
Significance
0
2
Segue 2
Significance
0
2
4
Willman 1
Significance
0
5
10
Coma Berenices
Significance
0
5
Bootes I
Significance
0
5
10
Draco
Significance
0
10
20
30
40
Ursa Minor
Significance
0
10
20
Sextans
Significance
0
5
10
Ursa Major I
Significance
0
2
4
Hercules
Significance
0
2

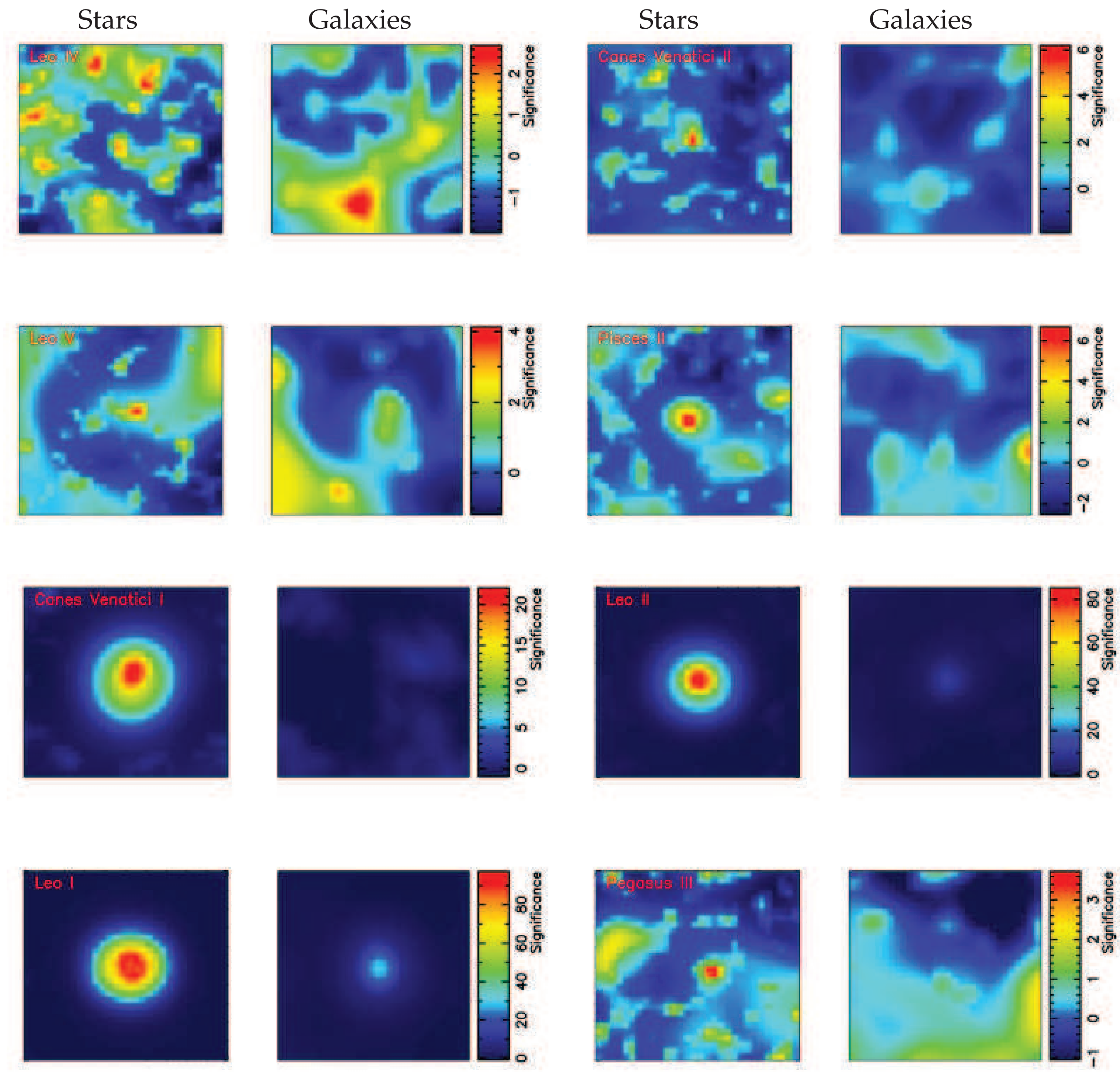

Figure 2.20 - Signal to Noise of all the MW DGs observable in PS1: Segue 1, Ursa Major II, Boötes II, Segue 2, Willman 1, Coma Berenices, Boötes I, Draco, Ursa Minor, Sextans, Ursa Major I, Hercules, Leo IV, Canes Venatici II, Leo V, Pisces II, Canes Venatici I, Leo II, Leo I and Pegasus III. For each dwarf, the left panel shows the S/N in the stellar map, whereas the right panel shows the S/N in the galaxies' map. In most of the cases, the S/N in the stellar map corresponds to a dearth in signal in the galaxies' map. Adopting a 4.5 σ cut, all DGs are retrieved except Boötes II, Segue 2, Hercules, Leo IV, Leo V and Pegasus III. All of these satellites – with the exception of Hercules – are among the faintest satellites and therefore not wholly unsurprisingly not retrieved with the intermediate PV2 data. In addition to this, the SN plot, shows Leo IV to be in very noisy parts, hinting at suboptimal data coverage at these places. Hercules' low S/N is investigated more in depth in Section 2.23.

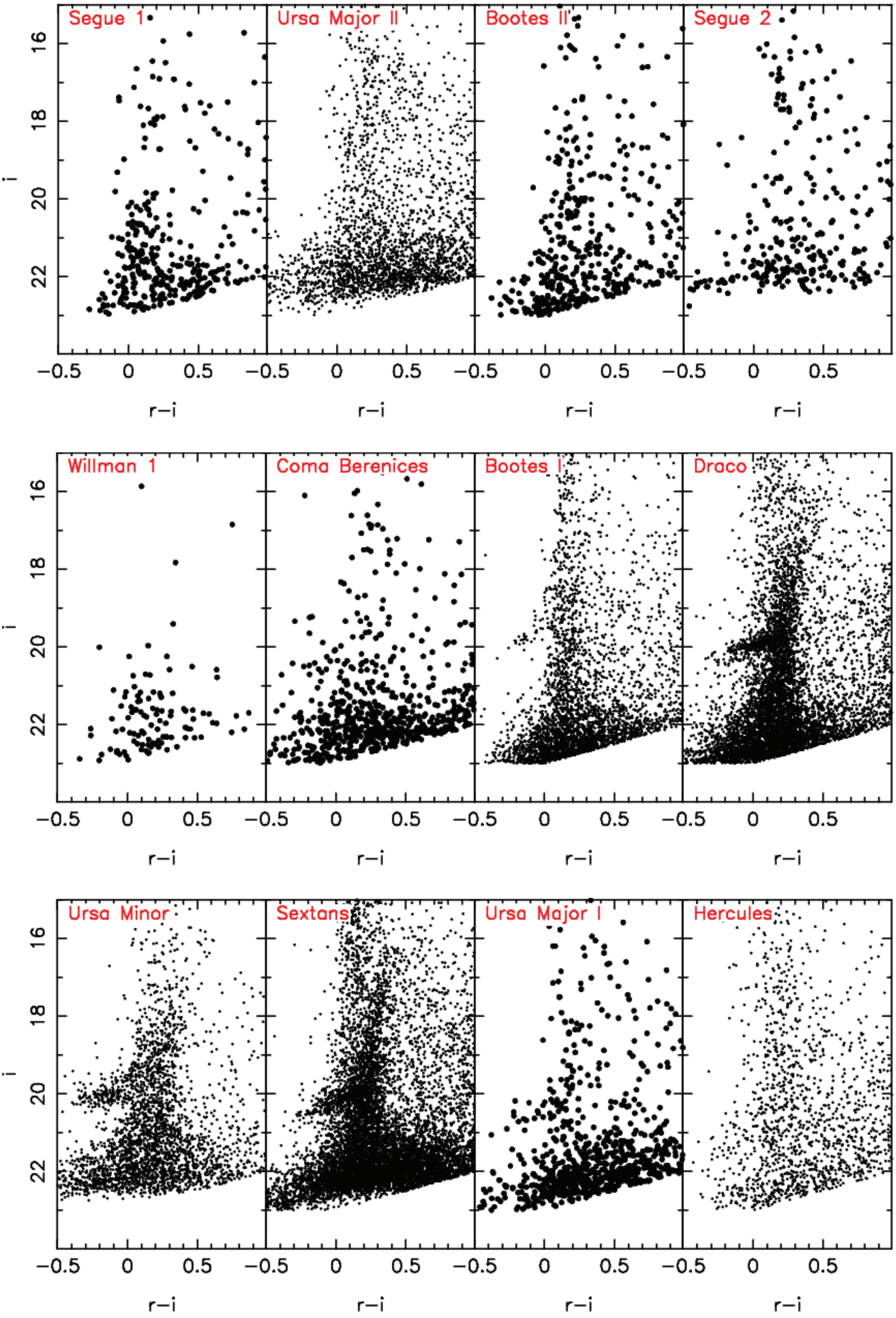
Segue 1
Ursa Major II
Bootes II
Segue 2
Willman 1
Coma Berenices
Bootes I
Draco
Ursa Minor
Sextans
Ursa Major I
Hercules
i
16
18
20
22
−0.5
0
0.5
r−i

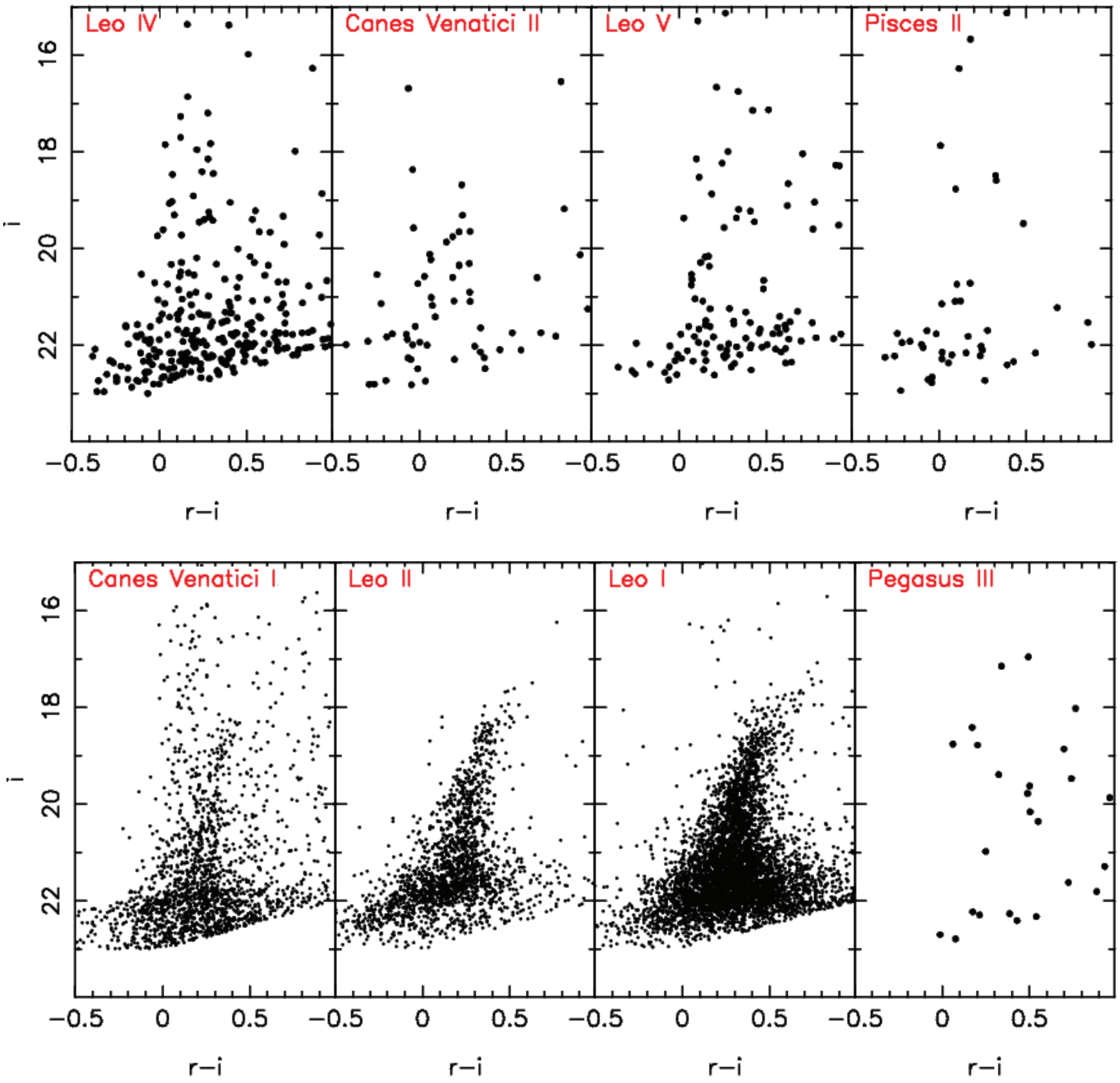

Figure 2.21 - CMDs of all twenty SDSS and 'classical' satellites, detectable in the PS1 survey: Segue 1, Ursa Major II, Boötes II, Segue 2, Willman 1, Coma Berenices, Boötes I, Draco, Ursa Minor, Sextans, Ursa Major I, Hercules, Leo IV, Canes Venatici II, Leo V, Pisces II, Canes Venatici I, Leo II, Leo I and Pegasus III. In each panel all stars are shown that lie within $2r_h$, using the structural parameters as described in Martin et al. (2008) and Kim & Jerjen (2015). In many cases, the main features in the CMD are clearly visible, such as a clear horizontal branch and a red giant branch. Other satellites show evidence of blue stars, corresponding to either a horizontal branch or a main sequence turn off, but in some cases these are difficult to make out. Examples of these are Pisces II, Leo IV, Willman 1 and Segue 2.

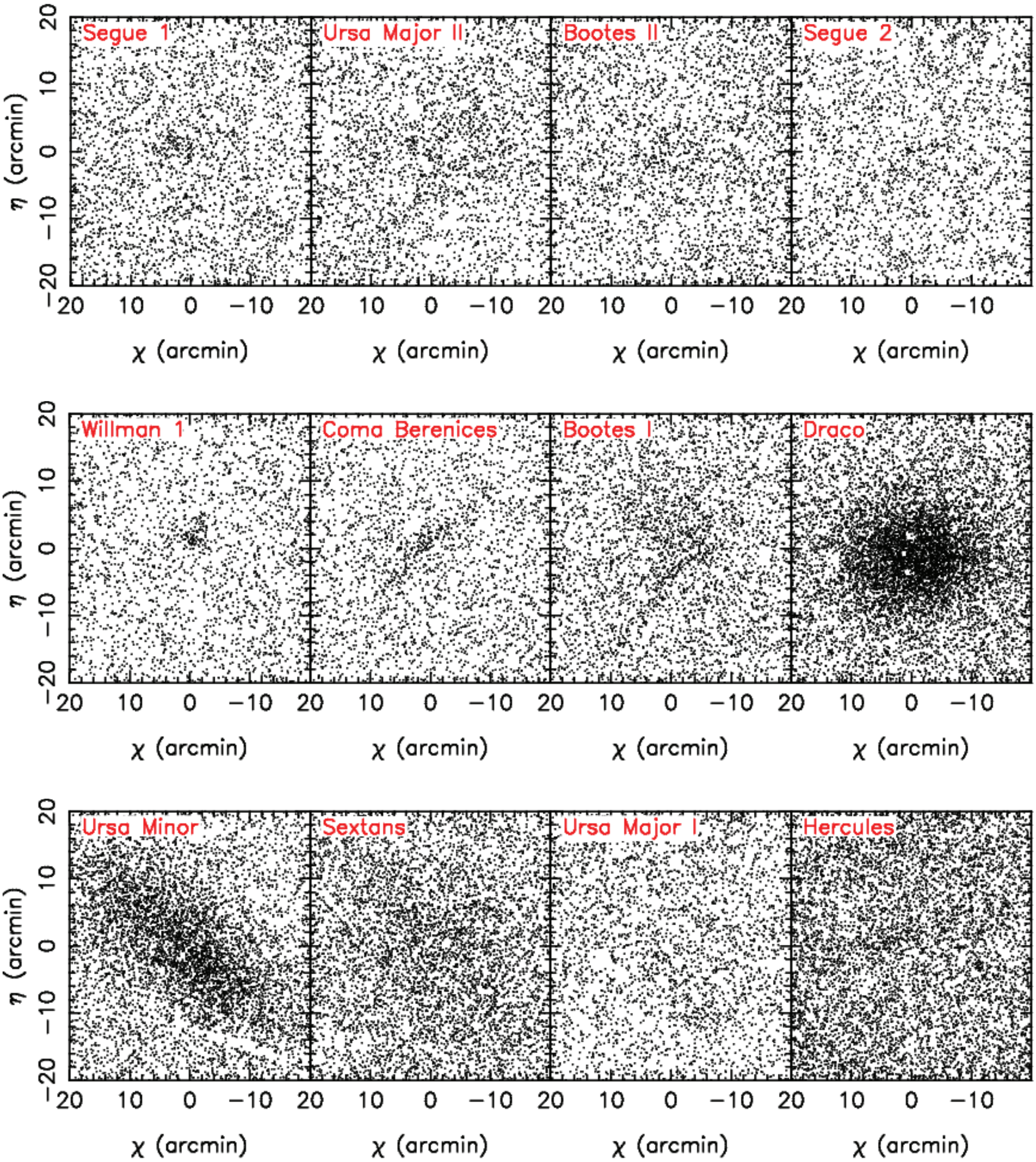
Segue 1
Ursa Major II
Bootes II
Segue 2
Willman 1
Coma Berenices
Bootes I
Draco
Ursa Minor
Sextans
Ursa Major I
Hercules
η (arcmin)
χ (arcmin)
20
10
0
−10
−20

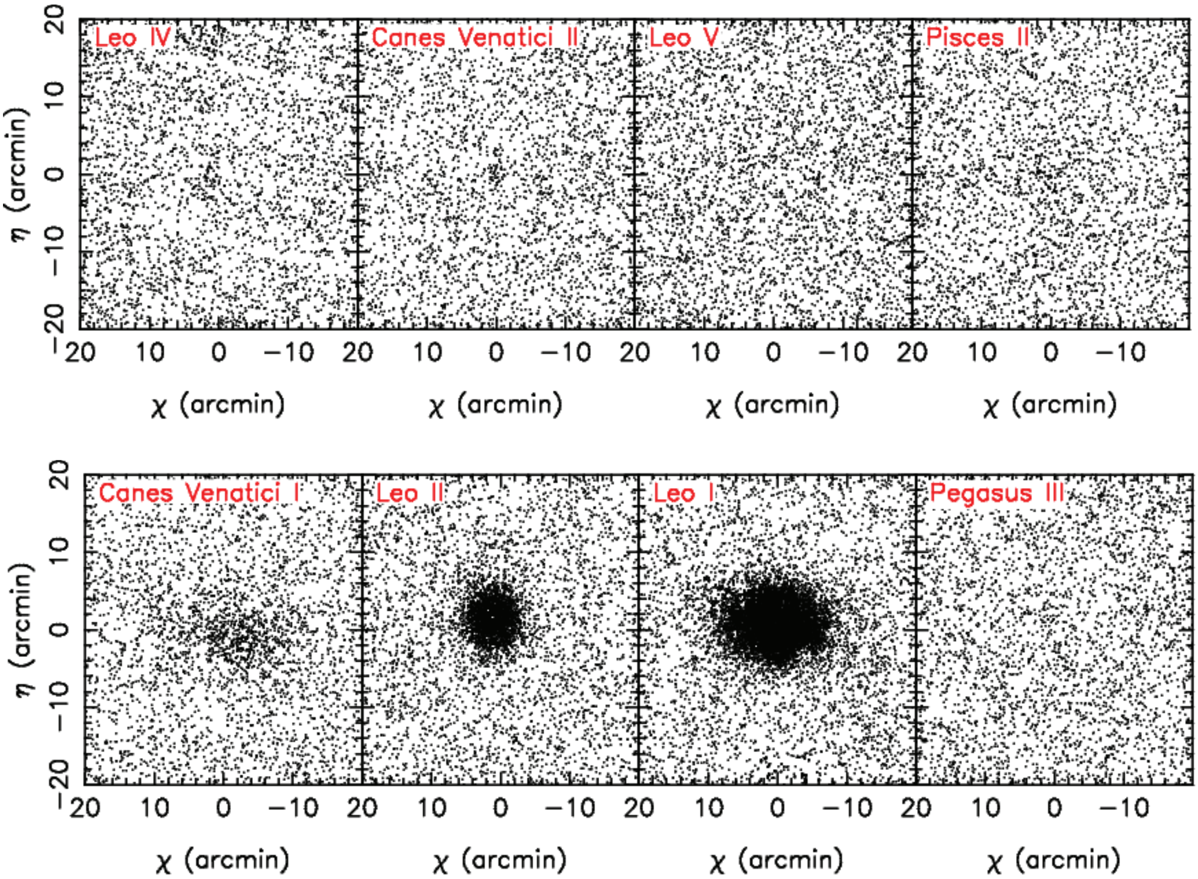

Figure 2.22 - Spatial distribution of all blue stars ($-2.0 < r - i < 1.0$) centred on the co-ordinates of the DGs. In many cases, clear over densities can be seen for these galaxies, most notably for the 'classical' as well as some of the first SDSS satellites to be discovered such as Boötes I, Canes Venatici I or Coma Berenices. In other cases, the over densities are incredibly faint such as Leo IV, Leo V or Segue 2.

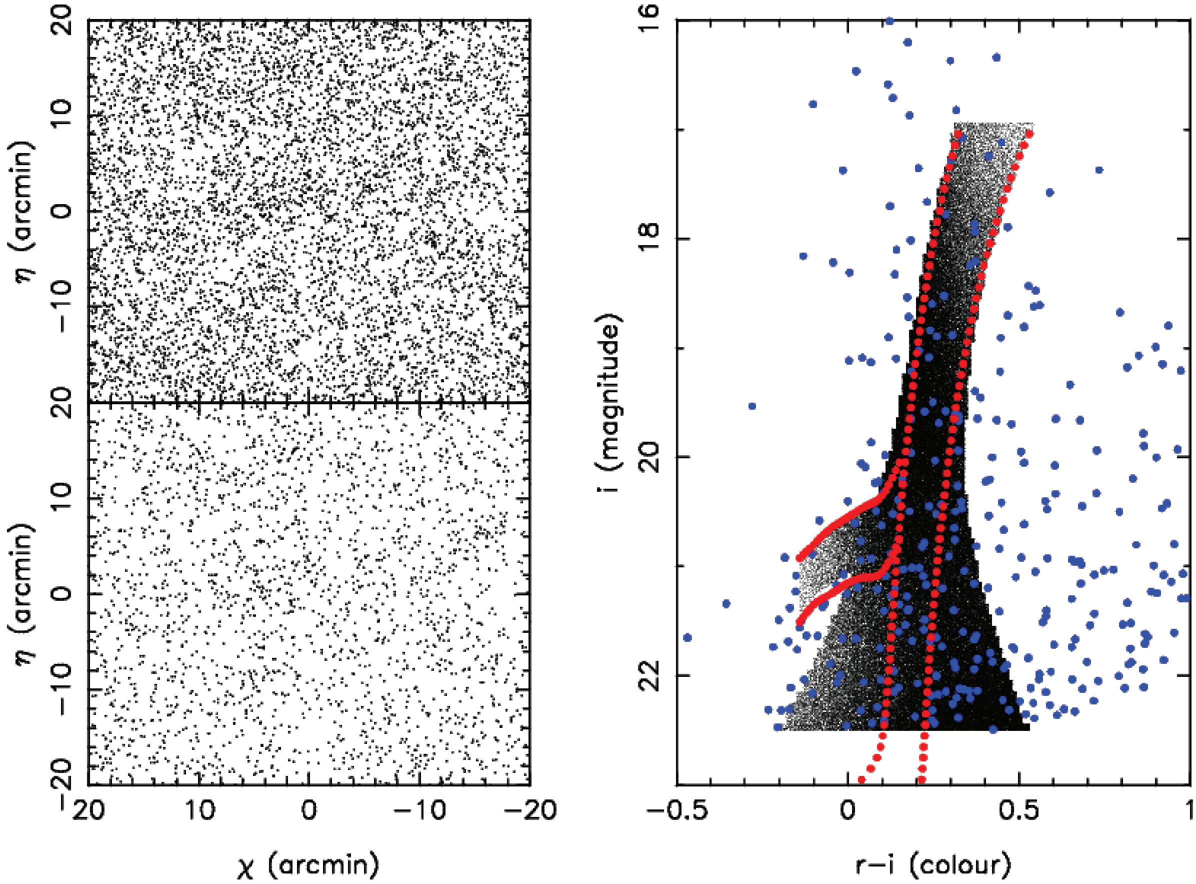

Figure 2.23 - Two spatial distribution plots centred on Hercules' co-ordinates are shown on the left. The top plot displays all stars that satisfy $-2.0 < r - i < 1.0$, with a clear ellipitical over density present, which is Hercules. The bottom plot shows all the stars that lie on the isochrone contour map for a distance-modulus of 20.5, the closest to Hercules' 20.6 (right-hand side plot). Here, the over density is far less pronounced. This is explained by considering the CMD on the right. The black contours correspond to the positions in colour-magnitude space for which stars are deemed likely DG candidates (at that distance).The blue stars correspond to all stars within $1r_h$ of Hercules. Just around 50% of these stars actually fall on the isochrone contour map. This explains why a general colour-box approach reproduces a more convincing over density corresponding to Hercules than the isochrone contours do.

Section 1.4).

An interesting test would be to re-run the code using a colour-box to see whether Hercules turns out to be more significant [14]. The reason I therefore propose for not convincingly finding Hercules in PS1 is due to an offset in photometry. This is not unexpected, since there are issues with the stacked photometry as already detailed in section 1.5. The issues surrounding Hercules are important to note as it highlights that an object such as this could be 'hiding' in the data, but for similar reasons is currently not found. This highlights in turn the teething problems with the PV2 data and how ultimately the forced photometry in PV3 will be necessary to conclusively 'find' Hercules.

Photometry of Leo IV, V and Boötes II reveals a similar picture. When applying a colour–box

---

[14] Unfortunately due to a lack of time this was not done.

to the regions near these satellites, the satellites appear there quite convincingly as spatial over densities. However, isolating just stars with the isochrone mask is too limiting as many stars are discarded. The over density becomes less pronounced and is not obvious with respect to the surrounding background. This explains for example the apparent paradox between the significances of Leo IV and Leo V. When considering the spatial distribution in Figure 2.22, it is obvious that Leo IV has a far more pronounced over density than Leo V. This figure was made with a colour–box. When isolating just stars that lie within the contour mask (Figure 2.21), Leo V's over density is picked up more convincingly relative to its surrounding, resulting in a higher S/N for Leo V, even though Leo IV is the more obvious detection. In these four cases the uncertainties that widened the mask were determined for the 1600 degrees^2 patch in its entirety. For localised regions within the patch where the magnitudes are slightly offset, a fraction of the stars are rejected, which can also explain why a satellite is lost.

2.5.2 Candidate list of detections

An initial investigation into the galaxies' counts for all of these satellites showed that some of these galaxies had very high galaxies' counts. Coma Berenices, for example, was originally found to have a galaxies' count of $\sim 5\sigma$. This is problematic since the galaxies' counts are meant to be used to weed out background contamination, as previously described. Since the 2′ kernel maps are very noisy, an investigation into stacking just the 4′ and 8′ maps for all the distance-modulus bins for the galaxies' map, largely appeared to resolve the problem. In other words, the prescription detailed in Section 1.4 was different depending on the map. The stellar map was stacked for 2′, 4′ and 8′, whereas the galaxies' maps were just stacked for 4′ and 8′. Dividing the S/N in the stellar map by that in the galaxies' map found that Ursa Major II was the highest detection in the galaxies' map (relative to its stellar significance) by 31 %. Ursa Major II was used as the threshold to distinguish significant stellar detections. Specifically, the first threshold imposed in the PS1 detections should be that the stellar counts should be at least three times higher than the galaxies' count (3.2 for Ursa Major II)[15]. Figure 2.24 shows SN_{Stars} vs. SN_{Gals} pixel values for the usual patch containing Canes Venatici I, Boötes I and II and various MW GCs. The orange line shows which part of this 2–D parameter space is interesting for the search. This plot corroborates the fact that significant detections are at $\sim$ 4.5 or $\sim$ 5 as the black data points start to detach from the central black blob in the bottom left.

Now that we have a sensible cut on galaxies, the last thing that remains to be done is to assess the limit at which to cut the stellar map. The determination of this threshold should be determined by demanding that a majority of the satellites be retrieved while at the same time, avoiding a gigantic list of detections by digging too much into the noise. The previous section already hinted at what this limit could be since Hercules, Leo IV, Leo V and Boötes II were deemed to have been detected with very low significance. Any cut including these objects would be a bad idea because this would include far too many detections, of which the majority would be noise. Neglecting these low S/N satellites a cut between 4.5 and 5 σ would be sensible. Experimenting with an initial cut at 4.5σ and $SN_{Stars} > 3 \times SN_{Gals}$ reveals 1438 detections, including all known objects. After inspection, just over a sixth of these can be discarded because they are artefacts in the data. These are due to very bright stars ($i < 12$), which

---

[15] Note that the reason why the stellar S/N for UMa II is so low to start with is because of its large size (16′; Martin et al. 2008), a factor of two larger than the largest kernel size: 8′.

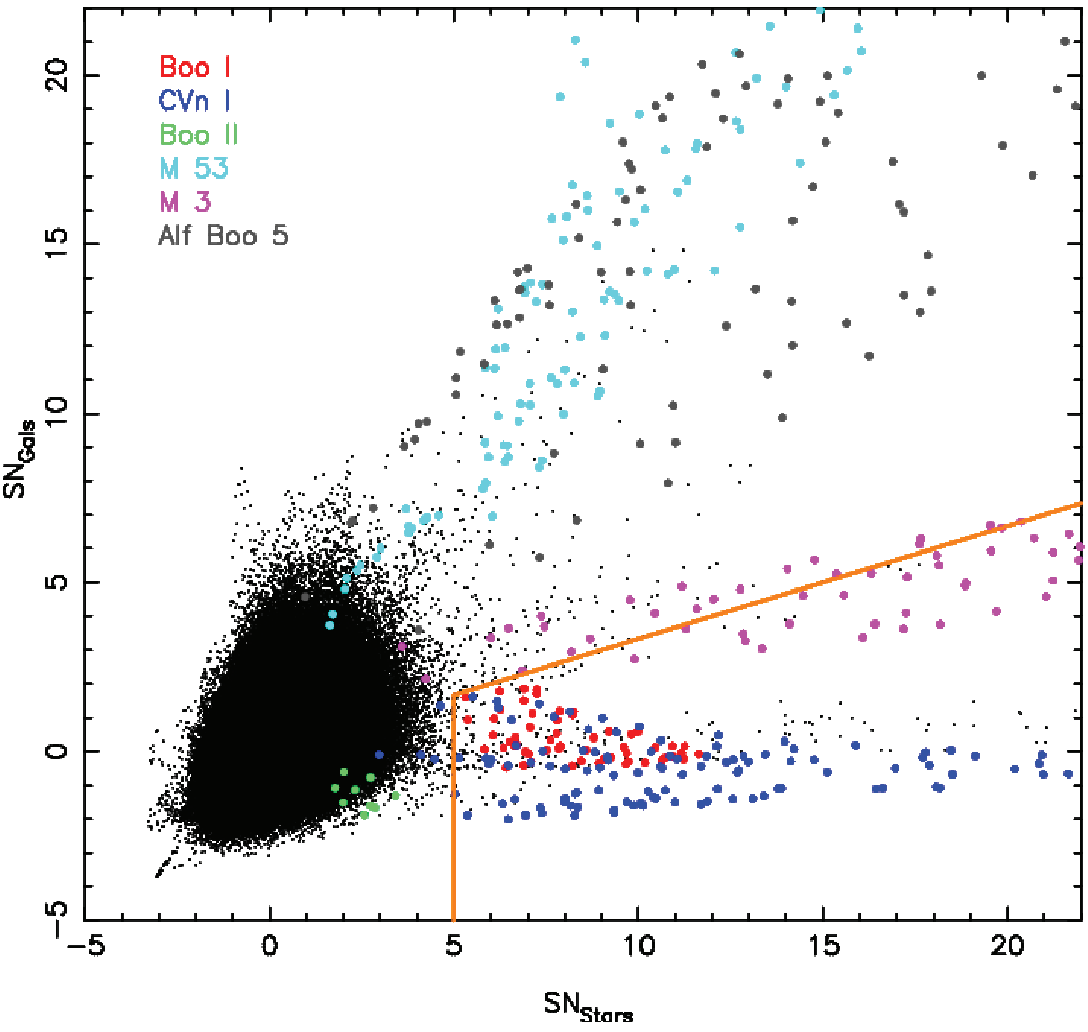

Figure 2.24 - S/N in the stellar map (x–axis) vs. S/N in galaxies' map (y–axis) for the usual patch centred on $(l,\ b) = (30°,\ 70°)$. The black dots represent all the pixel values for the aforementioned patch. Coloured dots represent the S/N values of the pixels and their surroundings centred on known objects in this field, such as the three MW DGs: Boötes I (red), Canes Venatici I (dark blue), Boötes II (green), two MW GCs: M53 (light blue), M3 (pink) and one galaxy cluster: Alf Boo 5 (grey). The orange line denotes those pixels of interest, namely those that pass the detection threshold criteria: S/N>4.5 or 5 for the stellar map and a stellar significance three times the galaxy significance. While Boötes I and Canes Venatici I convincingly satisfy those criteria, Boötes II does not (though it is at the boundary of points for its stellar and galaxies' S/N). For M53, there are clearly issues with the star–galaxy separation, with counts that are even a little higher in the galaxies' map, compared to the stellar map. M3 on the other hand sits in the right side, along with the two other DGs. Finally, Alf Boo 5 is a good example of how the galaxies' map is a powerful tool for weeding out background systems. Though displaying high stellar counts, it also has high counts in the galaxies' map, meaning it does not survive the threshold.

saturate and create bogus over densities with many sources appearing like blue stars and/or over densities.

Table 2.3 - Significance of known objects in PV2

ID	RA	Dec	l	b	SN_{Stars}	SN_{Gals}	Name
3	152.1	12.3	225.9	49.1	97.5	27.1	Leo I
4	168.4	22.1	220.2	67.2	89.6	11.5	Leo II
15	19.1	33.4	128.9	-29.1	59.8	9.3	Andromeda II
19	260.0	57.9	86.4	34.7	47.7	5.8	Draco
20	326.7	-21.3	30.5	-47.7	46.6	3.2	Palomar 12
25	229.0	-0.1	0.8	45.8	40.6	1.1	Palomar 5
28	346.7	12.8	87.1	-42.7	38.2	3.6	Palomar 13
31	8.9	36.5	119.4	-26.3	33.6	5.1	Andromeda II
32	344.6	41.3	101.1	-16.7	33.0	4.2	Lacerta I
36	202.0	33.6	74.4	79.8	31.2	0.0	Canes Venatici I
42	227.1	67.2	105.0	44.9	27.3	3.1	Ursa Minor
49	242.8	14.9	28.7	42.2	25.5	3.6	Palomar 14
53	16.0	21.9	126.7	-40.9	23.7	1.4	Pisces I
56	30.7	-3.3	161.6	-60.7	22.6	0.6	Whiting 1
57	172.3	29.0	202.3	71.8	21.5	4.4	Palomar 4
66	53.2	79.6	130.0	19.0	17.8	0.2	Palomar 1
70	143.7	17.1	214.8	43.6	17.1	5.0	Leo T
71	151.4	0.1	240.1	41.9	16.9	0.4	Palomar 3
118	298.2	-22.1	18.9	-22.9	11.9	2.3	Sagittarius II
122	359.7	30.7	109.8	-30.8	11.8	1.4	Andromeda XXIX
127	210.0	14.5	358.0	69.6	11.6	-0.1	Bootes I
129	17.6	47.6	126.2	-15.1	11.6	2.6	Andromeda V
135	153.3	-1.6	243.5	42.3	11.2	0.1	Sextans
145	162.3	51.1	158.6	56.8	10.6	0.5	Willman 1
150	338.2	31.2	91.0	-22.9	10.4	2.9	Andromeda XXVIII
153	18.6	38.1	127.9	-24.6	10.2	1.3	Andromeda XV
169	45.3	41.0	147.8	-15.5	9.2	0.7	Perseus I
175	186.8	23.9	242.0	83.6	8.6	2.7	Coma Berenices
176	22.3	38.7	131.0	-23.6	8.5	1.9	Andromeda XXIII
187	119.5	26.3	195.1	25.5	7.9	0.6	Koposov 2
215	238.2	64.6	98.3	42.9	7.4	1.3	Draco II
217	151.8	16.1	220.5	50.4	7.3	-0.7	Segue 1
232	292.2	-30.4	8.5	-20.8	7.1	0.3	Arp 2
251	344.6	5.9	79.2	-47.1	6.7	-0.5	Pisces II
265	316.7	15.0	63.6	-21.2	6.5	0.5	Laevens 3
266	332.7	14.9	75.2	-32.7	6.5	-0.2	Balbinot 1
277	132.7	63.1	152.5	37.4	6.4	2.0	Ursa Major II
295	194.3	34.4	113.6	82.7	6.2	-1.2	Canes Venatici II
380	174.1	-10.9	274.8	47.8	5.7	0.6	Laevens 1
556	320.4	19.1	69.4	-21.3	5.2	-1.0	Segue 3
646	33.3	36.2	140.9	-23.8	5.1	-0.4	Triangulum II
790	34.8	20.2	149.4	-38.1	4.9	0.5	Segue 2
819	12.9	29.7	123.0	-33.2	4.8	1.1	Andromeda XXIV
1021	158.7	51.9	159.4	54.4	4.7	0.8	Ursa Major I

Removing these leaves 1249 candidates. Of these candidates, just 688 candidates are above 5σ, showing that this would in fact be a more sensible cut at the expense of losing Ursa Major II and Segue 2. However, a more liberal cut of 4.5σ was adopted to allow for any convincing candidate within the $4.5 < \sigma < 5$ range. Table 2.3 shows a list of Local Group objects of interest to this search, ranked in order of stellar significance. The galaxies' significance as well as the objects' co-ordinates are also quoted. New satellites that resulted from the search in PV1 and PV2 are discussed in the next chapter. For a complete list of all the significant detections, please see Appendix A.

Chapter 3

Discoveries in the Pan-STARRS 1 3 π Survey

3.1 Follow-up campaigns

3.1.1 WFI, BUSCA and LBC follow-up

In our search for stellar substructure, we devoted a considerable amount of time to the photometric follow up of our most significant PV1 and PV2 candidates. Our team applied for follow-up on telescopes with MPG access, which allowed us to get lots of follow-up time, with high–quality instruments, in a less competitive environment. These included the Wide Field Imager[1] (WFI) on the MPG's 2.2m telescope in La Silla (Chile), the Bonn University Simultanenous Camera[2] (BUSCA) on the 2.2 m telescope in Calar Alto (Spain) and the Large Binocular Camera[3] (LBC) at the Large Binocular Telescope (LBT) on Mount Graham (USA). In total we secured 97 hours of follow-up time: 70h in La Silla, 20h at Calar Alto and 7h on the LBT. Our La Silla follow-up consisted of two campaigns to observe the entire RA range for $-30^\circ < \delta < 20^\circ$. Data were acquired in May 2014 (15–20 hours) with the remaining hours spread between the months of May to September 2014. The first campaign was based on PV1 data, whereas the second campaign of 20h, conducted in January 2015, was based on PV2 data. Considerable less time was devoted to follow-up in the Northern hemisphere because of SDSS coverage. The PV1 data depth is shallower than the SDSS depth, and do not have forced photometry in any case. We therefore reasoned that follow-up on parts in the North, where the SDSS had already observed, would be unproductive [4]. The follow-up was conducted at Calar Alto in October 2014. The only other follow-up to date on PV2 (besides the second

---

[1] 4x2 mosaic CCDs, with a 34'x33' field of view in total. WFI has broadband B and V filters, which we used. For more information, please look at: `http://www.eso.org/sci/facilities/lasilla/instruments/wfi.html`

[2] This instrument images simultaneously in 4 bands, with a CCD detector system per filter. The filters here are Strömgren u, b, v and y. The field of view is 12'x12'. More information can be found at: `http://www.caha.es/newsletter/news01a/busca/`

[3] Two wide field cameras, each with a field of view of 23'x25' and containing 4 CCDs. This set-up allows for dual imaging in the blue and red arms of the telescope. See here for more information: `http://abell.as.arizona.edu/~lbtsci/Instruments/LBC/lbc_description.html`

[4] Note that one of the recent DG discoveries (Pegasus III) in the SDSS by Kim et al. (2015a), and therefore also in the PS1 survey, was such a case. With the PV2 data we currently have there was no way of finding that system before the SDSS did. It will be interesting to see how that changes when the search algorithm is re-run for PV3 (with forced photometry).

La Silla run) was conducted at the LBT, also in October 2014. We intend to conduct a fifth campaign of follow-up with candidates at the LBT in September–November 2015 for which we were awarded 4 hours of time. We hope to follow-up candidates identified in PV2 or PV3 (unforced photometry).

3.1.2 Follow-up results

After the campaign in May 2014 at La Silla, I adapted Branimir Sesar's pipeline for WFI image reduction to our follow-up data. I spent a considerable time ($\sim$ 6 months) getting this pipeline to work myself. This was an informative process because I learnt all the steps involved with data reduction, such as cleaning images, astrometric calibration, stacking images, running photometry amongst others. Unfortunately my adaptation of the pipeline did not work successfully: though all the individual steps seemed to work well, the extracted photometry always seemed too shallow compared to the depths we expected from the amount of time we spent observing each candidate. In the end, Nicolas Martin adapted his own pipeline to the La Silla data and extracted the photometry for these, down to the expected depths, i.e. $\sim$1–1.5 mags deeper than the limiting PS1 magnitude. For LBT data, Rodrigo Ibata already had a pipeline in place for the reduction of LBT data, which Nicolas Martin and he used to extract the photometry for the LBT images.

Out of 73 hours of data already reduced[5], just one satellite was confirmed through these means (Triangulum II). If I had had my time again, I would have probably conducted the follow-up effort in a different way to the route which was followed. Most of the follow-up was based on the PV1 data. When the PV2 data arrived, we noticed how much of an improvement this was relative to PV1: many artefacts had been cleaned up, the data were of course a lot deeper. PV2 and PV3 may have been better starting points for folllow–up. We may have been too enthusiastic. To demonstrate what the improvement could have been with WFI follow-up, we decided to devote one hour of WFI time to Segue 1. Figure 3.1 shows two panels: the left hand side is follow-up from WFI, whereas the right hand side panel is the PV2 data. This CMD was constructed using the structural parameters from Martin et al. (2008). Not only is the star–galaxy separation more reliable (because of the increased depth) and the Main-Sequence a lot tighter in WFI, these data also go $\sim 0.5 - 1.0$ mags deeper, with good photometry, allowing for any real new satellite to be found.

3.2 Andromedan discoveries

3.2.1 Lacerta I, Cassiopeia III and Perseus I

The first DGs to be found in the PS1 survey were in fact M31 satellites. These discoveries are briefly included here to be comprehensive about the whole PS1 search for stellar substructure. Nicolas Martin headed an initial search for these satellites and published two discovery papers as a result of these. The first contained the discoveries of Lacerta I and Cassiopeia III (Martin et al., 2013b). The second detailed the discovery of Perseus I (Martin et al., 2013a).

---

[5] We have not yet reduced Calar Alto data.

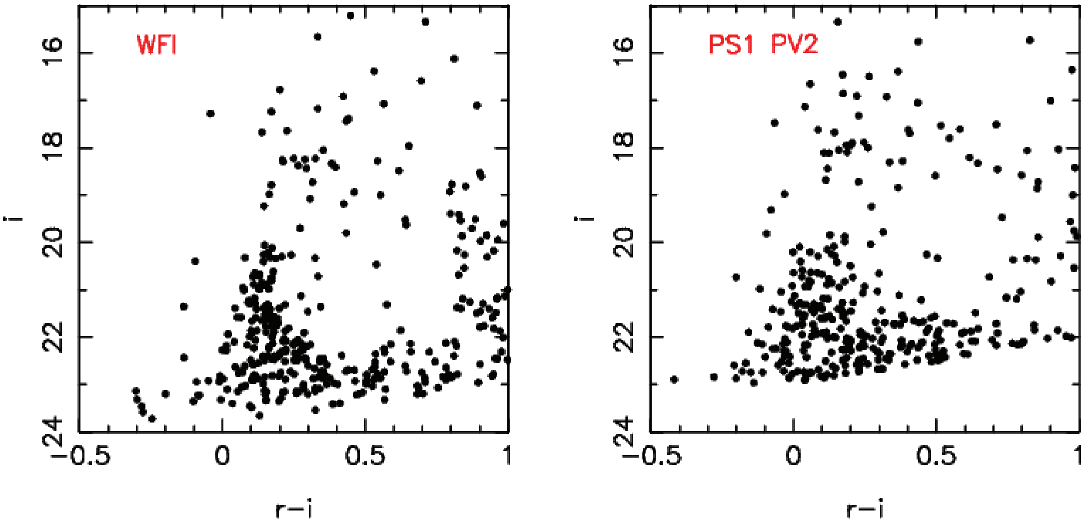

Figure 3.1 - *Left:* WFI data of Segue 1, with a very clear Main-Sequence, a turn off and a sparsely populated red giant brach. The photometric improvement is quite considerable, showing extra depth as well as a tighter Main Sequence *Right:* PV2 photometry from PS1 for Segue 1. Though it is clear that there is something here with a whole bunch of blue stars, the scatter in photometry does not allow for a clear Main Sequence to be determined.

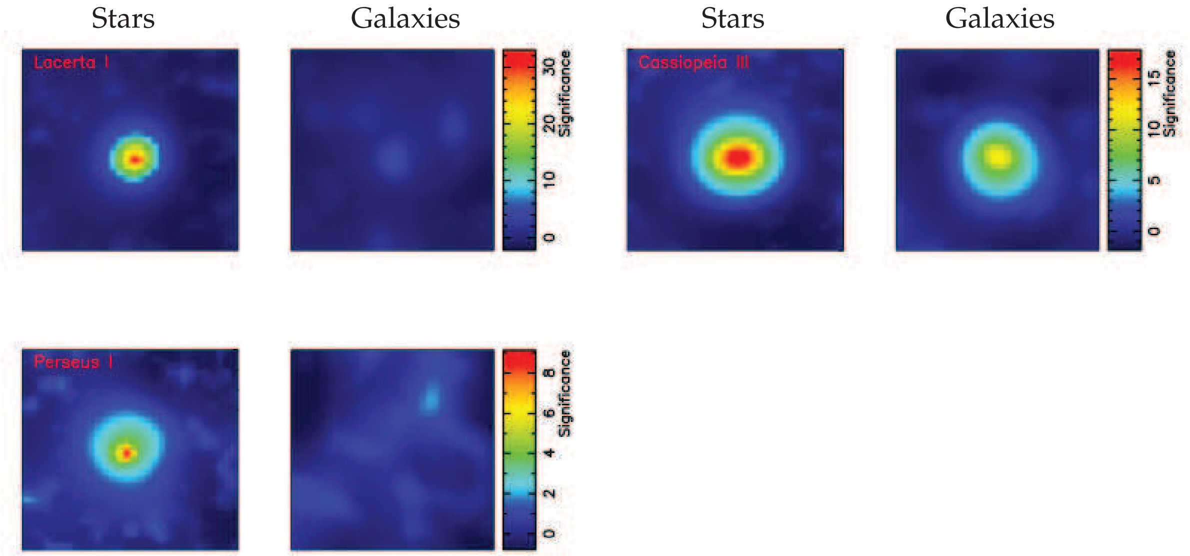

Figure 3.2 - S/N in the stellar (left) and galaxies' map (right) for the three Andromedan satellites: Lacerta I, Cassiopeia III and Perseus I. Two out of three are picked up by the convolution code, with Cassiopeia III containing galaxies' counts too high to survive the threshold as described in Section 2.5.

Nicolas Martin was the first to start using the stacked photometry in PV1 in March 2013, enabling their discovery. Applying a colour-box approach which isolates blue stars, he investigated all over densities in PS1, not coinciding with the PAndAS survey (Ibata et al., 2007; McConnachie et al., 2008) or the SDSS (York et al., 2000), in the vicinity of M31. Lacerta I and Cassiopeia III were discovered within a few days of each other. A few months later Perseus I was discovered. Martin et al. (2014) spectroscopically confirmed these satellites as members of M31. The properties of these three M31 satellites are summarised in Table 3.1. For further information about these satellites, the reader is invited to read Martin et al. (2013b,a, 2014)

Table 3.1 - Properties of Lacerta I, Cassiopeia III and Perseus I

	Lacerta I	Cassiopeia III	Perseus I
α (ICRS)	22:58:16.3	00:35:59.4	03:01:23.6
δ (ICRS)	+41:17:28	+51:33:35	+40:59:18
$\ell(^\circ)$	101.1	120.5	147.8
$b(^\circ)$	-16.7	-11.2	-15.5
$(m-M)_0$	24.40 ± 0.12	24.45 ± 0.14	24.49 ± 0.18
Heliocentric distance (kpc)	756^{+44}_{-28}	772^{+61}_{-56}	785 ± 65
M31–centric distance (kpc)	275 ± 7	144^{+6}_{-4}	374^{+14}_{-10}
M_V	-11.7 ± 0.7	-12.3 ± 0.7	-10.3 ± 0.7
μ_0 (mag arsec^{-2})	25.8 ± 0.8	26.4 ± 0.8	$25.7^{+1.0}_{-0.9}$
Ellipticity (ϵ)	0.43 ± 0.07	0.50 ± 0.09	$0.43^{+0.15}_{-0.17}$
r_h (arcmin)	$4.2^{+0.4}_{-0.5}$	$6.5^{+1.2}_{-1.0}$	1.7 ± 0.4
r_h (pc)	912^{+124}_{-93}	1456 ± 267	400^{+105}_{-85}
$< v_r >$ (km s^{-1})	-198.4 ± 1.1	-371.6 ± 0.7	-326 ± 3
$< v_{r,gsr} >$ (km s^{-1})	$+9 \pm 2$	-186 ± 2	-220 ± 4
σ_{vr} (km s^{-1})	10.3 ± 0.9	8.4 ± 0.6	$4.2^{+3.6}_{-4.2}$
M$_{half}$ (M$_\odot$)	$4.2^{+0.8}_{-0.9} \times 10^7$	$4.1^{+0.7}_{-1.1} \times 10^7$	–
(M/L)$_{V,half}$ (M$_\odot$/L$_\odot$)	15^{+12}_{-9}	8^{+9}_{-5}	–
median [Fe/H]	-2.0 ± 0.1	-1.7 ± 0.1	–
stacked [Fe/H]	–	–	-2.0 ± 0.2

If Nicolas Martin had not found these satellites, two out of the three would have been picked up very convincingly by the search convolution code in either PV1 or PV2. These are Lacerta I ($S/N = 33.0$) and Perseus I ($S/N = 9.2$). Cassiopeia III was not found in PV1 since the code was not run on patches $|b| < 15^\circ$, as detailed in Section 2.2.1. Though Cassiopeia appears to have a stellar S/N well above the detection threshold (S/N= 17.9), the galaxies' count is very high here (S/N= 11.9)[6], indicating that the star–galaxy separation needs to be improved for PV3. A likely cause for the high galaxies' counts is the combination of its high brightness and crowding at the centre. This last result is once again demonstrating that besides a Hercules, there is the possibility of a Cassiopeia III concealed in the data, that is not found either through photometry or star–galaxy separation. The S/N of these discoveries in both maps can be seen in Figure 3.2

---

[6] Note that Nicolas Martin did not cross–match with a galaxies' map.

3.3 Milky Way discoveries

3.3.1 PSO J174.0675–10.8774/Laevens 1/Crater

The first Milky Way (MW) discovery to result from the search was by far the most controversial. Initially discovered in October or November 2013, in PV1 data, there was a clear over density of stars on the sky, compared to neighbouring field regions (See Figure 3.3). Unfortunately the PS1 CMD was less than convincing: there were no clear features such as a main sequence, a turn-off, an red giant brach or a horizontal branch (See Figure 3.3). We were reasonably sure we had found something new since the clumping of stars on the sky was very real, the PS1 postage stamp showed an over density of resolvable stars, the DSS plates showed an over density of stars and the CMD showed a significant number of blue stars. Note that the S/N for this satellite can be seen in Figure 3.6. We applied for Director's Discretionary Time[7] (DDT) using WFI and obtained follow-up on 1 January 2014. Unbeknownst to our group, the same object had also been discovered by Belokurov et al. (2014) in The VST Atlas survey (Shanks et al., 2013). Faced with the pre-print of this paper on arxiv, we advertised our own paper a week later, with an outcome that differed significantly to Belokurov et al. (2014). In the aforementioned paper, a DG classification was favoured, whereas a GC classification was favoured by our team. Having named the object Crater, which follows the naming convention (if assumed to be a dwarf), we renamed our object to PSO J174.0675-10.8774[8]. Though the conflict in interpretation of the satellite is briefly described in the letter (See Chapter 4[9]), a more in-depth analysis of the conflicting views as well as further studies devoted to Laevens 1/Crater are described in the next few paragraphs.

The Belokurov et al. (2014) DG interpretation rests mainly on the follow-up photometry that they acquired for the satellite on the 4m William Herschell Telescope. Their and our CMD shows the presence of two (Cambridge) or three (PS1) bright, blue stars at $g \sim 19.0$, $g - r \sim 0.2$, bluewards of the brightest point of the red giant brach as well as a collection of blue stars bluer and brighter than the main sequence turn off. The Cambridge team argues that these stars are evidence of recent star formation, associated with the blue-loop phase, which some stars experience, when they start to ignite He in their cores. The Belokurov et al. (2014) paper shows this by fitting isochrones in the $-2.5 < [\mathrm{Fe/H}] < -1.5$ range for 0.16, 0.35 and 1 Gyrs. If these stars are associated with the new satellite, this points to recent star formation. Since no GC has accomplished this, the DG classification was argued because the system would need to have retained its gas, and therefore have a deeper potential well than implied by its baryons.[10]. Other factors that undoubtedly contribute to their classification are the brighter magnitude they obtained ($M_V = -5.5 \pm 0.5$), the larger distance ($d \sim 170\,\mathrm{kpc}$) and size ($r_h = 30\,\mathrm{pc}$), all of which push this satellite more towards the DG regime. Our measured properties are: $M_V = -4.3 \pm 0.2$, $d = 145 \pm 17\,\mathrm{kpc}$ and $r_h = 20 \pm 2\,\mathrm{pc}$. We argue that the cluster shares properties with outer halo GCs in M31 and the MW such as Palomar 14 and Palomar 4. We note that HST CMDs of these two clusters (see Chapter 4), particularly that of Palomar 14, show the same features as Laevens 1/Crater, namely some bluer and brighter stars near the main sequence turn off and near the red giant brach branch. We argue that the

---

[7] Note that this was before our follow-up campaigns in 2014.

[8] Note that Bianchini et al. (2015) were the first to refer to this object as Laevens 1/Crater reflecting the double interpretation of the object, a naming convention we have since adopted.

[9] `http://adsabs.harvard.edu/abs/2014ApJ...786L...3L`

[10] The paper briefly considers the case of a peculiar GC as well.

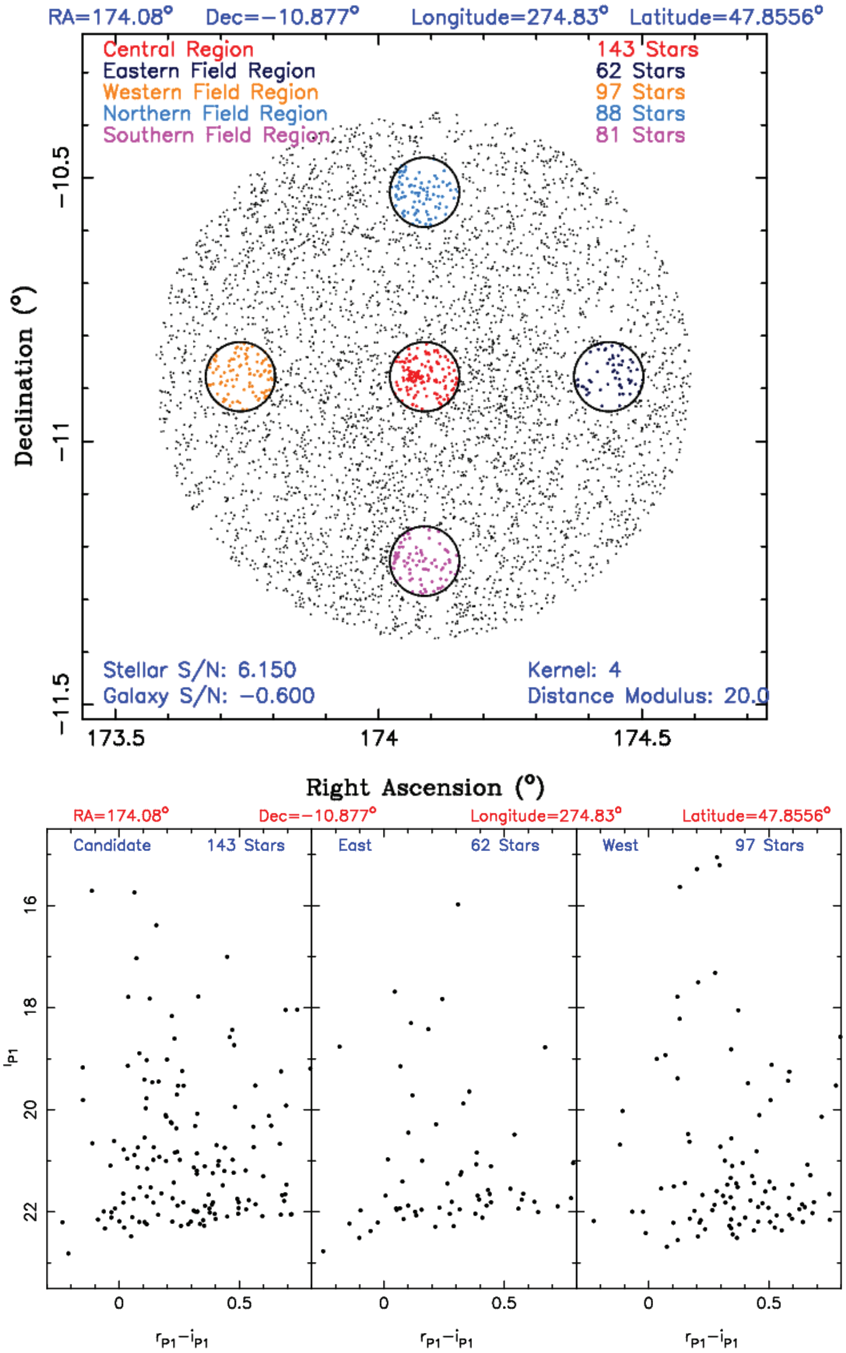

Figure 3.3 - *Top:* spatial distribution of all stars within 0.5 degrees of Laevens 1/Crater (centre). The stellar S/N (in PV1) was 6.2, with a galaxies' count of -0.6. The circles reflect a 4′ radius (all coloured stars are within these circles). This shows a very clear over density of stars at the centre, relative to the neighbouring field regions. *Bottom:* CMD corresponding to the centre and two neighbouring field regions from the top plot. The stars in this CMD correspond to all the stars within the circles in the above plot. Though no clear features are discernable in the leftmost CMD, there are clearly a whole collection of blue stars, that are not present in the neighbouring field regions.

Table 3.2 - Spectra for five stars

		B. Sesar				Kirby et al. (2015)			
RA	Dec	ID	v_r	δv_r	Type	ID	v_r	δv_r	member
11:36:15.940	-10:52:44.09	1	90.0	9.1	RGB	93	147.2	1.6	Y
11:36:13.896	-10:52:27.24	2	119.0	11.0	RGB	420	149.8	1.5	Y
11:36:17.269	-10:52:46.58	3	177.9	11.0	BL	1717	266.0	2.2	N
11:36:16.616	-10:52:46.69	4	81.3	6.9	BL	1715	72.0	1.8	N
11:36:19.593	-10:52:37.70	5	152.4	8.7	BL	399	155.3	1.8	N

size, magnitude, age and metallicity of the stellar system are wholly consistent with the 6 or 7 distant outer halo clusters known in the MW such as AM-1, the most distant cluster known until this system was discovered.

We attempted to resolve the conflict in interpretation by acquiring velocities for the putative blue loop and red giant brach stars. In April 2014, two attempts were undertaken using DBSP[11]on the 200 inch[12] telescope at Palomar observatory[13] and MODS [14] on the 8m LBT telescope. Unfortunately both attempts were unsuccessful. The first attempt was headed by Branimir Sesar, who managed to obtain the velocities of five stars. Figure 3.4 shows the cluster image and where those five stars are situated. Three stars were the putative blue-loop stars, with two stars on the red giant branch. Table 3.2 shows the velocities of the stars as determined by Branimir Sesar. As can be seen from the first six columns in Table 3.2 the two stars thought to be part of the red giant brach did not agree with each other. The other three "blue-loop stars" had velocities different from one another, consistent with them being field stars. Since the two red giant brach star measurements were inconclusive, we could not say anything meaningful about membership for any of the five stars.

The second attempt was part of a DDT proposal at the LBT. The weather during that particular dark time run was far from ideal and other programmes were given higher priority during good weather. Due to the compact nature of the cluster, we were only able to place 15 single slits on the mask. Because our programme was observed with bad weather, many of the slits had low S/N and only around three stars turned out to be of any use. Three measurements were not enough to say anything sensible about the velocity of the cluster and the (non-)membership of the "blue-loop" stars. My part in this endeavour was the design of the mask (placing the slits, choosing guide and alignment stars etc.). Once the data had been taken, I passed these on to other people in–house who had the necessary reduction tools in place to allow a fast reduction and publication. Michelle Collins, Mark Norris and Rodrigo Ibata, all tried to reduce the data to get as much information out as possible, but this amounted to little, reinforcing the view that the data quality was just too poor.

Since the discovery, numerous people have acquired data for this interesting stellar system.

---

[11] Double Spectrograph.

[12] In the world of metric units, that is 5 metres.

[13] `http://www.astro.caltech.edu/palomar/about/telescopes/hale.html`

[14] Multi-Object Double Spectrograph. Please see: `http://abell.as.arizona.edu/~lbtsci/Instruments/MODS/mods.html`

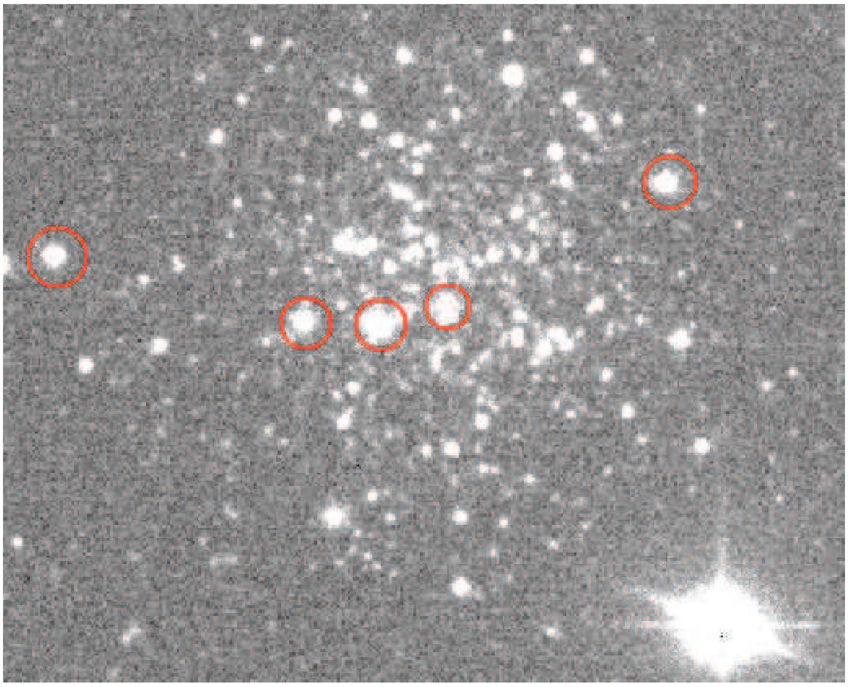

Figure 3.4 - 1.5′x1.5′ image of Laevens 1/Crater. The red circles show the five stars that were followed up with DBSP at the Palomar Observatory. From left to right these are: 5, 3, 4, 2, 1, which are quoted as ID numbers in Table 3.2. 3, 4 and 5 are the putative blue loop stars. 1 and 2 were thought to be red giant brach members.

One of the first published results was Kirby et al. (2015), confirming the system to be a GC and thereby renaming it Laevens 1. Amongst the stars they followed up were the five stars that we had followed up a year earlier. The measurements from this paper confirm that our velocities were inaccurate. The Kirby et al. (2015) velocities are included in table 3.2 for comparison. For stars 1, 2 and 3 the results do not agree at all, while the last two agree within $\sim$ 10 km s^{-1} of each other. The paper concluded that the “blue-loop stars” were not members and that the satellite is more likely to be a GC. Firstly, the satellite does not have strong evidence for DM ($M/L < 130 M_{\odot}/L_{\odot}$, 90% confidence). Secondly the metallicity dispersion is less than 0.4 dex (90% confidence). Finally, its metallicity ($[\mathrm{Fe/H}] = -1.68 \pm 0.05$) means that it does not follow the luminosity–metallicity relation for DGs (Kirby et al., 2013), with a metallicity too low for its magnitude to fit the relation. Kirby et al. (2015) do note that the upper limit on their DM measurement does not rule out a dark-matter dominated system, but conclude that the overall evidence points to a GC.

Bonifacio et al. (2015), on the other hand, favoured a DG interpretation. They favour such a classification for a variety of reasons. They repeat the Belokurov et al. (2014) observation that the system lies close to Leo IV and V, has a similar distance and velocity compared to those two satellites. They also note that the number of blue-loop stars relative to the total magnitude of the system are too high for those stars to be blue stragglers. They claim to measure a velocity dispersion of $\sigma > 3.7 kms^{-1}$ using the measurements of two stars. The big caveat is that the uncertainties of these stars were not taken into account for the determination of the velocity dispersion. When taking these into account the velocity dispersion is consistent with being zero, therefore ruling out any definitive conclusion about the velocity dispersion. The metallicity measurements of the two stars they measure are entirely consistent (within the errors) of Kirby et al. (2015). Other groups have more follow-up data for this stellar system such as Karina Voggel (MUSE) and Daniel Weisz (HST/ACS). These papers should appear in the foreseeable future.

3.3.2 Triangulum II

In October 2014, we had a three hour programme on the LBT to follow-up our most significant DG candidates around M31. Having identified five M31 candidates we wanted to follow-up, we were one candidate short. At the last minute, Nicolas Martin and I were reviewing several candidates and stumbled across a messy CMD (See figure 3.5), containing many blue stars. We included this one as a MW satellite to follow-up. Ironically while our five M31 candidates came back as background galaxy clusters, the sixth turned out to be Triangulum II, a MW satellite. Nicolas Martin and Rodrigo Ibata were instrumental in the reduction of the data (as was already described in Section 3.1). This satellite was the first satellite discovered with PV2 data and at 5.45σ was just above the 5σ threshold we were applying to PV2 at the time. Had it not been for the M31 follow-up, Triangulum II would probably have been discovered much later. For further information about this satellite, please see Chapter 5[15]. The S/N plot can be seen in Figure 3.6.

3.3.3 Sagittarius II, Draco II and Laevens 3

Sagittarius II, Draco II and Laevens 3 were found at the end of June 2015 as the finalised list of detections in PV2 was being analysed[16]. The S/N plots can be seen in Figure 3.6. Contrary to our two previous objects, these objects did not need follow-up because of the booming detections (with the exception of Draco II). Also due to the later discovery, we were able to obtain the PV3 forced photometry, which was definitely necessary to convince ourselves that Draco II was a real detection. These discoveries are quantified in the most recent paper in Chapter 6. This paper was submitted at the end of July and has just been accepted.

---

[15] `http://adsabs.harvard.edu/abs/2015ApJ...802L..18L`

[16] Please note that the reason why Sgr II and Lae 3 were not discovered as part of the second La Silla campaign in January 2015, was due to the observability of the two objects. More importantly the 2′ kernel which seems to have greatly changed the efficiency of the search algorithm had not been fully implemented at this point. This would have definitely impacted the obvious detection of Lae 3. It is also interesting to note that had the 2′ kernel been implemented on the PV1 data in 2014, this would almost certainly have yielded the discovery of Sgr II in May 2014, maybe even Lae 3.

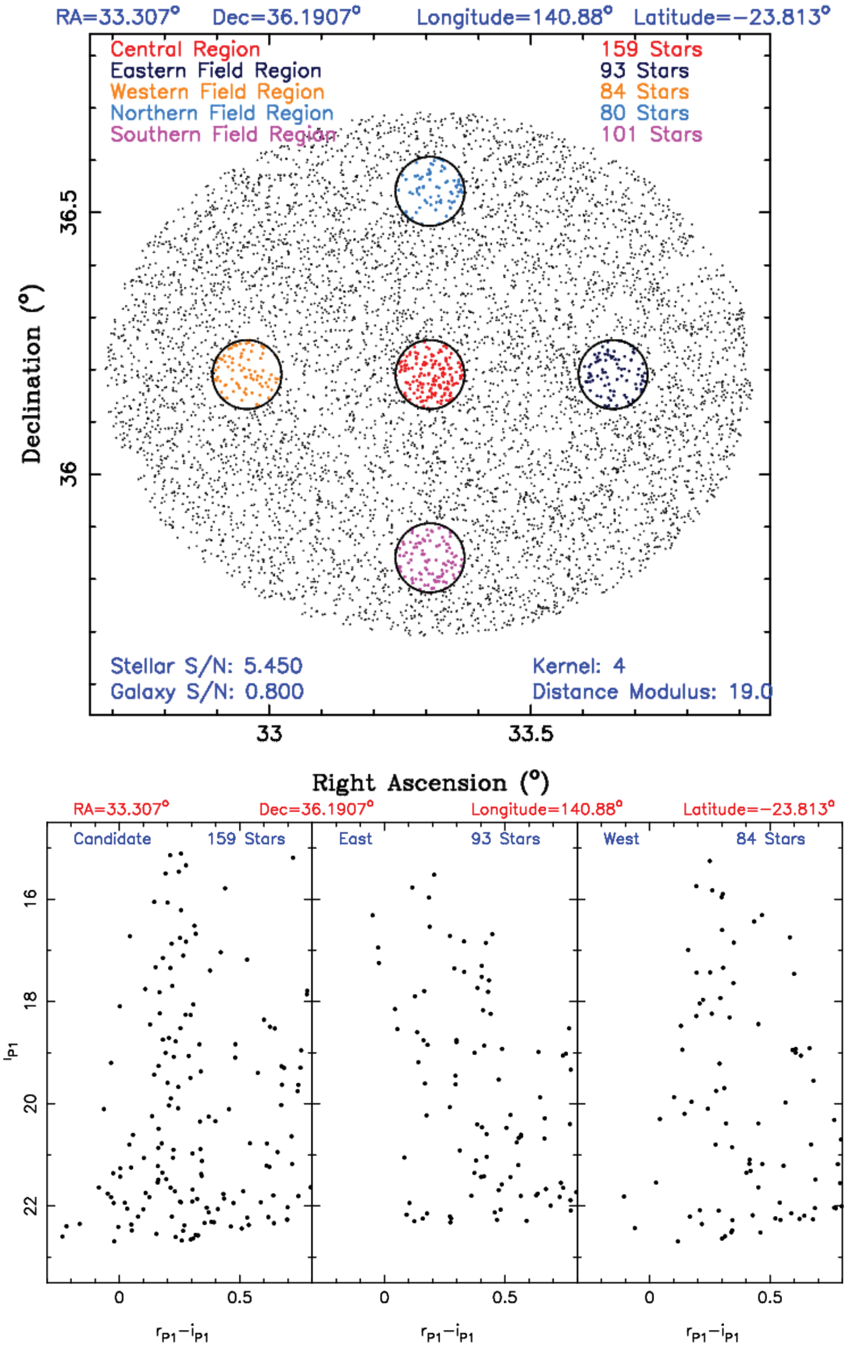

Figure 3.5 - *Top:* Spatial distribution of stars within 0.5 degrees of Triangulum II (centre). Once again the circles represent 4′ radii for the detection at the centre as well as four neighbouring field regions. There is a clear over density of stars at the centre: $\sim$ 50% more stars than in the neighbouring field regions. *Bottom:* CMDs for the central region (Tri II) and two neighbouring field regions. All the stars shows here correspond to all the coloured stars in the top plot. There are a lot of blue stars at the faint end: $i \sim 21 - -22$ and $0.0 < r - i < 0.3$. These stars turned out to be the top of the Main Sequence (and turn-off) of Triangulum II. See Chapter 5 for a beautiful LBT CMD of Triangulum II.

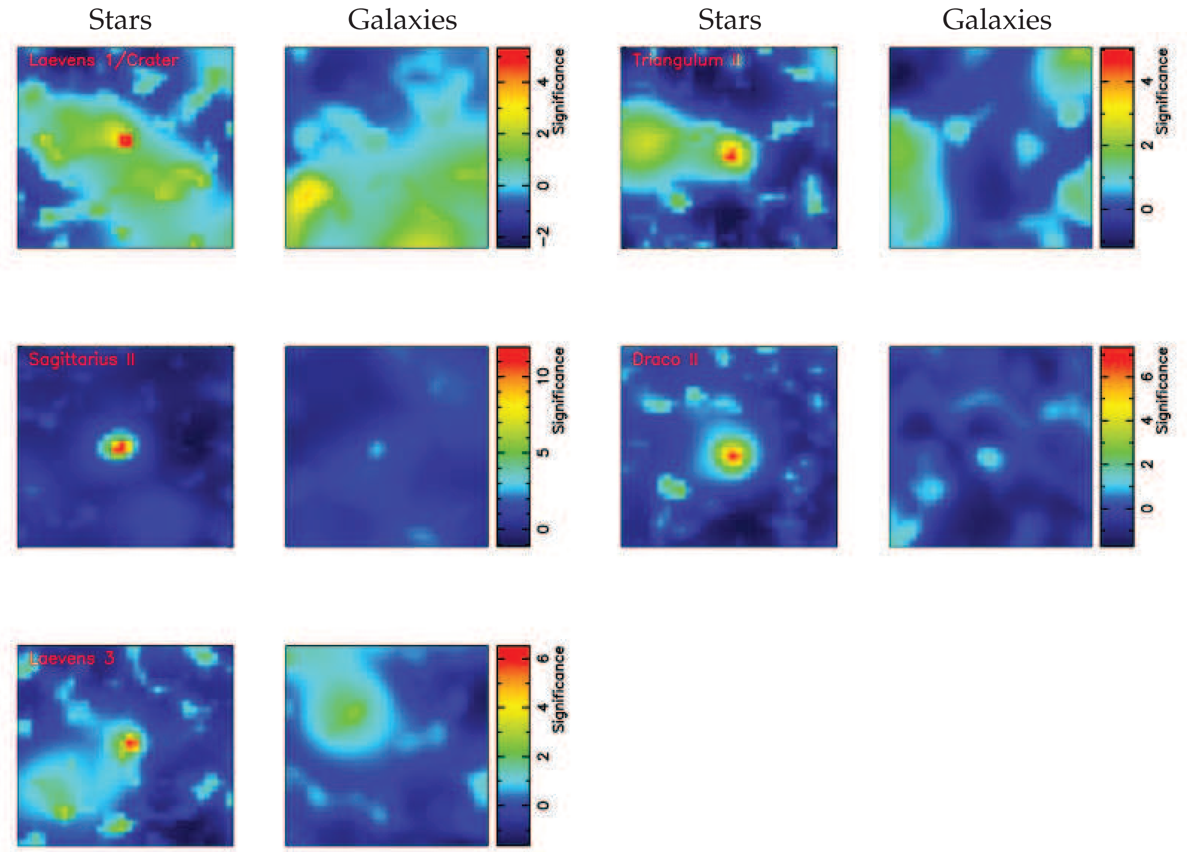

Figure 3.6 - S/N for stellar maps (left) and galaxies' maps (right) for all five MW satellites found to date in PS1: Laevens 1/Crater, Triangulum II, Sagittarius III, Draco II and Laevens 3.

Chapter 4

Discovery of the most distant Milky Way globular cluster

The Astrophysical Journal Letters, 786:L3 (6pp), 2014 May 1 doi:10.1088/2041-8205/786/1/L3

A NEW DISTANT MILKY WAY GLOBULAR CLUSTER IN THE PAN-STARRS1 3π SURVEY

Benjamin P. M. Laevens[1,2], Nicolas F. Martin[1,2], Branimir Sesar[2], Edouard J. Bernard[3], Hans-Walter Rix[2],
Colin T. Slater[4], Eric F. Bell[4], Annette M. N. Ferguson[3], Edward F. Schlafly[2], William S. Burgett[5],
Kenneth C. Chambers[5], Larry Denneau[5], Peter W. Draper[6], Nicholas Kaiser[5], Rolf-Peter Kudritzki[5],
Eugene A. Magnier[5], Nigel Metcalfe[6], Jeffrey S. Morgan[5], Paul A. Price[7], William E. Sweeney[5],
John L. Tonry[5], Richard J. Wainscoat[5], and Christopher Waters[5]
[1] Observatoire astronomique de Strasbourg, Université de Strasbourg, CNRS, UMR 7550, 11 rue de l'Université,
F-67000 Strasbourg, France; benjamin.laevens@astro.unistra.fr
[2] Max-Planck-Institut für Astronomie, Königstuhl 17, D-69117 Heidelberg, Germany
[3] Institute for Astronomy, University of Edinburgh, Royal Observatory, Blackford Hill, Edinburgh EH9 3HJ, UK
[4] Department of Astronomy, University of Michigan, 500 Church St., Ann Arbor, MI 48109, USA
[5] Institute for Astronomy, University of Hawaii at Manoa, Honolulu, HI 96822, USA
[6] Department of Physics, Durham University, South Road, Durham DH1 3LE, UK
[7] Department of Astrophysical Sciences, Princeton University, Princeton, NJ 08544, USA

Received 2014 March 20; accepted 2014 March 24; published 2014 April 8

ABSTRACT

We present a new satellite in the outer halo of the Galaxy, the first Milky Way satellite found in the stacked photometric catalog of the Panoramic Survey Telescope and Rapid Response System 1 (Pan-STARRS1) Survey. From follow-up photometry obtained with WFI on the MPG/ESO 2.2 m telescope, we argue that the object, located at a heliocentric distance of 145 ± 17 kpc, is the most distant Milky Way globular cluster yet known. With a total magnitude of $M_V = -4.3 \pm 0.2$ and a half-light radius of 20 ± 2 pc, it shares the properties of extended globular clusters found in the outer halo of our Galaxy and the Andromeda galaxy. The discovery of this distant cluster shows that the full spatial extent of the Milky Way globular cluster system has not yet been fully explored.

Key words: globular clusters: individual (PSO J174.0675-10.8774) – Local Group

Online-only material: color figures

1. INTRODUCTION

As compact stellar systems that can be discovered at large distances, globular clusters (GCs) located in the outskirts of massive galaxies are valuable tracers of the hierarchical formation of their host (Searle & Zinn 1978; Law & Majewski 2010; Mackey et al. 2010; Pota et al. 2013). In particular, the detailed study of nearby GCs has shown that the most distant Milky Way (MW) GCs preferentially belong to the class of so-called "young halo" clusters (Mackey & van den Bergh 2005). These clusters are expected to have formed in dwarf galaxies (DGs) that were later accreted onto our Galaxy and destroyed by tidal forces (Dotter et al. 2011). Young halo GCs are preferentially younger (8–12 Gyr old), more metal-rich ([Fe/H] ∼ −1.5), and more extended than other halo GCs (Dotter et al. 2010). Similar conclusions are reached for some GCs in the outskirts of M31 (Mackey et al. 2013).

Although large sky surveys like the Sloan Digital Sky Survey (SDSS) have transformed our view of the MW satellite DG system (e.g., Willman et al. 2005; Belokurov et al. 2007), only a handful of GCs were discovered within the survey (Koposov et al. 2007; Belokurov et al. 2010; Balbinot et al. 2013); all of these are extremely faint ($M_V \gtrsim -2.0$) and within the inner ∼60 kpc of the halo. Additionally two other GCs within this spatial regime were found on sky survey plates (Pyxis and Whiting 1; Irwin et al. 1995, Whiting et al. 2002), yet no new distant MW GC has been discovered since the searches that led to the discovery of the Palomar clusters (e.g., Arp & van den Bergh 1960) and AM-1, the most distant MW GC to date at a galactocentric distance of ∼125 kpc (Madore & Arp 1979; Aaronson et al. 1984; Dotter et al. 2008).

Here, we report the discovery of the most distant MW GC, PSO J174.0675-10.8774, found in the Pan-STARRS 1 (PS1) 3π photometric survey. We argue that PSO J174.0675-10.8774 shares the properties of known young halo GCs. The Letter is structured as follows: in Section 2 we briefly describe the PS1 survey and the satellite search that led to the discovery of PSO J174.0675-10.8774. Section 3 focuses on the analysis of follow-up wide-field imager data. We derive the properties of the cluster in Section 4 and discuss their implication on the nature of the cluster in Section 5.

Whenever necessary, magnitudes are dereddened using the Schlegel et al. (1998) maps, assuming the extinction coefficients of Schlafly & Finkbeiner (2011). We also assume a heliocentric distance of 8 kpc to the Galactic center.

We note that the same stellar system was discovered independently by Belokurov et al. (2014) using VST ATLAS data. In their pre-print, these authors favor a DG classification for this object.

2. THE 3π PS1 SURVEY AND DISCOVERY

The PS1 3π Survey (K. Chambers et al., in preparation) targets three quarters of the sky ($\delta > -30°$) in five photometric bands, $g_{\rm P1}$, $r_{\rm P1}$, $i_{\rm P1}$, $z_{\rm P1}$, $y_{\rm P1}$, with the 1.8 m PS1 telescope, located in Haleakala, Hawaii (Tonry et al. 2012). The sky is surveyed with a 1.4 gigapixel camera covering a 3.3 degree field of view, which, combined with short exposures four times per year per filter over the course of 3.5 yr, yields a deep, panoptic view of the MW's surroundings. Once the individual frames are downloaded from the summit, they are automatically processed with the Image Processing Pipeline (Magnier 2006, 2007;

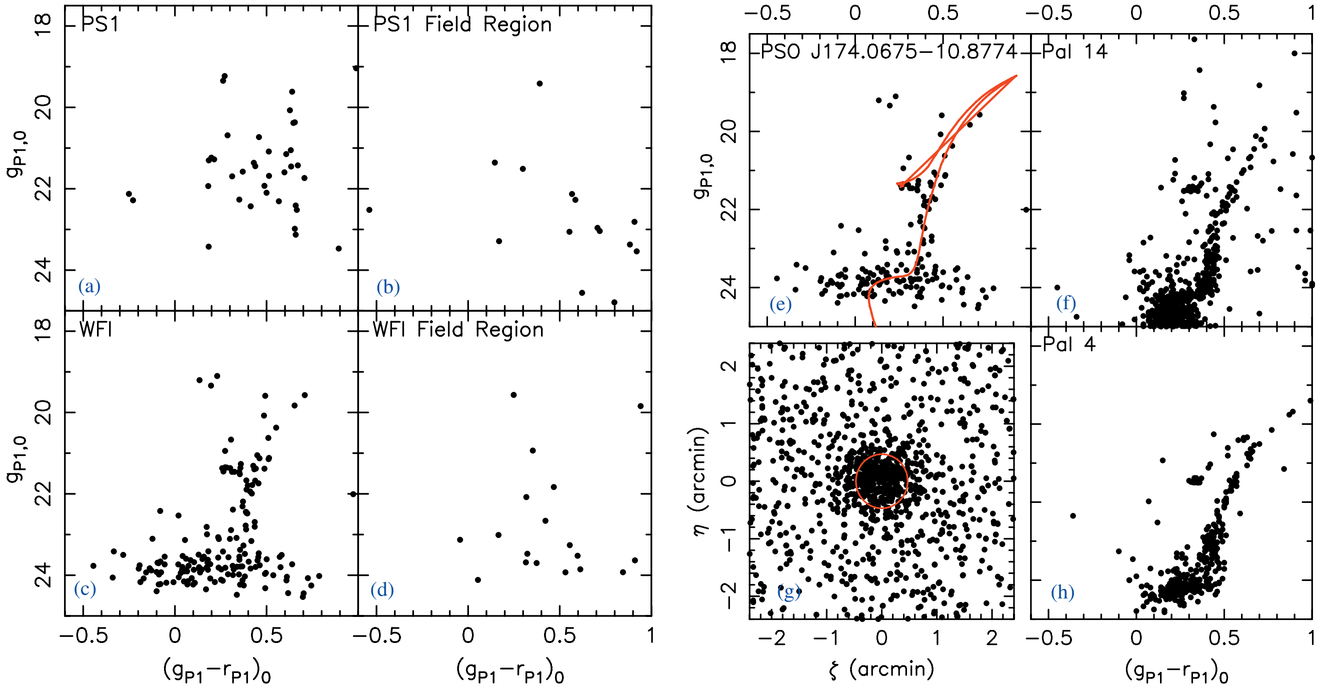

Figure 1. Left panels: (a) The CMD of PS1 stars within three half-light radii of the centroid of PSO J174.0675-10.8774. (b) The CMD of stars of a nearby field region (8.3 arcmin northeast away) of the same coverage. (c) WFI stars within two half-light radii of the centroid of PSO J174.0675-10.8774. (d) WFI stars within two half-light radii of the aforementioned field region. The CMD of the new GC shows a clear RGB, HB, and grazes its main sequence turn-off at the faint end. Right panels: (e) The CMD of PSO J174.0675-10.8774 with the Parsec isochrone of age 8 Gyr and [Fe/H] $= -1.9$ that matches the shape and location of the RGB, HB, and main sequence turn off. (g) The spatial distribution of the WFI stars, displaying the unambiguous overdensity produced by PSO J174.0675-10.8774. The red circle shows the region within two half-light radii of its centroid. (f) and (h) CMDs within two half-light radii of young outer halo GCs Pal 14 and Pal 4, shifted to the distance of the new GC. This photometry is taken from Saha et al. (2005). The CMDs of these two stellar systems show many similarities with that of PSO J174.0675-10.8774, especially their red HBs and sparsely populated RGBs.

(A color version of this figure is available in the online journal.)

Magnier et al. 2008) to generate a photometric catalogue. The PS1 survey is currently at the stage where stacked photometry and images have become available, reaching a similar depth to the SDSS in $g_{\rm P1}$ and reaching deeper magnitude for $r_{\rm P1}$ ($\sim$0.5 mag) and $i_{\rm P1}$ ($\sim$1 mag; Metcalfe et al. 2013). The PS1 survey represents a significant increase of the search volume for small scale stellar systems that orbit the MW.

PSO J174.0675-10.8774 was discovered in an on-going search for small-scale substructures in the PS1 data. A comprehensive paper about this search is in preparation (B. Laevens et al., in preparation), but we provide here a broad outline of the discovery method. Inspired by previous searches for stellar overdensities (Koposov et al. 2007; Walsh et al. 2009), we adopt a hybrid method of the two aforementioned papers. First, we identify stars which have colors and magnitudes compatible with old, metal-poor stars possibly pertaining to a GC or DG by constructing color–magnitude masks from typical isochrones describing such systems and accounting for the possible distance to the system. The subsample of stars for a given distance is then convolved with Gaussian kernels. A positive convolution is performed on the data with a Gaussian of $4'$ or $8'$ dispersion, tailored to the size of typical MW satellites, while a convolution with a large negative Gaussian kernel accounts for the slowly-varying contamination (Koposov et al. 2009). After this two-step process, the resultant differential density maps track localized stellar over- and underdensities over the PS1 footprint, which we then translate into detection significance by comparison with the local density values. This led to the discovery of PSO J174.0675-10.8774 as an unambiguous 10σ detection.

At this location, the PS1 stacked images reveal the presence of a compact stellar system, which is emphasized by the distribution of PS1 sources on the sky. In panel a of Figure 1, the color–magnitude diagram (CMD) of this compact overdensity confirms that these stars are blue ($(g_{\rm P1} - r_{\rm P1})_0 \lesssim 0.8$) and more numerous than in a field region (panel b) of the same coverage. Despite the detection of the object in the PS1 data, these are too shallow to reliably determine the properties of the system, which motivated us to gather deeper photometric data.

3. FOLLOW-UP

During the night of 2013 December 31–2014 January 1, we obtained follow-up imaging with the Wide Field Imager (WFI) on the MPG/ESO 2.2 m telescope located in La Silla, Chile. Equipped with eight CCDs the camera has a field of view of $34' \times 33'$. Given the small angular size of PSO J174.0675-10.8774, we focus here on the photometry from CCD 1, which contains the full extent of the new stellar system. We obtained imaging in the B (five six-minute dithered sub-exposures), V, and R bands (three seven-minute dithered sub-exposures) in good seeing conditions with a median image quality of $0''.9$. The individual sub-exposures were bias-subtracted, flat-fielded, and cleared of cosmic rays. The initial astrometric solution for sub-exposures was obtained using the Astrometry.net package (Lang et al. 2010), with the PS1 catalog acting as the astrometric reference catalog. We then used the software packages SExtractor and SCAMP (Bertin 2006) to align each individual frame to the frame with the best seeing before constructing composite images

Figure 2. *BVR* image of PSO J174.0675-10.8774 built from the stacked WFI images. The image is 4′ × 4′, north is to the top and east to the left.

(A color version of this figure is available in the online journal.)

for each band by average combining them with SWARP (Bertin 2006). The resulting *BVR* image of PSO J174.0675-10.8774 is shown in Figure 2 and unequivocally confirms that it is a compact stellar system.

We performed the photometry using the DAOPHOT/ALLSTAR/ALLFRAME suite of programs (Stetson 1994) as described in Martin et al. (2013; E. J. Bernard, in preparation). A point-spread-function model was built for each individual frame and the flux was extracted by applying the model to fixed positions of stars as measured from the deep *BVR* image. The instrumental magnitudes were then calibrated to the first sub-exposure in a band, averaged out. We use the exquisite photometry of the single epoch PS1 data (Schlafly et al. 2012) to derive our own transformations from the WFI filters to the PS1 $g_{\rm P1}$- and $r_{\rm P1}$-band magnitudes.

The final WFI photometry reaches ∼1.5 mag deeper than the stacked PS1 data, as shown in panel c of Figure 1. The CMD within two half-light radii of PSO J174.0675-10.8774 (see Section 4 for the determination of the structural parameters) unveils a sparse red giant branch (RGB), a red horizontal branch (HB), and the beginning of the system's main sequence turn off at the magnitude limit of the data. All of these features are absent from a field region (panel d) of similar coverage shown for comparison. The spatial distribution of stars in the WFI data is shown in panel g.

4. PROPERTIES OF THE STELLAR SYSTEM

A search for possible RR Lyrae stars varying in the multi-epoch PS1 photometry revealed no good candidate. However, although the CMD of PSO J174.0675-10.8774 is only sparsely populated, the presence of a well defined (red) HB allows for an accurate determination of the heliocentric distance to the system. We therefore measure the median apparent magnitude of the HB through a Monte Carlo resampling of the magnitude of stars in this part of the CMD, yielding $m_{g\rm P1} = 21.41 \pm 0.06$. To determine the absolute magnitude of the red HB in this band, we extract from the PS1 stacked photometry database the photometry of four GCs that share the morphological properties and CMD of PSO J174.0675-10.8774 (Pal 3, Pal 4, Pal 5, and Pal 14). We repeat the same procedure on the red HB of these systems, shifted by their distance modulus as listed in Harris (2010). The weighted average of these four HBs' absolute magnitude measurements yields $M_{g\rm P1} = 0.60 \pm 0.10$. The distance modulus of PSO J174.0675-10.8774 is therefore $(m - M)_0 = 20.81 \pm 0.12$, yielding both a heliocentric and a Galactocentric distance of 145 ± 17 kpc.

Having pinned down the distance to the system, we can now estimate its age and metallicity through a comparison with a set of isochrones. Since the photometric data does not reach the main sequence of the cluster, these estimates should be taken with caution, but they nevertheless give a broad understanding of the age and metallicity of the cluster. Fixing the distance modulus at $(m - M)_0 = 20.81$, we cycle through the PARSEC isochrones for a metallicity range $-2.3 < [{\rm Fe/H}] < -1.5$ and an age between 8 and 13 Gyr (Bressan et al. 2012). The top-right panel (e) of Figure 1 presents the best fit to the data, obtained for the isochrone with an age of 8 Gyr and $[{\rm Fe/H}] = -1.9$. Allowing the distance to vary within the formal distance uncertainties, we obtain a metallicity and age range of 8–10 Gyr and [Fe/H] varies between −1.5 and −1.9. These are fairly typical properties of young, outer halo GCs and this impression is further bolstered by panels f and h of Figure 1, which present literature photometry (Saha et al. 2005) of Pal 14 (11.3 Gyr, $[{\rm Fe/H}] = -1.5$; Dotter et al. 2011) and Pal 4 (10.9 Gyr, $[{\rm Fe/H}] = -1.3$) shifted to the distance of the new GC. The CMDs of the three GCs exhibit similar features, with sparsely populated RGBs and red HBs.

To determine the structural parameters of PSO J174.0675-10.8774, we use a variant of the technique presented in Martin et al. (2008), updated to allow for a full Markov Chain Monte Carlo treatment. Briefly, the algorithm uses the location of every single star in the WFI data set to calculate the likelihood of a family of radial profiles with flattening and a constant background. The parameters are: the centroid of the system, its ellipticity[8], the position angle of its major axis from N to E, the number of stars in the system, and one or two scale parameters. We use three different families of radial density models (exponential, Plummer, and King), for which the scale parameters are the half-light radius, the Plummer radius, and the core and King radii, respectively. The resulting structural parameters are listed in Table 1. Figure 3 also shows the probability distribution function (pdf) of the exponential model parameters, as well as the comparison between the favored radial distribution profile and the data, binned with the favored structural parameter model. They show a very good agreement, testament to the quality of the structural parameter's inference. The results for the Plummer profile and the King profile are equally good. From the determination of the structural parameters, we find that PSO J174.0675-10.8774 is a round, compact system with a half-light radius of only $0\farcm47^{+0.04}_{-0.03}$ or 20 ± 2 pc at the distance of 145 ± 17 kpc.

The absolute magnitude of PSO J174.0675-10.8774 is also derived using the technique presented in Martin et al. (2008), which accounts for "CMD shot-noise" that stems from the impact of the sparsely populated CMD on the derivation of its

---

[8] The ellipticity is here defined as $1 - b/a$ with a and b the major and minor axis scale lengths, respectively.

Table 1
Properties of PSO J174.0675-10.8774

α (J2000)	11:36:16.2
δ (J2000)	-10:52:38.8
ℓ	$274\overset{\circ}{.}8$
b	$+47\overset{\circ}{.}8$
Distance modulus	21.81 ± 0.12
Heliocentric distance	145 ± 17 kpc
Galactocentric distance	145 ± 17 kpc
M_V	-4.3 ± 0.2
[Fe/H]	~ -1.9
Age	$\sim$8 Gyr
$E(B-V)$[a]	0.026
Exponential profile	
Ellipticity	$0.00^{+0.10}_{-0.00}$
Position angle (from N to E)	$-56^{+88\,\circ}_{-68}$
r_h	$0.47^{+0.04\,\prime}_{-0.03}$ 20 ± 2 pc
Plummer profile	
Ellipticity	$0.0^{+0.11}_{-0.00}$
Position angle (from N to E)	$-64^\circ \pm 64^\circ$
r_h	$0\overset{\prime}{.}52 \pm 0\overset{\prime}{.}04$ 22 ± 2 pc
King profile	
Ellipticity	$0.00^{+0.11}_{-0.00}$
Position angle (from N to E)	$+70^{+48\,\circ}_{-36}$
r_c	$0\overset{\prime}{.}61 \pm 0\overset{\prime}{.}18$ 24^{+9}_{-6} pc
r_t	$1.30^{+0.19\,\prime}_{-0.12}$ 56^{+9}_{-6} pc

Note. [a] From Schlegel et al. (1998).

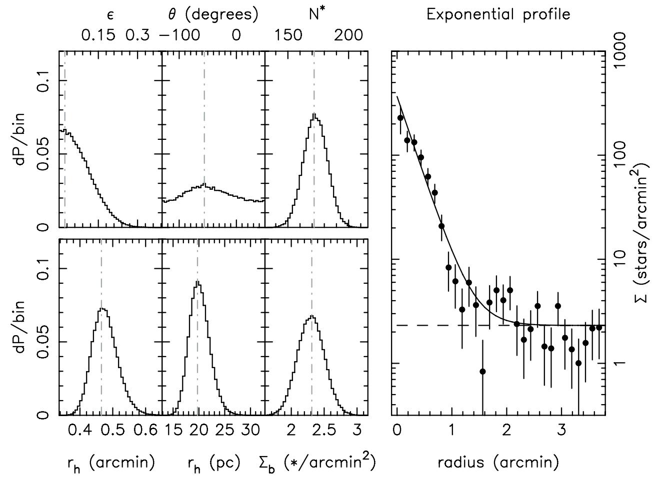

Figure 3. Left-hand panels show the pdf of the structural parameters for the exponential radial density model. From top-left to bottom-right, the parameters correspond to the ellipticity (ϵ), the position angle (θ), the number of stars in the GC for our CMD selection (N^*), the angular and physical half-light radii (r_h), and the field density (Σ_b). The right-most panel compares the favored radial distribution profile (full line) and the data, binned following with the favored structural parameters (dots). The field density is shown as the dashed line and the uncertainties on the data point were calculated assuming Poisson uncertainties.

total magnitude. Using the favored Parsec isochrone presented above (8 Gyr, [Fe/H] $= -1.9$) and its associated luminosity function shifted to the distance of the cluster, we build a color–magnitude pdf of where PSO J174.0675-10.8774 stars should lie given the photometric uncertainties. We then populate a mock CMD from this pdf until the number of stars brighter than $r_{\rm P1} = 23.5$ equals the number of stars, N^*, that we determine from the estimate of the structural parameters for the same region of the CMD. Summing up the flux of all the stars in the mock CMD yields the absolute magnitude of this realization. Finally, we iterate this procedure 300 times, accounting for the uncertainties on the heliocentric distance and on N^*, as well as the shot-noise uncertainties that come from randomly populating the mock CMDs. This procedure yields absolute magnitudes of $M_g = -4.02 \pm 0.22$ and $M_r = -4.49 \pm 0.25$, which converts to $M_V = -4.3 \pm 0.2$ when using the Tonry et al. (2012) color transformations. The total luminosity of the system is $4.5 \pm 0.7 \times 10^3\,L_\odot$, which, assuming a typical mass-to-light ratio in solar units of $\sim$1.5 for GCs of this metallicity (e.g., Strader et al. 2011), yields a total stellar mass of $\sim 6.8 \pm 1.1 \times 10^3\,M_\odot$.

5. DISCUSSION AND CONCLUSION

We have presented a new stellar system found within the PS1 3π data in the outer halo of the MW. Located at a heliocentric distance of 145 ± 17 kpc, this system is rather faint ($M_V = -4.3 \pm 0.2$), compact ($r_h = 20 \pm 2$ pc), round ($\epsilon = 0.0^{+0.10}_{-0.00}$), younger than the oldest GCs ($\sim$8 Gyr), and fairly metal-poor ([Fe/H] ~ -1.9). Figure 4 compares the properties of PSO J174.0675-10.8774 with MW GCs and DGs. Although it is slightly more distant than any known MW GC, all the other properties of this system are similar to those of outer halo GC systems (e.g., Mackey & Gilmore 2004; Mackey & van den Bergh 2005). In particular, the size and the roundness of the system differentiate it from DGs at the same magnitude, which are all larger than at least $r_h = 60$ pc and tend to favor elliptical radial density profiles (Martin et al. 2008; Sand et al. 2012). Furthermore, the age and metallicity we determine from the comparison with isochrones are quite typical of young, outer halo GCs, as made evident by the direct comparison of PSO J174.0675-10.8774's CMD with that of Pal 4, and Pal 14 (Figures 1(e), (f), and (h)).

Beyond our local environment, this new stellar system is also similar to the population of extended GCs recently found in the vicinity of M31, many of which lie on faint stellar streams (Huxor et al. 2005; Mackey et al. 2010). Those systems are similarly round, rather fluffy for GCs, but compact for DGs, and can also exhibit red HBs (e.g., Mackey et al. 2006, 2013; Huxor et al. 2011). The discovery of this most distant MW GC supports the idea that very remote GCs are a common feature of large spiral galaxies as has been shown in M31 (Huxor et al. 2011), in M33 (Cockcroft et al. 2011) and M81 (Jang et al. 2012). Further investigation in the vicinity of this object would therefore be interesting in the context of stellar streams and their association with GCs.

After the work for this Letter had been completed, we learned of the independent discovery of this object by Belokurov et al. (2014) from the VST ATLAS survey and follow-up data. Their determination of the system's properties are consistent with ours, even though they derive a slightly larger distance ($\sim$170 kpc) and size ($r_h \sim 0\overset{\prime}{.}6 = 30$ pc at their distance). Their interpretation of the nature of the system nevertheless differs from ours as they favor a scenario in which the system is a DG. Their conclusion is partly driven by the larger size they measure, but also by their interpretation of a handful of blue stars being blue loop stars indicative of recent star formation. We do indeed

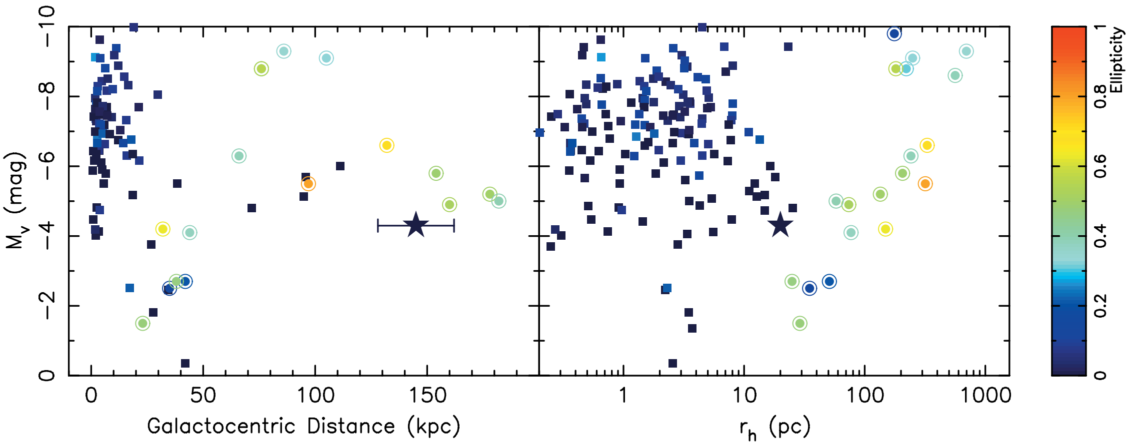

Figure 4. Distribution of MW satellites in the distance–magnitude space (left) and the size–magnitude space (right). GCs are shown as squares, DGs are shown as circles, and PSO J174.0675-10.8774 is represented by the large star symbol. The color scale indicates the ellipticity of the various satellites. PSO J174.0675-10.87740's ellipticity and half-light radius show very similar values to those of other MW GCs. The data for the GCs were taken from Harris (2010) and those for the DGs from McConnachie (2012).

(A color version of this figure is available in the online journal.)

retrieve these stars in our data set; however, we are cautious as to their interpretation. Performing our structural parameter analysis on these blue stars only yields a detection of an overdensity at the $\sim 2\sigma$–3σ detection level. Furthermore, if these were truly blue loop stars, one would expect the presence of a higher number of their low-mass analogs at fainter magnitudes and bluer colors, which do not appear in the CMD. Finally, it cannot be ruled out that the two blue stars residing barely above the red HB could in fact be asymptotic giant branch stars. Taking into account the derived properties of this stellar system, we rather conclude that we are in the presence of a distant GC and not of a faint and extremely compact DG. We stress that this conclusion must be confirmed or infirmed with radial velocities through follow-up spectroscopy of these blue loop stars, thus ascertaining the definite nature of this new distant satellite.

We would like to thank the editor and referee for their celerity. We wish to thank P. Bianchini, M. A. Norris, and D. Martinez-Delgado for fruitful discussions about globular clusters and R. A. Ibata for a careful reading of the manuscript. B.P.M.L. acknowledges funding through a 2012 Strasbourg IDEX (Initiative d'Excellence) grant, awarded by the French ministry of education. N.F.M. and B.P.M.L. gratefully acknowledge the CNRS for support through PICS project PICS06183. N.F.M., H.-W.R. and E.F.S. acknowledge support by the DFG through the SFB 881 (A3). E.F.B. and C.T.S. acknowledge support from NSF grant AST 1008342.

The Pan-STARRS1 Surveys (PS1) have been made possible through contributions of the Institute for Astronomy, the University of Hawaii, the Pan-STARRS Project Office, the Max-Planck Society and its participating institutes, the Max Planck Institute for Astronomy, Heidelberg and the Max Planck Institute for Extraterrestrial Physics, Garching, the Johns Hopkins University, Durham University, the University of Edinburgh, Queen's University Belfast, the Harvard-Smithsonian Center for Astrophysics, the Las Cumbres Observatory Global Telescope Network Incorporated, the National Central University of Taiwan, the Space Telescope Science Institute, the National Aeronautics and Space Administration under grant No. NNX08AR22G issued through the Planetary Science Division of the NASA Science Mission Directorate, the National Science Foundation under grant No. AST-1238877, the University of Maryland, and Eotvos Lorand University (ELTE).

REFERENCES

Aaronson, M., Schommer, R. A., & Olszewski, E. W. 1984, ApJ, 276, 221
Arp, H., & van den Bergh, S. 1960, PASP, 72, 48
Balbinot, E., Santiago, B. X., da Costa, L., et al. 2013, ApJ, 767, 101
Belokurov, V., Irwin, M. J., Koposov, S. E., et al. 2014, arXiv:1403.3406
Belokurov, V., Walker, M. G., Evans, N. W., et al. 2010, ApJL, 712, L103
Belokurov, V., Zucker, D. B., Evans, N. W., et al. 2007, ApJ, 654, 897
Bertin, E. 2006, in ASP Conf. Ser. 351, Astronomical Data Analysis Software and Systems XV, ed. C. Gabriel et al. (San Francisco, CA: ASP), 112
Bressan, A., Marigo, P., Girardi, L., et al. 2012, MNRAS, 427, 127
Cockcroft, R., Harris, W. E., Ferguson, A. M. N., et al. 2011, ApJ, 730, 112
Dotter, A., Sarajedini, A., & Anderson, J. 2011, ApJ, 738, 74
Dotter, A., Sarajedini, A., Anderson, J., et al. 2010, ApJ, 708, 698
Dotter, A., Sarajedini, A., & Yang, S.-C. 2008, AJ, 136, 1407
Harris, W. E. 2010, arXiv:1012.3224
Huxor, A. P., Ferguson, A. M. N., Tanvir, N. R., et al. 2011, MNRAS, 414, 770
Huxor, A. P., Tanvir, N. R., Irwin, M. J., et al. 2005, MNRAS, 360, 1007
Irwin, M. J., Demers, S., & Kunkel, W. E. 1995, ApJL, 453, L21
Jang, I. S., Lim, S., Park, H. S., & Lee, M. G. 2012, ApJL, 751, L19
Koposov, S., de Jong, J. T. A., Belokurov, V., et al. 2007, ApJ, 669, 337
Koposov, S. E., Yoo, J., Rix, H.-W., et al. 2009, ApJ, 696, 2179
Lang, D., Hogg, D. W., Mierle, K., Blanton, M., & Roweis, S. 2010, AJ, 139, 1782
Law, D. R., & Majewski, S. R. 2010, ApJ, 718, 1128
Mackey, A. D., & Gilmore, G. F. 2004, MNRAS, 355, 504
Mackey, A. D., Huxor, A., Ferguson, A. M. N., et al. 2006, ApJL, 653, L105
Mackey, A. D., Huxor, A. P., Ferguson, A. M. N., et al. 2010, ApJL, 717, L11
Mackey, A. D., Huxor, A. P., Martin, N. F., et al. 2013, ApJL, 770, L17
Mackey, A. D., & van den Bergh, S. 2005, MNRAS, 360, 631
Madore, B. F., & Arp, H. C. 1979, ApJL, 227, L103
Magnier, E. 2006, in The Advanced Maui Optical and Space Surveillance Technologies Conf., ed. S. Ryan (Maui, HI: The Maui Economic Devt. Board), 50
Magnier, E. 2007, in ASP Conf. Ser. 364, The Future of Photometric, Spectrophotometric and Polarimetric Standardization, ed. C. Sterken (San Francisco, CA: ASP), 153
Magnier, E. A., Liu, M., Monet, D. G., & Chambers, K. C. 2008, in IAU Symp. 248, The Extended Solar Neighborhood: Precision Astrometry from the Pan-STARRS1 3π Survey, ed. W. J. Jin, I. Platais, & M. A. C. Perryman (Cambridge: Cambridge Univ. Press), 553
Martin, N. F., de Jong, J. T. A., & Rix, H.-W. 2008, ApJ, 684, 1075

Martin, N. F., Schlafly, E. F., Slater, C. T., et al. 2013, ApJL, 779, L10
McConnachie, A. W. 2012, AJ, 144, 4
Metcalfe, N., Farrow, D. J., Cole, S., et al. 2013, MNRAS, 435, 1825
Pota, V., Forbes, D. A., Romanowsky, A. J., et al. 2013, MNRAS, 428, 389
Saha, A., Dolphin, A. E., Thim, F., & Whitmore, B. 2005, PASP, 117, 37
Sand, D. J., Strader, J., Willman, B., et al. 2012, ApJ, 756, 79
Schlafly, E. F., & Finkbeiner, D. P. 2011, ApJ, 737, 103
Schlafly, E. F., Finkbeiner, D. P., Jurić, M., et al. 2012, ApJ, 756, 158
Schlegel, D. J., Finkbeiner, D. P., & Davis, M. 1998, ApJ, 500, 525
Searle, L., & Zinn, R. 1978, ApJ, 225, 357
Stetson, P. B. 1994, PASP, 106, 250
Strader, J., Caldwell, N., & Seth, A. C. 2011, AJ, 142, 8
Tonry, J. L., Stubbs, C. W., Lykke, K. R., et al. 2012, ApJ, 750, 99
Walsh, S. M., Willman, B., & Jerjen, H. 2009, AJ, 137, 450
Whiting, A. B., Hau, G. K. T., & Irwin, M. 2002, ApJS, 141, 123
Willman, B., Blanton, M. R., West, A. A., et al. 2005, AJ, 129, 2692

Chapter 5

A new faint stellar system in the constellation of Triangulum

The Astrophysical Journal Letters, 802:L18 (6pp), 2015 April 1 doi:10.1088/2041-8205/802/2/L18

A NEW FAINT MILKY WAY SATELLITE DISCOVERED IN THE PAN-STARRS1 3π SURVEY*

Benjamin P. M. Laevens[1,2], Nicolas F. Martin[1,2], Rodrigo A. Ibata[1], Hans-Walter Rix[2], Edouard J. Bernard[3], Eric F. Bell[4], Branimir Sesar[2], Annette M. N. Ferguson[3], Edward F. Schlafly[2], Colin T. Slater[4], William S. Burgett[5], Kenneth C. Chambers[6], Heather Flewelling[6], Klaus A. Hodapp[6], Nicholas Kaiser[6], Rolf-Peter Kudritzki[6], Robert H. Lupton[7], Eugene A. Magnier[6], Nigel Metcalfe[8], Jeffrey S. Morgan[6], Paul A. Price[7], John L. Tonry[6], Richard J. Wainscoat[6], and Christopher Waters[6]

[1] Observatoire astronomique de Strasbourg, Université de Strasbourg, CNRS, UMR 7550, 11 rue de l'Université, F-67000 Strasbourg, France; benjamin.laevens@astro.unistra.fr

[2] Max-Planck-Institut für Astronomie, Königstuhl 17, D-69117 Heidelberg, Germany

[3] Institute for Astronomy, University of Edinburgh, Royal Observatory, Blackford Hill, Edinburgh EH9 3HJ, UK

[4] Department of Astronomy, University of Michigan, 500 Church Street, Ann Arbor, MI 48109, USA

[5] GMTO Corporation, 251 S. Lake Avenue, Suite 300, Pasadena, CA 91101, USA

[6] Institute for Astronomy, University of Hawaii at Manoa, Honolulu, HI 96822, USA

[7] Department of Astrophysical Sciences, Princeton University, Princeton, NJ 08544, USA

[8] Department of Physics, Durham University, South Road, Durham DH1 3LE, UK

Received 2015 February 20; accepted 2015 March 17; published 2015 March 31

ABSTRACT

We present the discovery of a faint Milky Way satellite, Laevens 2/Triangulum II, found in the Panoramic Survey Telescope And Rapid Response System 3π imaging data and confirmed with follow-up wide-field photometry from the Large Binocular Cameras. The stellar system, with an absolute magnitude of $M_V = -1.8 \pm 0.5$, a heliocentric distance of 30^{+2}_{-2} kpc, and a half-mass–radius of 34^{+9}_{-8} pc, shows remarkable similarity to faint, nearby, small satellites such as Willman 1, Segue 1, Segue 2, and Boötes II. The discovery of Laevens 2/Triangulum II further populates the region of parameter space for which the boundary between dwarf galaxies and globular clusters becomes tenuous. Follow-up spectroscopy will ultimately determine the nature of this new satellite, whose spatial location hints at a possible connection with the complex Triangulum–Andromeda stellar structures.

Key words: galaxies: dwarf – Galaxy: structure – globular clusters: general – Local Group

1. INTRODUCTION

The last couple of decades saw the discovery of numerous satellites in the Milky Way (MW) halo. While the Sloan Digital Sky Survey (SDSS; York et al. 2000) satellite discoveries have provided us with greater observational constraints in our backyard, especially to understand the faint end of galaxy formation in the preferred cosmological paradigm of ΛCDM (Belokurov 2013), they have also led to debates about the nature of the faintest satellites (Gilmore et al. 2007). It has become apparent that the previously clear distinction between the compact globular clusters (GCs) and the brighter, more extended, and dark-matter-dominated dwarf galaxies (DGs), blurs out for faint systems (Willman & Strader 2012). This is exemplified by the discoveries of Willman 1 (Wil1; Willman et al. 2005) and Segue 1 (Seg1; Belokurov et al. 2007), followed up by those of Boötes II (BoöII; Walsh et al. 2007), and Segue 2 (Seg2; Belokurov et al. 2009), all nearby satellites within 25–45 kpc, and just slightly larger than extended outer halo GCs. At the same time, these systems are fainter than most GCs and all the other DGs. Theoretical expectations show that these objects could well be the faintest DGs and that tens or hundreds of DGs with these properties could populate the MW halo (Tollerud et al. 2008; Hargis et al. 2014). As of yet, just two objects have been found in the Panoramic Survey Telescope And Rapid Response System (Pan-STARRS 1; PS1) survey (Laevens et al. 2014), reinforcing the tension between theory and observations (Klypin et al. 1999). Only the closest DGs would be detected with current photometric surveys (Koposov et al. 2007; Walsh et al. 2009). Spectroscopic studies do show that the faint systems found so far are dynamically hotter than their mere stellar content would imply, hinting that they are indeed DGs (Martin et al. 2007; Simon et al. 2011; Willman et al. 2011; Kirby et al. 2013). However, the low velocity dispersion of these satellites (<4 km s^{-1}), combined with the possibly large impact of binaries (McConnachie & Côté 2010), the complexity of disentangling member stars from foreground contaminants, and the overall dimness of their member stars renders any definite conclusion difficult.

Here, we present the discovery of another faint MW satellite, Laevens 2/Triangulum II,[9] with very similar photometric properties to Wil1, Seg1, BoöII, and Seg2. The new system was found in our ongoing effort to mine the PS1 3π survey for localized stellar overdensities. This Letter is structured as follows: in Section 2, we describe the PS1 survey along with the detection method that led to the discovery. We continue by discussing follow-up imaging obtained with the Large Binocular Cameras (LBC) in Section 3. We discuss the nature of the satellite and its implication in Section 4. In the final section, we summarize and conclude our results.

---

* The LBT is an international collaboration among institutions in the United States, Italy, and Germany. LBT Corporation partners are The University of Arizona on behalf of the Arizona university system; Instituto Nazionale di Astrofisica, Italy; LBT Beteiligungsgesellschaft, Germany, representing the Max-Planck Society, the Astrophysical Institute Potsdam, and Heidelberg University; The Ohio State University, and The Research Corporation, on behalf of The University of Notre Dame, University of Minnesota, and University of Virginia.

[9] In the absence of spectroscopic confirmation, we wish to remain agnostic about the nature of this object and therefore propose a double name. For future reference in this paper, we abbreviate to Lae 2/Tri II.

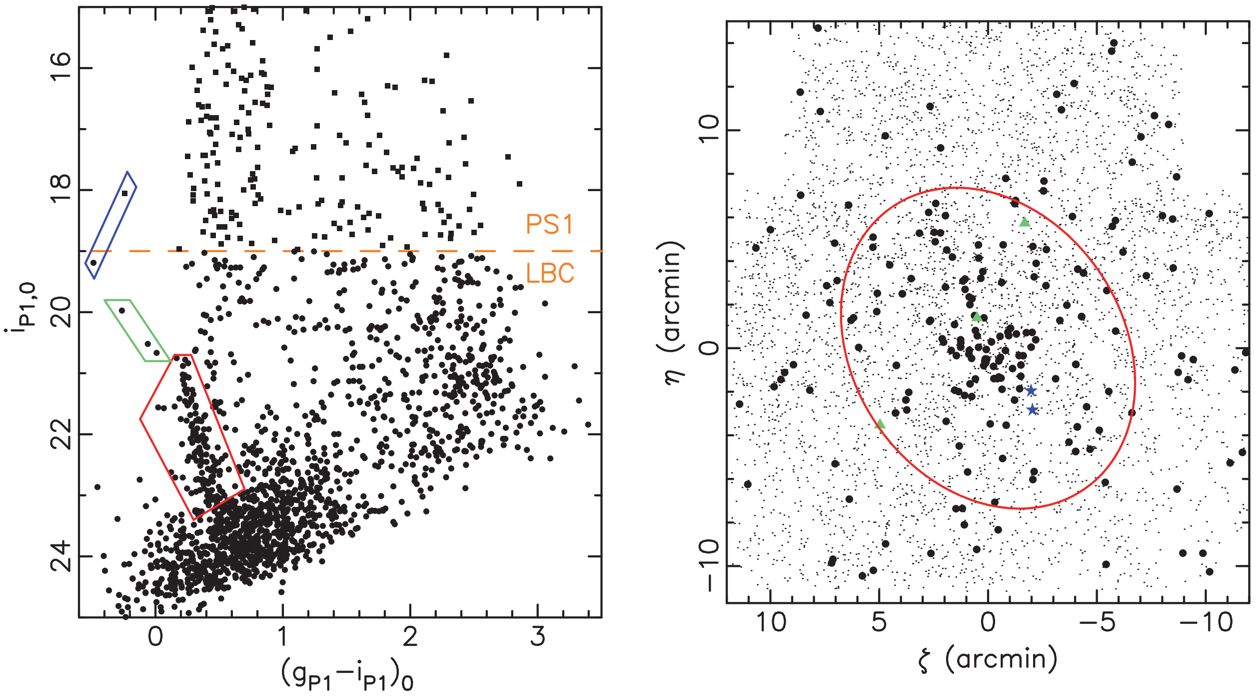

Figure 1. Left: the combined PS1-LBC CMD of all sources within the central $2r_h$ region of Lae 2/Tri II. The single epoch PS1 photometry was used at the bright end ($i_{P1,0} < 19$; squares), with LBC photometry supplementing the faint end ($i_{P1,0} > 19$; large dots). The orange dashed line indicates the separation between the LBC and PS1 data. The red box highlights the clear main sequence of the stellar system, the blue box indicates two possible HB stars, and the green box identifies likely blue stragglers. Right: spatial distribution of all sources corresponding to the CMD on the left. Large dots correspond to the stars falling within the red CMD box in the left panel and show a clear overdensity. The two blue stars indicate the possible HB stars, whereas the red ellipse corresponds to the region within the favored two half-mass–radius of the system, as inferred below.

In this paper, magnitudes are dereddened using the Schlegel et al. (1998) maps, adopting the extinction coefficients of Schlafly & Finkbeiner (2011). A heliocentric distance of 8 kpc to the Galactic center is assumed.

2. THE 3π PS1 SURVEY AND DISCOVERY

With a spatial extent encompassing three quarters of the sky ($\delta > -30°$), PS1 (K. Chambers et al., in preparation) gives us an unprecedented panoptic view of the MW and its surroundings. Over the course of 3.5 yr, the 1.8 m telescope, equipped with its 1.4 gigapixel camera covering a 3°.3 field of view, has collected up to four exposures per year in each of 5 bands ($g_{P1} r_{P1} i_{P1} z_{P1} y_{P1}$; Tonry et al. 2012). A photometric catalog is automatically generated with the Image Processing Pipeline (Magnier 2006, 2007; Magnier et al. 2008), once the individual frames have been downloaded from the summit. The preliminary stacked photometry used in this paper has a g_{P1} depth (23.0) that is comparable to SDSS g-band depth and r_{P1}/i_{P1} observations that reach ~0.5/ ~ 1.0 magnitude fainter: 22.8, 22.5 for r and i, respectively (Metcalfe et al. 2013).

Inspired by past searches for small stellar overdensities in MW and M31 surveys, we apply a convolution technique (Laevens et al. 2015, in preparation), successfully used to find new GCs and DGs in the SDSS (Koposov et al. 2007; Walsh et al. 2009). In a nutshell, we build a mask in $(r-i, i)$ color–magnitude space to isolate potential metal-poor, old, and blue member stars that could belong to a MW satellite at a chosen distance. This mask is applied to star-like sources in the stacked PS1 photometric catalog. We then convolve the distribution of isolated sources with two Gaussian spatial filters: a positive Gaussian tailored to the size of the overdensities we are searching for (2′, 4′, or 8′) and a negative Gaussian with a much larger kernel (14′, 28′, or 56′), to account for the slowly varying contamination of sources that fall within the color–magnitude mask. By convolving the data with the sum of these two (positive and negative) filters and accounting for the survey's spatial incompleteness on the arcminute scale, we obtain maps tracking stellar over- and under-densities in PS1. We convert these density maps into maps of statistical significance by comparison with the neighboring regions after cycling through distances and filter sizes. This procedure already led to the discovery of Laevens 1[10] (Laevens et al. 2014) also discovered concomitantly as Crater within the ATLAS survey by Belokurov et al. (2014). The new satellite, Lae 2/Tri II, is located ~20° east of M31 and appears as a 5.2σ detection, only slightly higher than our significance criteria[11] of 5σ tailored to weed out spurious detections.

3. FOLLOW-UP

To confirm the nature and the properties of Lae 2/Tri II, follow-up imaging was obtained with the LBC on the Large Binocular Telescope (LBT), located on Mount Graham, USA during the night of 2014 October 17–18. With its 23′ × 25′ field of view and equipped with 4 CCDs, the LBC are ideal to follow-up MW satellites that usually span a few arcminutes on the sky. Imaging was conducted in the g and i bands, making use of the time-saving dual (binocular) mode using the red and blue eye simultaneously. Six dithered 200 s sub-exposures

---

[10] Following the naming convention established in Bianchini et al. (2015).

[11] These also include a check that potential detections do not also correspond to a significant overdensity of background galaxies (Koposov et al. 2007).

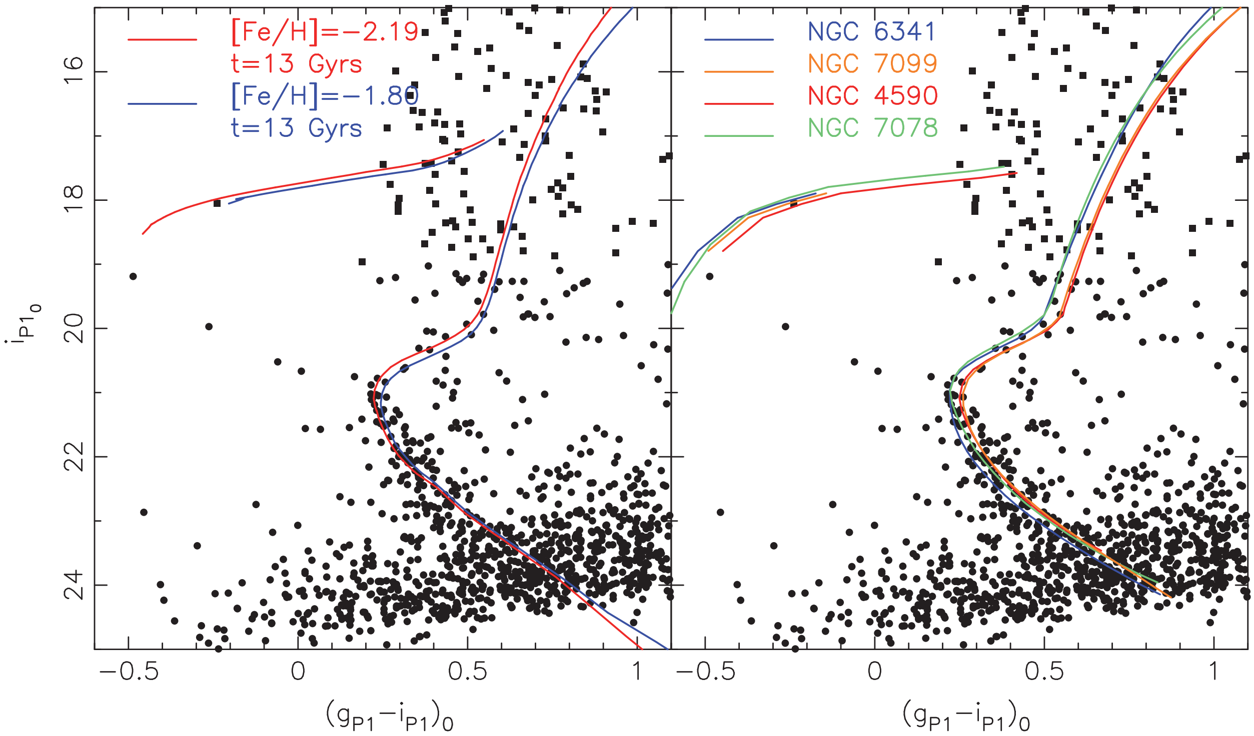

Figure 2. Left: the CMD of Lae 2/Tri II within $2r_h$, with best-fit isochrones overplotted. Both isochrones have an age of 13 Gyr and are shifted to a distance modulus of 17.3. The red/blue isochrones have metallicities [Fe/H] = −2.19 and [Fe/H] = −1.80, respectively. Right: the same CMD of Lae 2/Tri II with four metal-poor fiducial isochrones from GCs observed in PS1 (Bernard et al. 2014), dereddened assuming the reddening values of (Harris 2010) and shifted to match the observed features. The green fiducial (NGC 7078; [Fe/H] = −2.37), shifted to a distance-modulus of 17.5 best represents the features of the new stellar system, with the other fiducials, i.e., red: NGC 4590 ([Fe/H] = −2.23), blue: NGC 6341 ([Fe/H] = −2.31), orange: NGC 7099 ([Fe/H] = −2.27) appearing too red or to blue to accurately reproduce the MS and MSTO. NGC 4590 is shifted to a distance-modulus of 17.5, whereas NGC 6341 and 7099 are at 17.3.

were acquired in each band, with a seeing of 1″. The field was centered on the location of Lae 2/Tri II.

The images were processed and the photometry performed using a version of the CASU pipeline (Irwin & Lewis 2001) updated to work on LBC data. The instrumental magnitudes were calibrated onto the PS1 system (g_{P1} and i_{P1}), by comparison with the PS1 single epoch data (Schlafly et al. 2012) to derive the relevant color equations. The final LBC photometry reaches more than 2 magnitudes deeper than the stacked PS1 data. The left-hand panel of Figure 1 shows the combined PS1/LBC color–magnitude diagram (CMD) of all stars within 2 half-light radii ($\pm 2\ r_h$), for which all sources brighter than $i_{\mathrm{P1,0}} = 19.0$ are taken from the PS1 single epoch photometry so as to extend the CMD beyond the saturation limit of the LBC photometry. The main sequence (MS) of an old and metal-poor stellar system is readily visible, with a clear turn off at $i_{\mathrm{P1,0}} \sim 20.8$. Given the low density of the MS, the red giant branch (RGB) of the stellar system is very likely sparsely populated and hidden within the foreground contamination of bright stars. However, two blue stars are consistent with being blue horizontal branch (HB) stars and are highlighted in the CMD. The other panel of Figure 1 presents the spatial distribution of sources in the four chips, with a red ellipse indicating the satellite's two half-light radii extent (as determined by the structural parameter analysis, see Section 4). Stars with colors and magnitudes consistent with the MS are shown as large dots and reveal a clear spatial overdensity. Likely blue straggler stars are identified and given by the green triangles. The two blue stars correspond to the potential HB stars; their location close to the center of the stellar overdensity supports them being member HB stars.

4. PROPERTIES OF THE STELLAR SYSTEM

Since the RGB and HB are so sparsely populated, an investigation into the presence of member RR Lyrae stars in the multi-epoch PS1 data unsurprisingly led to no candidate from which to derive a distance estimate. However, due to the well defined MS and MS turnoff (MSTO) at $i_{\mathrm{P1,0}} \sim 20.8$, a reliable distance estimate can nevertheless be determined through a comparison with isochrones and fiducials by eye (Figure 2). We assess the stellar system's metallicity, age, and distance modulus by first cycling through Parsec isochrones (Bressan et al. 2012) for a metallicity range $-2.2 < \mathrm{[Fe/H]} < -1.3$ ($Z = 0.0001$ to 0.0007, assuming $Z_\odot = 0.152$) and an age between 9 and 13 Gyr. We investigate the effects that various metallicities and ages have on the distance determination, by cycling through distance-modulus steps of 0.1 between 16.9 and 17.5. The isochrone which best represents the CMD features is a metal-poor, old isochrone ([Fe/H] = −2.19 and age of 13 Gyr), for a distance modulus of 17.3. We further strengthen these conclusions by comparing the CMD of Lae 2/Tri II with the fiducials from 13 GCs and 3 Open Clusters of varying metallicity, derived directly from the PS1 data (Bernard et al. 2014). The 4 most metal-poor GCs of the sample provide a good fit to the MS and MSTO of Lae 2/Tri II provided they are shifted to distance moduli in the 17.3–17.5 range.

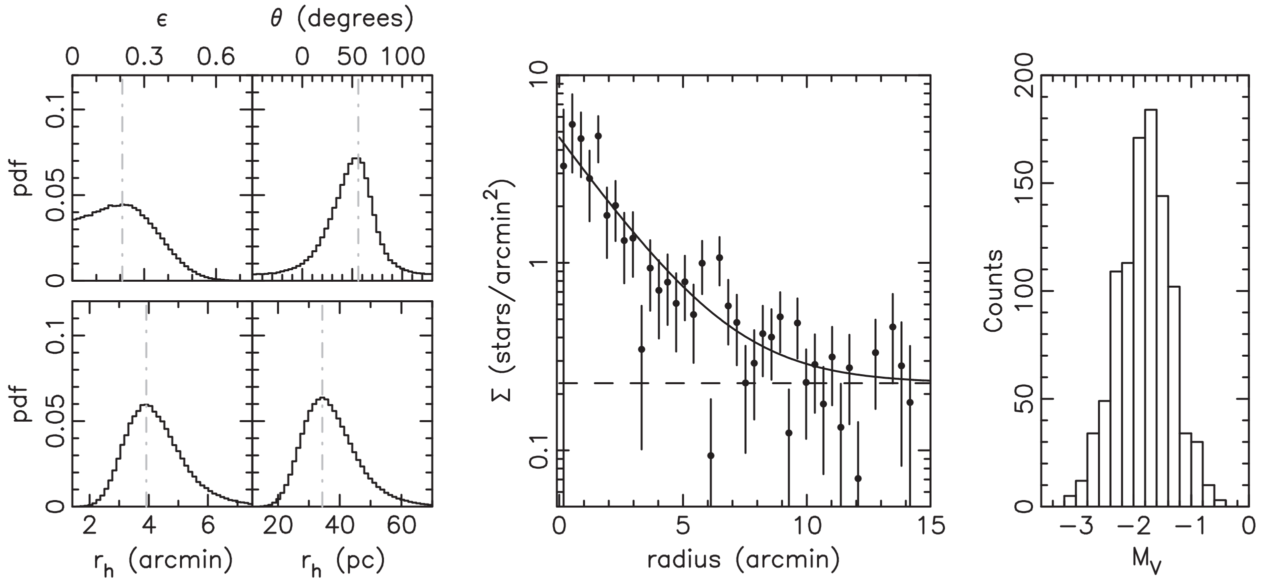

Figure 3. Left: probability distribution functions for the ellipticity (ϵ), the position angle (θ), the angular and the physical half-mass radii (r_h) of Lae 2/Tri II (from top left to bottom right). Middle: comparison between the favored radial distribution profile (full line) and the data, binned according to the preferred structural parameters (dots). The error bars assume Poissonian uncertainties, and the dashed line represents the field density. Right: probability distribution function of the absolute magnitude of Lae 2/Tri II in the V band ($M_V = -1.8 \pm 0.5$).

Combining these two analyses by averaging the six best-fit fiducials and isochrones, we therefore conclude that Lae 2/Tri II is old and metal-poor, and is located at a distance modulus of $17.4^{+0.1}_{-0.1}$, which translates to a heliocentric distance of 30^{+2}_{-2} kpc, or 36^{+2}_{-2} kpc from the Galactic center. In both cases (isochrone and fiducial), the HB of the favored track also overlaps almost exactly with the two potential HB stars. Please note that the uncertainty in the distance measurement is propagated through for the derivation of the structural parameters, further detailed in the next few paragraphs. We also draw to the reader's attention that a more involved analysis of "CMD-fitting" would likely enhance the quality of the distance measurement; however, the limitation of the field of view prevent us from obtaining a large enough sample of background stars to perform such an analysis.

We derive the structural parameters of Lae 2/Tri II by using a modified version of the technique described in Martin et al. (2008), updated in Martin et al. (2015, in preparation). The updated technique allows for a Markov Chain Monte Carlo approach, based on the likelihood of a family of exponential radial density profiles (allowing for flattening and a constant contamination over the field) to reproduce the distribution of the system's MS stars. The parameters of the model are: the centroid of the system, its ellipticity,[12] its position angle (defined as the angle of the major axis from north to east), its half-mass–radius,[13] r_h, and the number of stars, N^*, within the chosen CMD selection box. Although it is located in the Triangulum constellation, Lae 2/Tri II is so far from both M31 (~20°) and M33 (~10°) that any contamination by M31 or M33 stellar populations is vanishingly small and does not impact our results. The resulting probability distribution functions are presented in the left-most panels of Figure 3 for the most important parameters and summarized in Table 1. Figure 3 also shows a favorable comparison of the preferred exponential profile with the data binned following the preferred structural parameters.

Table 1
Properties of Lae 2/Tri II

α(J2000)	02:13:17.4
δ (J2000)	+36:10:42.4
ℓ	140°.9
b	−23°.8
Distance Modulus	$\sim 17.4^{+0.1}_{-0.1}$
Heliocentric Distance	30^{+2}_{-2} kpc
Galactocentric Distance	36^{+2}_{-2} kpc
M_V	-1.8 ± 0.5
[Fe/H]	~−2.2
Age	~13 Gyr
$E(B - \mathrm{V})$[a]	0.081
Ellipticity	$0.21^{+0.17}_{-0.21}$
Position angle (from N to E)	56^{+16}_{-24} °
r_h	$3.9^{+1.1}_{-0.9}$′
r_h	34^{+9}_{-8} pc

[a] From Schlegel et al. (1998).

It should however be noted that the properties of Lae 2/Tri II as observed by the LBC could be slightly biased by the low contrast of the stellar overdensity. Indeed, Muñoz et al. (2012) show that satellite properties are most accurately measured when the central density of stars relative to that of the background is larger than 20, which is not the case here. Deeper data would be necessary to strengthen our size measurement.

To determine the absolute magnitude of the stellar system, we follow the same procedure we used for Laevens 1/Crater (Laevens et al. 2014) as was initially described in Martin et al. (2008). After drawing a value of N^* from the structural

---

[12] The ellipticity is defined here as 1 – b/a with a and b the major and minor axis scale lengths, respectively.

[13] Note that, assuming no mass segragation in the system, the half-mass–radius is equivalent to the half-light radius.

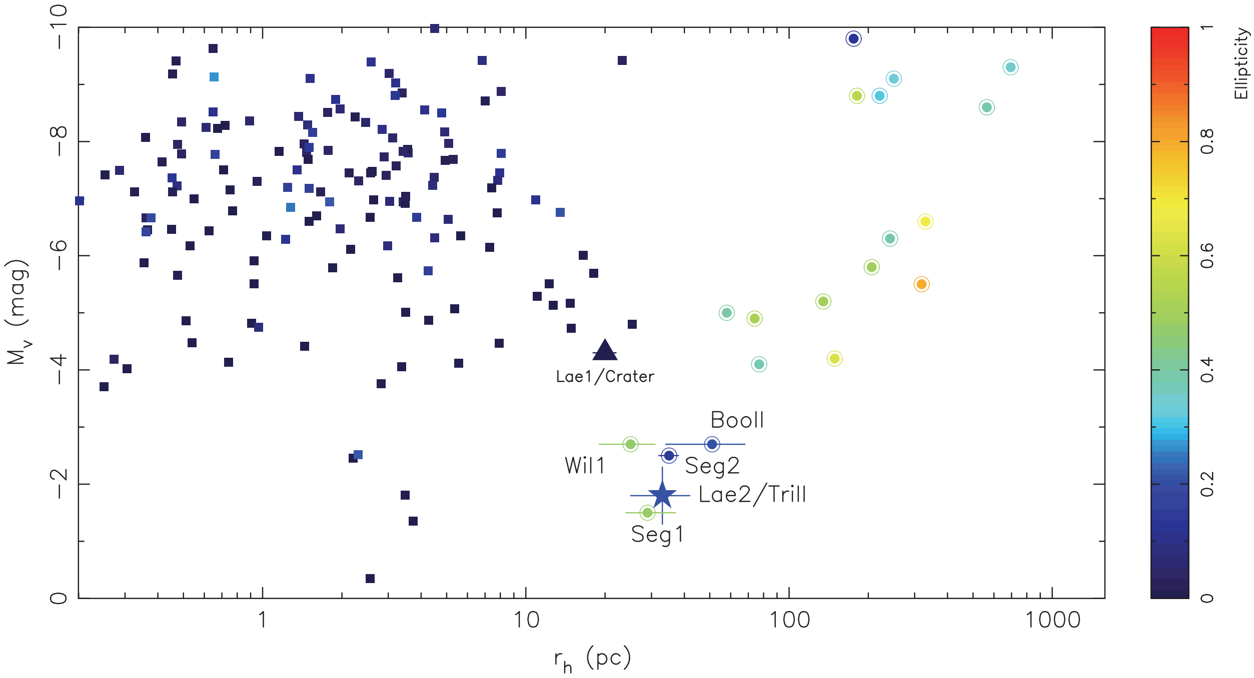

Figure 4. The distribution of MW satellites in size magnitude space. GCs are shown as squares, DGs are shown as circles, and Lae 2/Tri II is represented by the large star symbol. The color scale indicates the ellipticity of the various satellites. Lae 2/Tri II's ellipticity and half-mass–radius show very similar values to those of the four satellites: Seg1, Seg2, BoöII, and Wil1. Finally, we also indicate the recently discovered MW satellite, Laevens 1/Crater, given by the large triangle. The data for the GCs were taken from Harris (2010) and the DGs from McConnachie (2012).

parameter chain, we sample the CMD of the best-fitting Bressan et al. (2012) isochrone (see Figure 2), with its associated luminosity function and photometric uncertainties, until it contains N^* stars in the CMD selection box used for the structural parameter analysis. Adding up the flux of all the stars drawn in this artificial CMD yields the absolute $g_{\rm P1}$- and $i_{\rm P1}$-band magnitudes of Lae 2/Tri II ($M_g = -1.7 \pm 0.5$ and $M_i = -2.1 \pm 0.5$), which converts to $M_V = -1.8 \pm 0.5$. This technique has the benefit of accounting for the effect of sampling such a small population of stars may have on the determination of the system's magnitude (i.e., CMD "shot-noise"; Martin et al. 2008).

5. DISCUSSION AND CONCLUSION

We have presented the discovery of a new MW satellite, Lae 2/Tri II, discovered within the PS1 3π data and confirmed from deep and wide LBC follow-up. Located at a heliocentric distance of 30^{+2}_{-2} kpc, this system is very faint ($M_V = -1.8 \pm 0.5$), old (~13 Gyr), metal-poor ([Fe/H] ~ −2.2), small (34^{+9}_{-8} pc), and mildly elliptical ($0.21^{+0.17}_{-0.21}$). Figure 4 places Lae 2/Tri II in relation to other MW GCs and DGs. This new system's magnitude and half-mass–radius are very similar to the properties of the faint satellites Seg1, Seg2, Wil1, and BoöII, which were all recently discovered in the SDSS. Ultimately, high quality spectroscopic follow-up and an assessment of its dynamics are necessary to confirm the nature of this new satellite. However, its similarity in distance, size, absolute magnitude, age, and metallicity to those of Wil1, Seg1, BoöII, and Seg2, that all have larger velocity dispersion than implied by their tiny stellar mass (Martin et al. 2007; Simon et al. 2011; Willman et al. 2011; Kirby et al. 2013) hints that Lae 2/Tri II could well be another one of these systems that appear to populate the faint end of the galaxy realm.

It is also worth noting that the location of Lae 2/Tri II, $(\ell, b) = (141\overset{\circ}{.}4, -23\overset{\circ}{.}4)$, ~20° east of M31, places it within the Triangulum–Andromeda stellar structure(s) (TriAnd; Majewski et al. 2004; Rocha-Pinto et al. 2004; Sheffield et al. 2014). Although this MW halo stellar overdensity is very complex, with evidence for multiple substructures (Bonaca et al. 2012; Martin et al. 2013; Martin et al. 2014), it spans a large enough distance range to encompass Lae 2/Tri II (~15–35 kpc). A recent spectroscopic study of stars within TriAnd by Deason et al. (2014) confirmed that, as initially proposed by Belokurov et al. (2009), Seg2 is also likely embedded within it and follows a systematic trend of these faint satellites being part of MW halo stellar streams. Seg1 has been proposed to be tied to the Orphan Stream (Newberg et al. 2010), though differences in abundance patterns between both have also been observed (Vargas et al. 2013; Casey et al. 2014). Similarly, BoöII's distance and radial velocity are compatible with it being part of the Sagittarius stream (Koch et al. 2009), whereas high resolution abundance measurements for BoöII stars question this association (Koch & Rich 2014). It remains possible, however, that the small stellar systems were satellites of the larger, now disrupted progenitor of these stream, thereby alleviating the need for them to share similar abundances. In this context, it is particularly interesting that Lae 2/Tri II is situated on the linear extrapolation of the Pan-Andromeda Archaeological Survey (PAndAS) MW stream (Martin et al. 2014), 10° beyond the PAndAS footprint where this dwarf galaxy remnant was discovered. The stream and satellite are not aligned; however, the uncertainties on the position angle and ellipticity are not conclusive in ruling this out. Here as well, spectroscopy is necessary to derive the systemic velocity of Lae 2/Tri II and confirm it is compatible with the global motion of Triangulum–Andromeda and, in particular, with the velocity of the PAndAS MW stream. Follow-up will help reinforce or disprove such a hypothesis.

Although PS1 is only slightly deeper than the SDSS, the extra coverage provided by its 3π footprint leaves hope for more discoveries of faint objects like Lae 2/Tri II. Building up the statistics of these systems through more discoveries in current (PS1) and (DES; The Dark Energy Survey Collaboration 2005) or future surveys (LSST; Tyson et al. 2002) is essential if we are to understand the true nature of these incredibly faint stellar systems that can only be found in the MW surroundings.

B.P.M.L. acknowledges funding through a 2012 Strasbourg IDEX (Initiative d'Excellence) grant, awarded by the French ministry of education. N.F.M. and B.P.M.L. gratefully acknowledge the CNRS for support through PICS project PICS06183. H.-W.R. and E.F.T acknowledge support by the DFG through the SFB 881 (A3). E.F.B. and C.T.S. acknowledge support from NSF grant AST 1008342. We thank the LBT and the observers for the splendid job that enabled the confirmation of this object.

The Pan-STARRS1 Surveys have been made possible through contributions of the Institute for Astronomy, the University of Hawaii, the Pan-STARRS Project Office, the Max-Planck Society and its participating institutes, the Max Planck Institute for Astronomy, Heidelberg and the Max Planck Institute for Extraterrestrial Physics, Garching, the Johns Hopkins University, Durham University, the University of Edinburgh, Queen's University Belfast, the Harvard-Smithsonian Center for Astrophysics, the Las Cumbres Observatory Global Telescope Network Incorporated, the National Central University of Taiwan, the Space Telescope Science Institute, the National Aeronautics and Space Administration under grant No. NNX08AR22G issued through the Planetary Science Division of the NASA Science Mission Directorate, the National Science Foundation under grant No. AST-1238877, the University of Maryland, and Eotvos Lorand University (ELTE).

REFERENCES

Belokurov, V. 2013, NewAR, 57, 100
Belokurov, V., Irwin, M. J., Koposov, S. E., et al. 2014, MNRAS, 441, 2124
Belokurov, V., Walker, M. G., Evans, N. W., et al. 2009, MNRAS, 397, 1748
Belokurov, V., Zucker, D. B., Evans, N. W., et al. 2007, ApJ, 654, 897
Bernard, E. J., Ferguson, A. M. N., Schlafly, E. F., et al. 2014, MNRAS, 442, 2999
Bianchini, P., Renaud, F., Gieles, M., & Varri, A. L. 2015, MNRAS, 447, L40
Bonaca, A., Geha, M., & Kallivayalil, N. 2012, ApJL, 760, L6
Bressan, A., Marigo, P., Girardi, L., et al. 2012, MNRAS, 427, 127
Casey, A. R., Keller, S. C., Da Costa, G., Frebel, A., & Maunder, E. 2014, ApJ, 784, 19
Deason, A. J., Belokurov, V., Hamren, K. M., et al. 2014, MNRAS, 444, 3975
Gilmore, G., Wilkinson, M. I., Wyse, R. F. G., et al. 2007, ApJ, 663, 948
Hargis, J. R., Willman, B., & Peter, A. H. G. 2014, ApJL, 795, L13
Harris, W. E. 2010, arXiv:1012.3224
Irwin, M., & Lewis, J. 2001, NewAR, 45, 105
Kirby, E. N., Boylan-Kolchin, M., Cohen, J. G., et al. 2013, ApJ, 770, 16
Klypin, A., Kravtsov, A. V., Valenzuela, O., & Prada, F. 1999, ApJ, 522, 82
Koch, A., & Rich, R. M. 2014, ApJ, 794, 89
Koch, A., Wilkinson, M. I., Kleyna, J. T., et al. 2009, ApJ, 690, 453
Koposov, S., de Jong, J. T. A., Belokurov, V., et al. 2007, ApJ, 669, 337
Laevens, B. P. M., Martin, N. F., Sesar, B., et al. 2014, ApJL, 786, L3
Magnier, E. 2006, in The Advanced Maui Optical and Space Surveillance Technologies Conf., ed. S. Ryan (Maui, HI: The Maui Economic Development Board)
Magnier, E. 2007, in ASP Conf. Ser. 364, The Future of Photometric, Spectrophotometric and Polarimetric Standardization, ed. C. Sterken (San Francisco, CA: ASP), 153
Magnier, E. A., Liu, M., Monet, D. G., & Chambers, K. C. 2008, in IAU Symp., 248,, ed. W. J. Jin, I. Platais, & M. A. C. Perryman (Cambridge: Cambridge Univ. Press), 553
Majewski, S. R., Ostheimer, J. C., Rocha-Pinto, H. J., et al. 2004, ApJ, 615, 738
Martin, C., Carlin, J. L., Newberg, H. J., & Grillmair, C. 2013, ApJL, 765, L39
Martin, N. F., de Jong, J. T. A., & Rix, H.-W. 2008, ApJ, 684, 1075
Martin, N. F., Ibata, R. A., Chapman, S. C., Irwin, M., & Lewis, G. F. 2007, MNRAS, 380, 281
Martin, N. F., Ibata, R. A., Rich, M. R., et al. 2014, ApJ, 787, 19
McConnachie, A. W. 2012, AJ, 144, 4
McConnachie, A. W., & Côté, P. 2010, ApJL, 722, L209
Metcalfe, N., Farrow, D. J., Cole, S., et al. 2013, MNRAS, 435, 1825
Muñoz, R. R., Padmanabhan, N., & Geha, M. 2012, ApJ, 745, 127
Newberg, H. J., Willett, B. A., Yanny, B., & Xu, Y. 2010, ApJ, 711, 32
Rocha-Pinto, H. J., Majewski, S. R., Skrutskie, M. F., Crane, J. D., & Patterson, R. J. 2004, ApJ, 615, 732
Schlafly, E. F., & Finkbeiner, D. P. 2011, ApJ, 737, 103
Schlafly, E. F., Finkbeiner, D. P., Juric, M., et al. 2012, ApJ, 756, 158
Schlegel, D. J., Finkbeiner, D. P., & Davis, M. 1998, ApJ, 500, 525
Sheffield, A. A., Johnston, K. V., Majewski, S. R., et al. 2014, ApJ, 793, 62
Simon, J. D., Geha, M., Minor, Q. E., et al. 2011, ApJ, 733, 46
The Dark Energy Survey Collaboration 2005, arXiv: astro-ph/0510346
Tollerud, E. J., Bullock, J. S., Strigari, L. E., & Willman, B. 2008, ApJ, 688, 277
Tonry, J. L., Stubbs, C. W., Lykke, K. R., et al. 2012, ApJ, 750, 99
Tyson, J. A. 2002, Proc. SPIE, 4836, 10
Vargas, L. C., Geha, M., Kirby, E. N., & Simon, J. D. 2013, ApJ, submitted (arXiv:1302.6594)
Walsh, S. M., Willman, B., & Jerjen, H. 2009, AJ, 137, 450
Walsh, S. M., Willman, B., Sand, D., et al. 2007, ApJ, in press (arXiV:0712.3054)
Willman, B., Blanton, M. R., West, A. A., et al. 2005, AJ, 129, 2692
Willman, B., Geha, M., Strader, J., et al. 2011, AJ, 142, 128
Willman, B., & Strader, J. 2012, AJ, 144, 76
York, D. G., Adelman, J., Anderson, J. E., Jr., et al. 2000, AJ, 120, 1579

Chapter 6

Three new Milky Way satellites in Sagittarius, Draco and Delphinus

Draft version July 26, 2015
Preprint typeset using LaTeX style emulateapj v. 12/16/11

SAGITTARIUS II, DRACO II AND LAEVENS 3: THREE NEW MILKY WAY SATELLITES DISCOVERED IN THE PAN-STARRS 1 3π SURVEY

Benjamin P. M. Laevens[1,2], Nicolas F. Martin[1,2], Edouard J. Bernard[3], Edward F. Schlafly[2], Branimir Sesar[2], Hans-Walter Rix[2], Eric F. Bell[4], Annette M. N. Ferguson[3], Colin T. Slater[4], William E. Sweeney[5], Rosemary F. G. Wyse[6], Avon P. Huxor[7], William S. Burgett[9], Kenneth C. Chambers[5], Peter W. Draper[8], Eugene A. Magnier[5], Nigel Metcalfe[8], John L. Tonry[5], Richard J. Wainscoat[5], Christopher Waters[6]

Draft version July 26, 2015

ABSTRACT

We present the discovery of three new Milky Way satellites from our search for compact stellar overdensities in the photometric catalog of the Panoramic Survey Telescope and Rapid Response System 1 (Pan-STARRS 1, or PS1) 3π survey. The first satellite, Laevens 3, is located at a heliocentric distance of $d = 67 \pm 3\,\mathrm{kpc}$. With a total magnitude of $M_V = -4.4 \pm 0.3$ and a half-light radius $r_h = 7 \pm 2\,\mathrm{pc}$, its properties resemble those of outer halo globular clusters. The second system, Draco II/Laevens 4 (Dra II), is a closer and fainter satellite ($d \sim 20\,\mathrm{kpc}$, $M_V = -2.9 \pm 0.8$), whose uncertain size ($r_h = 19^{+8}_{-6}\,\mathrm{pc}$) renders its classification difficult without kinematic information; it could either be a faint and extended globular cluster or a faint and compact dwarf galaxy. The third satellite, Sagittarius II/Laevens 5 (Sgr II), has an ambiguous nature as it is either the most compact dwarf galaxy or the most extended globular cluster in its luminosity range ($r_h = 37^{+9}_{-8}\,\mathrm{pc}$ and $M_V = -5.2 \pm 0.4$). At a heliocentric distance of $67 \pm 5\,\mathrm{kpc}$, this satellite lies intriguingly close to the expected location of the trailing arm of the Sagittarius stellar stream behind the Sagittarius dwarf spheroidal galaxy (Sgr dSph). If confirmed through spectroscopic follow up, this connection would locate this part of the trailing arm of the Sagittarius stellar stream that has so far gone undetected. It would further suggest that Sgr II was brought into the Milky Way halo as a satellite of the Sgr dSph.

Keywords: Local Group — Milky Way, satellites, dwarf galaxies, globular clusters, streams: individual: Sagittarius II, Draco II, Laevens 3

1. INTRODUCTION

Two decades ago the prevalent view of the Milky Way (MW) as an isolated system was radically changed by the discovery of a tidally disrupting dwarf galaxy, embedded in a stream in the constellation of Sagittarius (Ibata et al. 1994), highlighting the underrated importance of Milky Way-satellite interactions. With ΛCDM models predicting a whole new population of faint satellite dwarf galaxies (DGs) orbiting the MW (e.g. Bullock et al. 2000, 2001), the new challenge was to find these, until then, elusive objects. At the turn of the century, the advent of large CCD surveys such as the Sloan Digital Sky Survey (SDSS; York et al. 2000) uncovered some 16 dwarf galaxies among the faintest ever found (e.g. Willman et al. 2005; Zucker et al. 2006; Belokurov et al. 2007; Walsh et al. 2007). Though revolutionizing our view of the satellite galaxies, just a handful of new globular clusters (GCs) were found, faint and nearby (Koposov et al. 2007; Belokurov et al. 2010; Muñoz et al. 2012; Balbinot et al. 2013). In addition, the SDSS enabled the discovery of several tidal streams (e.g. Belokurov et al. 2006; Grillmair & Dionatos 2006), further illustrating the central role of satellite and cluster disruption in building up the MW's halo.

With the second generation of surveys emerging such as the Dark Energy Survey (DES, The Dark Energy Survey Collaboration 2005), PS1 (Chambers et al. in preparation), later data releases of the SDSS, the Survey of the MAgellanic Survey History (SMASH, Nidever et al. in preparation), and VST Atlas have seen the number of known MW likely dwarf galaxies expand further from ∼25 to ∼35. These once elusive systems appear to be more common as deeper, but also wider coverage, data are gathered (Laevens et al. 2015; Bechtol et al. 2015; Koposov et al. 2015; Martin et al. 2015; Kim et al. 2015a; Kim & Jerjen 2015). In parallel, these systematic surveys also revealed a smaller number of faint new GCs (e.g. Laevens et al. 2014; Kim & Jerjen 2015). The increase in the number of MW satellites led to the blurring of the traditional distinction between small, baryon-dominated GCs and more extended, dark-matter dominated DGs. Taking the photometric properties of these new satellites at face value shows that they straggle the DG and GC boundary in the size–luminosity plane, in the so-called

benjamin.laevens@astro.unistra.fr
[1] Observatoire astronomique de Strasbourg, Université de Strasbourg, CNRS, UMR 7550, 11 rue de l'Université, F-67000 Strasbourg, France
[2] Max-Planck-Institut für Astronomie, Königstuhl 17, D-69117 Heidelberg, Germany
[3] Institute for Astronomy, University of Edinburgh, Royal Observatory, Blackford Hill, Edinburgh EH9 3HJ, UK
[4] Department of Astronomy, University of Michigan, 500 Church St., Ann Arbor, MI 48109, USA
[5] Institute for Astronomy, University of Hawaii at Manoa, Honolulu, HI 96822, USA
[6] Department of Physics and Astronomy, Johns Hopkins University, 3400 N. Charles St, Baltimore, MD 21218, USA
[7] Astronomisches Rechen-Institut, Zentrum für Astronomie der Universität Heidelberg, Mönchhofstrae 12 - 14, D-69120 Heidelberg, Germany
[8] Department of Physics, Durham University, South Road, Durham DH1 3LE, UK
[9] GMTO Corporation, 251 S. Lake Ave, Suite 300, Pasadena, CA 91101, USA

"valley of ambiguity" (Gilmore et al. 2007). Though follow-up observations have implied velocity dispersions higher than that expected from the stellar content for most of the new satellites (Martin et al. 2007; Simon & Geha 2007; Willman et al. 2011; Simon et al. 2011; Kirby et al. 2013), those measurements suffer from small number statistics and the unknown effect of binary stars on the kinematics of these small systems (McConnachie & Côté 2010).

The recent discoveries of such faint candidate DGs out to ~ 70 kpc within DES confirms that they are in fact common and that they could indeed correspond to the large population of faint dark-matter dominated systems expected to inhabit the MW halo (e.g. Tollerud et al. 2008; Bullock et al. 2010). These new satellites, located close to the Magellanic Clouds (Bechtol et al. 2015; Kirby et al. 2015; Koposov et al. 2015), have emphasized the tendency of these faint stellar systems to be brought into the MW surroundings in groups. Moreover, apparently isolated systems often share a proximity with stellar streams (e.g. Belokurov et al. 2008; Deason et al. 2014; Laevens et al. 2015; Martin et al. 2015).

Over the last three years, our group has focused on the search for compact stellar systems in PS1, which has so far revealed two new MW satellites: a likely GC, Laevens 1/Crater (Laevens et al. 2014; Belokurov et al. 2014), as well as a very faint satellite Triangulum II (Laevens et al. 2015), whose nature has not yet been confirmed by spectroscopy. In this paper, we present the discovery of three new MW satellites discovered from the latest PS1 photometric catalog: a faint GC, Laevens 3 (Lae 3); a faint satellite, Draco II/Laevens 4 (Dra II), whose uncertain properties make its nature ambiguous; and another ambiguous system, Sagittarius II/Laevens 5 (Sgr II)[10] [11]. This paper is structured in the following way: in section 2 we describe the PS1 survey and briefly outline the method which led to the discovery of the three satellites. In section 3 we discuss the properties of Lae 3, Dra II, and Sgr II, concluding and discussing the implications of the discoveries in section 4.

In this paper, all magnitudes are dereddened using the Schlegel et al. (1998) maps, adopting the extinction coefficients of Schlafly & Finkbeiner (2011). A heliocentric distance of 8 kpc to the Galactic center is assumed.

2. THE 3π PS1 SURVEY AND DISCOVERY

The PS1 survey (K. Chambers et al. in preparation) observed the whole sky visible from Hawaii ($\delta > -30°$), providing an unparalleled panoptic view of the MW and the Local Group. Throughout the 3.5 years of the 3π survey, the 1.8 m PS1 telescope, equipped with its 1.4-gigapixel camera capable of observing a 3.3-degree field of view, collected up to four exposures per year in five different optical filters: ($g_{\rm P1} r_{\rm P1} i_{\rm P1} z_{\rm P1} y_{\rm P1}$; Tonry et al. 2012). Once the individual frames have been taken at Haleakala and downloaded from the summit, the photometry is generated through the Image Processing Pipeline (Magnier 2006, 2007; Magnier et al. 2008).

The internal 3π stacked catalogs were released in three processing versions (PV), with each consecutive version corresponding to a higher number of individual exposures and improved photometry. The three stellar systems described in this paper were found using the intermediate PV2 catalog and supplemented with the upcoming PV3 photometry for their analysis, when beneficial. Although there are many small differences between the two processing versions, their most interesting features for our study are that the PV2 psf photometry is performed on the stacked images, whereas for PV3, the stacks are only used to locate sources before performing the photometry on each individual sub-exposure, with its appropriate psf. As a consequence, the PV3 photometry is more accurate, but the PV2 star/galaxy separation is more reliable. The depths of the bands of PV2, enabling the discoveries, are comparable to the SDSS for the $g_{\rm P1}$ band (23.0) and reach $\sim 0.5/\sim 1.0$ magnitude deeper for $r_{\rm P1}$ (22.8) and $i_{\rm P1}$ (22.5; Metcalfe et al. 2013).

With large CCD surveys, automated search algorithms were developed to perform fast and efficient searches of these massive data sets for the small stellar overdensities that betray the presence of faint MW satellites. These techniques, originally implemented on the SDSS data (Koposov et al. 2008; Walsh et al. 2009) have proven very successful. Inspired by this, we have developed our own similar convolution technique (Laevens et al. in preparation), adapted to the intricacies of the PS1 survey. The technique consists in isolating typical old, metal-poor DG or GC stars using de-reddened color-magnitude information $[(r-i)_0, i_0]$. For a chosen distance, masks in color-magnitude space are determined based on a set of old and metal-poor isochrones. The distribution of sources thereby extracted from the PS1 stellar catalog is convolved with two different window functions or Gaussian spatial filters (Koposov et al. 2008). The first Gaussian is tailored to the typical dispersion size of DGs or GCs ($2'$, $4'$, or $8'$), whereas the second one accounts for the slowly-varying contamination on far larger scales ($28'$ and $56'$). Subtracting the map produced from convolving the data with the larger Gaussian from that obtained with the smaller Gaussian results in maps of the PS1 sky tracking over- and under-densities once we further account for the small spatial inhomogeneities present in the survey. After cycling through different distances and the aforementioned sizes, we convert and combine all the density maps into statistical significance maps, allowing for a closer inspection of highly significant detections that do not cross-match with known astronomical objects (Local Group satellites, background galaxies and their GC systems, or artifacts produced by bright foreground stars). We further weed out spurious detections, by checking that these over densities do not correspond to significant background galaxy overdensities (Koposov et al. 2008). Applied to PV1, this method already led to the discovery of the most distant MW globular cluster Laevens 1/Crater (Laevens et al. 2014; Belokurov et al. 2014), as well as one of the faintest MW satellites, Triangulum II (Laevens et al. 2015), whose nature is not yet known. Sgr II, Dra II, and Lae 3 were detected as 11.9, 7.4, and 6.5 σ detections, comfortably above our 5σ

---

[10] We assign double names for these last two systems, pending spectroscopic confirmation as to the nature of these stellar systems. For convenience and clarity, throughout the remainder of the paper, we refer to these satellites by their constellation name

[11] We assign Roman numeral II to this system and refer to the Sagittarius dwarf spheroidal galaxy discovered by Ibata et al. (1994) as Sgr dSph.

threshold[12]. All three new satellites lie outside the SDSS footprint, which explains why they were not discovered before. Sgr II and Lae 3 are located at fairly low Galactic latitude[13] ($b \sim -20°$) and Dra II is quite far north ($\delta \sim +65°$).

3. PROPERTIES OF THE THREE STELLAR SYSTEMS

3.1. *Color-Magnitude Diagrams and Distances*

3.1.1. *Sagittarius II*

The color-magnitude diagram (CMD) of stars within one half-light radius of Sgr II ($1.9'$; see below for the structural parameters) is displayed in the top row of panels in Figure 1, next to the CMD of a field region of the same size. Since the features of Sgr II are so obvious we rely here only on the more accurate PV3 photometry at the cost of a poorer star/galaxy separation at the faint end. Given the location near the MW bulge $[(\ell, b) = (18.9°, -22.9°)]$ the field CMD is very populated, but the Sgr II CMD features are nevertheless clearly defined with a red giant branch (RGB) visible between $[(r_{\rm P1} - i_{\rm P1})_0, i_{\rm P1,0}] \simeq [0.30, 16.5]$ and [0.15,21.5], before its main sequence turnoff at $i_{\rm P1,0} < 22.0$. The most obvious feature, however, is the horizontal branch (HB) of the system, clearly visible for $19.5 < i_{\rm P1,0} < 20.0$ and $(r_{\rm P1} - i_{\rm P1})_0 < 0.0$. When selected with the box overlaid in orange on the CMD of the second Sgr II CMD panel of Figure 1, these stars correspond to a well-defined spatial overdensity (right-most panel). Isolating the HB stars (blue box) also highlights how clustered they are on the sky. We further highlight a single star that is bluer and brighter than the turn off and could potentially correspond to a blue straggler (green box and green triangle).

The presence of the reasonably well-populated HB, with 13 stars within 3 half-light radii, allows for a robust estimation of the distance to the satellite. Equation 7 in (Deason et al. 2011) describes the relation between the absolute magnitude of these HB stars and their SDSS $g-r$ colors. Converting the PS1 magnitudes to the SDSS bands, for which the relation holds, reveals a median $g = 19.60 \pm 0.03$ and $M_g = 0.47 \pm 0.04$ when we perform a Monte Carlo resampling of the stars' uncertainties. These leads to a distance-modulus of 19.13 ± 0.15, where an uncertainty of 0.1 was assumed on the Deason et al. (2014) relation. This translates into a Heliocentric distance of 67 ± 5kpc or a Galactocentric distance of 60 ± 5 kpc. Fixing the satellite at this distance modulus, we experiment with isochrones. Overlaid on the Sgr II CMD of Figure 1, we also show the old and metal-poor isochrone from the Parsec library (12 Gyr, [Fe/H] $= -2.2$; Bressan et al. 2012) that provides the best qualitative fit to the CMD features at this distance.

The properties of Sgr II are summarized in Table 1.

3.1.2. *Draco II*

Draco II is much closer and less luminous than Sgr II, as can be seen in the CMD of stars within $2r_h$ of the satellite's center in the second row of panels in Figure 1. Here, since we need both depth and a good star/galaxy separation to clean the main sequence of Dra II, we use the PV3 photometry combined with the superior PV2 star/galaxy flags. This has the consequence of removing some faint PV3 stars misidentified as galaxies but more optimally cleans the main sequence of the satellite. A field CMD is shown in the right-most CMD panel and helps identify the Dra II features: a populated main sequence between $[(r_{\rm P1} - i_{\rm P1})_0, i_{\rm P1,0}] \simeq [0.0, 20.2]$ and [0.2,22.0]. At brighter magnitudes, Dra II shows no HB and no prominent RGB. However, a group of stars at [0.2,17.0] is compatible with being the system's sparsely sampled RGB. As for Sgr II, isolating the stars in these CMD features (orange box in the central CMD panel) highlights the stellar overdensity in the spatial distribution shown in the right-most panel. As for Sgr II, we identify a potential blue straggler in green.

Due to the absence of any HB star[14], we cannot reliably break the distance-age-metallicity degeneracy with the PS1 data alone. Consequently, we explored isochrones of different ages and metallicities, located at varying distance. The best fit is provided by the Parsec isochrone shown in Figure 1; it has an age of 12 Gyr and [Fe/H] $= -2.2$ and is located at a distance modulus of 16.9 ± 0.3 but we caution the reader on the reliability of this particular isochrone that needs to be confirmed from deeper data.

3.1.3. *Laevens 3*

As can be seen in Figure 2, Lae 3 is a compact stellar system[15]. As such, the automated PS1 pipeline fails to extract the photometric information of the central region that suffers from crowding. We therefore perform custom photometry of this sky cell using DAOPHOT, using the same method as (Laevens et al. 2014). The resulting CMD for stars within $3r_h$ of the stellar system's centroid is shown on the bottom row of panels in Figure 1. This CMD is still likely to suffer from crowding, yet it reveals features that are clearly not expected in the field population: the Lae 3 RGB between $[(r_{\rm P1} - i_{\rm P1})_0, i_{\rm P1,0}] \simeq [0.75, 18.0]$ and [0.15,21.0], followed by the system's MSTO at fainter magnitudes. As for the two other satellites, selecting these stars only (orange box in the middle CMD) highlight a clear stellar overdensity.

An investigation into the presence of RR Lyra stars in the PS1 temporal data (Hernitschek et al. 2015, in prep.; Sesar et al. 2015, in prep.) reveals one obvious candidate, 0.6 arcmins away from the center of the cluster (highlighted by the blue box in the middle CMD and represented by a blue star in the right-most panel). Briefly, RR Lyrae stars are identified in PS1 data by providing average PS1 colors and various variability statistics to a trained Random Forest classifier (Richards et al. 2011). The resulting RR Lyrae sample is 80% complete (up to 80 kpc) and 90% pure. The distances of PS1 RR Lyrae stars are uncertain at the 5% level. The RR Lyra star in Lae 3 has also been observed more than 100 times by the Palomar Transient Factory (PTF; Law et al. 2009;

---

[12] For context, applying this technique leads to the recovery of the faint satellites Segue 1 and Bootes I, originally discovered in the SDSS, with a significance of 7.3 and 11.6σ, respectively.

[13] In fact, Lae 3 is clearly visible on the DSS plates and could have been discovered before the PS1 era.

[14] This is not per se surprising as, for instance, the similarly faint system Willman 1 only contains two HB stars (Willman et al. 2011).

[15] Note that the PS1 postage stamp images show no clear stellar over density for Sgr II and Dra II, hence why we do not include them.

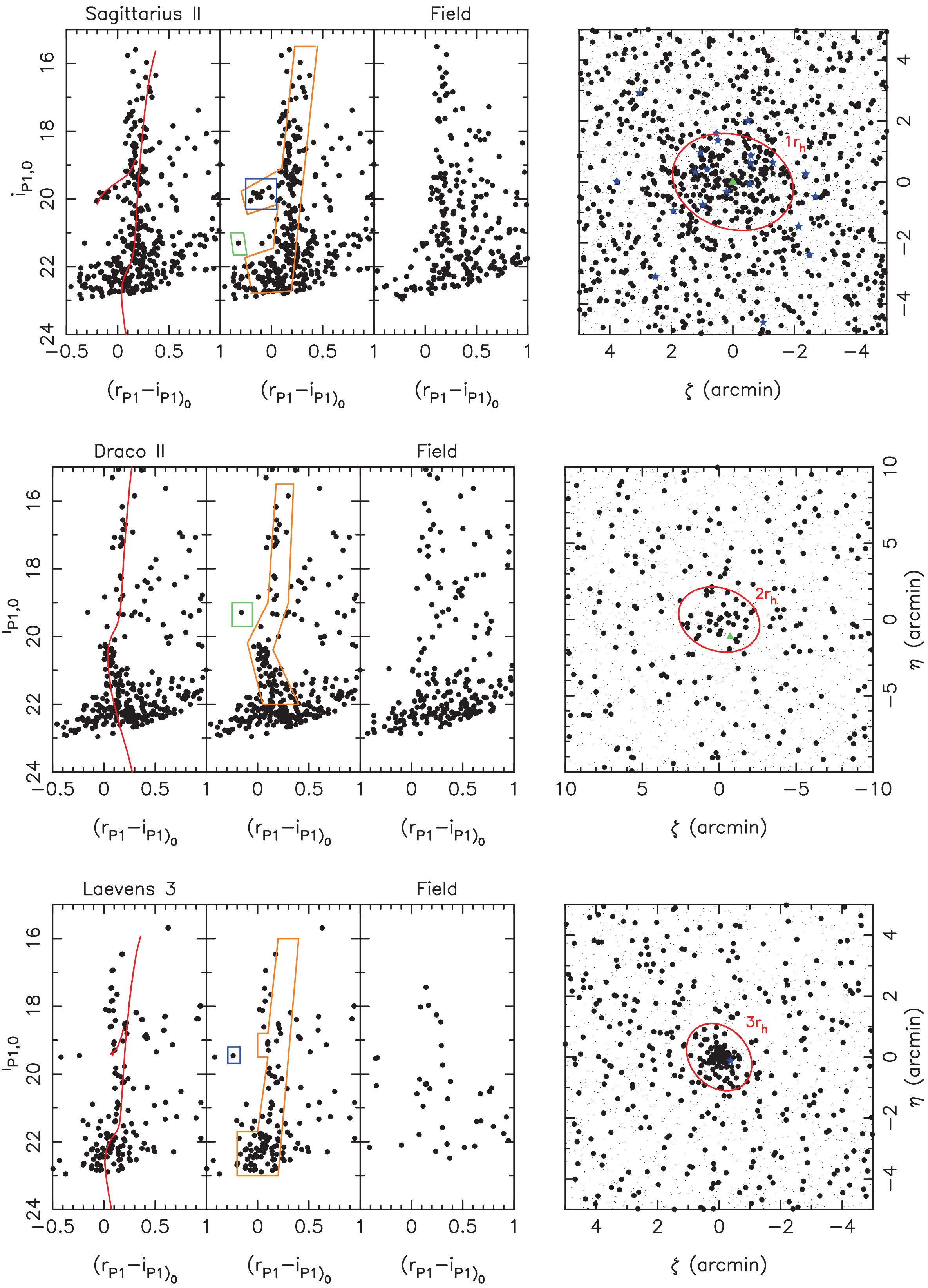

Figure 1. *Left:* from top to bottom, CMD of stars within 1 half-light radius (Sgr II), 2 half-light radii (Dra II) or 3 half-light radii (Lae 3) with the favored isochrone: 12 Gyr and [Fe/H] ~ -2.2 for Sgr II and Dra II, and 9 Gyr and [Fe/H] $= -1.9$ (Lae 3). *Middle-left:* Same as left-most panel with the CMD selection box used to isolate the RGB, HB, MSTO, and/or MS stars of the satellites (orange), and an HB selection box (blue) for Sgr II. The RR Lyra star for Lae 3 is highlighted in blue. Candidate blue straggler stars are identified for Sgr II and Dra II (green). *Middle-right:* CMD of field regions for stars 15 arcmin West of the satellites of similar sizes to those used for the left-most panels. *Right:* Spatial distribution of all stars around the three satellites (light black dots) and of stars selected with the orange CMD selection boxes in the middle-left panel (big black dots). For Sgr II, HB stars corresponding to the blue HB selection box in the middle panel are represented by blue stars symbols. Finally, candidate blue straggler stars corresponding to the green box are displayed as green triangles.

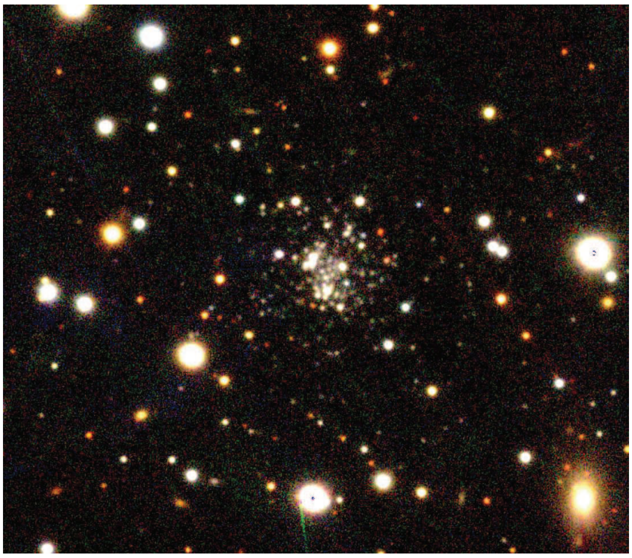

Figure 2. : $g_{\rm P1}r_{\rm P1}i_{\rm P1}$ image of Laevens 3, built from the stacked PV3 PS1 images. The image is $2.5' \times 2.5'$ and North is to the top and East is to the left.

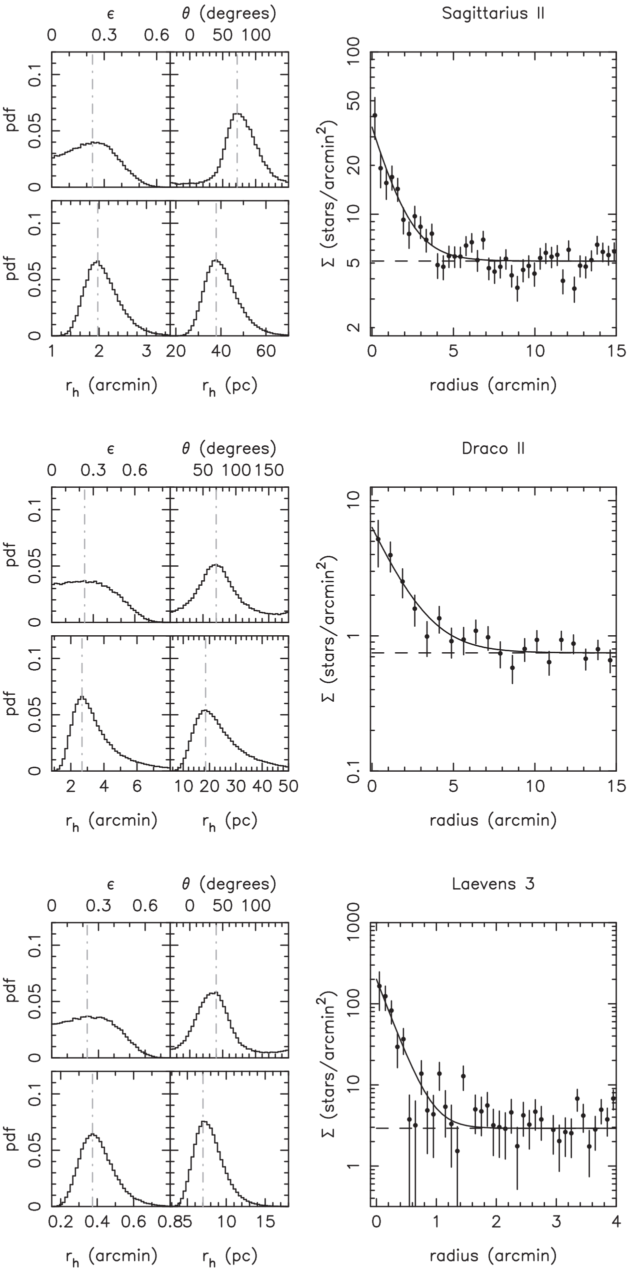

Figure 3. *Left:* Probability distribution functions for the ellipticity (ϵ), the position angle (θ), and the angular and physical half-light radii, r_h, of Sgr II (top), Dra II (middle), and Lae 3 (bottom). *Right:* Comparison between the favored radial distribution profile (full line) and the data, binned according to the preferred structural parameters (dots), selected as the mode of the PDFs (grey line in the left-hand panels). The error bars assume Poissonian uncertainties and the dashed line represents the field density.

Rau et al. 2009). The distance and period measured from PS1 data agree within 2 sec and 5% with those measured from the PTF data. The RR Lyra star is at $(m-M)_0 = 19.14 \pm 0.10$, or a distance of 67 ± 3 kpc. The ~14 hour period of the star suggests a star with a metallicity range of $-1.9 <$ [Fe/H] < -1.6. Fixing this distance, we once again experiment with various isochrones and conclude that the CMD feature are best tracks by an isochrone with a comparatively young age of 9 Gyr and [Fe/H] ~ -1.9, compatible with the properties of the RR Lyra star. The isochrone fit, fixed at that distance, tracks the main features of the satellite such as the RGB and the MSTO. Though two blue stars are also present at the same magnitude as the tentative red HB, the bluest of the two is a field variable star, incompatible for being a member of Lae 3. We further compare the CMD features with the GC fiducial published by Bernard et al. (2014) in the PS1 photometric system. The fiducials of globular clusters NGC 1904, NGC 5897 and NGC 7089, with $-1.9 <$ [Fe/H] < -1.6 provide a good fit to the CMD features and confirm our impression from the isochrones.

The derived properties are summarized in Table 1 for all three satellites.

3.2. *Structural Parameters and Absolute Magnitudes*

The structural parameters of Sgr II, Dra II, and Lae 3 are derived using a version of the Martin et al. (2008) likelihood technique updated to a full Markov Chain Monte Carlo framework (Martin et al. 2015, in prep.). Using the star's location in the vicinity of satellite, the algorithm calculates the posterior probability distribution function (PDF) of a family of exponential radial density profiles, allowing for flattening and a constant contamination from field stars. The parameters of the models are the centroid of the system, the ellipticity, ϵ[16], the position angle, θ (defined as the angle of the major axis East from North), the half-light radius r_h[17], and finally the number of stars, N^* within the chosen CMD selection box. We further determine the physical half-light radius from the angular one by randomly drawing distances from the distance modulus values.

The PDF for the ellipticity, position angle, as well as the angular and physical half-light radii may be seen in Figure 3 for, from top to bottom, Sgr II, Dra II, and

---

[16] The ellipticity, here, is defined as $\epsilon = 1 - b/a$ with a and b the major and minor axis scale lengths, respectively.

[17] In fact, the algorithm constrains the half-density radius, but this is similar to the more common half-light radius if there is no mass segregation in the system.

Table 1
Properties of Laevens 3, Draco II and Sagittarius II

	Laevens 3	Draco II/Laevens 4	Sagittarius II/Laevens 5
α (ICRS)	21:06:54.3	15:52:47.6	19:52:40.5
δ (ICRS)	+14:58:48	+64:33:55	−22:04:05
$\ell(^\circ)$	63.6	98.3	18.9
$b(^\circ)$	−21.2	+42.9	−22.9
Distance Modulus	19.14 ± 0.10	$\sim 16.9 \pm 0.3$	19.13 ± 0.15
Heliocentric Distance (kpc)	67 ± 3	20 ± 3	67 ± 5
Galactocentric Distance (kpc)	64 ± 3	22 ± 3	60 ± 5
M_V	-4.4 ± 0.3	-2.9 ± 0.8	-5.2 ± 0.4
L_V	$10^{3.7\pm0.1}$	$10^{3.1\pm0.4}$	$10^{4.0\pm0.1}$
[Fe/H]	~ -1.9	~ -2.2	~ -2.2
Age (Gyr)	~ 9	~ 12	~ 12
$E(B-V)^a$	0.073	0.016	0.097
Ellipticity	0.21 ± 0.21	$0.24^{+0.27}_{-0.24}$	$0.23^{+0.17}_{-0.23}$
Position angle (from N to E °)	40^{+16}_{-28}	70 ± 28	72^{+28}_{-20}
r_h (arcmin)	$0.40^{+0.07}_{-0.11}$	$2.7^{+1.0}_{-0.8}$	$2.0^{+0.4}_{-0.3}$
r_h (pc)	7 ± 2	19^{+8}_{-6}	38^{+8}_{-7}

^{a} from Schlegel et al. (1998) and Schlafly & Finkbeiner (2011)

Lae 3. The three right-most panels of the figure compare the radial profile of a given satellite, binned following the favored centroid, ellipticity, and position angle to the favored exponential radial density profile; they display the good quality of the fit in all cases. All three systems are rather compact, with angular half-light radii of $2.0^{+0.4}_{-0.3}$, $2.7^{+1.0}_{-0.8}$, and $0.40^{+0.07}_{-0.11}$ arcmin for Sgr II, Dra II, and Lae 3, respectively. However, the different distances to these systems lead to different physical sizes: 38^{+8}_{-7}, 19^{+8}_{-6}, and 7 ± 2 pc. In all three cases, the systems appear mildly elliptical but the PDFs show that this parameter is poorly constrained from the current data. It should be noted that, in the case of Lae 3, the crowding at the center of the stellar system could lead to an underestimation of the compactness and luminosity of the system. However, the Lae 3 radial profile shows no sign of a central dip.

The absolute magnitude of the three stellar systems was determined using the same procedure as for Laevens 1 and Triangulum II (Laevens et al. 2014, 2015), as was also described for the first time in Martin et al. (2008). Using the favored isochrones and their associated luminosity functions for the three satellites, shifted to their favored distances, we build CMD pdfs after folding in the photometric uncertainties. Such CMDs are populated until the number of stars in the CMD selection box equals the favored number of stars N^* as determined by the structural parameters[18]. The flux of these stars is summed up, yielding an absolute magnitude. In practice, this operation is repeated a hundred times with different drawings of the Markov chains, thus taking into account three sources of uncertainty: the distance modulus uncertainty, the uncertainty on the number N^* of stars in the CMD selection box, and shot-noise uncertainty, originating from the random nature of populating the CMD. This procedure yields total magnitudes in the PS1 r_{P1} band, which we then convert to the more commonly used V-band magnitudes through a constant color offset ($V - r = 0.2$) determined from the analysis of more populated, known, old and metal-poor MW satellites. This yield $M_V = -5.2 \pm 0.4$, -2.9 ± 0.8, and -4.4 ± 0.3 for Sgr II, Draco II, and Laevens 3, respectively. All three systems are rather faint, as expected from their sparsely populated CMDs.

4. DISCUSSION

Figure 4 displays the properties of the three new discoveries in the context of the other MW satellites (GCs or DGs). The top panel shows the size-luminosity plane while the bottom panel focuses on the distance-luminosity plane. These parameters can already be a first indicator as to the nature of these objects, which we proceed to discuss here as well as the possible stream associations these objects may have.

4.1. *Sagittarius II*

Sgr II occupies an interesting place in the r_h vs. M_V plane as it lies in the very middle of the "valley of ambiguity[19]" highlighted by Gilmore et al. (2007). Although other MW satellites are known with similar absolute magnitudes, Sgr II is smaller than Coma Berenices ($r_h = 74 \pm 4$ pc; Muñoz et al. 2010, Pisces II ($r_h = 58 \pm 10$ pc; Sand et al. 2012), Hydra II ($r_h = 68 \pm 11$ pc; Martin et al. 2015), or the even larger Leo IV and Leo V ($r_h = 205 \pm 36$ and 133 ± 31 pc; de Jong et al. 2010), or Ursa Major I ($r_h = 318 \pm 45$ pc; Martin et al. 2008). On the other hand, Sgr II remains larger than the largest GC, Pal 14 ($r_h \sim 25$ pc; Hilker 2006), or the recently discovered Laevens 1/Crater system ($r_h = 20 \pm 2$ pc), recently confirmed to be a GC (Kirby et al. 2015). It should however be noted that, recently, M31 satellite assumed to be GC have been discovered with similar sizes

---

[18] For this part of the analysis, we make sure to use a selection box that remains ~ 1 magnitude brighter than the photometric depth so the data is close to being complete. In the case of Lae 3, the sparsely populated CMD prevents us from doing so as we need to use the full extent of the CMD to reach convergence in the structural parameter analysis. This is likely to slightly underestimate the luminosity of the cluster.

[19] The region in r_h vs. M_V space that straggles the 'classical' boundaries between DGs and GCs.

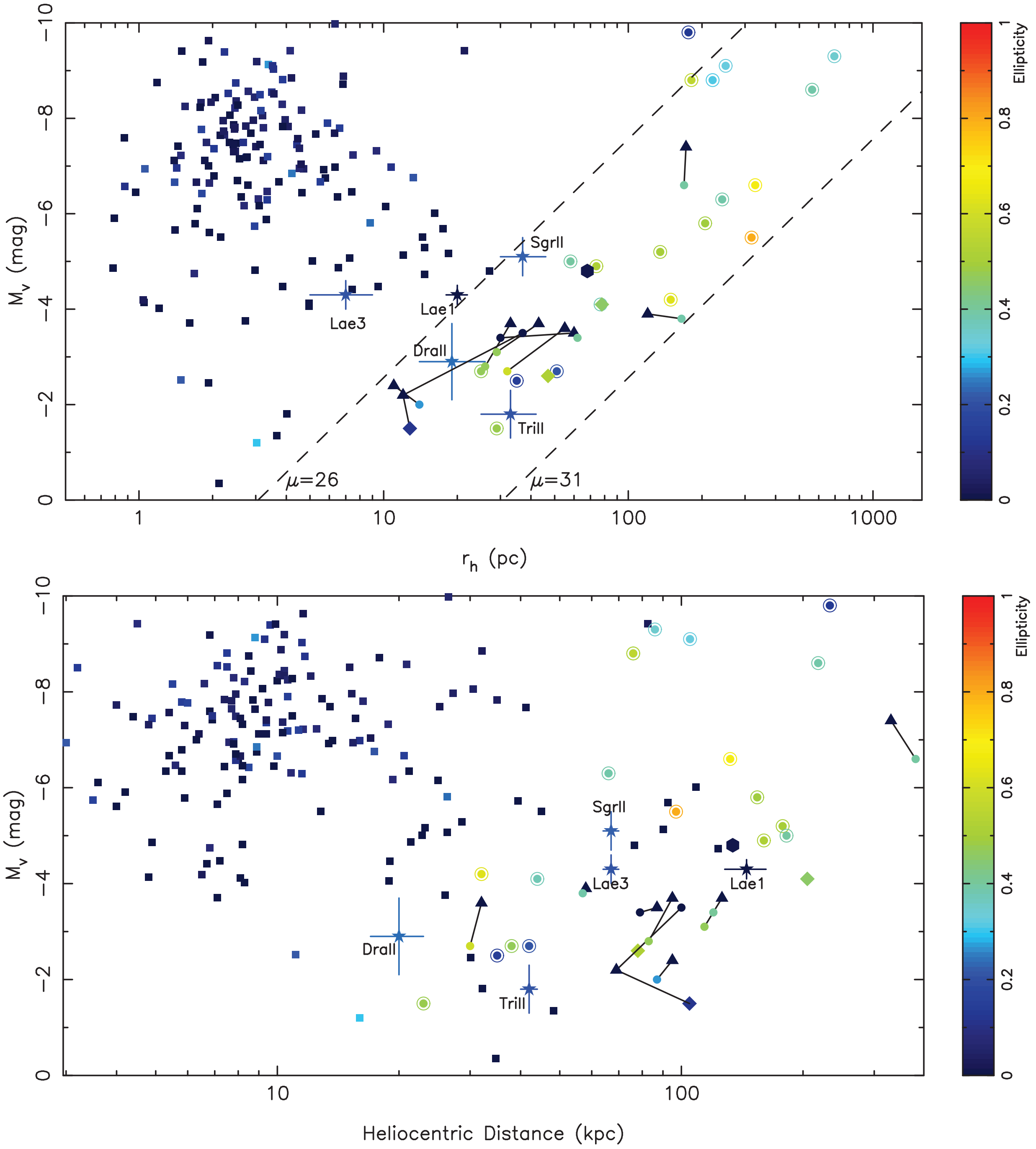

Figure 4. *Top:* Distribution of MW satellites in the size-luminosity plane, color-coded by their ellipticity. Squares represent GCs from the Harris (2010) catalog, supplemented by the more recent discoveries of Segue 3 (Belokurov et al. 2010), Muñoz 1 (Muñoz et al. 2012), and Balbinot 1 (Balbinot et al. 2013). Milky Way confirmed dwarf galaxies are shown as circled dots, with their properties taken from McConnachie (2012). The co-discoveries by Bechtol et al. (2015) and Koposov et al. (2015) are shown with triangles and filled circles respectively, with the co-discoveries linked to each other by a black solid line reflecting the two groups' different measurements. The Kim et al. (2015a), Kim et al. (2015b),and Kim & Jerjen (2015) satellites are shown with diamonds. Hydra II, discovered in SMASH is shown by a hexagon. Finally, the five PS1 discoveries (Lae 1, Tri II, Sgr II, Dra II, and Lae 3) are shown as stars. *Bottom:* The same for the size-Heliocentric distance plane.

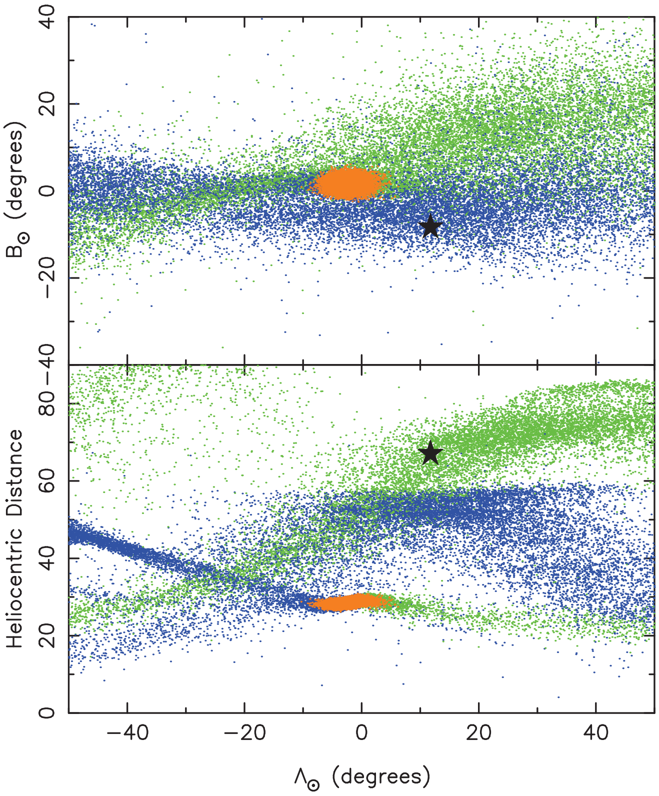

Figure 5. *Top:* Particles of the Law & Majewski (2010b) N-body model of the Sgr stream, projected on the Sgr dSph co-ordinate system (Majewski et al. 2003). Particles of the leading/trailing arm of the Sgr stream are shown in blue/green, whereas the body of the Sgr dSph is shown in orange. The position of Sgr II is represented by the black star. *Bottom:* The same for the Heliocentric distance vs. Sgr dSph longitude plane. Sgr II clearly overlaps with the trailing arm.

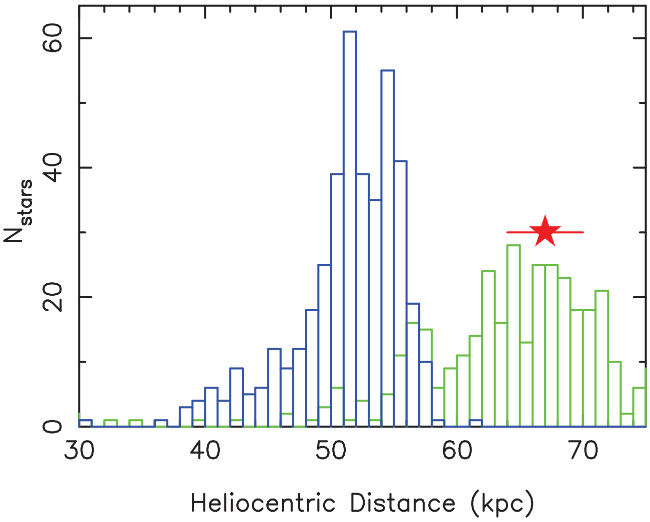

Figure 6. Heliocentric distance histogram of all particles in the Law & Majewski (2010b) model within 1 degree of Sgr II's longitudinal position (no constraint was applied on the latitude). As in Figure 5, blue and green dots represent particles from the leading and trailing arm, respectively. The distance to Sgr II and its uncertainty are represented by the red star and the error bar and show that Sgr II is perfectly compatible with belonging to the trailing arm of the Sgr stream.

(Huxor et al. 2014), although the nature of some of these systems is also ambiguous (Mackey et al. 2013). The CMD of Figure 1 shows that the satellite hosts a clear blue HB, which is not a common feature of outer halo GCs that tend to favor red HBs (see, e.g., Figure 1 of Laevens et al. 2014). Ultimately, spectroscopic follow-up and a measure of the satellite's velocity dispersion is necessary to fully confirm the nature of this satellite and whether it is dark-matter dominated.

The location of Sgr II, $\sim 15°$ from Sgr dSph and in the expected plane of the Sgr stellar stream is particularly interesting as it could point to an association. The fact that it lies 40–45 kpc behind Sgr dSph rules out a direct connection between the two satellites but a comparison with the Law & Majewski (2010b) N-body model for the Sgr stream (Figure 5) reveals that Sgr II is located at the expected distance of model particles from the trailing arm of the Sgr stream stripped out of their host more than 3 Gyr ago. It is therefore likely that Sgr II was brought into the MW halo along with this part of the Sgr stream that has so far eluded detection, in a similar fashion to numerous other MW halos GCs (e.g. Law & Majewski 2010a). The fact that the sky location of Sgr II is slightly offset from this section of the model's trailing arm is not necessarily surprising since a former Sgr dSph satellite is not expected to be as concentrated on the sky as its former stars the model. In addition, the location of these older wraps of the Sgr stream are very poorly constrained in the model. In fact, the discovery of Sgr II and its association with the Sgr stream could add valuable constraints on the modeling of the Sgr stream once confirmed through radial velocities.

4.2. *Draco II*

Draco II also has an ambiguous nature, although it is here driven mainly by the large uncertainties on its structural parameters and distance, stemming from the faint nature of the object in the PS1 data. With the current photometry, the satellite appears to share the properties of Kim 2 or Eridanus III, believed to be GCs (Kim et al. 2015b; Bechtol et al. 2015; Koposov et al. 2015). On the other hand, its uncertain properties are also completely compatible with those of Wil 1, favored to be a DG (Willman et al. 2011). Here as well, deep photometry and/or spectroscopy are necessary to classify this system.

Given the common connection between faint stellar systems and stellar streams, we investigate possible associations of the satellite to known MW halo streams. The closest stream to Dra II is the GD-1 stream (Grillmair & Dionatos 2006). Placing the new satellite onto the stream coordinate system defined by Koposov et al. (2010), we find that it is located at $\phi_1 \sim 17.1°$ and $\phi_2 \sim 3.8°$. Though Koposov et al. (2010) do not have any measurements in this region (their measurements range from $\phi_1 = -60.00°$, $\phi_2 = -0.64° \pm 0.15°$ to $\phi_1 = -2.00°$, $\phi_2 = -0.87° \pm 0.07°$), the extrapolation of the orbit at the location of Dra II yield $\phi_2 \sim -2.7°$, only 5–6° away from the satellite. However, the extrapolated distance of the stream reaches only ~ 12 kpc there, to be compared with Dra II's ~ 20 kpc. Therefore, if the GD-1 stream does not significantly deviate from the Koposov et al. (2010) orbit, the current distance estimate for Dra II appears too high for a direct association.

4.3. *Laevens 3*

The small half-light radius of Lae 3 (7 ± 2 pc) places it well within the regime of GCs. With a relatively young age (~ 9 Gyr) and stellar populations that are not very metal-poor ([Fe/H] ~ -1.9), it would be natural to classify Lae 3 as a "young outer halo" GC found in the outer region of the MW halo (Mackey & van den Bergh 2005). However, some caveats should be noted: the isochrone fit relies on the photometry currently available, which suffers from crowding. The presence of an RR Lyra star could be at odds with a young halo scenario since its presence would point to a system that is at least 10 Gyrs old. We find no possible connection of this new system with known stellar streams in the MW halo.

5. CONCLUSION

In this paper, we have presented the discovery of three new faint Milky Way satellites, discovered in the photometric catalog of the PS1 3π survey. The characterization of Lae 3 suggests that it is a GC, with properties similar to 'young outer halo' GCs. The two other systems, Dra II and Sgr II, have an ambiguous classification. Dra II contains mainly main sequence stars, as well as a handful of probable RGB stars. It is very faint but its structural parameters are uncertain enough to prevent a classification as an extended GC or a compact dwarf galaxy. It is located close to the orbital path of the GD-1 stream but its distance is in disagreement with the expectations of the stream's orbit (~ 20 vs. ~ 12 kpc) and appear to rule out an association. Finally, Sgr II is located in a part of the size-luminosity plane that contains no other known system, either more extended than known MW GCs, or more compact than known MW DGs in its luminosity range. Independently of its nature, Sgr II is particularly interesting as it lies at the expected location of the Sgr dSph stellar stream behind the bulge. In particular, the distance to the new satellite favors a connection with the currently undiscovered part of the trailing arm of the Sgr stream produced by stars stripped from the dwarf galaxy more than 3 Gyr ago. Ultimately, spectroscopic follow-up will be necessary to conclusively establish the nature of the last two satellites or confirm their connection with the GD-1 and Sgr stellar streams.

We thank Paolo Bianchini, Mark Norris, and Dougal Mackey for their thoughts and reflections. B.P.M.L. acknowledges funding through a 2012 Strasbourg IDEX (Initiative d'Excellence) grant, awarded by the University of Strasbourg. N.F.M. and B.P.M.L. gratefully acknowledges the CNRS for support through PICS project PICS06183. H.-W.R. and E.F.T acknowledge support by the DFG through the SFB 881 (A3). E.F.B. acknowledges support from NSF grant AST 1008342.

The Pan-STARRS1 Surveys have been made possible through contributions of the Institute for Astronomy, the University of Hawaii, the Pan-STARRS Project Office, the Max-Planck Society and its participating institutes, the Max Planck Institute for Astronomy, Heidelberg and the Max Planck Institute for Extraterrestrial Physics, Garching, the Johns Hopkins University, Durham University, the University of Edinburgh, Queen's University Belfast, the Harvard-Smithsonian Center for Astrophysics, the Las Cumbres Observatory Global Telescope Network Incorporated, the National Central University of Taiwan, the Space Telescope Science Institute, the National Aeronautics and Space Administration under Grant No. NNX08AR22G issued through the Planetary Science Division of the NASA Science Mission Directorate, the National Science Foundation under Grant No. AST-1238877, the University of Maryland, and Eotvos Lorand University (ELTE).

REFERENCES

Balbinot, E., et al. 2013, ApJ, 767, 101
Bechtol, K., et al. 2015, ApJ, 807, 50
Belokurov, V., Irwin, M. J., Koposov, S. E., Evans, N. W., Gonzalez-Solares, E., Metcalfe, N., & Shanks, T. 2014, MNRAS, 441, 2124
Belokurov, V., et al. 2008, ApJ, 686, L83
—. 2010, ApJ, 712, L103
—. 2006, ApJ, 642, L137
—. 2007, ApJ, 654, 897
Bernard, E. J., et al. 2014, MNRAS, 442, 2999
Bressan, A., Marigo, P., Girardi, L., Salasnich, B., Dal Cero, C., Rubele, S., & Nanni, A. 2012, MNRAS, 427, 127
Bullock, J. S., Kravtsov, A. V., & Weinberg, D. H. 2000, ApJ, 539, 517
—. 2001, ApJ, 548, 33
Bullock, J. S., Stewart, K. R., Kaplinghat, M., Tollerud, E. J., & Wolf, J. 2010, ApJ, 717, 1043
de Jong, J. T. A., Martin, N. F., Rix, H.-W., Smith, K. W., Jin, S., & Macciò, A. V. 2010, ApJ, 710, 1664
Deason, A. J., Belokurov, V., & Evans, N. W. 2011, MNRAS, 416, 2903
Deason, A. J., et al. 2014, MNRAS, 444, 3975
Gilmore, G., Wilkinson, M. I., Wyse, R. F. G., Kleyna, J. T., Koch, A., Evans, N. W., & Grebel, E. K. 2007, ApJ, 663, 948
Grillmair, C. J., & Dionatos, O. 2006, ApJ, 643, L17
Harris, W. E. 2010, ArXiv:1012.3224
Hilker, M. 2006, A&A, 448, 171
Huxor, A., Mackey, A. D., Ferguson, N., A. M., et al. 2014, MNRAS, submitted
Ibata, R. A., Gilmore, G., & Irwin, M. J. 1994, Nature, 370, 194
Kim, D., & Jerjen, H. 2015, ArXiv e-prints
Kim, D., Jerjen, H., Mackey, D., Da Costa, G. S., & Milone, A. P. 2015a, ArXiv e-prints
Kim, D., Jerjen, H., Milone, A. P., Mackey, D., & Da Costa, G. S. 2015b, ApJ, 803, 63
Kirby, E. N., Boylan-Kolchin, M., Cohen, J. G., Geha, M., Bullock, J. S., & Kaplinghat, M. 2013, ApJ, 770, 16
Kirby, E. N., Simon, J. D., & Cohen, J. G. 2015, ArXiv e-prints
Koposov, S., et al. 2008, ApJ, 686, 279
—. 2007, ApJ, 669, 337
Koposov, S. E., Belokurov, V., Torrealba, G., & Evans, N. W. 2015, ApJ, 805, 130
Koposov, S. E., Rix, H.-W., & Hogg, D. W. 2010, ApJ, 712, 260
Laevens, B. P. M., et al. 2015, ApJ, 802, L18
—. 2014, ApJ, 786, L3
Law, D. R., & Majewski, S. R. 2010a, ApJ, 718, 1128
—. 2010b, ApJ, 714, 229
Law, N. M., et al. 2009, PASP, 121, 1395
Mackey, A. D., et al. 2013, ApJ, 770, L17
Mackey, A. D., & van den Bergh, S. 2005, MNRAS, 360, 631
Magnier, E. 2006, in The Advanced Maui Optical and Space Surveillance Technologies Conference
Magnier, E. 2007, in Astronomical Society of the Pacific Conference Series, Vol. 364, The Future of Photometric, Spectrophotometric and Polarimetric Standardization, ed. C. Sterken, 153
Magnier, E. A., Liu, M., Monet, D. G., & Chambers, K. C. 2008, in IAU Symposium, Vol. 248, IAU Symposium, ed. W. J. Jin, I. Platais, & M. A. C. Perryman, 553–559
Majewski, S. R., Skrutskie, M. F., Weinberg, M. D., & Ostheimer, J. C. 2003, ApJ, 599, 1082
Martin, N. F., de Jong, J. T. A., & Rix, H.-W. 2008, ApJ, 684, 1075

Martin, N. F., Ibata, R. A., Chapman, S. C., Irwin, M., & Lewis, G. F. 2007, MNRAS, 380, 281

Martin, N. F., et al. 2015, ApJ, 804, L5

McConnachie, A. W. 2012, AJ, 144, 4

McConnachie, A. W., & Côté, P. 2010, ApJ, 722, L209

Metcalfe, N., et al. 2013, MNRAS

Muñoz, R. R., Geha, M., Côté, P., Vargas, L. C., Santana, F. A., Stetson, P., Simon, J. D., & Djorgovski, S. G. 2012, ApJ, 753, L15

Muñoz, R. R., Geha, M., & Willman, B. 2010, AJ, 140, 138

Rau, A., et al. 2009, PASP, 121, 1334

Richards, J. W., et al. 2011, ApJ, 733, 10

Sand, D. J., Strader, J., Willman, B., Zaritsky, D., McLeod, B., Caldwell, N., Seth, A., & Olszewski, E. 2012, ApJ, 756, 79

Schlafly, E. F., & Finkbeiner, D. P. 2011, ApJ, 737, 103

Schlegel, D. J., Finkbeiner, D. P., & Davis, M. 1998, ApJ, 500, 525

Simon, J. D., & Geha, M. 2007, ApJ, 670, 313

Simon, J. D., et al. 2011, ApJ, 733, 46

The Dark Energy Survey Collaboration. 2005, ArXiv Astrophysics e-prints

Tollerud, E. J., Bullock, J. S., Strigari, L. E., & Willman, B. 2008, ApJ, 688, 277

Tonry, J. L., et al. 2012, ApJ, 750, 99

Walsh, S. M., Jerjen, H., & Willman, B. 2007, ApJ, 662, L83

Walsh, S. M., Willman, B., & Jerjen, H. 2009, AJ, 137, 450

Willman, B., et al. 2005, AJ, 129, 2692

Willman, B., Geha, M., Strader, J., Strigari, L. E., Simon, J. D., Kirby, E., Ho, N., & Warres, A. 2011, AJ, 142, 128

York, D. G., et al. 2000, AJ, 120, 1579

Zucker, D. B., et al. 2006, ApJ, 643, L103

Chapter 7

Quantifying the detection limits of the Pan-STARRS 1 3 π Survey

7.1 Generating artificial galaxies

7.1.1 Introduction

Determining the detection limits of the PS1 survey is an important exercise because it will assess two different aspects: the quality of the PS1 data and the efficiency of the developed search technique. Before embarking on this, a general idea can already be hypothesised about which results such an endeavour may yield. Firstly, the PS1 survey is very similar to the SDSS in terms of depth, therefore one could expect that the results for PS1 should be similar to the SDSS (assuming an efficient search technique). Secondly, results in Chapter 2 have already given a global indication as to the properties of substructure that can be found. If the photometry and star–galaxy separation are optimised (which is not the case over the PS1 sky in its entirety), the search yields similar results to the SDSS, with convincing retrieval of the faintest and brightest SDSS DGs and GCs. To date just five new satellites have been found, which is a relatively low number, when considering that the PS1 search volume is $\sim 1.5 - 2$ times that of the SDSS, which all in all revealed 16 MW DGs and $\sim$ 5 MW GCs [1]. Even more striking, when considering these discoveries, is that not one of them is an unambiguous DG such as Boötes I or Pisces II: two of these satellites are GCs (Laevens 1/Crater and Laevens 3), one is a probable Segue 1 type DG (Triangulum II), with the last two unconfirmed, but both displaying properties between GCs and DGs (Sagittarius II, Draco II). The low number therefore further illustrates the need to quantify the detection limits. This effort in turn can lead to quantifying the (an)isotropy of the distribution of MW DGs.

The aim of this chapter is therefore to quantify the answer to the following question: "If x-number of galaxies are ingested into the PS1 survey with y-parametres in z-location, what is the likelihood of observing galaxy i with parameter y_i in location z_i?" Let us relate this to the case of two specific SDSS DGs: Boötes I ($M_V = -6.3$, $r_h = 242\,\mathrm{pc}$ and $d = 67\,\mathrm{kpc}$) and Segue 1 ($M_V = -1.5$, $r_h = 29\,\mathrm{pc}$ and $d = 23\,\mathrm{kpc}$). In the first case one could be fairly confident of retrieving this galaxy (at that distance) in most places in the sky, because of its properties

---

[1] Several M31 satellites (e.g Zucker et al., 2004, 2007; Slater et al., 2011; Bell et al., 2011) were found too, but let us restrict ourselves to the MW.

(i.e. bright, large and quite close). Segue 1, on the other hand, is so faint that the successful retrieval of such a galaxy will be very location-sensitive. For instance, placing this DG a little closer to the disc, could mean that its 30-40 blue stars are not very significant relative to its neighbouring regions. In other words, this exercise will be very interesting to probe the limit of low surface brightness.

Undertakings to quantify the detection limits of surveys have been undertaken in the past, notably on the SDSS, with exactly the same aim in mind as ours. For the reader's information, a short overview of one of the SDSS–efforts will be given in the remainder of this section. This will in turn lay the ground for the main steps that will be outlined in the rest of this chapter and which will be expanded upon in the next sections. Koposov et al. (2007) ingested 8000 simulated DGs over the SDSS footprint. They did this by first simulating objects in CMD space, using the SDSS photometry of the GC M92. The authors construct a luminosity function for the various stellar evolutionary sequences, given the M92 cluster, which they smooth. They subsequently use the ridgeline by Clem (2006), containing a Main-Sequence and a Red Giant Branch (they add a horizontal branch themselves) to populate it with the properties of a certain type of satellite. In other words, the luminosity function is used to populate the ridgeline in the right proportions for a given satellite. Since this is a ridgeline, they need to scatter the stars around, to make the CMD look realistic. They therefore spread the stars using the photometric uncertainties as a function of magnitude. Once that is completed, they connect each star they have generated in CM space to a spatial component. They do this by using a Plummer profile.

In this chapter, I expand and detail these steps. In section 7.1.2, the method for generating DG photometry in PS1 is explained. In section 7.1.3, an explanation is given regarding the inhomogeneity of the PS1 survey and how it is taken into account. In sections 7.1.4 and 7.1.5, the generation of spatial components for the member stars and how the whole operation is implemented in PS1 is detailed.

7.1.2 Photometry

As already briefly touched upon in section 7.1.1, the first key step in generating artificial galaxies is to generate photometry that accurately describes the type of system we wish to consider, i.e. old, blue and metal-poor populations. Many aspects of the PS1 approach resemble the Koposov et al. (2008) effort, with one of the key differences being our respective starting points. Instead of using photometry for a large, bright GC, a 'Master DG' is generated. This is a bright DG of some $\sim$120 000 000 stars, distributed in CM space according to the luminosity function. This DG fulfils the same purpose as the Clem (2006) ridgeline. Stars are drawn from this Master DG to generate the DG of interest. The Master DG was generated using Dartmouth isochrones and Luminosity functions (Dotter et al., 2008)[2]. A metallicity of $[\mathrm{Fe/H}] = -2.0$ and Age=12 Gyrs[3] was chosen, which represents a typical MW satellite. Table 7.1 describes the various parameters that were used when downloading the isochrones and luminosity functions from the Dartmouth website. For the horizontal branch (which is not included in the initial set of isochrones and luminosity functions), the synthetic horizontal

---

[2] http://stellar.dartmouth.edu/models/

[3] This is roughly the same age and metallicity as for M92.

branch models were downloaded, containing the same properties as the main sequence and red giant brach. Figure 7.1 shows the isochrone of the Master DG on the left and the corresponding luminosity function on the right.

Table 7.1 - Darmouth Isochrone and Luminosity Function parameters

Age	12 Gyrs
[Fe/H]	-2.0
Helium Mass Fraction	Y=0.25+1.5*Z
α/Fe	+0.2
Colors	Pan-STARRS
Bin size	0.1
IMF Type	Power Law
Power Law Slope	-2.35

The Master DG is generated by populating the isochrone ridgeline with the number of stars as determined by the luminosity function. To do this, the luminosity function is splined such that it is defined at every value of i (in 0.01 magnitude bins). Subsequently, one billion stars can be generated in luminosity function–magnitude space. Using the "acceptance-rejection" method, the stars under the luminosity function curve are retained. Specifically, each star is randomly assigned a magnitude and luminosity function value. The star is subsequently binned into the closest magnitude bin: if the luminosity function of the star is below the curve, the star is accepted, otherwise it is rejected. Afterwards, each star is connected to a colour. This time, the isochrone is splined such that for each 0.01 magnitude value, there is an associated colour. Each magnitude is now connected to a colour by once again binning the star into its closest magnitude bin. This process is done for the main-sequence and red giant branch. For the horizontal branch a slightly more involved procedure is necessary. As detailed in the previous paragraph, the horizontal branch was constructed with a different synthetic isochrone from the Dartmouth website. These isochrones were only available in the SDSS bands. Using the Tonry et al. (2012) conversion equations, the PS1 magnitudes and colours could be derived. The same process is repeated in terms of splining the isochrone and luminosity function. The main luminosity function (main sequence and red giant brach) and the horizontal branch isochrone are combined to assess the ratio of the number of objects that should be distributed on the horizontal branch relative to the red giant brach for the overlapping magnitude range. The number of horizontal branch stars was estimated to be 1.5 times the red giant brach stars in that magnitude range. The number of horizontal branch stars this produces roughly coincides with the number of stars that lie on the red giant brach, brighter than the brightest point of the horizontal branch, which from stellar evolution are expected to be roughly the same number. Finally, the horizontal branch is populated separately, but again using the "acceptance–rejection" method. For the overlapping magnitude range, the number of stars is drawn randomly to equal 1.5 the number of red giant brach stars.

This Master DG was generated in this way since it now allows for any type of DG to be drawn from the file efficiently, effectively drawing a smaller version of that larger DG. This can only be done on the condition that the $\sim$ 120 000 000 stars are randomised within the file such that when the file is read in from the beginning, it draws on average the right proportions of

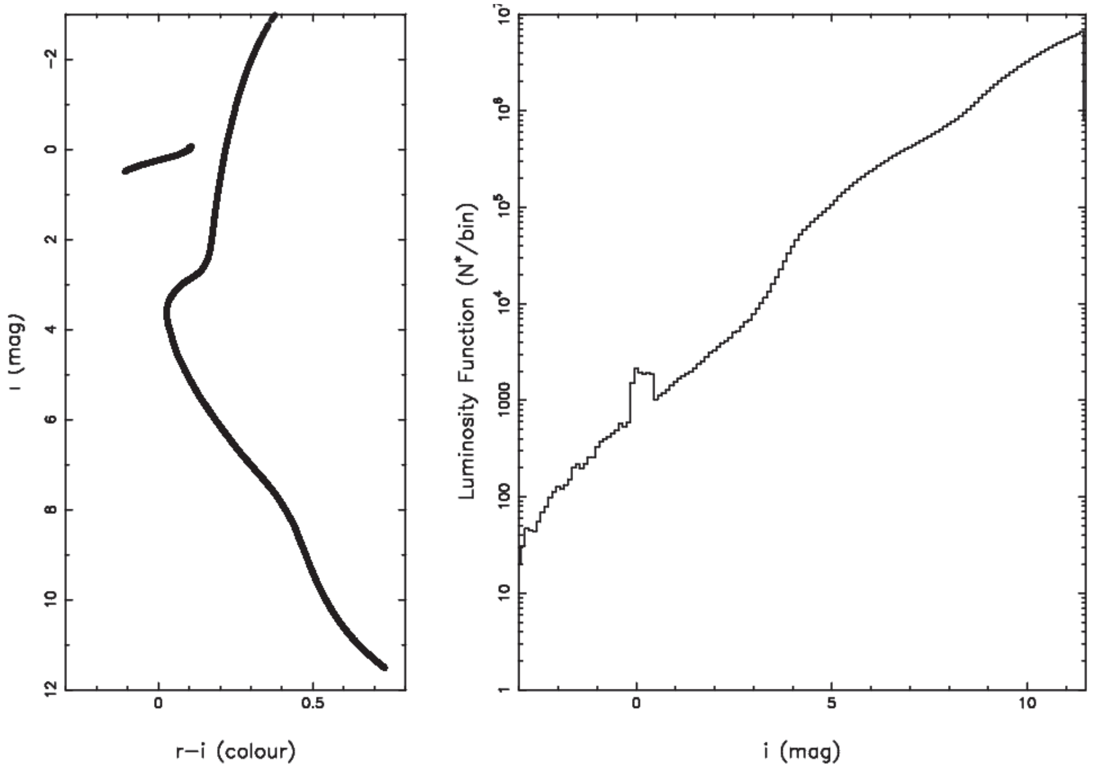

Figure 7.1 - *L*eft: CMD of Master DG (essentially a metal-poor and old isochrone: [Fe/H]=-2.0 and t=12 Gyrs) from which stars are drawn and scattered taking into account the photometric uncertainties. *R*ight: The luminosity function for the Master DG, describing the proportions by which to populate the isochrone with stars (left). The bump at $i \sim 0$ corresponds to the horizontal branch.

horizontal branch stars, main-sequence stars and red giant brach stars. Hence, once the fluxes have been summed and reach $M_V = x$, where x is the brightness of the galaxy we wish to generate, the file continues reading from where it left off, such that the second galaxy can be generated and so on. This means that each galaxy is generated from a different part of the file, until the end of the file is reached, in which case the generation of galaxies continues at the beginning of the file again. Having accounted for the magnitude of the galaxy we wish to generate, we can account for the distance, by converting the absolute magnitudes of the stars to apparent magnitudes using the distance–modulus equation. The final thing to do is to make the CMD realistic, since clearly the stellar evolutionary features of the satellite galaxy will not follow a pristine ridgeline. To do this, a similar approach to section 2.3.2 was adopted. In this section, the widening of the isochrone contour mask was described, taking into account the average photometric uncertainties in colour of the patch. Here, stars for a given magnitude bin are scattered in colour and magnitude using the median photometric uncertainties [4], thus creating a realistic CMD containing patch dependent photometric information. Figure 7.2 shows the photometry (completeness-corrected: see next section) for six simulated DGs, whose properties resemble those of six known DGs: Andromeda XV, Boötes I, Segue 1, Canes Venatici I, Leo IV and Coma Berenices.

---

[4] Note that here, contrary to section 2.3.2, an additional scatter term of $\sigma = 0.03$ is added in quadrature to the uncertainties, such that these inflated uncertainties better reflect the distribution of stars in known MW DGs.

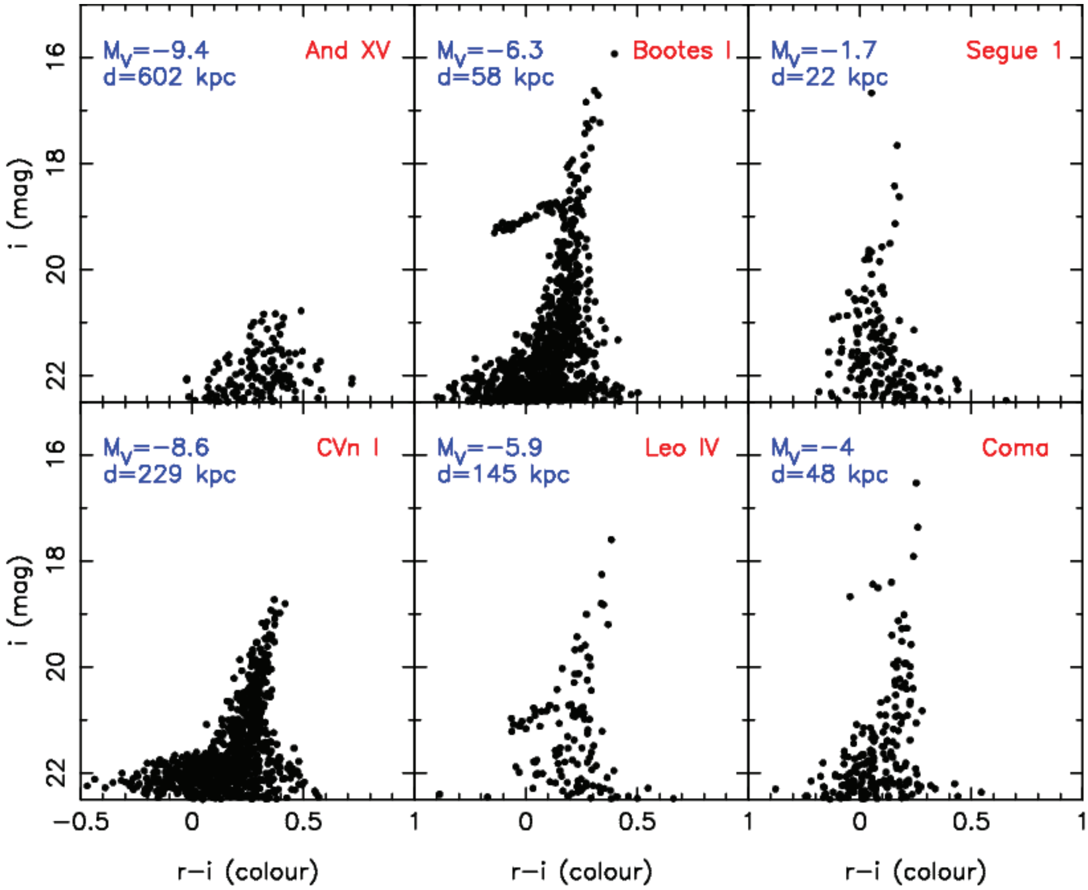

Figure 7.2 - CMDs of simulated DGs with properties that resemble six known DGs: Andromeda XV, Boötes I, Segue 1, Canes Venatici I, Leo IV and Coma Berenices. The magnitude and distances quoted are those of the simulated galaxies. With the exception of Segue 1 ($M_V = -1.5$), all of the magnitudes quoted are in fact those of the known dwarfs. The distances agree to within 10 kpc of the known distances as quoted in McConnachie (2012). Note that these CMDs are already completeness corrected (see 7.1.3 for further information).

7.1.3 Magnitude completeness

The PS1 coverage is by no means homogenous as already highlighted at various points throughout this thesis. This second aspect must be taken into account when satellite ingestion is performed. Failing to do so can bias or influence the recovery rate of satellite galaxies later on. Let us illustrate this with an example: assume we have a DG with certain properties which is ingested in different places. The galaxy is put at location 1 in the PS1 data, where $\sigma_i = 0.1$ at $i{\sim}21.0$ and location 2 where $\sigma_i = 0.1$ for a fainter magnitude, say $i{\sim}22.0$. Clearly location 1 is a place with poorer depth, since the photometric uncertainties increase more quickly with larger magnitude. In region 1, the chance of a star being observed at a faint magnitude is less high than in location 2. To account for this, the completeness of the PS1 survey can be modelled, with the following function:

$$c(mag) = \frac{A}{1 + exp^{\frac{mag - mag_0}{D}}} \tag{7.1}$$

where c(mag) represents the completeness as a function of magnitude, A is a completeness

Table 7.2 - CFHTLS Completeness parameters

	r-mag	i-mag
A	0.95	0.95
D	0.36	0.24
50% mag	23.36	23.02

factor, dominant at brighter magnitudes before the effect of the exponential starts to dominate. Finally mag_0 is the magnitude at which the completeness is 50%. To assess the completeness, the PS1 survey must be compared to a deeper survey, with which the fit can be made. Here, overlapping regions between PS1 and CFHTLS containing stars within ±0.4 degrees of (RA,Dec) $\sim$ (37.4, -6.0) were selected. The stars in the two different surveys are matched to one another using their spatial information and then binned in 0.2 magnitude bins. Unsurprisingly, this shows that the surveys broadly match at bright magnitudes, but at fainter magnitudes the number of stars matched relative to the total number of CFHTLS stars in the bins decreases. Using this information, the best-fit parameters are calculated using a χ^2 fit[5]. The parameters are shown in Table 7.2. The completeness fraction as a function of magnitude for the r (blue) and i-band (red) may be seen in figure 7.3, essentially a representation of the function as described in equation 7.1. Figure 7.4 shows the probability distribution functions of the parameters in equation 7.1.

Now that we have the CFHTLS-PS1 comparison, with the 50% completeness magnitude known, the value of mag_0 (from equation 7.1) can be offset according to the following:

$$mag_0 = i_{CFHTLS} - i_{PS1}(CFHTLS) + i_{PS1}(A) \tag{7.2}$$

where i_{CFHTLS} is the 50% completeness magnitude as a result of the PS1 and CFHTLS comparison, $i_{PS1}(CFHTLS)$ is the median i-mag at which $\sigma_i = 0.1$ for the PS1 observation of the CFHTLS patch and $i_{PS1}(A)$ is the median i-mag at which $\sigma_i = 0.1$ for region A where the galaxy will be ingested in PS1. To compute this all the ingredients are available except the last mentioned one: median i-magnitude for which $\sigma_i = 0.1$ in square A. Because the completeness can vary quite sharply over the sky, a patch-dependent factor cannot be computed because the 1600 degree^2 patches are too big. Instead, the usual patch is subdivided into 4 degree^2 subsquares. For each of these, the median i-magnitude at which $\sigma_i = 0.1$ occurs, is calculated. Figure 7.5 shows what this corresponds to for the usual patch centred on $(l, b) = (30°, 70°)$. As can be seen the $\sigma_i = 0.1$ uncertainty can vary from 22.6 to 21.9.

Finally, the CMD of the artificially generated DG can be corrected to take into account the completeness curve, i.e. the fainter the magnitude, the higher the fraction of stars that are not ‘observed’ and are removed from the CMD. Here again, the “acceptance-rejection” method can be used following the same logic as described before. Each star is randomly assigned a completeness factor between 0 and 1. For any given star of a certain magnitude, equation 7.1 can be used to find out the exact value of c(mag). If the random completeness factor is lower

---

[5] Note that Nicolas Martin did the fit.

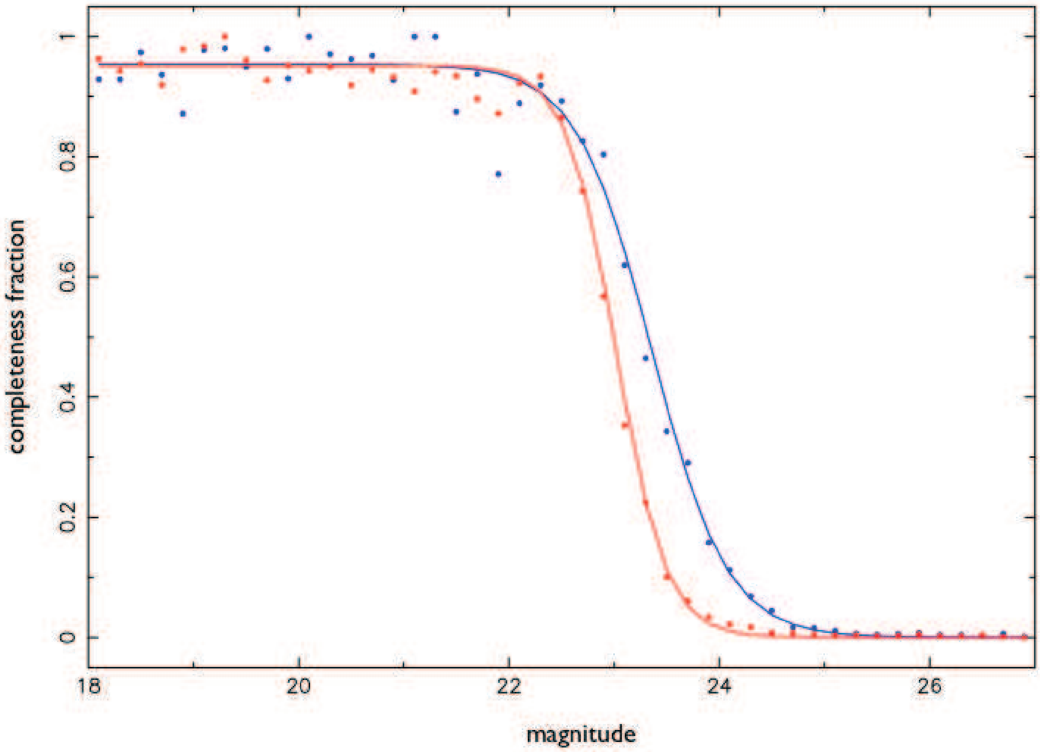

Figure 7.3 - The completeness as a function of magnitude, with blue representing the r-band and red showing the i-band. The dots represent the match between PS1 and CFHTLS sources in 0.2 magnitude bins, with the lines representing the best fit for the two bands.

than c(mag), the star is accepted, otherwise it is rejected.

7.1.4 Spatial distribution

With photometry generated (taking into account the photometric uncertainties), and the completeness accounted for, the final major step is to connect the remaining stars to positions on the sky [6]. To determine the stars' configuration the Plummer function (Binney & Tremaine, 2008) is used, given by the following:

$$f(r) = \frac{r}{(1 + \frac{r^2}{r_h^2})^2} \tag{7.3}$$

where r_h is the half-light radius of the system.

Using the Plummer function formulation the "acceptance-rejection" method is used for the final time, analogously to the completeness. Stars can be randomly drawn in Plummer – radius space and either accepted or rejected, depending on where they lie below or above the curve.

---

[6] Please note that no correlation between the stars' stellar evolutionary phase and their positions relative to the centre of the system is assumed.

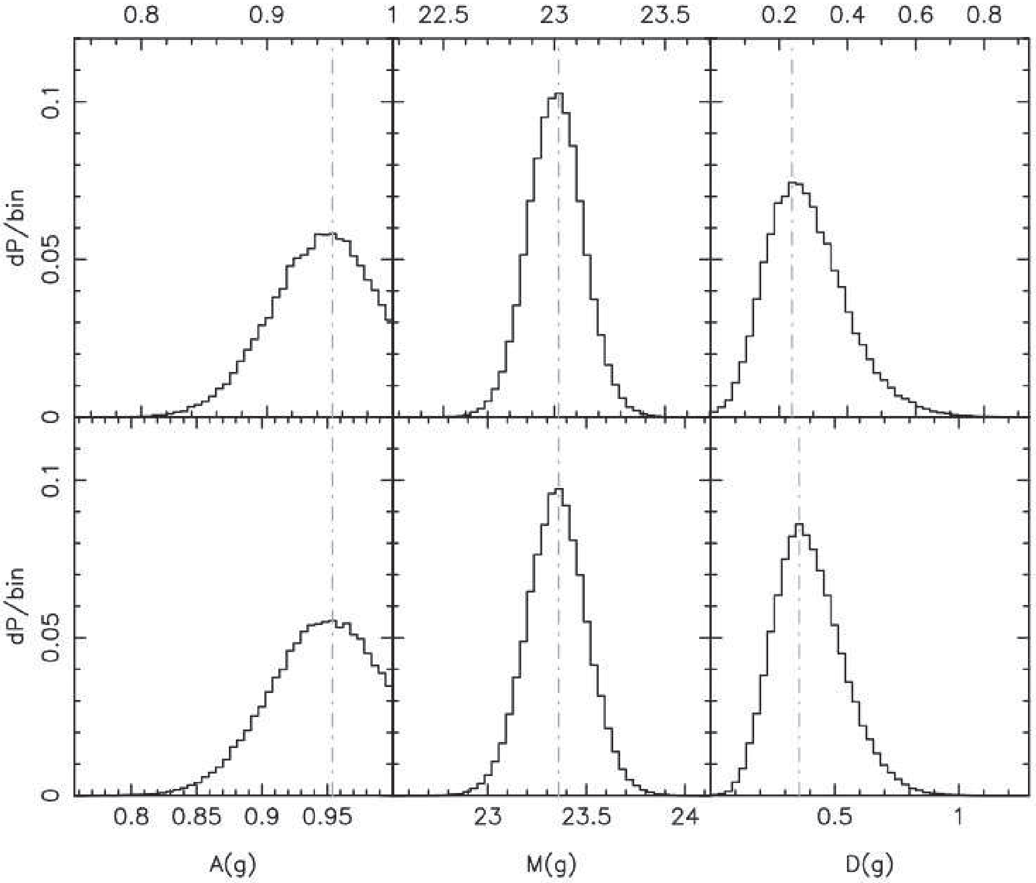

Figure 7.4 - The best-fit parameters for the completeness function parameters from equation 7.1 using the χ^2 fit.

This results in a peaked distribution of stars at the centre, dropping off with increased radius as defined by the Plummer formulation. This number of stars is generated until the number of stars surviving this cut equals the number of stars that survived the magnitude–cut. The last thing that remains to be done is to convert 1-D into 2-D by scattering the stars within an angle of 2π. This generates a 2D distribution of stars following the 1D Plummer curve.

7.1.5 Implementation over the PS1 sky

In this final section – before discussing the results – the specific implementation of this endeavour in the PS1 data will be detailed. Until now I have described how artificial galaxies are generated, but what is less clear is how to do this on an industrial scale and which galaxies to generate. How many galaxies are necessary to constitute a statistically significant sample? The answer to this question can only be answered when it is known which types of galaxies should be generated. For example, generating a Segue 1 look–alike at 150 kpc makes no sense as there is zero chance of finding it. As already touched upon in the introduction, Koposov et al. (2009) showed that in surveys such as the SDSS galaxies of this type can only be found out to $\sim 40 - 50$ kpc. Similarly, generating a "Sculptor" and placing it at 30 kpc would also be pointless as we know that something like this will always be retrieved by the search convolution (otherwise there is a serious problem!). Something more interesting to consider is for example taking Pisces II ($M_V = -5.0$, $r_h = 58$ pc and $d = 182$) and seeing how its recovery

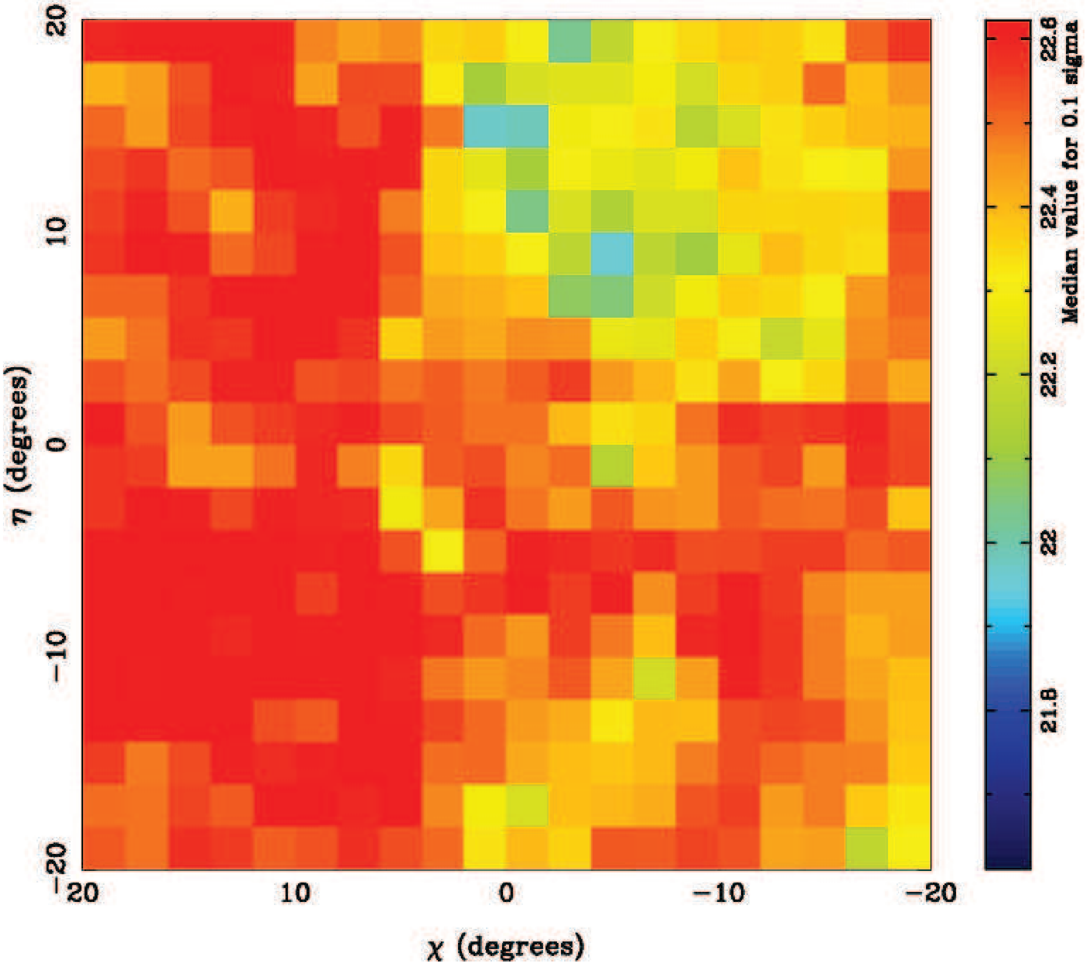

Figure 7.5 - The usual 1600 degree^2 patch, centred on $(l, b) = (30°, 70°)$, colour-coded by the median i-band magnitude at which the photometric uncertainty is $\sigma_i = 0.1$. This value in inserted into equation 7.2, which is in turn is inserted into equation 7.1, giving the completeness function, used to accept and reject "observed" stars.

rate is impacted by changing its size to $r_h = 120$ kpc or making it more diffuse or keeping it at its present size, but putting it further out, i.e. 300 kpc [7].

The most global parameter that can be used as a starting point is distance, since it will be necessary to generate artificial galaxies all the way out to M31 and slightly beyond, to quantify the recovery rate over the whole probe-able PS1 sky. Following the Koposov et al. (2008) approach, distances for artificial galaxies are generated in logarithmic space. The choice for this follows from the mathematical properties of a logarithm. If one draws between a range of $log_{10}(D) = 1.2$ ($d = 16$ kpc) and $log_{10}(D) = 3.01$ ($d = 1024$ kpc) this allows one to draw around the same number of satellites in bins that scale as factors of 2, i.e. the same number in each of the following bins: $16 < D < 32$, $32 < D < 64$, $64 < D < 128$... This has the convenient advantage that half of the ingested satellites will be in the inner 128 kpc. It would be a waste of available resources to generate half the satellites between 512 kpc and 1024 kpc, which probes a very small subset of parameter space, as the most likely galaxies to be found

---

[7] Both cases should coincide with a lower recovery rate.

Table 7.3 - 3–D parameter space (d, M_V and r_h) for which DGs are simulated

		16 kpc $< D <$ 32 kpc		32 kpc $< D <$ 64 kpc		64 kpc $< D <$ 128 kpc	
$M_{V,min}$	$M_{V,max}$	$r_{h,min}$	$r_{h,max}$	$r_{h,min}$	$r_{h,max}$	$r_{h,min}$	$r_{h,max}$
0	-1	10.0	63.0	10.0	63.0	–	–
-1	-2	10.0	100.0	10.0	63.0	–	–
-2	-3	10.0	158.0	10.0	100.0	10.0	40.0
-3	-4	25.0	398.0	10.0	251.0	10.0	158.0
-4	-5	40.0	631.0	25.0	398.0	16.0	251.0
-5	-6	63.0	631.0	40.0	631.0	63.0	1000.0
-6	-7	100.0	1000.0	100.0	1000.0	158.0	1000.0
-7	-8	–	–	158.0	1000.0	158.0	1000.0
-8	-9	–	–	251.0	1000.0	398.0	1000.0
-9	-10	–	–	–	–	–	–

		128 kpc $< D <$ 256 kpc		256 kpc $< D <$ 512 kpc		512 kpc $< D <$ 1024 kpc	
$M_{V,min}$	$M_{V,max}$	$r_{h,min}$	$r_{h,max}$	$r_{h,min}$	$r_{h,max}$	$r_{h,min}$	$r_{h,max}$
0	-1	–	–	–	–	–	–
-1	-2	–	–	–	–	–	–
-2	-3	–	–	–	–	–	–
-3	-4	10.0	63.0	–	–	–	–
-4	-5	10.0	158.0	10.0	158.0	–	–
-5	-6	10.0	631.0	10.0	158.0	–	–
-6	-7	100.0	1000.0	10.0	398.0	40.0	158.0
-7	-8	100.0	1000.0	25.0	1000.0	10.0	251.0
-8	-9	100.0	1000.0	158.0	1000.0	10.0	1000.0
-9	-10	–	–	158.0	1000.0	10.0	1000.0

here are bright and compact dwarfs. For each distance bin, 1.0 magnitude bins can be defined, within which half-light radius sizes may be drawn. These sizes are once again drawn in logarithmic space such that many more smaller objects will be drawn, which are preferentially more interesting as there is a higher chance of resolving these. Through trial and error, the parts of parameter space (M_V, r_h and d) that are the most interesting to probe are determined. This is done by starting with lenient limits for all three parameters and modifying these limits to narrower ranges until the parts of parameter space are identified which do not coincide with either definite 0% or 100% recovery rates. Figure 10 in Koposov et al. (2010), which shows magnitude versus size plots for seven different distance bins, colour-coded by recovery rate, also serves as a useful guide. Table 7.3 shows which parts of parameter space are probed.

Having defined the properties of the satellites, the final task is to ingest them into the PS1 data. To do this, random positions are drawn for the locations of these satellites in tangentially projected co–ordinates. Once an initial random χ and η position are drawn, the subsequent galaxies are positioned exactly two degrees further away. On one patch of the sky, 361 galaxies are ingested. This is an odd number of galaxies to ingest, but is as a consequence of the significance algorithm (see section 2.4), which ignored the outer most 1 degree to determine

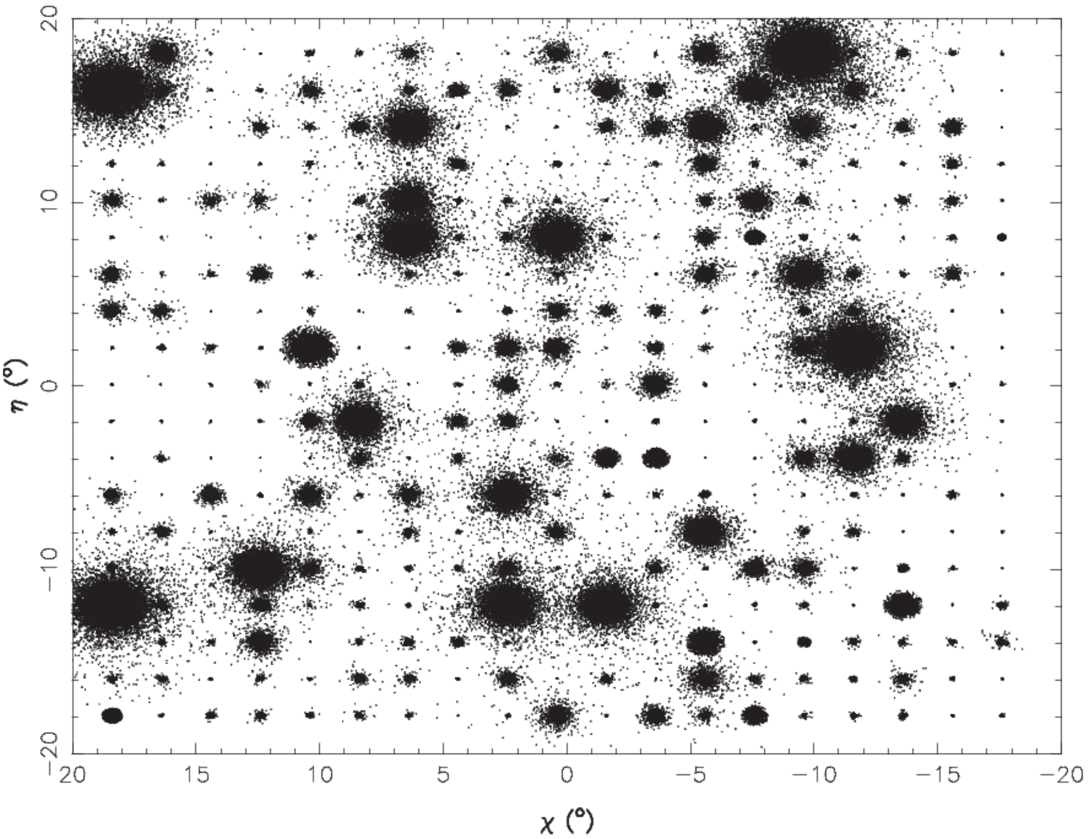

Figure 7.6 - Spatial distribution of 361 simulated satellite galaxies (completeness corrected) on the usual 1600 deg^2 patch. These are a variety of galaxies satisfying the galaxy parameters in Table 7.3. This process is repeated 20 times (20x361=7220 galaxies) per patch. No two galaxies are positioned in the same place, but are allowed to vary within one degree, such that recovery rates are not impacted, by for example the same bad pixel being targeted.

the significance i.e. for either $|\chi| > 19.0$ or $|\eta| > 19.0$. So, while 400 galaxies would fit on the patch, Instead 19x19 galaxies are placed. Figure 7.6 shows a selection of 361 galaxies (completeness-corrected) with varying sizes.

Let us now return to the question concerning the number of galaxies that need to be inserted into the data. Ingesting 20 times 361 galaxies per patch is enough to result in the order of ∼15–20 satellites per bin as quoted in Table 7.3. Though this number will vary as a function of the latitude[8], it number is high enough to sample parameter space convincingly.

The galaxies now have photometry $(r, r-i)$, position $(\chi,\ \eta)$ and have been completeness corrected for their location on the sky. The simulated galaxy properties are placed in the original stellar maps for which the convolution code was run. It took around 2 months to run the convolution search algorithm over the entire sky in PV2. Therefore a twenty–fold increase in the computational time would extend the timescale of the project quite considerably. The search algorithm code is therefore modified to increase its speed. This is done by realising that the search algorithm need not be run for every single pixel of the sky, since it is known where

---

[8] One would need a higher number of galaxies per bin at lower latitudes as they are more difficult to retrieve, as will be seen in Section 7.2.

the centres of those galaxies are. Hence, the search algorithm simply can be run just for those pixels of interest. For the 4′ and 8′ kernels, this is done for 9 pixels centred on the different galaxies. If 361 galaxies are placed and 9 pixels are calculated, this amounts to 3249 pixels for 361 different galaxies. The total number of pixels on the grid is 1 440 000. Hence just 0.2% of the pixels are calculated. For the 2′ kernel, the percentage of pixels calculated is also 0.2%, but a higher number of pixels will be calculated because of the finer grid that the 2′ kernel convolution needs for its calculation. The S/N is determined by dividing the calculated pixels by the noise maps that were calculated when the search algorithm was originally run.

7.2 Recovery results

7.2.1 High–latitude vs. low–latitude

With everything at hand to simulate artificial galaxies, we can now discuss the results that such simulations produce and compare these to the SDSS. Figure 7.7 shows the recovery rates of M_V vs. r_h for the six different distance bins, as quoted in Table 7.3. The top six panels show the recovery rate for the usual patch centred on $(l, b) = (30°, 70°)$ and therefore at high latitude, whereas the bottom six panels show the patch just below it, which is centred on $(l, b) = (30°, 35°)$ and therefore at low latitude. Squares containing black or white dots are regions that were assumed to be 100% or 0% recoverable, respectively and therefore not simulated. Both plots display trends which intuitively make sense. To first order, the satellites are more easily recoverable when the magnitude scales with distance, i.e. at larger distances, just the brightest satellites will be observed, whereas at nearby distances any satellite in a given magnitude bin will be observed. When folding in the size, the recoverability of a satellite of a certain magnitude at a given distance is also influenced: i.e. for nearby faint satellites, just small compact systems can be observed since otherwise for a wider distribution of stars on the sky, the system will be too diffuse to be resolved. At higher distances, the size plays less of a role as satellites are bright enough to be resolved no matter what the distance. At the distance of M31, the size interplay re–appears as the distance starts to impact the recoverability. The statements made so far are effectively a statement on surface brightness limits.

Let us now consider the effect that ingestion of satellites at different latitudes will have on their recoverability. Since, broadly speaking, the density of stars increases as $|b|$ decreases[9], the natural thing to expect is that the recoverability reduces. Even though many of the stars closer to the disc do not satisfy the isochrone mask criteria, the absolute number of these stars will mean that the DGs are more easily 'lost' in the data. If we consider Figure 7.7, then we can see that the global behaviour between high and low latitude patches agrees, but that areas that tend to 100% completeness at higher latitude are not yet 100% complete, but generally become 100% for the same size or distance, but in one magnitude bin brighter. To understand this better, consider the following properties: $32\,\mathrm{kpc} < D < 64\,\mathrm{kpc}$, $-4 < M_V < -3$ and $1.0 < log_{10}(r_h) < 1.8$. It can be seen that for the higher latitude patch, the recoverability is nearing or at 100%. At lower latitude, these pixel bins still fluctuate at values of $70 - 95\%$. The global change between high and low latitude is therefore around 0.5–1.0 mags. Hargis et al. (2014) point out that lower latitude is likely to impact detections of new DGs because

---

[9] This is not quite true, there are also variations in longitude, notably when approaching the bulge.

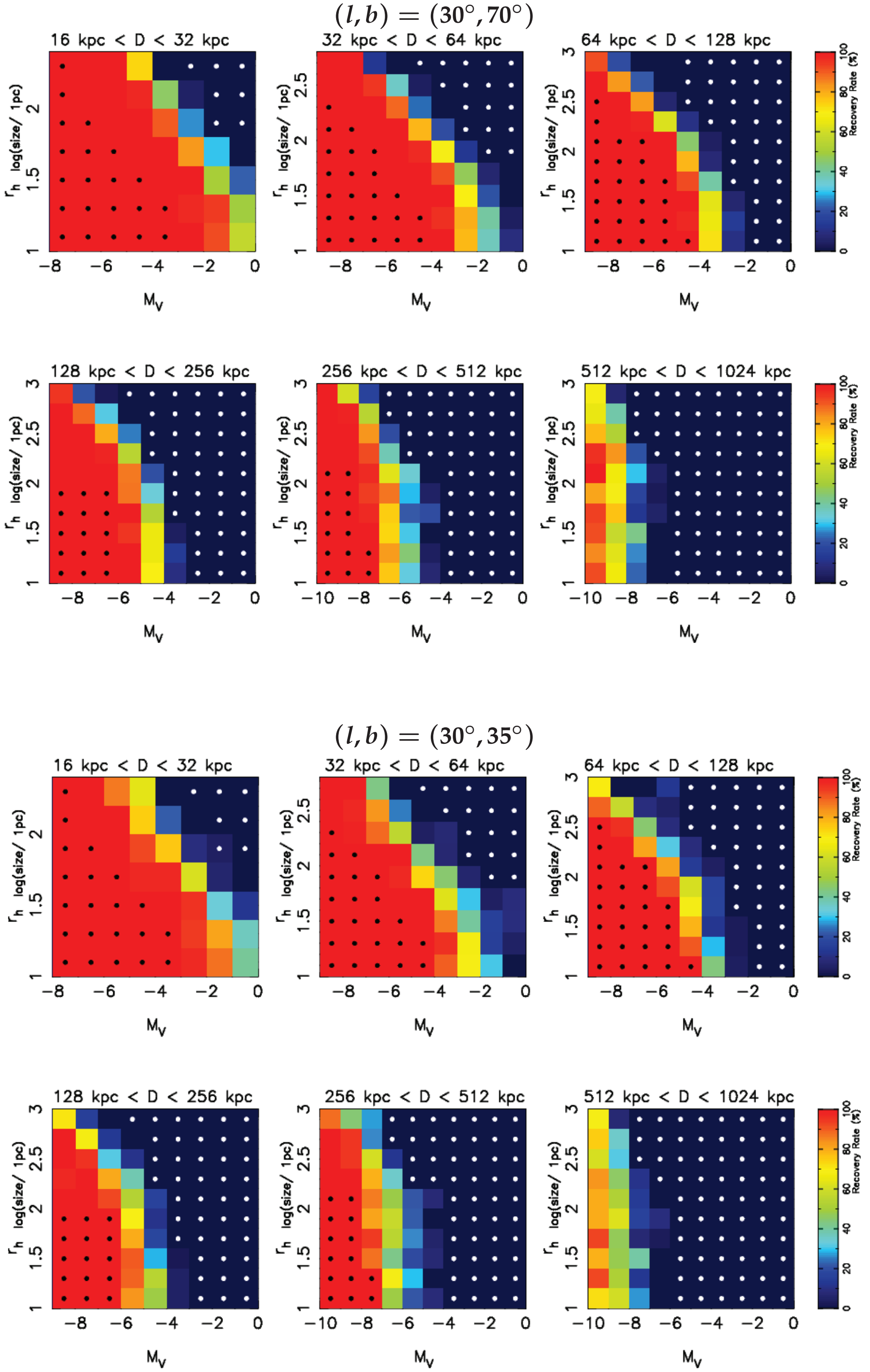

Figure 7.7 - Recovery rate for artificial galaxies simulated for a patch at high latitude: $(l, b) = (30°, 70°)$ and low latitude: $(l, b) = (30°, 35°)$ at the top and bottom respectively. The six panels indicate the six distance bins. Each panel contains the recovery rate for that distance bin for a given size (0.2 bins) and magnitude (1.0 bin). Black dots and white dots represent those regions that were deemed to be 100% or 0% complete respectively.

of higher contamination. Please see Appendix B for plots such as those in Figure 7.7 for the whole PS1 sky.

Table 7.4 - Structural parameters (M_V, r_h and D) of four SDSS dwarfs

	Segue 1	Boötes I	Leo IV	Andromeda IX
M_V	-1.5 ± 0.8	-6.3 ± 0.2	-5.8 ± 0.4	-8.1 ± 1.1
$r_h(pc)$	29^{+8}_{-5}	242 ± 21	206 ± 37	557 ± 29
r_h (′)	$4.4^{+1.2}_{-0.6}$	12.6 ± 1	4.6 ± 0.8	2.5 ± 0.1
D	23 ± 2	66 ± 2	154 ± 6	766 ± 25

7.2.2 Recovery rates of 4 SDSS satellites in PS1

Although the recovery rates in Figure 7.7 instinctively make sense, another useful test which can be easily done is to check the recoverability of some typical satellites. The main question that we wish to answer is how well a satellite with properties: $M_V = x$, $r_h = y$ and $d = z$ can be recovered and how much this is a function of its place in the sky. To do this, four satellites of various properties are chosen, which occupy different parts of parameter space. These satellites are Segue 1, Boötes I, Leo IV and Andromeda IX. The properties, as a reminder, are provided in Table 7.4.

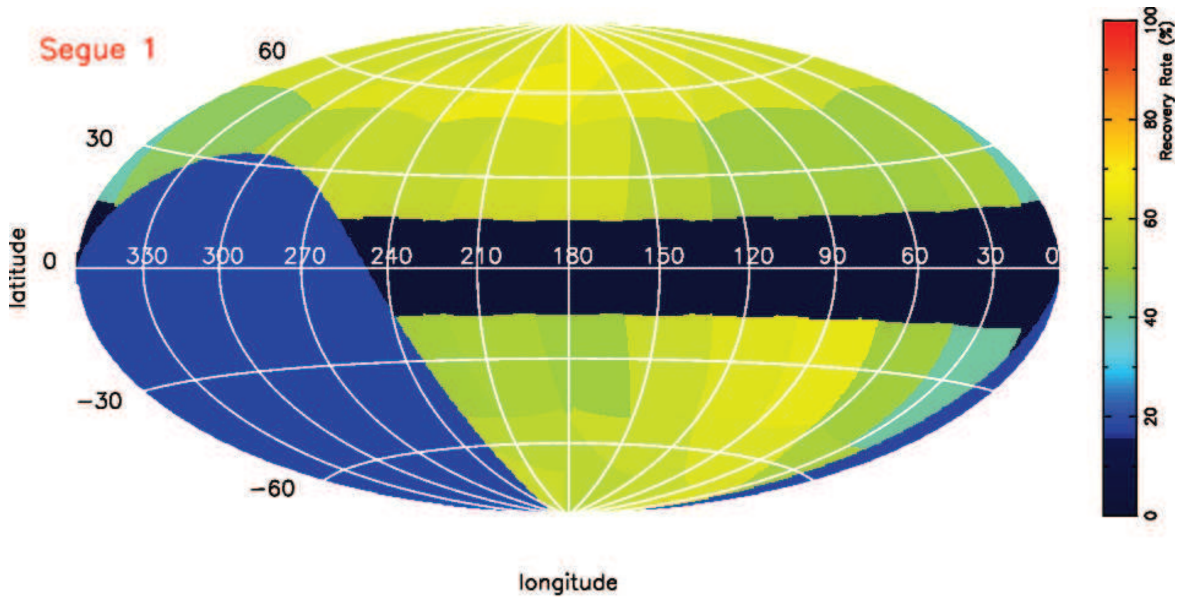

Figure 7.8 - Recovery rates of a Segue 1 like satellite over the whole sky. These recovery rates range from ∼ 39% near the bulge to ∼ 63% in halo regions. Dark blue reflects regions near the disc, where the recovery efficiency will be run in the future ($|b > 5°$). Lighter blue corresponds to those parts where PS1 does not observe.

The recoverability may be assessed by carrying out the following steps. Using the properties in Table 7.4, new properties, resembling these satellites, may be randomly drawn by sampling

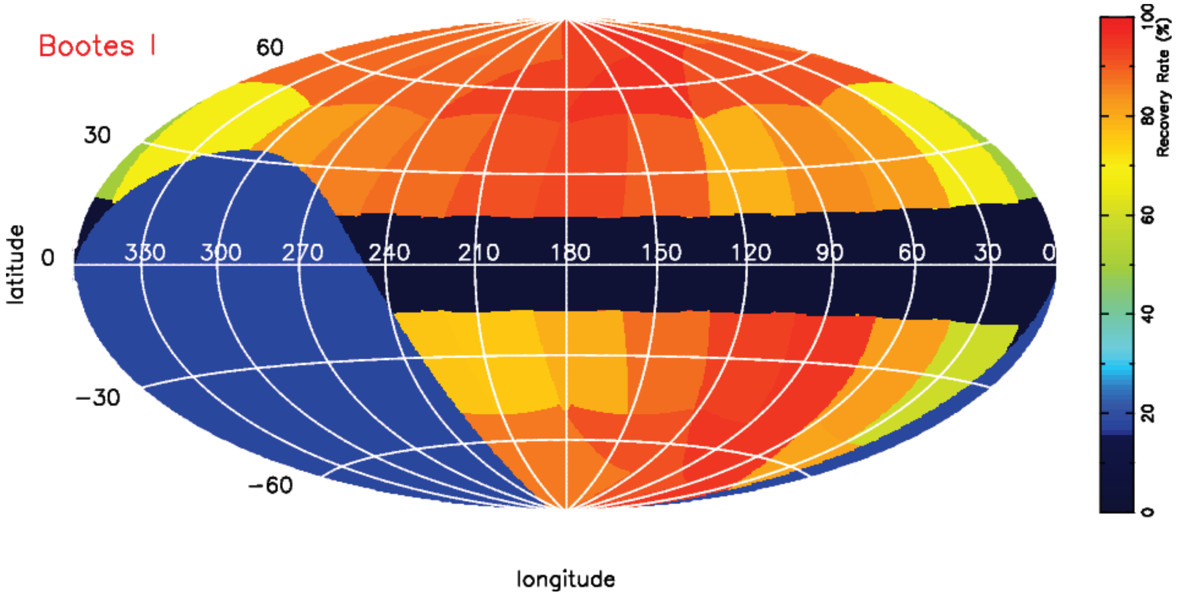

Figure 7.9 - Recovery rates of a Bootes I like satellite over the whole sky. These recovery rates range from $\sim$ 49% near the bulge to $\sim$ 96% in halo regions. Dark blue reflects regions near the disc, where the recovery efficiency will be run in the future ($|b > 5°$). Lighter blue corresponds to those parts where PS1 does not observe.

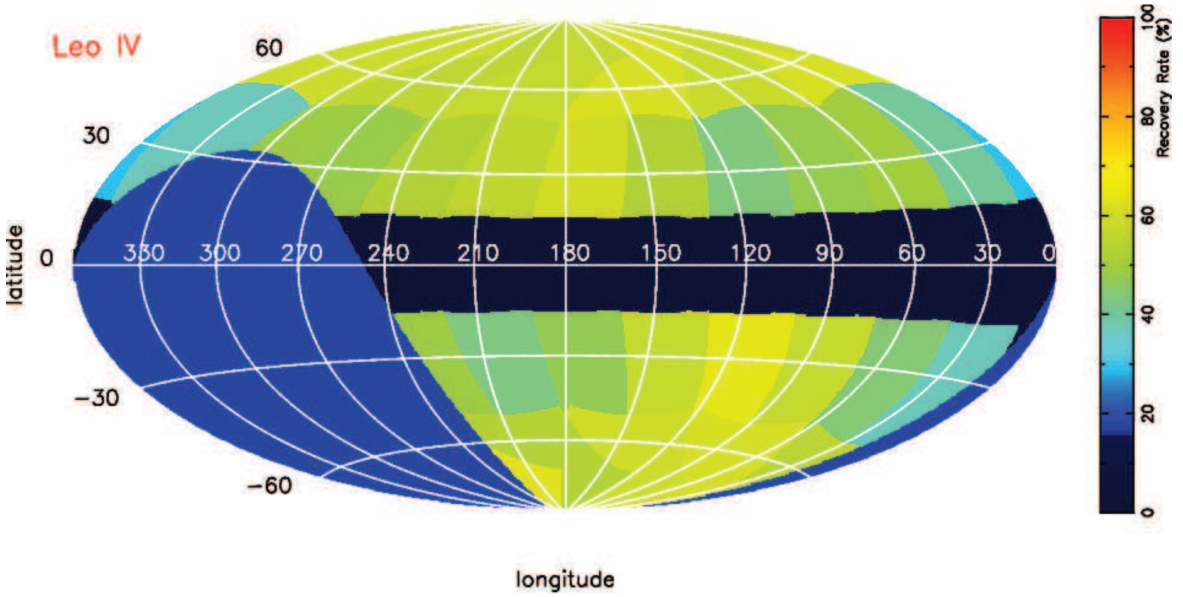

Figure 7.10 - Recovery rates of a Leo IV like satellite over the whole sky. These recovery rates range from $\sim$ 30% near the bulge to $\sim$ 64% in halo regions. This plot looks similar to Segue 1, but noticeably under performs in some areas relative to Segue 1, where the distance of Leo IV and therefore the depth of the survey come into play resulting in a lower recovery rate. Dark blue reflects regions near the disc, where the recovery efficiency will be run in the future ($|b > 5°$). Lighter blue corresponds to those parts where PS1 does not observe.

their uncertainties. Such a sampling can be done for each part of the PS1 sky. Using an Aitoff co–ordinate system, we can define 1 degree^2 pixels for which we can randomly draw the properties. For the given pixel, the galactic co–ordinates can be computed through a simple reverse Hammer Aitoff projection. Using the computed co–ordinates, the relevant

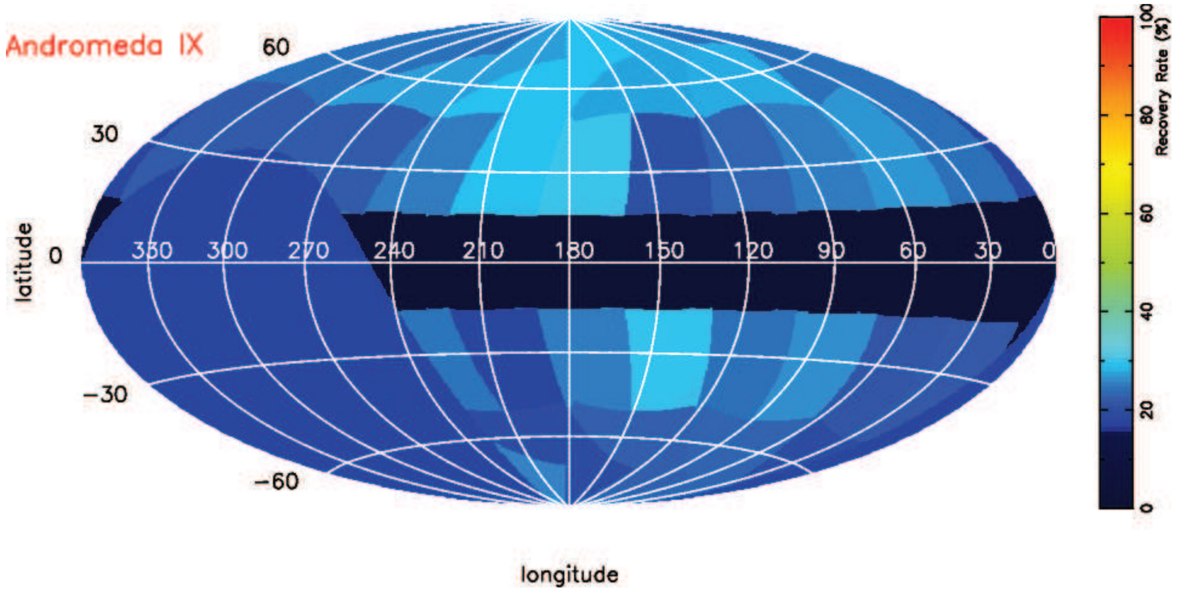

Figure 7.11 - Recovery rates of an Andromeda IX like satellite over the whole sky. These recovery rates range from ∼ 17% near the bulge to ∼ 30%. At the distance of M31, the differences between recovery rates in the various patches reduce as the distance sets the recovery rates to very similar values over the whole sky. Andromeda IX was chosen because of its discovery in the SDSS and therefore has features that are possible to resolve in PS1. Dark blue reflects regions near the disc, where the recovery efficiency will be run in the future ($|b > 5°$). Lighter blue corresponds to those parts where PS1 does not observe.

1600 degree^2 patch can be found. For this patch, the pixel as was seen in Figure 7.7 can be found, i.e. the distance, size and magnitude that the drawn properties satisfy. The recovery fraction can thus be determined. For pixels, in galactic co–ordinate space, which are found in more than one patch (e.g. at the boundary between two patches), the higher recovery rate is taken. The values are then averaged out for a given patch to give a general recovery rate for a particular satellite whose properties were randomly drawn.

The result of this operation may be seen in figures 7.8, 7.9, 7.10 and 7.11 over the entire PS1 sky ($|b| > 15°$). The values of this graphical representation for each of the four satellites can be seen in Table 7.5. Several general trends for these satellites are apparent. The recoverability of the four satellites is at its greatest in the halo regions (e.g. $|b| > 55$). These are 66.2%, 95.8%, 63.7% and 30.5% for Segue 1, Boötes I, Leo IV and Andromeda IX (table 7.5 indicates, in bold, which patch has the maximum recovery rate). The highest recovery rates are in the Northern halo (Segue 1, Boötes I and Andromeda IX) and the Southern halo patch (Leo IV), which is logical because the contamination from the Milky Way (MW) is at its lowest here. The greater distance at which Andromeda IX lies indicates that contamination can be less of an issue as the main features of the dwarf at its distance are so faint that the search algorithm ignores the contamination. This explains the smaller fluctuation in recoverabilities between the different patches. Conversely at those regions closest to the disc and especially near the bulge, the recovery rate plummets quite impressively. For all four satellites, the recovery rate is at its lowest in the patch centred on $(l, b) = (0°, 35°)$. These recovery rates are: 39.1%, 48.6%, 29.9%, 17.0% for Segue 1, Boötes I, Leo IV and Andromeda IX. The recovery rates of the individual satellites with respect to each other also make sense. The satellite with the highest recoverability is Boötes I, which concurs with its brightness relative to its distance, even if

Table 7.5 - Recovery Rates for Segue 1, Boötes I, Leo IV and Andromeda IX-like satellites

Co-ordinates		Recovery Rate (%)			
l	b	Segue 1	Bootes II	Leo IV	Andromeda IX
0	35	39.1	48.6	29.9	17.0
30	35	49.1	68.3	41.0	23.0
60	35	48.9	82.5	50.7	26.7
90	35	51.4	83.9	48.2	24.8
120	35	47.8	78.5	42.7	22.6
150	35	55.8	90.8	52.1	18.6
180	35	59.8	93.3	59.0	30.2
210	35	60.2	90.7	55.2	27.9
240	35	56.6	88.7	52.6	25.0
270	35	57.1	85.9	47.7	24.6
300	35	52.9	82.3	48.3	21.2
330	35	47.0	69.5	36.6	23.6
30	-35	39.8	58.3	37.6	24.1
60	-35	48.5	80.4	45.1	21.0
90	-35	64.4	94.4	57.5	23.2
120	-35	62.7	92.5	63.4	24.9
150	-35	57.6	87.4	60.8	27.2
180	-35	48.6	79.4	47.4	25.1
210	-35	50.8	75.7	43.4	18.6
240	-35	49.2	74.8	50.8	26.0
30	70	63.0	89.4	60.4	22.8
90	70	61.8	91.4	59.5	28.1
150	70	63.2	**95.8**	62.4	28.6
210	70	**66.2**	93.1	59.4	**30.5**
270	70	61.8	89.2	56.1	25.5
330	70	58.7	88.5	59.5	23.6
30	-70	52.6	83.1	57.4	17.0
90	-70	63.3	94.3	60.5	25.7
150	-70	57.9	91.2	58.1	22.5
210	-70	55.2	88.1	54.1	19.8
270	-70	55.2	87.2	**63.7**	25.7

it is very large. The lowest recoverability is Andromeda IX, which is impacted by its large distance, therefore only recovered with 30% at best. It is worth noting that some of the highest recoverable regions are actually in the vicinity of M31, therefore boosting chances of finding satellites near M31 in the future, especially with the extra depth from PV3. The recoverability of Segue 1 and Leo IV is quite similar. An Interesting feature to note about the recoverability of these satellites is the discrepancy in the recovery rates for some parts of the sky where shallower depth impacts Leo IV (due to its larger distance) a lot more than Segue 1, e.g. $(l, b) = (210°, -35°)$. In general, this patch and the two other adjacent patches seem to have low recoverability which could not only be due to shallow depth, but also dust which extends further in these regions. This could cause holes in the data, which impact the recoverability.

There are two caveats worth pointing out at this point in the discussion. The recovery rate plots are a good indicator of global trends such as the ones already discussed (e.g. high latitude versus low latitude or bulge vs. anti-centre). The illustration of the recovery rate would be better served by adopting a different way of binning the recovery rate. As can be seen from the figures, the recovery rates are in some sense a statement of the geometry of the search algorithm i.e. the 1600 degree^2 patches. Ideally smaller squares, such as 5 by 5 degree^2 patches, would be used. This would be more elegant as it would take into account the density of stars near the disc and bulge and the small scale variations in the halo for example. As was already discussed, in the case of the patch centred on $(l, b) = (0°, 35°)$, this would provide a different picture, because at higher latitudes in this patch, the recovery rate would appear higher than it currently does. Similarly at very low latitude in this patch, the recovery rate would be lower. The reason why this was not done, is that the number of galaxies ingested to do this would need to be a lot higher: at least a 500% increase in the number of galaxies ingested. This is a direct result of sampling a smaller area where enough galaxies of the satellites' properties need to be ingested. We did not consider ingesting more galaxies because of time constraints as well as the intermediate nature of the PV2 data (it is worth spending this time on the final PV3 data). The second caveat is that this recovery rate is probably a little optimistic. Remember that 10–20% of PV2 data suffer from a photometric scatter of 0.1–0.2 mags, especially at the faint end. The photometry of the simulated galaxies does not take this into account, since, a priori, we do not know which regions have this scatter and which do not. In other words, the simulated photometry more or less assumes a data set with forced photometry. The recovery rates are therefore boosted by some undetermined, but probably small factor.

A form of comparison can be made between the PS1 and SDSS efforts. For this, I refer the reader back to the Koposov et al. (2008) paper. The global trend is that the recovery rates are lower in PS1 than SDSS. Table 2 of Koposov et al. (2008) shows a recovery rate of 100%, 100% and 79% for Segue 1, Boötes I and Leo IV (a recovery rate for Andromeda IX is not quoted). In the best cases for PS1, we have seen that these are $\sim$ 66%, 96% and 64% for those three satellites. I argue that the results of PS1 are broadly consistent with SDSS, when taking into account the difference in methodology used and the changes in structural parameters of the satellites since the Koposov et al. (2008) paper was published. While the recovery rates are lower than the SDSS, the recovery rates in Figure 10 Koposov et al. (2008) shows that these parts of parameter space are always on the border with the region where the recovery rate starts to decrease, something which is also pointed out by the authors in the caption of the corresponding figure. Figure 10 of the paper shows the recovery rate of the entire SDSS survey, with the three satellites positioned at the places with the structural parameters that were known at the time. These structural parameters have since changed as more follow–up has since been acquired. For example, Boötes I with 66 kpc would sit in the distance bin $64\,\mathrm{kpc} < d < 128\,\mathrm{kpc}$ rather than the $32\,\mathrm{kpc} < d < 64\,\mathrm{kpc}$ bin where it is shown now in the figure. The recovery rate is lower in these cases and fits with the PS1 recovery rate. Furthermore, the Koposov et al. (2008) paper does not sample the uncertainties of the measurements of the satellites' structural parameters. Therefore in many cases, the structural parameters coincide with 100% pixels, whereas, if the uncertainties had been sampled, the recovery rates would be lowered.

7.3 The route to quantifying (an)isotropy of the MW satellite distribution

The chapter thus far has provided a detailed outline of how the search efficiency can be quantified. Initial results show clearly what impact latitude and depth have on the recovery rate of some typical SDSS satellites. This has therefore provided a snapshot of something that can be done on an industrial scale for PV3. This effort will be used as a stepping stone towards re–deriving the luminosity function of MW satellites and quantifying the (an)isotropy of the spatial distribution of the MW satellites.

From our efforts in PS1, there are several factors which can point towards the anisotropic distribution of MW satellites. A very rough calculation, based on Figures 1.6 and 2.1 would show that the search volume in PS1 has been increased by a factor of ~ 1.6 relative to the latest SDSS DR or by a factor of ~ 2 relative to the published original searches in DR5 and DR6, which only concentrated on the Northern galactic hemisphere and the Segue stripes in the Southern galactic hemisphere. Though in total coverage PS1 is at least twice that of the SDSS, the increase in area is smaller because of the search algorithm not being able to target regions at $|b| < 5^{\circ}$ because of the very high density of stars near the disc. Even in regions near the bulge where the search algorithm stopped at $|b| = 5^{\circ}$, the density was probably getting too high to efficiently deliver any results. An over–simplified calculation, assuming isotropy, the number of SDSS satellite discoveries and equivalent search depth [10], would point towards a PS1 discovery rate of ~ 10 DGs. We currently have five new discoveries. It is interesting to further note the nature and location of these satellites. Two of these are almost certainly GCs and the other three are ambiguous. The two GCs are probably young outer halo GCs. Laevens 1 sits very close to Leo IV and Leo V (~ 20 degrees away), whereas Laevens 3 is not so distant from Kim 2, Pegasus III and Pisces II, i.e. in the plane of satellites. According to Pawlowski et al. (2012) the Vast Polar Structure (VPOS) also includes the young outer halo GCs. The locations and distances of Laevens 1 and 3 are perfectly consistent with such a plane. The other three discoveries also all happen to be in places that don't challenge the validity of the plane too much. Draco II and Triangulum II all lie near ($d < 30\,\mathrm{kpc}$) the MW centre. Their locations will therefore not impact the fitting of a plane, which is driven by the more distant, brighter satellites. The location of Sagittarius II is ominous as its position puts it outside of the plane. Without a proper analysis, it is unclear how its distance ($\sim 65 - 70\,\mathrm{kpc}$) will impact the VPOS. The investigation of the satellite's association with the Sagittarius stream will further shed light on this matter. Finally, the lack of discovery of very bright satellites with similar properties to Boötes I, Canes Venatici I or Ursa Major II could help reinforce the observations of anisotropy.

It therefore seems that there is first of all a paucity of the number of satellites, though we have not looked in PV3 (and with forced photometry) and that the locations or distances do not greatly challenge anisotropy. The first thing to do with the efficiency maps in PV3 is to re–determine the luminosity function of the MW satellites. The Koposov et al. (2008) paper derived the luminosity function for the MW satellites through binning the galaxies discovered in SDSS in magnitude space and correcting for the number density of satellites in those magnitude bins by using the information of the search efficiency to boost the number density up to account for the total volume. At the time the paper was published the number

---

[10] This is more or less true for PV2 and will definitely be the case for PV3.

of SDSS satellites and the VPOS had not yet been postulated [11]. The luminosity function that Koposov et al. (2008) determined for the whole sky was for DR5, which roughly covers 1/5 of the sky. They therefore extrapolated the luminosity function by multiplying by five to account for the whole sky search volume. This assumption inherently assumes isotropy. Another caveat to the whole Koposov et al. (2008) analysis is the use of a combination of MW and M31 satellites to determine the luminosity function at the bright end. This assumption, which was valid at the time because many M31 satellites had not yet been discovered in PAndAS for example, is now flawed because the satellites population of M31 greatly differs to that of the MW[12]. This approach would have boosted the number of satellites by too much at the bright end, while also increasing them too much at the faint end because of the multiplication by five, assuming isotropy. Re–deriving the luminosity function, taking into account anistropy (if robustly confirmed), will be a first step to carry out in PV3.

To derive a luminosity function, it will be necessary to first (dis)prove the plane of satellites. There are several things that should be done to assess the distribution of MW satellites. A first step that could be taken is to make numerous realisations of the satellites' distances by fixing their positions and drawing a distance by sampling the uncertainty. The data could then be binned and compared to the VPOS disc to assess the relative thickness of these realisations. Similarly the distances could be fixed, but the positions randomised by some angle and the binning exercise repeated to assess how different these two bins are through a chi squared fit. The analysis described would have to also fold in the detection efficiency to account for selection effects.

---

[11] Though as was seen in the Introduction, other papers had been making the case for decades.

[12] In fact, even though M31 is more distant than the MW, prior to 2014, the number of M31 satellites known was higher than for the MW, further reinforcing the view that the MW and M31 satellite populations differ significantly: M31 has many more bright satellites.

Chapter 8

Summary and outlook

"Never look backwards, or you will fall down the stairs", Rudyard Kipling

8.1 Summary

In this section, I would like to summarise the work that was presented in this PhD thesis and highlight its key results..

CHAPTER 2 – AN AUTOMATED SEARCH FOR LOCAL GROUP SATELLITES WITH PAN-STARRS 1 3π. In this chapter I outlined the convolution search technique, allowing for an automated search of stellar substructure in the Local Group. The search technique is largely inspired by those developed in the SDSS (Koposov et al., 2008; Walsh et al., 2009). This technique consists of inspecting the 4–dimensional parameter space of age, metallicity, distance and size to determine the most probably parts of this parameter space that Local Group satellites occupy, hence maximising the search technique efficiency. The first step consisted of using age and metallicity information as a means of isolating the most likely candidate stars for a satellite. We saw that a combination of old and metal–poor isochrones corresponding to $t = 8, 13$ Gyrs and $[\mathrm{Fe/H}] = -1.5, -2.27$, allow for an isochrone contour mask to be defined. Accounting for photometric uncertainties, this contour mask is widened in the colour direction. Stars are deemed potential candidate stars if they lie on this contour, other stars are simply excluded for any further analysis. The second step consisted of accounting for the distances of the potential satellite, by shifting the isochrone mask in $\mu = m - M = 0.5$ steps from $\mu = 17$ – around the distance of Segue 1 – out to the distance of M31 and beyond ($\mu = 24.5$). This allows for features such as a horizontal branch, a red giant branch or a main–sequence to be identified at different distances. Finally, the isolated stars, for a given distance are convolved with two Gaussians. The first Gaussian is tailored to the size of the potential satellite (2′, 4 and 8′), whereas the second one is far larger (28′–56′) to account for the slowly varying galactic background. Subtracting one map from the other reveals maps of local under and over densities. This operation is performed for three different satellite kernel sizes and for sixteen distance-moduli, resulting in 48 operations.

At the beginning of chapter 2, we saw that three additional elements need to be taken into account when performing this analysis. The first was the adaptation of this technique to manageable sizes of data. It is impossible to run a search technique in one single go on the entire PS1 catalogue. Not only would it be very confusing to keep track of the entire operation, the memory issues would be enormous. Hence, the operation was performed on 1600 degrees^2 patches in local tangentially projected co-ordinates, centred on b=±35°, ±70° for PV1 and later extended to include lower latitude patches probing regions all the way down to $b = \pm 5°$ in PV2. The second issue that needed to be taken care of was the star–galaxy separation. A combination of a PS1 flag (stellar) and a psf-ap cut (galaxies) was used to isolate stars and galaxies. Finally, the spatial inhomogeneity, as a result of bad weather, chip gaps etc. was taken into account when performing the convolution technique. Specifically, normalisation factors were introduced to artificially boost the counts to account for regions of the sky that had patchy or bad coverage. Prior to analysis, all magnitudes were de–reddened to account for dust.

The convolution maps for every given distance and kernel size were converted into statistical significance maps. For a given patch, a master significance map was created, combining the information of the 48 operations. This was achieved by stacking all the S/N maps, such that for every pixel the maximum S/N was retained. The entire technique was performed twice: once on a stellar map and a second time on a galaxies' map. The former was used to obtain a list of significant detections over the whole PS1 sky, while the latter was used to cross–reference those detections to exclude any that appear significant in both maps. These are eliminated from the list since they are background galaxies or galaxy clusters that were picked up in the stellar map. A threshold for which to investigate significant detections was decided by assessing the significance of known SDSS satellites in both maps. Ursa Major II had the highest galaxies' count relative to the stellar counts (30%) and a threshold of $\sigma_{stars} > 3 \times \sigma_{gals}$ was decided. Finally, the list of detections was cut at $\sigma_{stars} > 4.5$ such that most of the SDSS satellites are 'detected' and thus any other new satellites that may have similar properties.

CHAPTER 3 – DISCOVERIES IN THE PAN-STARRS 1 3π SURVEY. This chapter comprised two main parts: the first detailed the various follow–up efforts that were conducted in search of new satellites. The second part provided some background information and science regarding the eight discoveries made in PS1 so far.

Just under 100 hours of telescope time were devoted to the follow–up of candidate Milky Way (MW) satellites. Since a major part of the new PS1 coverage (relative to the SDSS) is in the South, our efforts focused more on the Southern hemisphere. Therefore, we spent 70 hours of Wide Field Imager (WFI) time on the MPG's 2.2m telescope in La Silla. This follow–up campaign yielded no new discoveries. The 70 hours campaign was based on PV1 (50 hours) and PV2 (20 hours) data. This instrument was however used to confirm the presence of our first MW discovery: Laevens 1 with Director's Discretionary Time (DDT). We spent 20 hours using BUSCA on the 2.2m telescope at the Calar Alto Observatory. The data from this search have still not been reduced to date. Though it is unclear what these images contain, I suspect the chances are low of this campaign yielding new satellites because the same PS1 data version (PV1) was used as the basis for further follow–up at Calar Alto. We spent 3 hours at the Large Binocular Telescope (LBT) and have been awarded a further four hours. The last LBT campaign was intended for M31 follow–up. Since M31 is further away, this motivated the choice of a larger telescope. Among the M31 candidates, a MW candidate was also followed–up. While the M31 candidates came back negative, the LBT follow–up yielded our second MW discovery: Triangulum II.

The latter half of this chapter expands on the M31 and MW PS1 discoveries, last of which are subjects of chapters 3, 4 and 5. The three (spectroscopically confirmed) discoveries around M31 of Lacerta I, Cassiopeia III and Perseus I, led by Nicolas Martin were described briefly (Martin et al., 2013b,a, 2014). The next discovery, receiving much of the attention of this chapter is that of Laevens 1, also known as Crater, because of its controversial nature in the literature. This satellite was discovered concomitantly in PS1 and VST Atlas. Belokurov et al. (2014) favoured a DG interpretation for the satellite, whereas our paper favoured a young outer halo GC classification. The rationale behind a a DG classification, for the Cambridge team, was the presence of a number of bluer stars, brighter than the Main–Sequence and near the red giant brach. They propose that these stars could be blue–loop stars and indicative of recent star formation, therefore excluding a GC. Our paper argued that the new stellar system was entirely consistent with the class of young outer halo GCs. Its structural parameters, such as its size and the red horizontal branch, among others, further reinforce this view. The satellite has been the subject of a couple of papers, most notably Kirby et al. (2015), who measured velocities of this satellite and confirmed that the "blue–loop" stars were not member stars and that the cluster did not lie on the metallicity–luminosity relation, expected for DGs. This chapter concluded by briefly mentioning the discoveries of Triangulum II, Sagittarius II, Draco II and Laevens 3, as a result of PV2 data.

CHAPTER 4 – DISCOVERY OF THE MOST DISTANT MILKY WAY GLOBULAR CLUSTER. The discovery of the most distant MW GC: PSO J174.0675–10.8774, Crater or Laevens 1 is detailed in this chapter. The stellar system lies at a galacto–centric distance of $145 \pm 17\,\mathrm{kpc}$ at the following co–ordinates $l = 274.8^\circ, b = 47.8^\circ$. Its size and magnitude are $20 \pm 2\,\mathrm{pc}$ and -4.3 ± 0.2 respectively. Isochrone fitting yielded a best–fit age of ~ 8 Gyr and $[\mathrm{Fe/H}] \sim -1.9$. In the size–luminosity plane, the satellite sits at the outer edge of the GC distribution, just before the "valley of ambiguity". The satellite sits close to Pal 14, with which Laevens 1 shares many similarities.

CHAPTER 5 – A NEW FAINT STELLAR SYSTEM IN THE CONSTELLATION OF TRIANGULUM. The second PS1 MW stellar system to be discovered lies at low–latitude at $l = 140.9^\circ$, $b = -23.8^\circ$ in Triangulum. The satellite lies at a galacto–centric distance of $36 \pm 2\,\mathrm{kpc}$ and has $r_h = 34^{+9}_{-8}\,\mathrm{kpc}$ and $M_V = -1.8 \pm 0.5$. These structural parameters, along with derived metallicities and ages of $[\mathrm{Fe/H}] \sim -2.2$ and $t \sim 13$ Gyrs, place this object in the realm of the Segue 1, Willman 1, Bootes II and Segue 2 stellar systems. The satellite lies in the general region of the complex Triangulum–Andromeda structure further prompting a possible association with this structure.

CHAPTER 6 – THREE NEW MILKY WAY SATELLITES IN SAGITTARIUS, DRACO AND DELPHINUS. This paper and chapter detail the discovery of three stellar systems: Sagittarius II, Draco II and Laevens 3. Sagittarius II has the following properties: $d = 60 \pm 5\,\mathrm{kpc}$, $r_h = 38^{+8}_{-7}\,\mathrm{pc}$ and $M_V = -5.2 \pm 0.4$ and lies some 15 degrees away from Sgr dSph, which prompted an investigation into a possible association with the stream of the same namesake. From the Law & Majewski (2010) models, the position and distance of Sgr II are consistent with the location of the stream. Its small size make the object interesting as it is either the most extended MW

GC known or the smallest satellite in its luminosity range. Its metallicity ([Fe/H] ~ -2.2) and age ($t \sim 12$ Gyrs) do not help in breaking the ambiguity of the nature of the satellite. Draco II is a very ambiguous object with $d = 22 \pm 3$, $r_h = 19^{+8}_{-6}$ and $M_V = -2.9 \pm 0.8$. Its size, which is poorly constrained could place the object near Segue 1 or in the realm of GCs. It lies ~ 5 degrees away from the GD–1 stream (Grillmair & Dionatos, 2006). If confirmed to be a DG, this makes the satellite the closest and smallest type yet known. It has the same metallicity and age as Sgr II. The final satellite, Laevens 3, has the following properties: $d = 64 \pm 3\,\mathrm{kpc}$, $r_h = 7 \pm 2\,\mathrm{pc}$ and $M_V = -4.4 \pm 0.3$, with a tentative metallicity and age determination of [Fe/H] $=\sim -1.9$ and $t \sim 9$ Gyr. The distance was measured through the presence of an RR Lyra star on the horizontal branch. The properties of this satellite are consistent with the population of young outer halo GCs. The crowding in this compact object make some of the parameters uncertain and will benefit from further follow–up data.

CHAPTER 7 – QUANTIFYING THE DETECTION LIMITS OF THE PAN-STARRS 1 3π SURVEY. In the final chapter of the thesis, I quantify the detection limit of the PS1 survey ($|b| > 15°$). The aim of this is to quantify the quality of the PS1 data and more importantly the efficiency of the search technique as was detailed in Chapter 2. This is achieved by simulating artificial galaxies and ingesting them into the data. The search algorithm is subsequently re–run to determine the fractional recovery of satellites of various properties at different locations in the PS1 sky. A slightly more conservative threshold of $\sigma_{stars} > 5$ was imposed as the recovery limit. To simulate the galaxies, three main steps are necessary. First photometry is generated for the various mock galaxies. Photometric uncertainties as a function of magnitude are taken into account by scattering the stars in colour–magnitude space. Secondly the survey completeness is taken into account such that unobservable stars are eliminated from the mock samples. Finally, the resultant stars were matched to positions which were generated using the Plummer function. For each 1600^2 degrees patch, 7220 galaxies were ingested.

Results showed that the search efficiency works well. The recovery rate is at its highest at higher latitudes where contamination is reduced. The recovery rates as a function of position were investigated for four DGs with properties that correspond to those of Segue 1, Boötes I, Leo IV and Andromeda IX. By varying their structural parameters through sampling the uncertainties, the recovery rates for these satellites were shown to be broadly consistent with the SDSS efforts (Koposov et al., 2008) when taking into account the differences in methodology followed. The recovery rate can be used as a stepping stone to re–derive the luminosity function of MW satellites over the whole sky after the distribution of the MW satellites has been investigated. Tentative evidence shows that this distribution is anisotropic due to the paucity in new unambiguous DG discoveries. These steps and tests will be undertaken in PV3.

8.2 Outlook

Let us now turn our attention towards the future and the avenues of research which could be pursued. First, I would like to expand a little on the immediate research which I would like to conduct as well as some of the very latest developments regarding our satellite discoveries. I would then like to conclude by discussing or highlighting the current challenges for the future.

8.2.1 Immediate aims

With the discovery of five new satellites in the last year and a half (and four of them in the last eight months), the next obvious thing to do is characterise these satellites further with spectroscopic and deeper photometric follow–up. Much of this has been done by Nicolas Martin, as the final months of the thesis were hectic. On the photometric front, we secured MegaCam time on the Canada–France–Hawaii Telescope (CFHT) to enable follow–up for Laevens 1, Triangulum II, Draco II and Laevens 3. For Sagittarius II, we acquired 1.5 hours DDT time using WFI at La Silla, since this satellite is located in the South. The deeper photometry will be especially useful to constrain the structural parameters. For cases such as Laevens 1, which barely grazes the Main Sequence Turn off or very faint nearby satellites such as Triangulum II and Draco II, this can make a substantial difference. We have already received the WFI data for Sagittarius II and MegaCam observations for Laevens 3. A re–run of the structural parameters on Sagittarius II shows that the size is consistent with the initially calculation: $r_h = 34^{+5}_{-3}$ pc. Other structural parameters are quite similar to those published in Laevens et al. (2015a). The MegaCam observations of Laevens 3, whose PS1 CMD stopped at the main sequence turn off, shows a beautiful CMD and some initial isochrone fits which could point to this system being more metal–poor and older than initially thought. We still await the photometric follow–up for the other three satellites.

We have also been pro–active in obtaining spectroscopic follow–up for the last four satellites discovered (excluding Laevens 1). All of these efforts will be conducted with DEIMOS on Keck or Hectochelle[1] at the Multiple Mirror Telescope (MMT) Observatory[2]. The former instrument will be used to target Draco II, Triangulum II and Sagittarius II. Laevens 3 will only be observed if any observing time is left since this system is the most unambiguous system of them all. Hectochelle will be used to target Triangulum II and Sagittarius II; its wide field of view will be useful in assessing the possible associations of Sagitarrius II to the Sagittarius stream and Triangulum II to the Triangulum Andromeda structure. At the time of writing, we have already obtained spectra of stars for Draco II. Unfortunately, due to its faint nature, just nine stars were confirmed to be member stars. The small sample stems from the fact that all six stars that were targetted for the red giant brach, turned out to not be associated with the system. The sample has allowed for a heliocentric velocity of $-347.5^{+1.7}_{-2.0}$ kms^{-1} to be derived, thereby confirming it is associated with the MW and moving towards us. There is a marginally resolved velocity dispersion of $\sigma_r = 3.0^{+2.2}_{-2.0}$ kms^{-1}, which could hint that the system is dark–matter dominated and therefore a DG. These results are prone to uncertainties and therefore need the necessary caution. If the result is further confirmed, this would make Draco II the closest, smallest DG yet known. In light of the measurements, efforts for a second targetting of Draco II with Hectochelle is under way, before it sets in a couple of months.

Besides these follow–up campaigns, an other immediate work will be re–doing everything presented in this thesis on the PV3 data (forced photometry), which at the time of writing, are not yet available. Since the unforced photometry in PV3 data are already available, an initial new search can be conducted. Since the forced photometry will arrive in the next couple of months, a whole new search such as was done on PV2 with isochrone contours, will not be conducted on the unforced photometry of PV3. In light of the photometric follow–up

---

[1] `https://www.cfa.harvard.edu/mmti/hectochelle.html`

[2] `https://www.mmto.org/`

campaign with the LBT for significant candidates in September–November, this search would take too long as well. Instead, a simpler search will be conducted, returning to the Koposov et al. (2008) approach. Using a colour–box, it will be interesting to see if a bright satellite could be found, which thus far eluded us [3]. In particular, the extra $\sim$ 0.5 magnitude could make all the difference for M31 satellite detections. Because M31 is observable during the LBT run, half our candidates will be near M31. Once the forced photometry has arrived, the search algorithm will be re–run a final time. The search efficiency will be quantified again, attempting to go down to lower latitude ($5^\circ < b < 15^\circ$) as well. These results will be used to quantify the luminosity function and anisotropy as was already described in Section 7.3.

8.2.2 Perspectives for Local Group astronomy

We have seen throughout the Introduction in Chapter 1, the various challenges that are currently around. We saw that these were the "missing satellite problem" (Klypin et al., 1999), the postulation of the VPOS (Pawlowski et al., 2012, 2015) and the "valley of ambiguity" where satellites occupy parameter space (r_h vs. M_V) between GCs and DGs (Gilmore et al., 2007). To understand what the future challenges are, I think it worthwhile analysing the developments over the last three years. In some sense I would argue that this field of astronomy may have looked simpler when I started in 2012, than how it looks now in 2015. It seems that of these three issues, two of them have got more complicated (the plane of satellites and the satellites in the "valley of ambiguity"), while the "Missing satellite problem" could be solved or may never have been much of a problem to start with if we take into account that a lot of simulators do not include baryons in their simulations or do not yet have the resolving power to make accurate predictions about the number of satellites. Observers do not have the tools in hand to refute the simulators because observational effects are such that many satellites could exist but have not yet been discovered, either because surveys are too shallow or the MW is in the way. The number of discoveries in DES may be the sign that these hundreds of faint satellites really orbit the MW. The last couple of sentences are of course a generalised view and do not exclude smaller problems.

Let us return to the plane of satellites. In 2012, we knew of 26 DGs, many of which were found near the Northern galactic cap, causing a North–South imbalance. The VPOS (Pawlowski et al., 2012) has always been dependent on the search volumes that have been probed up until now, which have coincided with the plane of satellites. The sample of 26 dwarfs is quite small, with the VPOS fit driven by the most distant objects. In 2012, it would have been perfectly reasonable to question the plane, because of the reasons already mentioned. In my opinion, the last three years have not refuted the plane, but have implied it. This has been possible due to the DES and PS1 discoveries. The former has extended the plane to the South, though it also suffers from the same problem as the SDSS, in that it coincides with the plane. Even then, the distribution of DES satellites in the survey footprint show that these satellites are unlikely to be the result of isotropy (Pawlowski et al., 2015). The lack of numerous new PS1 satellites would further bolster that claim. One of the greatest challenges in the future will be to make these observations match simulations. Over the next decade. the resolution of the simulations will definitely increase. A finer grid may allow for more accurate results as the number of

---

[3] Remember the discussion about Hercules and how it is not found because of the restrictive isochrone contour, which does not take into account that Hercules sits in a part of the sky with bad photometry.

assumptions that go into these simulations decreases. Similarly if the VPOS is confirmed with current and future surveys, it could be worthwhile targeting the areas of the VPOS on the sky down to unprecedented depths to constrain its form even more and mine the regions for many more satellites.

One of the key challenges for the future will be to understand the Milky Way satellite population to a better extent. More specifically we need to understand how GCs, DGs and the intermediate stellar systems fit into galaxy formation. It is worth remembering how things have evolved in three years. In 2012, of all the satellites we knew of, just four of these (Willman 1, Segue 1, Boötes II and Segue 2) were found to straddle the GC–DG transition. Just three years later, around 40% of the DG candidate population consists of these objects. A natural expectation for the future is that many more of these satellites will be found, as inevitably most of the very brightest satellites should have been found. We have come to the point where satellite searches are becoming a little less interesting as many satellites are being found. The next natural step is to therefore to try and use the information of these satellites to fit this into ΛCDM simulations. The sample of satellites in the "valley of ambiguity" is now so large that we already have a statistically significant sample of these objects. We as a community need to spend as much time possible gathering new data for these satellites on the largest telescopes around the world. We need to accurately constrain DM contents, velocity dispersions and metallicities. There is a lot of ambiguity in these systems at present because different groups measuring these properties (as we saw for Segue 1 for example) return different results and usually based on small samples. We need to return to these objects throughout several years to check that their measured properties have not changed. The second step is to fold these measurements into the bigger picture. Are these the subhalos in the ΛCDM simulations? Are they the sub–sub halos, of which we know very little at present? Are many of these satellites associated with streams and possibly remnants of a larger entity? The big problem is that photometric searches for these faint satellites are way ahead of the spectroscopic means of following them up afterwards. With current telescope sizes it is already incredibly difficult to get precise and accurate measurement for these faint satellites just 40 kpc away. Many of the DES discoveries are at much larger distances ($\lesssim$ 120 kpc). Many of the challenges will only be resolved if we had an infinite amount of telescope time on current telescopes or if we wait for the next generation of telescopes.

So as can be seen, there are plenty of things to do in the next decade. The Large Synoptic Survey Telescope (LSST) will be the next survey to watch out for. The 8.4 m telescope will surely revolutionise our view of the satellite population even further and no doubt throw up some unexpected surprises. This field of astronomy is particularly vibrant today and the next decade should be even more tantalisingly mind–boggling, interesting and exciting!

Bibliography

Aaronson, M. 1983, ApJ, 266, L11

Aaronson, M., & Olszewski, E. W. 1987, AJ, 94, 657

Abdo, A. A., et al. 2010, ApJ, 712, 147

Armandroff, T. E., Olszewski, E. W., & Pryor, C. 1995, AJ, 110, 2131

Arp, H., & van den Bergh, S. 1960, PASP, 72, 48

Ashman, K. M., & Zepf, S. E. 1998, The Observatory, 118, 387

Balbinot, E., et al. 2013, ApJ, 767, 101

Battaglia, G., Tolstoy, E., Helmi, A., Irwin, M., Parisi, P., Hill, V., & Jablonka, P. 2011, MNRAS, 411, 1013

Battaglia, G., et al. 2006, The DART imaging and CaT survey of the Fornax dwarf spheroidal galaxy, 459, 423

Bechtol, K., et al. 2015, ApJ, 807, 50

Bell, E. F., Slater, C. T., & Martin, N. F. 2011, ApJ, 742, L15

Bellazzini, M., Ferraro, F. R., & Pancino, E. 2001, MNRAS, 327, L15

Belokurov, V. 2013, New Astronomy Review, 57, 100

Belokurov, V., Irwin, M. J., Koposov, S. E., Evans, N. W., Gonzalez-Solares, E., Metcalfe, N., & Shanks, T. 2014, MNRAS, 441, 2124

Belokurov, V., et al. 2008, ApJ, 686, L83

—. 2010, ApJ, 712, L103

—. 2009, MNRAS, 397, 1748

—. 2006a, ApJ, 642, L137

—. 2007, ApJ, 654, 897

—. 2006b, ApJ, 647, L111

Bernard, E. J., et al. 2014a, MNRAS, 443, L84

—. 2014b, MNRAS, 442, 2999

Bianchini, P., Renaud, F., Gieles, M., & Varri, A. L. 2015, MNRAS, feb, L40

Binney, J., & Tremaine, S. 2008, Galactic Dynamics: Second Edition (Princeton University Press)

Bonifacio, P., Caffau, E., Zaggia, S., François, P., Sbordone, L., Andrievsky, S. M., & Korotin, S. A. 2015, A&A, 579, L6

Bonnivard, V., et al. 2015, ApJ, 808, L36

Boylan-Kolchin, M., Bullock, J. S., & Kaplinghat, M. 2011, MNRAS, 415, L40

—. 2012, MNRAS, 422, 1203

Brasseur, C. M., Martin, N. F., Macciò, A. V., Rix, H.-W., & Kang, X. 2011, ApJ, 743, 179

Bressan, A., Marigo, P., Girardi, L., Salasnich, B., Dal Cero, C., Rubele, S., & Nanni, A. 2012, MNRAS, 427, 127

Brown, T. M., et al. 2012, ApJ, 753, L21

Bullock, J. S., Kravtsov, A. V., & Weinberg, D. H. 2000, ApJ, 539, 517

—. 2001, ApJ, 548, 33

Bullock, J. S., Stewart, K. R., Kaplinghat, M., Tollerud, E. J., & Wolf, J. 2010, ApJ, 717, 1043

Cannon, R. D., Hawarden, T. G., & Tritton, S. B. 1977, MNRAS, 180, 81P

Casey, A. R., Keller, S. C., Da Costa, G., Frebel, A., & Maunder, E. 2014, ApJ, 784, 19

Chakrabarti, S., Saito, R., Quillen, A., Gran, F., Klein, C., & Blitz, L. 2015, ApJ, 802, L4

Clem, J. L. 2006, PhD thesis, University of Victoria, Canada

Coleman, M. G., et al. 2007, ApJ, 668, L43

de Jong, J. T. A., Martin, N. F., Rix, H.-W., Smith, K. W., Jin, S., & Macciò, A. V. 2010, ApJ, 710, 1664

de Vaucouleurs, G. 1948, Annales d’Astrophysique, 11

Deason, A. J., Belokurov, V., Evans, N. W., Watkins, L. L., & Fellhauer, M. 2012, ArXiv e-prints

Deason, A. J., et al. 2014, MNRAS, 444, 3975

Dotter, A., Chaboyer, B., Jevremović, D., Kostov, V., Baron, E., & Ferguson, J. W. 2008, ApJSupp, 178, 89

Dotter, A., Sarajedini, A., & Anderson, J. 2011, ApJ, 738, 74

Drlica-Wagner, A., et al. 2015, ApJ, 809, L4

Faber, S. M., & Lin, D. N. C. 1983, ApJ, 266, L17

Garrison-Kimmel, S., Rocha, M., Boylan-Kolchin, M., Bullock, J. S., & Lally, J. 2013, MNRAS, 433, 3539

Geha, M., Willman, B., Simon, J. D., Strigari, L. E., Kirby, E. N., Law, D. R., & Strader, J. 2009, ApJ, 692, 1464

Geringer-Sameth, A., Walker, M. G., Koushiappas, S. M., Koposov, S. E., Belokurov, V., Torrealba, G., & Evans, N. W. 2015, ArXiv e-prints

Gilmore, G., Wilkinson, M. I., Wyse, R. F. G., Kleyna, J. T., Koch, A., Evans, N. W., & Grebel, E. K. 2007, ApJ, 663, 948

Grebel, E. K., Gallagher, III, J. S., & Harbeck, D. 2003, AJ, 125, 1926

Green, G. M., et al. 2014, ApJ

—. 2015, ArXiv e-prints

Grillmair, C. J. 2009, ApJ, 693, 1118

Grillmair, C. J., & Dionatos, O. 2006, ApJ, 643, L17

Gunn, J. E., Lee, B. W., Lerche, I., Schramm, D. N., & Steigman, G. 1978, ApJ, 223, 1015

Hargis, J. R., Willman, B., & Peter, A. H. G. 2014, ApJ, 795, L13

Harrington, R. G., & Wilson, A. G. 1950, PASP, 62, 118

Harris, W. E. 1996, AJ, 112, 1487

—. 2010, ArXiv:1012.3224

Hodge, P. W. 1961a, AJ, 66, 384

—. 1961b, AJ, 66, 249

—. 1962, AJ, 67, 125

—. 1963, AJ, 68, 470

—. 1964, AJ, 69, 853

Huxor, A. P., Tanvir, N. R., Irwin, M. J., Ibata, R., Collett, J. L., Ferguson, A. M. N., Bridges, T., & Lewis, G. F. 2005, MNRAS, 360, 1007

Ibata, R., Chapman, S., Irwin, M., Lewis, G., & Martin, N. 2006, MNRAS, 373, L70

Ibata, R., Martin, N. F., Irwin, M., Chapman, S., Ferguson, A. M. N., Lewis, G. F., & McConnachie, A. W. 2007, ApJ, 671, 1591

Ibata, R. A., Gilmore, G., & Irwin, M. J. 1994, Nature, 370, 194

Ibata, R. A., et al. 2013, Nature, 493, 62

Ibata, R. A., Wyse, R. F. G., Gilmore, G., Irwin, M. J., & Suntzeff, N. B. 1997, AJ, 113, 634

Illingworth, G. 1976, ApJ, 204, 73

Irwin, M., & Hatzidimitriou, D. 1995, MNRAS, 277, 1354

Irwin, M. J., et al. 2007, ApJ, 656, L13

Irwin, M. J., Bunclark, P. S., Bridgeland, M. T., & McMahon, R. G. 1990, MNRAS, 244, 16P

Kim, D., & Jerjen, H. 2015, ArXiv e-prints

Kim, D., Jerjen, H., Mackey, D., Da Costa, G. S., & Milone, A. P. 2015a, ArXiv e-prints

Kim, D., Jerjen, H., Milone, A. P., Mackey, D., & Da Costa, G. S. 2015b, ApJ, 803, 63

King, I. 1962, AJ, 67, 471

Kirby, E. N., Cohen, J. G., Guhathakurta, P., Cheng, L., Bullock, J. S., & Gallazzi, A. 2013, ApJ, 779, 102

Kirby, E. N., Simon, J. D., & Cohen, J. G. 2015, ArXiv e-prints

Kleyna, J. T., Wilkinson, M. I., Evans, N. W., & Gilmore, G. 2005, ApJ, 630, L141

Klypin, A., Kravtsov, A. V., Valenzuela, O., & Prada, F. 1999, ApJ, 522, 82

Koch, A., & Rich, R. M. 2014, ApJ, 794, 89

Koch, A., et al. 2009, ApJ, 690, 453

Komatsu, E., et al. 2009, ApJSupp, 180, 330

—. 2011, ApJSupp, 192, 18

Koposov, S., et al. 2008, ApJ, 686, 279

—. 2007, ApJ, 669, 337

Koposov, S. E., Belokurov, V., Torrealba, G., & Evans, N. W. 2015, ApJ, 805, 130

Koposov, S. E., et al. 2011, ApJ, 736, 146

Koposov, S. E., Rix, H.-W., & Hogg, D. W. 2010, ApJ, 712, 260

Koposov, S. E., Yoo, J., Rix, H.-W., Weinberg, D. H., Macciò, A. V., & Escudé, J. M. 2009, ApJ, 696, 2179

Kroupa, P. 1997, New Astronomy, 2, 139

Kroupa, P., et al. 2010, ArXiv:1006.1647K

Kroupa, P., Theis, C., & Boily, C. M. 2005, A&A

Kunkel, W. E., & Demers, S. 1976, in The Galaxy and the Local Group

Kusenko, A. 2006, Physical Review Letters, 97, 241301

Laevens, B. P. M., et al. 2015a, ArXiv e-prints

—. 2015b, ApJ, 802, L18

—. 2014, ApJ, 786, L3

Law, D. R., & Majewski, S. R. 2010, ApJ, 714, 229

Libeskind, N. I., Frenk, C. S., Cole, S., Helly, J. C., Jenkins, A., Navarro, J. F., & Power, C. 2005, MNRAS, 363, 146

Libeskind, N. I., Frenk, C. S., Cole, S., Jenkins, A., & Helly, J. C. 2009, MNRAS, 399, 550

Lin, C.-C., Chen, W.-P., Hou, J., Chen, L., & Shao, Z. 2015, IAU General Assembly, 22, 54260

Luque, E., et al. 2015, ArXiv e-prints

Lynden-Bell, D. 1976, MNRAS, 174, 695

Macciò, A. V., Kang, X., Fontanot, F., Somerville, R. S., Koposov, S., & Monaco, P. 2010, MNRAS, 402, 1995

Mackey, A. D., et al. 2013, MNRAS, 429, 281

Mackey, A. D., & van den Bergh, S. 2005, MNRAS, 360, 631

Madore, B. F., & Arp, H. C. 1979, ApJ, 227, L103

Magnier, E. 2006, in The Advanced Maui Optical and Space Surveillance Technologies Conference

Magnier, E. 2007, in Astronomical Society of the Pacific Conference Series, Vol. 364, The Future of Photometric, Spectrophotometric and Polarimetric Standardization, ed. C. Sterken, 153

Magnier, E. A., Liu, M., Monet, D. G., & Chambers, K. C. 2008, in IAU Symposium, Vol. 248, IAU Symposium, ed. W. J. Jin, I. Platais, & M. A. C. Perryman, 553–559

Majewski, S. R., Skrutskie, M. F., Weinberg, M. D., & Ostheimer, J. C. 2003, ApJ, 599, 1082

Martin, N. F., et al. 2014, ApJ, 793, L14

Martin, N. F., de Jong, J. T. A., & Rix, H.-W. 2008, ApJ, 684, 1075

Martin, N. F., Ibata, R. A., Chapman, S. C., Irwin, M., & Lewis, G. F. 2007, MNRAS, 380, 281

Martin, N. F., & Jin, S. 2010, ApJ, 721, 1333

Martin, N. F., et al. 2015, ApJ, 804, L5

—. 2013a, ApJ, 779, L10

—. 2013b, ApJ, 772, 15

Mateo, M., Mirabal, N., Udalski, A., Szymanski, M., Kaluzny, J., Kubiak, M., Krzeminski, W., & Stanek, K. Z. 1996, ApJ, 458, L13

Mateo, M., Olszewski, E. W., Pryor, C., Welch, D. L., & Fischer, P. 1993, AJ, 105, 105

Mateo, M. L. 1998, ARAA, 36, 435

McConnachie, A. W. 2012, AJ, 144, 4

McConnachie, A. W., & Côté, P. 2010, ApJ, 722, L209

McConnachie, A. W., et al. 2008, ApJ, 688, 1009

Metcalfe, N., et al. 2013, MNRAS

Milgrom, M. 1983, ApJ, 270, 365

Moore, B., Ghigna, S., Governato, F., Lake, G., Quinn, T., Stadel, J., & Tozzi, P. 1999, ApJ, 524, L19

Moster, B. P., Somerville, R. S., Maulbetsch, C., van den Bosch, F. C., Macciò, A. V., Naab, T., & Oser, L. 2010, ApJ, 710, 903

Muñoz, R. R., Carlin, J. L., Frinchaboy, P. M., Nidever, D. L., Majewski, S. R., & Patterson, R. J. 2006, ApJ, 650, L51

Muñoz, R. R., Geha, M., Côté, P., Vargas, L. C., Santana, F. A., Stetson, P., Simon, J. D., & Djorgovski, S. G. 2012, ApJ, 753, L15

Newberg, H. J., Willett, B. A., Yanny, B., & Xu, Y. 2010, ApJ, 711, 32

Olszewski, E. W., Aaronson, M., & Hill, J. M. 1995, AJ, 110, 2120

Pawlowski, M. S., Kroupa, P., & de Boer, K. S. 2011, A&A, 532, A118

Pawlowski, M. S., McGaugh, S. S., & Jerjen, H. 2015, ArXiv e-prints

Pawlowski, M. S., Pflamm-Altenburg, J., & Kroupa, P. 2012, MNRAS, 423, 1109

Peñarrubia, J., Belokurov, V., Evans, N. W., Martínez-Delgado, D., Gilmore, G., Irwin, M., Niederste-Ostholt, M., & Zucker, D. B. 2010a, MNRAS, 408, L26

Peñarrubia, J., Benson, A. J., Walker, M. G., Gilmore, G., McConnachie, A. W., & Mayer, L. 2010b, MNRAS, 406, 1290

Peñarrubia, J., McConnachie, A. W., & Navarro, J. F. 2008, ApJ, 672, 904

Pieri, L., Lattanzi, M., & Silk, J. 2009, MNRAS, 399, 2033

Pontzen, A., & Governato, F. 2012, MNRAS, 421, 3464

Richstone, D. O., & Tremaine, S. 1986, AJ, 92, 72

Roderick, T. A., Jerjen, H., Mackey, A. D., & Da Costa, G. S. 2015, ApJ, 804, 134

Schlafly, E. F., & Finkbeiner, D. P. 2011, ApJ, 737, 103

Schlafly, E. F., et al. 2014a, ApJ, 789, 15

—. 2014b, ApJ, 786, 29

—. 2015, ApJ, 799, 116

Schlegel, D. J., Finkbeiner, D. P., & Davis, M. 1998, ApJ, 500, 525

Seitzer, P., & Frogel, J. A. 1985, AJ, 90, 1796

Sellwood, J. A., & Sanders, R. H. 1988, MNRAS, 233, 611

Sesar, B., et al. 2015, ArXiv e-prints

Shanks, T., et al. 2013, The Messenger, 154, 38

Shapley, H. 1938a, Harvard College Observatory Bulletin, 908, 1

—. 1938b, Nature, 142, 715

Simon, J. D., & Geha, M. 2007, ApJ, 670, 313

Simon, J. D., et al. 2011, ApJ, 733, 46

Slater, C. T., Bell, E. F., & Martin, N. F. 2011, ApJ, 742, L14

Slater, C. T., et al. 2013, ApJ

—. 2014, ApJ, 791, 9

Spergel, D. N., et al. 2003, ApJSupp, 148, 175

Springel, V., et al. 2005, Nature, 435, 629

Starkenburg, E., et al. 2013, MNRAS, 429, 725

Suntzeff, N. B., Aaronson, M., Olszewski, E. W., & Cook, K. H. 1986, AJ, 91, 1091

The Dark Energy Survey Collaboration. 2005, ArXiv Astrophysics e-prints

Tollerud, E. J., Bullock, J. S., Strigari, L. E., & Willman, B. 2008, ApJ, 688, 277

Tolstoy, E., Hill, V., & Tosi, M. 2009, ArXiv e-prints

Tolstoy, E., et al. 2004, ApJ, 617, L119

Tonry, J. L., et al. 2012, ApJ, 750, 99

Tremaine, S., & Gunn, J. E. 1979, Physical Review Letters, 42, 407

van den Bergh, S. 2008, MNRAS, 385, L20

Vargas, L. C., Geha, M., Kirby, E. N., & Simon, J. D. 2013, ArXiv e-prints, ArXiv:1302.6594

Walker, M. 2013, Dark Matter in the Galactic Dwarf Spheroidal Satellites (Springer)

Walker, M. G., Mateo, M., Olszewski, E. W., Gnedin, O. Y., Wang, X., Sen, B., & Woodroofe, M. 2007, ApJ, 667, L53

Walker, M. G., Mateo, M., Olszewski, E. W., Peñarrubia, J., Wyn Evans, N., & Gilmore, G. 2009, ApJ, 704, 1274

Walsh, S. M., Jerjen, H., & Willman, B. 2007, ApJ, 662, L83

Walsh, S. M., Willman, B., & Jerjen, H. 2009, AJ, 137, 450

Wang, J., Frenk, C. S., & Cooper, A. P. 2013, MNRAS, 429, 1502

Watkins, L. L., Evans, N. W., & An, J. H. 2010, MNRAS, 406, 264

Weisz, D. R., et al. 2012, ApJ, 748, 88

White, S. D. M., & Rees, M. J. 1978, MNRAS, 183, 341

Whiting, A. B., Hau, G. K. T., Irwin, M., & Verdugo, M. 2007, AJ, 133, 715

Willman, B., et al. 2005a, AJ, 129, 2692

Willman, B., Dalcanton, J., Ivezić, Ž., Jackson, T., Lupton, R., Brinkmann, J., Hennessy, G., & Hindsley, R. 2002, AJ, 123, 848

Willman, B., et al. 2005b, ApJ, 626, L85

Willman, B., & Strader, J. 2012, AJ, 144, 76

Wilson, A. G. 1955, PASP, 67, 27

York, D. G., et al. 2000, AJ, 120, 1579

Zentner, A. R., Kravtsov, A. V., Gnedin, O. Y., & Klypin, A. A. 2005, ApJ, 629, 219

Zolotov, A., et al. 2012, ApJ, 761, 71

Zucker, D. B., et al. 2006a, ApJ, 650, L41

—. 2006b, ApJ, 643, L103

—. 2004, ApJ, 612, L121

—. 2007, ApJ, 659, L21

Appendix A

Significant detections in PV2

Table A.1 - List of significant detections in PV2

ID	RA	Dec	l	b	SN_{Stars}	SN_{Gals}	Name
1	323.4	-0.9	53.3	-35.8	116.1	29.6	NGC 7089/M2
2	259.3	43.1	68.3	34.9	101.0	31.3	NGC 6341/M92
3	152.1	12.3	225.9	49.1	97.5	27.1	Leo I
4	168.4	22.1	220.2	67.2	89.6	11.5	Leo II
5	205.6	28.4	42.1	78.7	83.2	16.0	NGC 5272/M3
6	211.4	28.5	42.2	73.6	76.0	5.1	NGC 5466
7	81.1	-24.5	227.2	-29.3	74.9	13.9	NGC 1904/M79
8	347.1	-15.6	53.4	-63.5	73.5	6.6	NGC 7492
9	325.1	-23.2	27.2	-46.8	70.0	18.2	NGC 7099/M30
10	189.9	-26.7	299.6	36.0	68.0	13.1	NGC 4590/M68
11	229.4	-21.0	342.9	30.3	64.3	13.7	NGC 5897
12	251.8	47.5	73.6	40.3	62.6	12.8	NGC 6229
13	182.5	18.5	252.8	77.2	62.0	17.1	NGC 4147
14	114.5	38.9	180.4	25.2	61.6	8.0	NGC 2419
15	19.1	33.4	128.9	-29.1	59.8	9.3	Andromeda II
16	217.4	-6.0	342.2	49.3	57.1	11.8	NGC 5634
17	251.8	-1.9	15.7	26.3	51.7	9.2	NGC 6218/M12
18	254.3	-4.1	15.1	23.1	48.3	11.8	NGC 6254/M10
19	260.0	57.9	86.4	34.7	47.7	5.8	Draco
20	326.7	-21.3	30.5	-47.7	46.6	3.2	Palomar 12
21	315.4	16.2	63.8	-19.4	44.9	4.2	NGC 7006
22	307.5	70.1	104.0	17.6	42.6	-0.1	
23	48.2	10.2	170.3	-39.3	41.6	0.0	
24	301.5	69.7	102.6	19.2	41.5	2.4	
25	229.0	-0.1	0.8	45.8	40.6	1.1	Palomar 5
26	303.1	69.0	102.2	18.4	39.6	6.7	
27	42.9	50.4	141.7	-8.0	38.6	1.5	
28	346.7	12.8	87.1	-42.7	38.2	3.6	Palomar 13
29	357.9	24.5	106.0	-36.4	38.1	10.8	Pegasus
30	248.5	-5.7	10.2	27.0	35.0	8.7	
31	8.9	36.5	119.4	-26.3	33.6	5.1	Andromeda II
32	344.6	41.3	101.1	-16.7	33.0	4.2	Lacerta I
33	301.4	-21.9	20.3	-25.7	32.5	8.8	NGC 6864/M75
34	295.8	7.5	45.6	-7.9	32.4	0.6	
35	18.0	54.1	125.9	-8.6	31.7	7.8	
36	202.0	33.6	74.4	79.8	31.2	0.0	Canes Venatici I
37	250.7	-6.2	11.1	24.9	30.8	1.7	
38	55.4	21.6	167.4	-26.2	30.4	6.7	
39	73.7	15.4	184.8	-17.3	29.9	0.9	
40	100.1	-15.7	225.8	-9.5	29.9	3.1	
41	35.4	50.6	137.2	-9.7	29.6	2.8	
42	227.1	67.2	105.0	44.9	27.3	3.1	Ursa Minor
43	20.4	54.0	127.4	-8.6	27.0	-0.5	

Continue to next page…

Table A.1 - Continued

ID	RA	Dec	l	b	SN_{Stars}	SN_{Gals}	Name
44	297.1	10.3	48.7	-7.7	27.0	1.2	
45	230.9	-29.6	338.4	22.6	26.8	0.1	
46	219.9	-26.5	331.1	30.4	26.3	4.6	NGC 5694
47	92.3	-11.3	218.4	-14.5	26.1	0.3	
48	250.8	-7.0	10.5	24.4	25.8	-0.5	
49	242.8	14.9	28.7	42.2	25.5	3.6	Palomar 14
50	100.6	-14.6	225.0	-8.6	25.0	0.5	
51	87.2	8.6	198.0	-9.8	24.5	0.0	
52	290.2	37.8	70.0	10.9	23.7	0.2	NGC 6791
53	16.0	21.9	126.7	-40.9	23.7	1.4	Pisces I
54	70.1	21.3	177.7	-16.4	23.1	0.2	
55	307.1	59.1	94.3	11.7	22.9	-0.0	
56	30.7	-3.3	161.6	-60.7	22.6	0.6	Whiting 1
57	172.3	29.0	202.3	71.8	21.5	4.4	Palomar 4
58	255.0	-0.5	18.8	24.3	20.6	3.1	GCl 50
59	309.5	77.9	111.4	21.3	19.9	-0.4	
60	266.8	-0.0	25.4	14.3	19.3	4.5	
61	297.8	40.5	75.2	7.0	19.2	-0.1	
62	187.7	12.3	283.9	74.4	18.7	3.0	GCs in M87
63	296.3	-8.0	31.8	-15.6	18.5	1.4	GCl 114
64	282.8	-16.6	18.1	-7.4	18.1	1.8	
65	311.1	62.1	98.0	11.9	18.0	-0.1	
66	53.2	79.6	130.0	19.0	17.8	0.2	Palomar 1
67	306.4	58.1	93.3	11.5	17.3	-0.0	
68	63.1	24.2	171.0	-19.4	17.1	-0.3	
69	295.8	8.4	46.4	-7.5	17.1	0.9	
70	143.7	17.1	214.8	43.6	17.1	5.0	Leo T
71	151.4	0.1	240.1	41.9	16.9	0.4	Palomar 3
72	22.4	72.3	125.9	9.7	16.9	0.2	
73	71.9	13.7	185.2	-19.7	16.5	-0.3	
74	245.6	-18.5	357.1	21.5	16.5	0.5	
75	299.7	45.4	80.2	8.2	16.4	-0.2	
76	355.8	74.4	118.3	12.1	16.3	0.2	
77	332.5	74.5	112.6	15.0	15.9	0.0	
78	46.4	44.4	146.8	-12.2	15.9	-0.2	NGC 1193
79	74.6	63.3	146.9	12.6	15.9	3.9	
80	20.6	55.6	127.3	-7.0	15.8	-0.1	
81	346.4	72.7	115.1	11.4	15.7	0.3	
82	312.6	67.9	103.2	14.9	15.6	-0.1	
83	295.4	9.5	47.2	-6.6	15.5	0.0	
84	64.9	17.4	177.6	-22.7	15.5	-0.3	
85	75.5	17.8	183.8	-14.5	15.4	-0.1	
86	324.2	75.1	111.3	16.8	15.2	-0.3	
87	58.0	30.2	163.1	-18.2	14.7	0.0	
88	85.0	14.8	191.5	-8.5	14.7	-0.1	
89	84.5	16.1	190.0	-8.2	14.7	0.1	
90	72.5	15.9	183.6	-17.9	14.6	-0.3	
91	82.9	8.4	196.0	-13.5	14.6	2.4	
92	338.5	40.8	96.7	-14.9	14.4	3.5	
93	282.8	-15.0	19.5	-6.7	14.4	1.4	
94	185.0	29.3	193.7	82.8	14.4	3.3	NGC 4278
95	93.8	-3.5	211.9	-9.6	14.2	-0.0	
96	46.0	87.6	124.4	25.1	14.2	0.6	
97	318.5	66.0	103.2	11.9	14.0	-0.2	
98	55.6	37.4	156.7	-14.0	14.0	-0.1	
99	310.6	29.1	71.6	-8.0	13.9	-0.5	
100	50.2	46.6	147.9	-8.9	13.9	0.8	
101	187.4	8.0	286.9	70.2	13.8	2.5	NGC 4472/M49
102	76.1	24.4	178.7	-10.2	13.7	0.3	
103	7.8	76.2	121.7	13.4	13.4	-0.0	
104	74.6	18.8	182.5	-14.6	13.3	0.3	
105	83.3	-4.5	207.9	-19.5	13.3	-0.5	
106	77.2	12.3	189.5	-16.2	13.3	0.0	
107	71.1	63.5	145.7	11.5	13.0	-0.3	
108	305.3	23.7	64.4	-7.3	12.9	-0.4	

Continue to next page...

Table A.1 - Continued

ID	RA	Dec	l	b	SN_{Stars}	SN_{Gals}	Name
109	90.3	-5.5	212.1	-13.7	12.9	-0.2	
110	21.8	78.4	124.8	15.6	12.7	0.1	
111	70.4	21.9	177.4	-15.9	12.6	0.5	
112	62.3	17.8	175.5	-24.3	12.6	-0.3	
113	43.7	75.6	130.5	14.6	12.4	-0.2	
114	282.0	-16.4	17.9	-6.6	12.3	-0.0	
115	309.0	60.7	96.3	11.9	12.3	-0.2	
116	116.7	-4.7	223.5	10.1	12.2	-0.8	Cl Berkely 39
117	262.8	-14.8	10.3	10.3	12.1	-0.0	
118	298.2	-22.1	18.9	-22.9	11.9	2.3	Sagittarius II
119	63.6	24.5	171.1	-18.9	11.9	-0.3	
120	58.1	69.0	138.0	11.6	11.9	-0.3	
121	26.5	75.1	126.5	12.6	11.8	-0.2	
122	359.7	30.7	109.8	-30.8	11.8	1.4	Andromeda XXIX
123	78.3	54.5	155.3	9.0	11.8	-0.4	
124	82.1	6.9	196.9	-15.0	11.8	-0.1	
125	77.1	57.6	152.3	10.2	11.7	-0.1	
126	71.7	10.4	187.9	-21.8	11.7	-0.0	
127	210.0	14.5	358.0	69.6	11.6	-0.1	Bootes I
128	348.8	73.9	116.3	12.3	11.6	0.0	
129	17.6	47.6	126.2	-15.1	11.6	2.6	Andromeda V
130	45.5	75.4	131.0	14.6	11.6	0.3	
131	348.7	71.6	115.4	10.2	11.5	0.0	
132	260.9	-14.6	9.5	12.0	11.4	0.6	
133	256.8	-21.3	1.6	11.5	11.3	0.3	
134	250.1	-20.2	358.6	17.1	11.3	-0.3	
135	153.3	-1.6	243.5	42.3	11.2	0.1	Sextans
136	86.2	45.7	165.5	8.5	11.1	0.1	
137	55.5	22.0	167.2	-25.8	11.1	-0.2	
138	266.2	3.1	28.1	16.2	11.0	1.7	NGC 6426
139	63.4	16.0	177.8	-24.7	10.9	-0.4	
140	63.3	69.4	139.1	13.2	10.9	-0.3	
141	13.5	77.1	123.1	14.2	10.8	-0.1	
142	343.0	71.1	113.5	10.4	10.7	-0.1	
143	83.1	0.2	203.5	-17.4	10.6	0.6	Berkeley 20
144	177.7	86.8	123.9	30.2	10.6	-0.6	
145	162.3	51.1	158.6	56.8	10.6	0.5	Willman 1
146	250.0	-27.5	352.7	12.6	10.5	0.1	
147	81.2	-4.1	206.6	-21.1	10.5	-0.5	
148	87.9	9.5	197.5	-8.7	10.4	-0.2	
149	14.8	32.4	124.9	-30.5	10.4	2.1	Pisces V
150	338.2	31.2	91.0	-22.9	10.4	2.9	Andromeda XXVIII
151	71.9	19.1	180.6	-16.5	10.3	0.0	
152	269.0	0.1	26.6	12.4	10.2	3.1	
153	18.6	38.1	127.9	-24.6	10.2	1.3	Andromeda XV
154	61.7	10.7	181.1	-29.4	10.2	-0.1	
155	84.0	0.3	203.8	-16.5	10.1	1.0	
156	64.5	18.4	176.5	-22.3	10.1	-0.3	
157	66.2	-21.2	218.1	-41.3	10.0	-0.6	CL ERID 1
158	62.2	26.2	168.9	-18.6	9.9	-0.3	
159	114.6	21.6	198.1	19.7	9.8	-1.8	NGC 2420
160	261.7	-14.4	10.1	11.4	9.8	0.2	
161	190.8	11.6	295.6	74.4	9.7	2.5	NGC 4647
162	93.3	-3.7	211.9	-10.2	9.7	-0.1	
163	199.2	17.7	336.0	78.9	9.6	3.0	NGC 5053
164	83.9	5.8	198.8	-14.0	9.5	-0.1	
165	43.7	76.1	130.3	15.0	9.3	0.1	
166	172.2	76.6	129.0	39.5	9.2	1.8	
167	75.3	19.1	182.6	-13.9	9.2	0.2	
168	80.4	-4.5	206.5	-22.0	9.2	-1.1	
169	45.3	41.0	147.8	-15.5	9.2	0.7	Perseus I
170	49.8	2.1	179.5	-43.9	9.1	1.4	
171	333.5	6.5	68.5	-39.2	9.1	1.4	
172	117.2	59.7	157.4	30.3	8.9	2.3	[ATZ98] B100
173	40.5	-28.1	221.6	-65.6	8.9	2.7	

Continue to next page...

Table A.1 - Continued

ID	RA	Dec	l	b	SN_{Stars}	SN_{Gals}	Name
174	55.8	71.6	135.7	13.1	8.7	0.4	
175	186.8	23.9	242.0	83.6	8.6	2.7	Coma Berenices
176	22.3	38.7	131.0	-23.6	8.5	1.9	Andromeda XXIII
177	200.1	42.3	103.6	73.7	8.5	2.4	
178	263.6	-14.3	11.2	9.9	8.3	0.2	
179	56.1	12.2	175.5	-32.5	8.2	0.7	
180	138.4	56.0	160.6	41.9	8.1	1.4	
181	56.4	34.2	159.3	-16.1	8.1	-0.2	
182	176.9	44.4	155.4	68.5	8.1	2.3	
183	165.3	31.4	196.3	65.7	8.0	-0.8	
184	127.4	37.0	185.0	34.7	8.0	0.3	
185	120.8	47.9	171.3	31.4	8.0	2.1	
186	100.3	-16.5	226.6	-9.6	7.9	0.4	Berkeley 25
187	119.5	26.3	195.1	25.5	7.9	0.6	Koposov 2
188	195.4	48.3	118.3	68.7	7.9	2.2	
189	187.8	38.4	142.2	78.0	7.9	1.3	
190	79.3	59.0	151.8	12.0	7.9	-0.0	
191	316.9	68.0	104.3	13.6	7.8	-0.2	
192	19.9	52.2	127.3	-10.4	7.8	2.4	
193	54.0	11.4	174.5	-34.5	7.8	0.8	
194	268.0	44.7	71.2	28.9	7.8	1.6	
195	186.0	16.7	270.2	77.8	7.7	1.7	NGC 4350
196	54.5	35.0	157.5	-16.5	7.7	-0.1	
197	202.1	-11.3	317.3	50.6	7.7	2.4	
198	258.7	-13.7	9.1	14.3	7.7	0.0	
199	59.6	-2.3	192.2	-38.9	7.7	2.4	
200	62.3	4.6	187.1	-32.7	7.6	0.1	
201	161.6	10.2	236.8	56.0	7.6	-0.3	
202	169.0	1.5	257.2	55.6	7.6	2.3	ZwCl 1113+0144
203	2.3	27.7	111.6	-34.2	7.6	1.7	NGC 16
204	252.3	-9.1	9.4	22.0	7.6	-0.2	
205	94.0	-5.5	213.9	-10.4	7.6	0.2	
206	162.9	42.3	173.2	61.3	7.5	2.0	NSC J105128+422216
207	122.0	29.5	192.4	28.6	7.5	0.2	
208	347.1	-14.3	55.9	-62.8	7.5	1.9	
209	342.2	1.8	72.4	-48.7	7.5	2.3	
210	105.8	-20.8	232.8	-6.9	7.5	-0.4	C 0701-207
211	243.9	43.0	67.9	46.1	7.4	-1.0	
212	92.7	-6.2	213.9	-11.9	7.4	-0.0	NGC 2183
213	101.7	19.8	194.7	7.9	7.4	-0.1	
214	206.9	41.1	87.0	71.9	7.4	1.4	
215	238.2	64.6	98.3	42.9	7.4	1.3	Draco II
216	177.8	20.8	234.2	74.8	7.3	1.8	
217	151.8	16.1	220.5	50.4	7.3	-0.7	Segue 1
218	293.8	1.5	39.3	-9.1	7.3	0.1	
219	45.8	75.4	131.1	14.7	7.3	0.1	
220	68.5	-14.1	210.6	-36.7	7.3	-0.8	
221	282.2	-16.2	18.2	-6.8	7.3	-0.2	
222	146.3	12.8	221.7	44.3	7.3	0.4	
223	186.4	12.9	278.6	74.6	7.2	0.7	NGC 4387
224	47.3	74.7	131.8	14.3	7.2	-0.0	
225	274.3	-30.5	2.1	-6.7	7.2	0.7	
226	1.5	20.4	108.7	-41.2	7.2	1.7	
227	302.4	54.6	89.1	11.5	7.2	0.2	
228	0.3	21.5	107.7	-39.8	7.2	1.4	
229	352.9	72.7	117.0	10.8	7.2	-0.1	
230	171.4	19.3	230.1	68.8	7.1	-0.8	
231	294.0	1.2	39.2	-9.3	7.1	0.7	
232	292.2	-30.4	8.5	-20.8	7.1	0.3	Cl Arp 2
233	113.6	56.1	161.3	28.1	7.1	1.2	
234	248.6	-29.5	350.3	12.2	7.0	-0.1	
235	65.8	30.5	167.9	-13.3	7.0	-0.2	
236	41.5	-8.6	184.0	-57.2	7.0	1.3	
237	11.0	10.6	119.9	-52.2	6.9	-0.0	
238	11.3	-3.5	119.1	-66.3	6.9	1.1	

Continue to next page…

Table A.1 - Continued

ID	RA	Dec	l	b	SN_{Stars}	SN_{Gals}	Name
239	200.0	40.8	101.4	75.2	6.9	-0.9	
240	71.1	21.8	177.9	-15.4	6.9	0.1	
241	5.8	14.8	112.7	-47.5	6.9	1.2	
242	166.6	61.5	142.7	51.4	6.9	2.0	
243	32.6	30.0	142.7	-29.9	6.8	0.3	
244	188.9	12.5	288.1	74.9	6.8	1.6	M89
245	354.1	35.2	106.1	-25.2	6.7	1.8	
246	142.7	28.9	198.4	46.0	6.7	2.1	
247	144.0	10.9	222.7	41.4	6.7	1.8	
248	252.4	17.5	36.2	34.6	6.7	2.0	
249	68.6	31.2	169.0	-11.1	6.7	-0.1	
250	149.8	13.4	223.0	47.5	6.7	1.5	
251	344.6	5.9	79.2	-47.1	6.7	-0.5	Pisces II
252	181.1	14.7	259.0	73.4	6.7	1.4	
253	78.6	58.6	151.9	11.5	6.6	-0.4	
254	209.8	67.5	113.3	48.4	6.6	1.2	
255	243.6	43.1	68.0	46.3	6.6	0.3	
256	355.1	21.8	101.8	-38.1	6.6	1.2	
257	187.8	82.4	123.7	34.7	6.6	1.3	
258	27.8	-29.0	224.6	-76.7	6.6	1.7	
259	173.1	-6.2	270.2	51.6	6.6	1.2	
260	152.9	9.2	230.6	48.3	6.6	1.0	
261	358.4	14.0	102.3	-46.5	6.5	0.8	
262	186.6	31.3	174.4	83.1	6.5	1.8	NGC 4414
263	256.9	-16.0	6.1	14.5	6.5	1.9	
264	14.6	3.9	126.4	-58.9	6.5	1.0	
265	316.7	15.0	63.6	-21.2	6.5	0.5	Laevens 3
266	332.7	14.9	75.2	-32.7	6.5	-0.2	Balbinot 1
267	157.2	5.9	238.5	50.0	6.5	1.8	
268	157.0	70.6	138.1	42.1	6.4	1.6	
269	345.8	1.5	76.2	-51.3	6.4	0.7	
270	247.1	-21.9	355.4	18.3	6.4	-0.5	
271	234.6	53.3	85.0	49.7	6.4	1.1	
272	216.8	61.4	104.5	52.2	6.4	2.0	
273	188.4	40.4	137.2	76.2	6.4	-0.1	
274	152.6	16.6	220.2	51.3	6.4	1.8	
275	64.0	19.7	175.1	-21.8	6.4	0.2	
276	282.7	-16.2	18.4	-7.2	6.4	0.3	
277	132.7	63.1	152.5	37.4	6.4	2.0	Ursa Major II
278	209.9	26.0	32.7	74.7	6.3	-0.1	
279	47.0	8.0	171.1	-41.8	6.3	-0.1	
280	133.9	31.8	192.6	39.1	6.3	1.2	
281	65.0	24.1	172.3	-18.2	6.3	-0.0	
282	112.6	83.9	129.8	28.0	6.3	0.8	
283	38.2	10.4	159.6	-45.1	6.3	1.8	
284	172.6	-17.2	276.7	41.5	6.3	1.9	
285	119.6	-6.9	226.9	11.5	6.3	1.0	
286	338.8	38.9	95.9	-16.7	6.3	1.5	
287	124.3	41.1	179.7	33.0	6.3	1.8	
288	80.6	14.6	189.3	-12.2	6.2	0.4	
289	281.5	51.6	81.0	21.7	6.2	1.1	
290	26.0	-26.3	211.9	-78.3	6.2	1.9	
291	53.1	-4.1	189.2	-45.3	6.2	1.1	
292	98.6	51.5	163.8	18.4	6.2	1.9	
293	172.2	-7.8	270.2	49.7	6.2	1.0	
294	0.0	28.5	109.5	-33.1	6.2	0.8	UGC 12897
295	194.3	34.4	113.6	82.7	6.2	-1.2	Canes Venatici II
296	357.7	32.5	108.4	-28.6	6.2	0.3	
297	226.9	63.6	101.4	47.4	6.2	0.6	
298	180.0	14.6	256.8	72.7	6.2	0.7	
299	170.5	14.4	239.8	65.6	6.2	1.7	
300	165.3	-28.4	275.3	28.5	6.2	1.0	
301	153.2	61.1	149.8	46.9	6.2	1.4	
302	195.6	30.7	89.8	85.7	6.2	1.9	
303	6.4	-0.0	108.9	-62.2	6.2	0.5	

Continue to next page. . .

Table A.1 - Continued

ID	RA	Dec	l	b	SN_{Stars}	SN_{Gals}	Name
304	173.2	21.2	227.0	71.1	6.1	0.8	
305	64.4	19.6	175.4	-21.6	6.1	-0.2	
306	232.0	6.8	11.5	47.7	6.1	1.0	
307	7.5	-20.1	87.0	-81.5	6.1	1.6	
308	177.8	33.6	182.7	75.5	6.1	-0.4	
309	186.3	45.5	137.0	70.9	6.1	-0.6	
310	31.6	5.4	154.9	-52.8	6.1	1.0	
311	212.9	38.2	71.4	69.9	6.1	2.0	UGC 9088
312	247.5	32.2	53.0	42.7	6.1	0.0	
313	358.3	33.3	109.1	-28.0	6.1	1.8	
314	352.9	22.8	99.9	-36.4	6.1	0.5	
315	206.9	-11.8	324.0	48.8	6.1	1.3	ClG J1347-1145
316	139.0	47.6	171.7	43.6	6.1	1.7	
317	352.9	-3.5	80.5	-59.7	6.1	1.8	
318	177.8	38.3	167.5	73.1	6.0	1.0	
319	166.4	-3.0	258.6	50.5	6.0	1.6	
320	44.1	0.1	175.9	-49.5	6.0	1.0	ClG J0256+0006
321	168.7	67.5	136.2	47.1	6.0	0.6	
322	180.3	-12.2	284.0	48.9	6.0	0.9	
323	355.2	41.2	108.9	-19.7	6.0	0.5	
324	166.4	-13.4	267.2	42.0	6.0	1.2	
325	148.6	47.3	170.6	50.2	6.0	0.7	
326	5.9	18.2	113.7	-44.1	6.0	1.0	
327	150.0	59.1	153.5	46.6	6.0	0.8	
328	178.1	46.1	150.7	67.7	6.0	1.5	
329	120.5	38.7	181.8	29.7	6.0	1.9	
330	350.3	72.8	116.3	11.1	6.0	-0.0	
331	252.3	51.6	78.9	39.6	5.9	0.6	
332	253.2	55.5	83.9	38.7	5.9	0.4	
333	188.7	19.2	276.3	81.2	5.9	1.6	
334	124.2	49.0	170.2	33.8	5.9	1.7	
335	123.7	69.6	145.7	32.5	5.9	0.9	
336	153.0	53.9	159.3	50.5	5.9	-0.1	
337	146.4	14.1	220.1	44.9	5.9	0.1	
338	179.9	-19.2	286.3	42.0	5.9	1.2	NGC 4027
339	109.1	37.3	180.6	20.7	5.9	1.2	
340	339.8	6.0	74.1	-44.0	5.9	1.7	
341	127.5	44.4	176.1	35.8	5.9	1.4	
342	64.4	-11.9	205.9	-39.5	5.9	1.3	PLCKESZ G205.96...
343	143.8	2.5	231.9	37.1	5.9	1.9	
344	200.5	23.7	8.0	82.3	5.9	-0.6	
345	49.8	-2.6	184.6	-47.0	5.9	1.6	
346	182.9	39.2	154.9	75.3	5.9	1.0	ClG 1208+39
347	144.7	-23.0	255.4	21.6	5.8	0.6	
348	132.5	36.1	187.0	38.6	5.8	1.4	ZwCl 0847+3617
349	206.7	26.8	34.6	77.7	5.8	0.2	
350	280.6	-20.0	14.0	-7.1	5.8	1.4	
351	343.6	3.8	76.1	-48.1	5.8	1.0	
352	214.6	46.6	87.3	64.0	5.8	1.3	
353	327.4	-19.0	33.9	-47.6	5.8	1.0	
354	155.9	3.3	240.4	47.4	5.8	1.7	
355	41.8	15.4	159.8	-39.0	5.8	0.5	UGC 2252
356	328.7	-26.8	23.0	-50.8	5.8	0.4	
357	190.4	44.3	128.9	72.8	5.8	0.0	
358	287.1	69.1	100.0	23.7	5.8	0.8	ACO 2317
359	156.4	21.1	215.1	56.3	5.8	0.6	
360	334.9	1.7	65.1	-43.5	5.8	0.5	
361	57.2	21.5	168.8	-25.1	5.8	0.8	
362	180.3	23.1	229.6	78.0	5.8	1.7	
363	202.8	18.6	351.9	77.5	5.8	1.0	
364	174.8	65.4	134.5	50.1	5.8	1.8	
365	354.7	9.3	94.6	-49.6	5.8	-0.2	
366	110.3	39.4	178.8	22.2	5.8	1.7	
367	1.9	13.5	106.9	-48.0	5.7	1.3	
368	337.8	-1.0	64.8	-47.4	5.7	1.2	

Continue to next page…

Table A.1 - Continued

ID	RA	Dec	l	b	SN_{Stars}	SN_{Gals}	Name
369	51.9	37.8	154.0	-15.5	5.7	-0.3	
370	21.2	-6.9	145.8	-68.3	5.7	0.7	
371	221.9	8.5	4.1	56.8	5.7	1.5	MCXC J1447.4+0827
372	133.9	45.3	175.1	40.3	5.7	0.2	
373	123.6	53.9	164.4	33.6	5.7	0.8	
374	156.7	42.2	176.3	57.0	5.7	1.4	
375	167.6	65.0	138.8	48.9	5.7	1.6	
376	213.9	32.9	55.6	70.9	5.7	-0.1	
377	193.1	-8.5	303.3	54.4	5.7	0.3	
378	123.0	52.2	166.4	33.2	5.7	0.2	
379	193.7	-2.3	304.7	60.5	5.7	0.4	
380	174.1	-10.9	274.8	47.8	5.7	0.6	Laevens 1
381	58.1	-14.1	205.1	-46.0	5.7	1.1	
382	167.2	17.8	229.2	64.6	5.7	1.2	
383	110.8	22.1	196.2	16.6	5.7	1.5	
384	149.1	11.1	225.6	46.0	5.7	-0.1	
385	151.6	41.0	179.8	53.5	5.7	-0.0	
386	242.0	42.0	66.5	47.5	5.7	1.5	
387	187.0	28.4	197.6	84.7	5.7	1.7	
388	182.1	54.8	135.9	61.3	5.6	1.2	
389	51.7	37.8	153.9	-15.6	5.6	-0.3	
390	124.5	32.7	189.4	31.5	5.6	-0.4	
391	145.3	-5.4	240.9	33.7	5.6	-0.5	
392	204.8	22.6	12.8	78.3	5.6	1.1	
393	26.4	-28.4	222.1	-77.9	5.6	1.9	
394	130.6	44.4	176.3	38.0	5.6	0.7	
395	23.5	-10.6	156.1	-70.7	5.6	1.9	[SPD2011] 1997
396	16.9	-14.8	140.8	-77.1	5.6	0.3	
397	19.2	37.0	128.5	-25.5	5.6	0.8	
398	137.3	36.6	186.9	42.5	5.6	1.8	
399	143.8	8.1	225.8	39.9	5.6	1.2	
400	183.7	28.4	201.8	81.8	5.6	-1.0	NGC 4196
401	165.7	29.0	202.0	66.0	5.6	1.4	
402	143.3	48.0	170.6	46.5	5.6	1.2	
403	105.8	52.7	164.1	23.0	5.6	0.6	
404	169.2	30.6	197.9	69.0	5.6	1.1	
405	190.8	23.2	276.8	85.7	5.6	0.8	
406	333.4	18.5	78.5	-30.4	5.6	-0.1	
407	330.3	18.3	75.9	-28.7	5.6	1.8	
408	29.7	-28.7	222.9	-75.1	5.6	1.6	
409	171.4	-1.5	263.6	54.7	5.6	0.6	
410	150.1	4.7	234.0	43.5	5.6	0.9	
411	224.0	40.3	68.1	61.2	5.6	-0.5	
412	190.6	45.8	128.0	71.3	5.6	1.4	
413	150.6	18.7	216.1	50.3	5.6	1.5	
414	159.0	3.9	242.7	50.2	5.6	1.4	
415	200.0	44.5	106.5	71.7	5.6	0.9	
416	1.4	26.4	110.3	-35.4	5.6	1.6	
417	144.3	56.1	159.2	45.0	5.6	0.7	
418	181.5	56.4	135.3	59.6	5.5	-0.3	
419	202.8	12.3	337.0	72.5	5.5	0.9	
420	74.8	17.0	184.0	-15.5	5.5	0.4	
421	198.3	-21.9	309.6	40.7	5.5	0.4	
422	358.9	18.6	105.0	-42.4	5.5	-0.1	
423	342.8	70.8	113.3	10.2	5.5	-0.2	
424	217.5	6.8	356.4	59.0	5.5	1.1	
425	158.8	-7.9	254.8	41.8	5.5	-0.7	
426	212.4	17.1	8.0	69.4	5.5	-0.4	
427	234.2	9.9	17.1	47.5	5.5	0.3	[SPD2011] 38876
428	39.0	-14.2	190.1	-62.4	5.5	0.3	
429	187.3	34.1	155.7	81.5	5.5	1.0	
430	129.3	42.6	178.4	36.9	5.5	-0.5	
431	159.0	-10.7	257.4	39.9	5.5	1.1	
432	275.9	69.2	99.5	27.7	5.5	0.8	
433	11.5	-4.0	119.6	-66.8	5.5	1.0	

Continue to next page…

Table A.1 - Continued

ID	RA	Dec	l	b	SN_{Stars}	SN_{Gals}	Name
434	175.9	-18.6	281.3	41.4	5.5	0.6	
435	287.1	70.5	101.5	24.1	5.5	0.8	
436	89.1	62.0	151.5	17.6	5.5	0.1	
437	355.5	15.8	99.4	-43.9	5.5	1.0	
438	2.7	2.9	103.2	-58.4	5.5	0.1	
439	16.3	13.0	128.1	-49.8	5.5	1.8	
440	143.1	-18.9	251.1	23.3	5.5	-0.4	
441	263.2	24.8	48.2	27.5	5.5	0.2	
442	261.1	69.9	100.7	32.8	5.5	0.2	
443	94.2	-5.8	214.2	-10.3	5.5	0.2	
444	186.3	-8.3	291.9	54.0	5.5	0.3	
445	23.9	-21.2	184.8	-78.3	5.5	-1.0	
446	24.4	-19.9	181.1	-77.3	5.5	1.4	
447	176.2	32.2	189.5	74.6	5.5	0.3	
448	63.7	-28.5	227.1	-45.4	5.5	1.3	NGC 1540
449	165.2	-26.9	274.5	29.8	5.5	1.7	
450	181.0	25.0	221.4	79.2	5.5	-0.6	
451	177.8	39.9	163.4	72.1	5.5	0.3	
452	223.1	38.6	65.1	62.3	5.5	0.5	
453	11.7	23.8	121.6	-39.1	5.5	1.3	
454	79.0	82.4	130.5	23.9	5.5	1.7	
455	154.9	58.6	152.2	49.0	5.5	0.9	
456	228.3	-9.1	351.3	40.1	5.5	0.9	
457	217.6	53.4	94.8	58.0	5.5	-0.1	
458	160.1	34.1	190.9	61.1	5.5	1.2	
459	74.0	-1.5	200.3	-26.2	5.5	1.2	
460	347.9	7.7	84.6	-47.6	5.4	1.8	
461	224.4	33.2	53.3	62.2	5.4	1.3	
462	155.9	38.5	183.3	57.2	5.4	1.1	
463	148.7	26.8	203.0	50.8	5.4	1.7	
464	161.0	4.1	244.4	51.8	5.4	-0.0	
465	343.4	28.5	93.7	-27.6	5.4	0.1	
466	26.7	19.0	140.6	-42.0	5.4	0.9	
467	359.8	19.5	106.4	-41.7	5.4	1.4	
468	120.5	30.5	190.9	27.7	5.4	0.6	
469	347.2	41.3	103.0	-17.6	5.4	-0.9	
470	342.6	-12.2	54.8	-58.0	5.4	1.4	
471	352.7	2.6	86.6	-54.5	5.4	-0.5	
472	192.2	64.5	123.4	52.7	5.4	1.3	
473	245.9	26.6	45.0	43.0	5.4	1.3	ClG 1621+26
474	127.2	11.8	213.1	26.9	5.4	0.8	
475	167.7	7.1	248.3	58.8	5.4	0.9	
476	172.2	1.7	261.6	57.7	5.4	0.5	
477	164.8	23.3	215.3	64.3	5.4	0.6	
478	353.4	22.5	100.3	-37.0	5.4	0.4	
479	85.1	-2.1	206.5	-16.7	5.4	0.4	
480	233.0	61.6	96.5	46.5	5.4	1.7	
481	288.7	71.0	102.3	23.7	5.4	1.7	
482	14.0	-20.3	132.3	-83.1	5.4	0.2	
483	331.1	18.9	77.0	-28.7	5.4	1.3	
484	67.1	12.4	183.3	-24.2	5.4	-0.3	
485	354.9	-14.1	67.2	-68.8	5.4	0.3	
486	144.1	4.3	230.2	38.2	5.4	-0.5	
487	349.2	36.5	102.5	-22.6	5.4	0.9	
488	231.1	0.6	3.5	44.7	5.4	1.2	
489	330.6	30.9	85.3	-19.3	5.4	0.1	
490	330.0	9.9	68.7	-34.4	5.4	0.5	
491	64.6	10.6	183.2	-27.2	5.3	0.6	
492	18.2	12.4	131.1	-50.1	5.3	0.9	
493	46.6	17.3	163.1	-34.8	5.3	1.8	ClG 0303+17
494	324.0	18.2	71.1	-24.4	5.3	1.5	
495	197.2	53.2	117.1	63.8	5.3	1.0	
496	156.2	72.0	137.0	40.9	5.3	0.8	
497	161.0	-17.9	264.9	35.4	5.3	0.7	
498	176.9	48.9	148.2	65.0	5.3	-0.1	

Continue to next page...

Table A.1 - Continued

ID	RA	Dec	l	b	SN_{Stars}	SN_{Gals}	Name
499	177.6	64.7	133.3	51.2	5.3	1.2	
500	225.0	15.1	17.5	57.8	5.3	0.7	
501	205.5	49.0	102.2	66.0	5.3	0.9	
502	341.3	28.1	91.8	-27.0	5.3	0.8	
503	178.0	30.9	193.1	76.5	5.3	1.3	
504	152.9	57.9	153.9	48.5	5.3	1.4	
505	92.0	64.6	149.6	19.8	5.3	1.6	
506	134.0	13.2	214.7	33.5	5.3	1.7	
507	152.1	61.6	149.6	46.2	5.3	0.4	
508	51.2	86.9	125.0	24.7	5.3	1.4	
509	357.3	-3.1	88.4	-61.7	5.3	-0.7	
510	220.2	29.5	44.9	65.9	5.3	1.2	
511	139.9	56.3	159.9	42.6	5.3	1.2	
512	331.0	-20.2	34.1	-51.2	5.3	1.6	
513	75.3	-25.4	226.3	-34.6	5.3	0.3	
514	41.5	42.8	144.3	-15.3	5.3	0.3	
515	6.7	10.6	113.1	-51.8	5.3	1.3	
516	231.0	59.9	95.2	48.2	5.3	0.6	
517	89.9	45.9	166.6	10.9	5.3	1.0	
518	6.6	1.3	110.0	-60.9	5.3	1.6	
519	66.4	-9.5	204.3	-36.7	5.3	1.2	
520	192.2	10.0	300.9	72.9	5.3	-0.7	
521	344.1	-13.5	54.1	-59.9	5.3	1.0	
522	199.2	47.6	110.9	68.9	5.3	-0.2	
523	343.1	18.6	87.5	-35.9	5.3	1.0	
524	145.5	14.3	219.3	44.2	5.3	1.1	
525	155.3	-13.5	256.3	35.4	5.3	1.6	
526	135.9	-10.7	239.4	23.1	5.3	1.6	
527	148.3	2.5	235.1	40.8	5.3	1.0	
528	179.0	-27.7	288.2	33.5	5.3	1.4	
529	189.7	47.6	129.0	69.4	5.3	0.7	
530	201.1	28.5	45.4	82.6	5.3	1.7	
531	204.8	30.9	55.4	78.9	5.3	0.0	
532	340.0	10.6	78.3	-40.7	5.3	1.0	
533	124.1	9.2	214.2	23.0	5.3	0.1	
534	159.9	11.3	233.5	55.2	5.3	1.3	
535	60.9	9.7	181.4	-30.7	5.3	1.4	
536	254.3	47.8	73.9	38.6	5.3	0.4	
537	111.2	33.2	185.4	20.9	5.3	0.9	
538	47.2	21.6	160.7	-31.0	5.3	1.1	
539	250.1	26.5	46.1	39.3	5.3	0.1	
540	21.8	-16.4	162.5	-76.5	5.3	1.0	
541	166.7	35.3	186.3	66.3	5.3	0.8	
542	72.8	-14.3	212.8	-33.0	5.3	0.7	
543	151.2	-15.4	254.4	31.3	5.2	-0.0	
544	125.7	64.9	151.0	34.0	5.2	0.5	
545	197.2	5.5	314.6	68.0	5.2	-0.3	
546	128.9	36.8	185.5	35.9	5.2	1.4	
547	191.2	29.2	158.4	87.5	5.2	1.6	
548	207.6	54.9	105.8	60.2	5.2	-1.7	
549	123.1	17.9	205.0	25.7	5.2	-1.1	
550	29.0	-28.6	222.8	-75.7	5.2	1.7	
551	29.4	11.3	147.7	-48.4	5.2	1.2	
552	123.4	22.1	200.8	27.4	5.2	1.6	
553	340.7	39.3	97.4	-17.2	5.2	1.4	
554	299.0	58.8	91.9	15.2	5.2	0.8	
555	124.8	46.2	173.7	34.0	5.2	1.2	
556	320.4	19.1	69.4	-21.3	5.2	-1.0	Segue 3
557	166.9	51.6	154.4	58.7	5.2	0.6	
558	178.7	63.9	133.0	52.1	5.2	1.6	
559	243.8	7.6	20.6	38.0	5.2	1.6	
560	19.1	26.8	129.8	-35.7	5.2	0.7	
561	177.5	-8.8	278.4	51.1	5.2	-0.7	
562	141.0	-12.6	244.4	25.9	5.2	1.5	
563	62.2	12.0	180.3	-28.2	5.2	0.4	

Continue to next page…

Table A.1 - Continued

ID	RA	Dec	l	b	SN_{Stars}	SN_{Gals}	Name
564	326.8	-17.2	36.1	-46.4	5.2	1.6	
565	146.7	-27.6	260.2	19.6	5.2	0.3	
566	350.2	25.2	98.3	-33.3	5.2	-0.2	
567	265.2	29.2	53.6	27.3	5.2	0.2	
568	130.9	55.3	162.4	37.8	5.2	1.3	
569	135.4	7.6	221.5	32.3	5.2	1.0	
570	160.2	4.1	243.6	51.2	5.2	0.4	
571	33.3	14.5	151.0	-43.9	5.2	0.7	
572	8.6	70.8	121.5	7.9	5.2	-0.3	
573	245.8	30.8	50.7	44.0	5.2	-0.4	
574	147.1	46.0	172.7	49.4	5.2	0.6	
575	126.1	30.0	192.9	32.1	5.2	1.6	
576	166.2	-8.9	263.6	45.7	5.2	1.1	
577	56.1	24.2	166.0	-23.8	5.2	1.0	Melotte 22
578	333.4	19.8	79.5	-29.5	5.2	-0.3	
579	253.0	38.7	62.2	39.1	5.2	-0.2	
580	14.5	26.0	124.8	-36.9	5.2	0.6	
581	63.2	14.9	178.5	-25.6	5.2	0.4	
582	196.4	-7.6	309.1	55.1	5.2	-0.7	
583	138.3	9.5	221.0	35.7	5.2	1.2	
584	10.7	-30.7	329.9	-85.9	5.1	-0.9	
585	208.4	39.9	81.6	71.9	5.1	0.3	
586	211.3	9.0	350.3	64.8	5.1	1.2	
587	46.3	7.9	170.4	-42.3	5.1	0.8	
588	156.8	44.9	171.6	56.3	5.1	1.1	
589	41.6	2.9	170.2	-49.1	5.1	0.8	
590	178.5	-20.6	285.2	40.3	5.1	1.1	NGC 3956
591	233.6	41.5	67.0	53.8	5.1	1.0	
592	355.3	18.5	100.6	-41.3	5.1	0.4	
593	6.0	20.6	114.3	-41.8	5.1	1.3	
594	20.6	33.9	130.2	-28.5	5.1	1.5	
595	208.6	29.2	45.3	76.0	5.1	0.5	
596	167.9	-8.0	264.8	47.4	5.1	0.3	
597	152.3	48.9	166.9	52.0	5.1	1.7	
598	19.6	41.2	128.4	-21.4	5.1	-0.2	
599	322.3	18.9	70.5	-22.8	5.1	0.5	
600	229.2	58.6	94.4	49.7	5.1	0.8	
601	117.6	45.2	174.0	28.9	5.1	1.7	
602	181.0	23.1	231.0	78.5	5.1	0.5	
603	118.4	40.3	179.6	28.5	5.1	1.5	
604	229.1	17.7	24.8	55.3	5.1	1.3	
605	35.9	-14.1	186.3	-64.8	5.1	1.5	
606	328.4	-27.0	22.6	-50.6	5.1	0.8	
607	276.5	-29.1	4.2	-7.8	5.1	0.1	
608	180.4	29.5	197.9	78.8	5.1	1.2	
609	200.0	29.9	58.1	83.2	5.1	0.5	
610	123.7	45.9	173.9	33.2	5.1	1.3	
611	39.2	-16.1	194.0	-63.2	5.1	0.3	
612	334.3	-14.0	45.1	-51.8	5.1	1.4	
613	191.8	31.6	133.8	85.4	5.1	0.9	
614	1.4	29.2	111.1	-32.7	5.1	0.4	
615	326.4	-16.5	36.9	-45.9	5.1	1.1	
616	247.2	-21.3	355.9	18.5	5.1	-0.4	
617	93.5	-20.2	227.3	-17.1	5.1	0.6	
618	248.1	-13.1	3.3	23.0	5.1	0.5	M107
619	198.4	-26.8	309.1	35.8	5.1	0.5	
620	127.7	6.3	218.8	24.9	5.1	1.4	
621	115.5	16.1	203.8	18.3	5.1	1.3	
622	190.3	48.3	127.6	68.8	5.1	0.0	
623	334.0	15.6	76.8	-33.0	5.1	-0.1	
624	136.2	30.6	194.6	40.8	5.1	1.0	
625	331.2	-4.3	55.3	-44.2	5.1	1.6	
626	40.3	-8.3	182.1	-57.9	5.1	0.1	NGC 1052
627	116.8	49.5	169.1	29.1	5.1	1.2	
628	314.2	32.9	76.5	-8.1	5.1	1.4	

Continue to next page…

Table A.1 - Continued

ID	RA	Dec	l	b	SN_{Stars}	SN_{Gals}	Name
629	7.1	-2.8	109.2	-65.0	5.1	1.0	
630	136.6	52.4	165.6	41.5	5.1	0.9	
631	160.1	-4.9	253.3	45.0	5.1	0.7	
632	199.9	-22.3	311.5	40.1	5.1	1.2	ESO 576-32
633	359.5	13.8	103.7	-47.1	5.1	0.2	
634	336.9	0.1	65.2	-46.1	5.1	1.1	
635	7.3	-1.6	110.3	-63.9	5.1	0.1	
636	2.2	0.2	100.7	-60.8	5.1	1.5	
637	220.6	66.5	107.1	47.1	5.1	1.6	
638	356.5	-22.3	47.4	-74.4	5.1	0.6	
639	157.2	40.8	178.6	57.7	5.1	1.4	
640	165.5	31.0	197.2	65.8	5.1	0.6	
641	153.9	50.2	164.3	52.5	5.1	1.0	
642	343.5	31.3	95.3	-25.2	5.1	1.6	
643	207.7	28.4	42.1	76.8	5.1	0.7	
644	4.8	9.0	109.6	-53.0	5.1	-0.0	
645	125.0	47.7	171.9	34.2	5.1	0.8	
646	33.3	36.2	140.9	-23.8	5.1	-0.4	Triangulum II
647	165.4	68.8	136.7	45.3	5.1	0.9	
648	189.3	-4.6	296.2	58.1	5.0	1.4	
649	95.4	60.0	154.7	19.7	5.0	0.0	
650	69.5	-18.1	215.8	-37.3	5.0	1.0	
651	214.2	51.3	95.1	60.9	5.0	1.4	
652	124.4	51.9	166.8	34.1	5.0	0.1	
653	207.3	12.3	348.1	69.9	5.0	1.4	
654	41.9	75.8	130.0	14.6	5.0	0.0	
655	111.7	62.0	154.5	27.8	5.0	0.5	
656	256.5	37.0	60.5	36.1	5.0	0.8	
657	281.8	-23.6	11.3	-9.7	5.0	0.9	
658	220.1	47.0	83.1	60.8	5.0	-0.6	
659	344.6	7.8	80.9	-45.6	5.0	0.6	
660	120.0	14.9	206.8	21.8	5.0	1.5	
661	178.8	-1.3	275.2	58.5	5.0	1.4	
662	132.6	-4.6	231.8	23.8	5.0	1.0	
663	214.5	17.3	11.4	67.7	5.0	-1.0	
664	10.1	32.8	120.2	-30.1	5.0	1.4	
665	169.8	58.5	143.7	54.7	5.0	0.5	
666	356.0	-24.3	39.9	-74.6	5.0	1.0	
667	61.8	77.0	133.2	18.3	5.0	0.6	
668	186.3	28.0	202.6	84.1	5.0	-0.4	
669	235.3	17.2	27.7	49.7	5.0	1.0	
670	130.3	3.3	223.1	25.8	5.0	1.5	
671	26.8	29.0	137.3	-32.3	5.0	0.6	
672	0.2	32.9	110.8	-28.8	5.0	-1.3	IC 5373
673	168.6	32.2	193.5	68.4	5.0	0.7	
674	161.6	48.8	162.5	57.6	5.0	1.4	
675	16.9	12.3	129.1	-50.4	5.0	0.8	
676	249.5	24.0	42.8	39.2	5.0	0.8	
677	65.5	23.8	172.8	-18.1	5.0	0.2	
678	63.6	14.9	178.8	-25.2	5.0	1.0	
679	158.6	38.9	181.7	59.2	5.0	1.3	
680	169.7	41.7	169.5	66.1	5.0	-0.4	
681	190.5	-26.1	300.3	36.7	5.0	1.1	
682	139.9	38.4	184.6	44.7	5.0	0.2	
683	162.1	36.4	185.7	62.4	5.0	0.8	
684	224.9	-3.6	353.1	46.4	5.0	0.6	
685	331.0	7.6	67.4	-36.7	5.0	1.3	
686	157.2	62.3	146.7	47.7	5.0	1.3	
687	115.9	74.6	140.3	29.5	5.0	1.4	
688	150.4	32.7	193.7	53.0	5.0	1.5	
689	145.2	7.7	227.1	41.0	5.0	1.1	
690	242.4	46.3	72.8	46.8	5.0	0.7	
691	329.9	-29.6	18.8	-52.3	5.0	0.7	
692	204.7	41.8	92.4	72.4	5.0	-0.4	
693	323.2	-29.6	17.5	-46.5	5.0	0.7	

Continue to next page...

Table A.1 - Continued

ID	RA	Dec	l	b	SN_{Stars}	SN_{Gals}	Name
694	245.1	50.5	78.3	44.3	5.0	1.6	
695	200.6	40.9	100.2	74.8	5.0	-0.6	
696	357.1	10.9	98.9	-49.0	5.0	1.4	
697	279.8	-24.1	10.0	-8.2	5.0	-0.0	
698	44.1	3.6	172.3	-47.0	5.0	0.9	
699	344.6	12.6	84.7	-41.8	5.0	-0.1	
700	6.8	14.2	114.1	-48.3	5.0	-1.5	
701	6.4	-16.6	92.1	-77.9	5.0	1.5	
702	226.4	11.1	12.5	54.6	5.0	1.2	
703	354.1	3.4	89.3	-54.5	5.0	-0.0	
704	191.6	32.5	134.3	84.5	5.0	1.1	
705	353.0	25.4	101.2	-34.1	5.0	0.1	
706	12.8	28.0	122.9	-34.8	5.0	0.9	
707	178.5	29.3	200.0	77.2	5.0	0.3	
708	104.7	52.1	164.5	22.1	5.0	0.2	
709	336.7	27.6	87.6	-25.1	5.0	0.6	
710	124.4	7.2	216.3	22.4	5.0	0.8	
711	37.5	-11.4	183.6	-62.1	5.0	1.5	
712	178.4	34.6	178.3	75.5	5.0	0.9	
713	149.4	28.9	199.8	51.8	5.0	1.6	
714	147.1	63.4	149.1	43.3	5.0	0.5	
715	219.5	41.7	73.5	63.8	5.0	0.0	
716	128.3	77.4	136.4	31.9	5.0	1.5	
717	17.2	15.2	129.2	-47.4	5.0	1.1	
718	11.0	6.8	119.7	-56.1	5.0	1.6	
719	237.5	57.5	89.6	46.5	5.0	0.2	
720	118.6	36.3	184.1	27.7	5.0	0.2	
721	286.8	-28.5	8.6	-15.7	5.0	-0.2	
722	24.6	12.9	140.4	-48.4	5.0	1.1	
723	228.7	36.4	59.0	58.3	5.0	1.3	
724	162.4	11.1	236.2	57.2	5.0	1.1	
725	211.8	44.6	87.0	66.9	5.0	-0.4	
726	138.3	50.1	168.5	42.9	5.0	0.7	
727	250.5	64.8	95.8	38.0	5.0	0.5	
728	135.9	34.2	189.9	41.2	5.0	0.0	
729	166.6	4.3	250.6	56.1	5.0	0.8	UGC 6155
730	142.3	33.1	192.3	46.3	5.0	1.4	
731	341.7	17.4	85.2	-36.2	5.0	1.5	
732	22.9	-13.6	159.8	-73.6	5.0	1.5	ACO 209
733	230.3	64.7	101.2	45.6	5.0	0.8	
734	100.1	51.4	164.2	19.2	4.9	1.0	
735	231.5	43.0	70.2	55.0	4.9	1.6	
736	207.9	64.7	112.7	51.2	4.9	-1.4	
737	173.7	54.9	144.4	58.9	4.9	1.2	NGC 3733
738	203.8	13.1	341.2	72.6	4.9	1.1	
739	3.7	-20.4	69.9	-79.3	4.9	1.6	
740	178.4	32.5	186.2	76.4	4.9	1.0	
741	147.2	67.1	144.8	41.5	4.9	1.5	
742	202.7	44.0	100.4	71.4	4.9	1.1	
743	227.5	-9.3	350.4	40.4	4.9	1.4	
744	65.1	-22.7	219.7	-42.8	4.9	0.7	
745	207.3	37.5	76.9	74.0	4.9	0.1	
746	65.4	10.1	184.2	-26.9	4.9	0.1	
747	153.6	42.6	176.7	54.7	4.9	0.8	
748	203.1	35.5	79.3	77.9	4.9	-0.2	
749	178.8	-25.3	287.2	35.9	4.9	1.4	
750	175.8	59.6	138.1	55.5	4.9	1.5	
751	260.4	53.4	80.9	34.6	4.9	1.1	
752	199.0	33.8	86.2	81.5	4.9	1.2	
753	168.1	7.9	247.7	59.7	4.9	1.1	
754	351.0	1.7	83.3	-54.3	4.9	1.1	
755	125.0	57.4	160.1	34.4	4.9	0.8	
756	140.6	24.5	203.9	43.2	4.9	-0.9	
757	65.1	12.6	181.8	-25.6	4.9	-0.2	
758	166.3	25.4	211.1	66.2	4.9	1.5	

Continue to next page. . .

Table A.1 - Continued

ID	RA	Dec	l	b	SN_{Stars}	SN_{Gals}	Name
759	238.0	-3.8	4.7	36.6	4.9	0.5	
760	238.8	41.4	66.0	50.0	4.9	1.3	
761	180.2	31.7	187.3	78.1	4.9	0.3	
762	342.8	22.5	89.7	-32.5	4.9	0.9	
763	17.0	55.6	125.3	-7.2	4.9	0.6	
764	132.0	14.8	212.1	32.4	4.9	1.2	
765	89.5	64.3	149.4	18.8	4.9	0.7	
766	235.0	-21.9	346.9	26.2	4.9	1.3	
767	137.4	55.1	161.9	41.5	4.9	0.5	
768	183.5	-12.9	288.9	49.0	4.9	1.3	
769	141.8	64.5	149.1	40.7	4.9	-0.6	
770	179.0	40.8	159.3	72.2	4.9	-0.6	
771	164.1	76.3	131.4	38.9	4.9	1.6	
772	24.9	22.3	137.3	-39.3	4.9	1.1	
773	23.3	35.6	132.4	-26.5	4.9	0.2	NGC 591
774	4.5	10.9	109.8	-51.1	4.9	0.7	
775	141.9	-9.0	241.8	28.8	4.9	1.2	
776	11.0	13.6	120.2	-49.2	4.9	0.2	
777	170.8	36.3	181.3	69.2	4.9	0.4	
778	163.2	36.7	184.6	63.2	4.9	-0.2	NGC 3432
779	257.1	64.3	94.3	35.4	4.9	1.1	
780	178.0	5.2	267.3	63.9	4.9	0.7	
781	14.5	45.3	124.1	-17.6	4.9	0.8	
782	1.0	30.9	111.1	-30.9	4.9	0.3	
783	5.4	15.2	112.4	-47.1	4.9	1.6	
784	180.0	55.7	137.5	60.0	4.9	1.6	
785	47.0	7.5	171.6	-42.1	4.9	1.3	
786	146.4	34.6	190.5	49.8	4.9	0.2	
787	134.9	-10.0	238.2	22.7	4.9	1.3	
788	144.4	6.4	228.1	39.6	4.9	1.0	
789	329.1	-1.3	57.0	-40.8	4.9	-0.0	
790	34.8	20.2	149.4	-38.1	4.9	0.5	Segue 2
791	359.1	-12.8	78.3	-70.7	4.9	0.2	
792	192.5	56.8	123.3	60.3	4.9	1.5	
793	164.0	12.7	235.3	59.4	4.9	-0.0	
794	149.2	7.4	230.2	44.2	4.9	1.1	
795	165.5	31.1	197.0	65.9	4.9	0.0	
796	201.4	16.0	340.2	76.4	4.9	1.1	
797	122.6	77.1	137.1	30.8	4.9	0.4	
798	181.1	29.0	199.8	79.4	4.9	0.2	
799	176.7	1.4	269.2	60.0	4.9	1.6	
800	300.8	1.6	42.8	-15.2	4.9	0.5	
801	64.1	19.7	175.2	-21.8	4.9	0.2	
802	186.1	2.2	287.2	64.2	4.9	0.7	
803	19.3	15.7	132.0	-46.7	4.9	0.0	
804	74.6	1.7	197.6	-24.0	4.9	-0.1	
805	181.4	49.5	141.4	66.0	4.9	1.0	NGC 4100
806	173.9	31.9	192.1	72.9	4.9	0.6	
807	208.3	42.6	87.7	70.1	4.9	-0.1	
808	65.3	-20.4	216.8	-41.8	4.9	1.5	
809	170.1	62.0	140.1	52.0	4.9	-0.2	
810	1.9	-22.7	54.8	-79.1	4.9	0.9	
811	146.2	32.1	194.2	49.5	4.9	0.8	UGC 5209
812	192.8	67.1	122.9	50.0	4.8	1.5	
813	210.0	11.9	352.8	67.8	4.8	0.1	
814	302.5	49.0	84.3	8.5	4.8	-0.3	
815	20.8	12.3	135.0	-49.9	4.8	1.3	
816	7.4	25.2	116.7	-37.4	4.8	1.3	
817	185.5	57.2	130.7	59.5	4.8	1.6	
818	177.8	85.5	124.3	31.5	4.8	0.0	
819	12.9	29.7	123.0	-33.2	4.8	1.1	Andromeda XXIV
820	127.7	76.5	137.4	32.1	4.8	-0.7	
821	31.3	34.4	139.8	-26.0	4.8	0.2	
822	318.1	-18.5	30.5	-39.2	4.8	0.6	
823	162.2	36.4	185.5	62.5	4.8	-0.1	

Continue to next page. . .

Table A.1 - Continued

ID	RA	Dec	l	b	SN_{Stars}	SN_{Gals}	Name
824	6.2	0.5	108.8	-61.6	4.8	0.1	
825	247.2	21.4	38.7	40.5	4.8	0.4	
826	177.0	-7.5	276.7	52.1	4.8	1.5	
827	202.4	-23.3	314.1	38.7	4.8	-1.6	
828	110.4	32.9	185.4	20.2	4.8	1.4	
829	36.1	3.5	162.7	-52.0	4.8	1.1	
830	146.2	46.9	171.7	48.6	4.8	1.0	
831	12.4	-1.5	121.9	-64.4	4.8	-0.2	
832	51.8	-9.0	194.2	-49.0	4.8	1.0	
833	9.2	-21.1	93.1	-83.1	4.8	1.2	
834	130.9	74.2	139.7	33.6	4.8	1.4	
835	137.4	51.6	166.6	42.1	4.8	0.7	ACO 746
836	160.1	70.8	136.9	42.6	4.8	0.9	
837	350.5	35.5	103.1	-23.9	4.8	0.0	
838	354.4	36.1	106.6	-24.4	4.8	0.6	
839	339.4	6.9	74.5	-43.1	4.8	1.2	
840	196.4	38.7	109.7	78.0	4.8	1.2	
841	164.5	-20.5	270.1	35.0	4.8	0.8	
842	186.3	15.3	274.4	76.7	4.8	-0.6	
843	123.0	56.5	161.3	33.3	4.8	1.3	
844	238.9	-3.2	6.0	36.3	4.8	-0.1	
845	160.4	2.4	245.8	50.2	4.8	1.3	
846	75.7	76.9	135.4	20.6	4.8	0.7	UGC 3227
847	346.3	25.1	94.4	-31.8	4.8	-0.9	
848	154.8	-28.4	266.7	23.6	4.8	1.3	
849	172.9	35.9	180.8	70.9	4.8	0.5	ACO 1292
850	196.5	51.0	117.3	66.0	4.8	-1.7	
851	178.2	32.5	186.3	76.2	4.8	1.1	
852	16.7	-14.4	139.3	-76.8	4.8	1.1	
853	27.0	16.5	142.0	-44.3	4.8	1.1	
854	40.1	28.2	150.4	-28.8	4.8	0.6	
855	161.3	54.2	154.7	54.4	4.8	1.1	
856	2.8	21.3	110.5	-40.6	4.8	0.7	
857	149.0	-28.2	262.3	20.5	4.8	1.3	
858	223.5	-9.9	345.9	42.5	4.8	0.7	
859	171.9	18.4	232.9	68.9	4.8	-0.0	
860	119.0	67.9	147.9	31.0	4.8	1.0	
861	24.0	-6.8	152.4	-67.1	4.8	1.0	
862	284.1	-13.3	21.6	-7.2	4.8	-0.2	
863	240.5	9.4	20.8	41.7	4.8	0.3	
864	65.9	13.4	181.7	-24.5	4.8	-0.2	
865	168.2	72.9	132.5	42.4	4.8	1.4	NGC 3562
866	170.6	-15.9	273.7	41.9	4.8	0.9	
867	185.8	52.5	132.8	64.1	4.8	1.5	
868	199.9	60.9	116.8	55.9	4.8	0.4	
869	2.4	-30.0	13.1	-80.4	4.8	1.3	
870	135.1	71.0	142.8	35.9	4.8	0.1	
871	307.0	-23.4	20.6	-31.0	4.8	0.6	
872	118.8	49.0	169.8	30.3	4.8	0.6	
873	150.3	23.6	208.4	51.5	4.8	0.8	
874	196.2	6.0	312.1	68.6	4.8	1.3	
875	111.6	43.2	175.1	24.3	4.8	-0.4	UGC 3844
876	114.8	30.1	189.6	22.8	4.8	-0.1	
877	220.2	64.1	105.1	49.0	4.8	0.6	
878	164.5	0.7	252.4	52.0	4.8	0.8	
879	8.2	12.2	115.8	-50.4	4.8	0.2	
880	158.2	72.3	136.2	41.0	4.8	0.6	
881	47.6	7.9	171.7	-41.4	4.8	1.4	
882	202.4	42.9	99.2	72.5	4.8	-1.1	
883	15.8	12.0	127.5	-50.8	4.8	-0.0	
884	319.0	13.1	63.5	-24.0	4.8	0.2	
885	184.0	29.8	191.9	81.8	4.8	0.4	UGC 7924
886	352.7	-14.5	62.9	-67.4	4.8	1.4	
887	321.5	27.6	76.7	-16.4	4.8	0.9	
888	358.0	26.1	106.7	-34.9	4.8	-1.2	

Continue to next page...

Table A.1 - Continued

ID	RA	Dec	l	b	SN_{Stars}	SN_{Gals}	Name
889	165.1	-2.6	256.6	50.1	4.8	0.7	
890	226.5	48.0	80.7	56.6	4.8	1.1	
891	23.1	43.1	130.8	-19.2	4.8	1.0	
892	121.1	34.5	186.7	29.2	4.8	-0.1	
893	204.5	34.0	70.2	77.9	4.8	0.9	
894	116.6	57.5	160.0	29.9	4.8	1.3	
895	164.7	73.8	133.0	41.0	4.8	1.4	
896	180.0	32.1	185.9	77.8	4.8	0.5	
897	321.6	17.7	69.1	-23.1	4.8	0.6	
898	57.2	-7.0	195.7	-43.4	4.8	1.1	
899	205.5	36.2	76.5	75.9	4.7	1.0	
900	342.8	11.9	82.2	-41.3	4.7	1.0	
901	258.2	-3.4	18.0	20.1	4.7	0.1	
902	171.4	31.0	196.2	70.9	4.7	1.0	
903	326.6	-17.6	35.5	-46.4	4.7	0.3	
904	28.8	-1.5	156.3	-60.2	4.7	1.1	
905	88.5	10.9	196.6	-7.5	4.7	0.2	
906	164.9	8.2	243.2	57.5	4.7	0.1	
907	123.2	30.5	191.6	29.9	4.7	0.7	
908	145.1	31.5	195.0	48.4	4.7	0.6	
909	56.9	18.2	171.2	-27.7	4.7	1.1	
910	133.5	54.5	163.3	39.4	4.7	1.4	
911	53.5	-2.6	187.8	-44.0	4.7	0.9	
912	267.8	53.0	80.7	30.2	4.7	0.7	
913	142.6	46.4	173.0	46.3	4.7	1.0	
914	353.8	10.0	93.9	-48.5	4.7	-0.2	
915	171.8	9.4	250.7	63.3	4.7	1.0	
916	264.1	-16.1	9.8	8.5	4.7	0.1	
917	14.2	-9.4	127.4	-72.2	4.7	1.3	
918	197.5	-14.0	309.7	48.6	4.7	0.8	
919	7.0	-7.2	106.3	-69.3	4.7	1.5	
920	140.0	-2.6	234.6	31.1	4.7	0.3	
921	23.3	-16.0	166.1	-75.2	4.7	0.3	
922	241.0	45.1	71.3	47.9	4.7	0.0	
923	72.0	19.4	180.5	-16.2	4.7	-0.1	
924	17.0	6.1	130.3	-56.6	4.7	0.3	
925	2.7	-24.1	48.7	-80.3	4.7	0.2	
926	125.9	50.2	168.9	35.0	4.7	-0.3	
927	208.7	31.0	52.4	75.6	4.7	0.3	
928	221.3	2.3	355.4	53.1	4.7	1.2	
929	167.6	2.2	254.4	55.3	4.7	0.3	
930	207.5	31.7	56.1	76.5	4.7	0.2	
931	315.2	-17.0	31.1	-36.0	4.7	0.8	
932	192.0	-9.0	301.4	53.8	4.7	1.2	
933	127.9	59.3	157.6	35.8	4.7	1.2	
934	97.6	60.6	154.5	20.9	4.7	-0.1	
935	103.0	55.5	160.6	22.2	4.7	1.1	
936	33.4	48.2	136.8	-12.5	4.7	-0.7	
937	212.7	58.9	105.0	55.4	4.7	0.2	
938	214.4	34.7	60.5	70.1	4.7	0.7	
939	252.4	-8.4	10.1	22.3	4.7	0.9	
940	62.2	11.9	180.4	-28.3	4.7	0.3	
941	203.6	41.4	93.9	73.2	4.7	0.2	
942	153.3	-9.9	251.4	36.7	4.7	0.6	
943	128.6	32.5	190.7	34.8	4.7	0.3	
944	345.8	7.3	81.8	-46.7	4.7	0.9	
945	225.1	35.4	57.7	61.4	4.7	0.1	
946	182.8	28.8	200.0	80.9	4.7	1.6	
947	187.6	46.4	133.8	70.3	4.7	-1.1	
948	198.9	-2.4	315.1	59.9	4.7	0.8	
949	221.4	54.7	93.8	55.4	4.7	0.3	
950	18.2	30.8	128.3	-31.9	4.7	1.0	
951	339.7	16.9	82.9	-35.4	4.7	0.4	
952	170.8	23.7	217.7	69.9	4.7	1.2	
953	156.1	40.3	179.8	57.0	4.7	0.2	

Continue to next page. . .

Table A.1 - Continued

ID	RA	Dec	l	b	SN_{Stars}	SN_{Gals}	Name
954	184.1	64.8	129.0	51.9	4.7	1.0	
955	20.1	36.6	129.4	-25.9	4.7	0.8	
956	251.2	-19.5	359.9	16.8	4.7	-0.4	
957	117.2	15.9	204.7	19.6	4.7	-0.0	
958	28.6	16.3	144.2	-44.0	4.7	1.3	
959	245.3	-14.6	0.2	24.2	4.7	1.1	
960	141.6	36.7	187.0	46.0	4.7	1.0	
961	153.5	2.6	239.2	45.1	4.7	1.2	
962	236.7	63.4	97.3	44.0	4.7	1.2	
963	119.5	19.6	201.9	23.1	4.7	-0.6	
964	148.1	61.2	151.5	44.7	4.7	1.4	
965	18.8	-26.4	206.3	-84.7	4.7	-0.1	ESO 475-14
966	139.2	31.9	193.5	43.5	4.7	-0.4	
967	276.6	-28.0	5.2	-7.4	4.7	-0.1	
968	7.3	4.8	112.4	-57.7	4.7	1.1	
969	131.7	-1.8	228.7	24.5	4.7	0.1	
970	176.7	65.1	133.6	50.7	4.7	0.4	
971	191.7	14.9	297.7	77.7	4.7	0.1	
972	66.0	73.7	136.5	16.7	4.7	1.1	
973	191.6	56.8	124.3	60.3	4.7	0.8	
974	344.0	44.0	101.9	-14.1	4.7	-0.5	
975	187.7	65.0	126.4	52.0	4.7	-0.5	
976	140.2	-20.9	250.7	20.0	4.7	1.5	
977	333.1	8.9	70.4	-37.3	4.7	1.4	
978	236.8	-20.2	349.6	26.4	4.7	0.6	
979	227.2	34.1	54.8	59.8	4.7	0.8	
980	23.4	32.4	133.1	-29.6	4.7	-0.2	
981	351.1	-3.4	77.9	-58.4	4.7	0.2	
982	161.8	21.0	218.4	61.0	4.7	-0.5	
983	349.3	3.3	82.4	-52.0	4.7	0.8	
984	61.6	-11.1	203.4	-41.6	4.7	0.3	
985	358.2	-1.3	91.8	-60.6	4.7	-0.0	
986	164.6	36.2	185.1	64.4	4.7	0.5	
987	352.1	-29.3	21.3	-71.6	4.7	1.5	
988	321.1	38.1	84.2	-8.7	4.7	1.5	
989	349.4	17.3	93.1	-40.1	4.7	0.6	
990	171.7	13.0	244.3	65.6	4.7	1.4	
991	215.1	-4.8	340.3	51.5	4.7	0.5	
992	357.9	26.9	106.8	-34.1	4.7	-0.3	
993	79.1	13.9	189.1	-13.8	4.7	-0.1	
994	189.9	-11.6	298.4	51.1	4.7	0.8	M 104
995	81.9	75.4	137.6	21.1	4.7	-0.1	
996	314.9	-9.1	39.6	-32.6	4.7	0.8	
997	190.8	22.3	281.4	84.8	4.7	1.5	
998	211.0	23.5	24.4	73.2	4.7	1.3	
999	176.2	63.2	135.1	52.3	4.7	1.0	
1000	332.1	16.8	76.2	-30.9	4.7	0.1	
1001	359.5	3.7	98.1	-56.6	4.7	1.5	
1002	162.3	-12.7	262.3	40.3	4.7	-0.5	
1003	170.6	46.7	158.9	63.8	4.7	0.8	
1004	6.8	44.1	118.4	-18.5	4.7	0.3	
1005	166.0	70.4	135.1	44.1	4.7	0.4	
1006	359.0	28.7	108.5	-32.7	4.7	-0.5	2E 4791
1007	188.8	16.7	282.3	78.9	4.7	1.1	
1008	136.9	43.7	177.2	42.5	4.7	-0.2	
1009	163.5	68.0	138.1	45.5	4.7	0.3	
1010	196.7	38.9	108.6	77.8	4.7	0.9	
1011	46.4	-6.6	186.3	-52.1	4.7	-0.8	
1012	166.1	-14.6	267.8	40.8	4.7	0.4	
1013	116.2	72.1	143.1	29.8	4.7	0.6	
1014	166.0	-11.7	265.5	43.2	4.7	1.1	
1015	180.6	40.9	156.0	72.9	4.7	0.3	
1016	260.0	38.5	62.9	33.7	4.7	-1.2	
1017	197.2	53.2	117.1	63.7	4.7	0.3	
1018	119.7	19.8	201.8	23.4	4.7	1.4	

Continue to next page...

Table A.1 - Continued

ID	RA	Dec	l	b	SN_{Stars}	SN_{Gals}	Name
1019	149.4	39.9	181.9	52.0	4.7	0.7	
1020	2.6	12.9	107.7	-48.7	4.7	0.0	
1021	158.7	51.9	159.4	54.4	4.7	0.8	Ursa Major I
1022	322.5	20.2	71.7	-22.1	4.7	1.1	
1023	57.6	-25.3	220.8	-50.0	4.6	0.8	
1024	349.0	-11.2	63.7	-62.5	4.6	1.5	
1025	177.2	40.9	162.1	71.1	4.6	1.0	
1026	204.3	26.8	33.8	79.8	4.6	1.5	
1027	56.6	23.6	166.8	-24.0	4.6	0.5	
1028	31.4	-12.6	176.7	-67.4	4.6	-1.2	
1029	20.8	21.7	132.7	-40.6	4.6	0.9	
1030	300.8	-12.9	29.1	-21.6	4.6	0.1	
1031	249.0	6.6	22.7	33.0	4.6	0.1	
1032	3.9	-1.2	103.2	-62.7	4.6	0.4	
1033	173.1	42.1	165.0	68.0	4.6	0.8	
1034	190.6	14.3	293.3	77.0	4.6	0.9	NGC 4634
1035	85.1	-1.9	206.4	-16.7	4.6	0.2	
1036	173.9	-22.8	281.0	36.9	4.6	0.6	
1037	216.3	-8.3	338.9	47.9	4.6	0.1	
1038	182.0	41.7	151.5	72.9	4.6	-1.1	
1039	9.9	22.5	119.3	-40.3	4.6	-0.4	
1040	208.6	29.8	47.5	75.9	4.6	-0.4	
1041	65.8	10.4	184.2	-26.4	4.6	0.1	
1042	20.4	23.8	131.8	-38.6	4.6	0.1	
1043	183.1	42.7	147.5	72.5	4.6	1.3	
1044	209.1	-27.2	320.3	33.5	4.6	-0.5	C 1353-269
1045	325.4	-15.4	37.8	-44.5	4.6	0.4	
1046	92.0	-11.1	218.1	-14.7	4.6	1.3	
1047	150.6	48.8	167.6	51.0	4.6	1.2	
1048	152.3	-20.9	259.4	28.0	4.6	0.8	
1049	246.6	67.7	100.0	38.4	4.6	1.4	
1050	152.2	40.4	180.7	54.1	4.6	1.0	
1051	312.0	24.4	68.6	-11.9	4.6	-1.2	
1052	334.7	-6.5	55.6	-48.3	4.6	1.3	
1053	162.8	13.9	232.1	59.0	4.6	1.5	NGC 3419
1054	282.4	76.9	108.2	26.5	4.6	0.5	
1055	295.0	9.3	46.8	-6.4	4.6	0.1	
1056	330.0	10.2	68.9	-34.1	4.6	0.7	
1057	160.4	-13.2	260.8	38.8	4.6	0.9	
1058	159.4	-20.0	264.8	32.8	4.6	0.8	
1059	307.6	82.2	115.2	23.7	4.6	0.8	
1060	19.5	21.1	131.2	-41.3	4.6	0.1	
1061	150.7	40.9	180.1	52.9	4.6	0.3	
1062	131.3	51.4	167.3	38.4	4.6	0.8	
1063	27.0	0.0	151.8	-59.7	4.6	0.6	
1064	342.1	36.6	97.0	-20.0	4.6	1.4	
1065	141.9	-26.7	256.4	17.2	4.6	0.5	
1066	263.7	77.9	109.6	30.5	4.6	1.4	
1067	30.5	40.9	137.0	-20.1	4.6	0.6	
1068	90.3	82.1	131.5	25.2	4.6	1.0	
1069	308.3	-30.1	13.4	-34.0	4.6	0.6	
1070	189.0	38.8	137.3	77.9	4.6	1.5	
1071	64.6	10.5	183.3	-27.3	4.6	0.1	
1072	101.6	-30.3	240.0	-14.3	4.6	0.5	
1073	357.4	7.6	97.3	-52.2	4.6	0.0	
1074	164.1	1.1	251.4	52.0	4.6	1.0	
1075	151.7	29.9	198.5	53.9	4.6	0.7	
1076	181.4	-1.9	280.3	59.0	4.6	1.1	
1077	344.7	51.2	105.6	-7.8	4.6	0.4	
1078	163.5	77.8	130.5	37.6	4.6	0.6	
1079	171.1	-10.8	271.0	46.6	4.6	0.2	
1080	20.4	22.8	132.0	-39.5	4.6	1.1	
1081	261.9	13.5	36.0	24.6	4.6	0.5	
1082	65.9	11.0	183.7	-26.0	4.6	-0.1	
1083	141.0	16.5	214.2	41.0	4.6	-0.6	

Continue to next page…

Table A.1 - Continued

ID	RA	Dec	l	b	SN_{Stars}	SN_{Gals}	Name
1084	151.1	27.7	202.1	53.1	4.6	1.3	
1085	183.8	20.0	251.7	79.1	4.6	0.5	
1086	56.2	37.4	157.1	-13.8	4.6	0.3	
1087	347.8	12.3	88.1	-43.7	4.6	1.0	
1088	354.6	24.3	102.3	-35.7	4.6	1.1	
1089	7.2	-28.0	22.3	-84.9	4.6	-0.3	
1090	277.1	-28.1	5.3	-7.8	4.6	1.5	
1091	241.4	27.1	44.5	47.1	4.6	0.2	
1092	158.1	55.4	154.9	52.3	4.6	1.0	
1093	140.1	7.0	224.8	36.2	4.6	0.7	
1094	14.3	54.6	123.8	-8.2	4.6	0.8	
1095	185.6	41.8	143.2	74.2	4.6	-1.6	
1096	89.2	8.8	198.8	-7.9	4.6	-0.1	
1097	166.1	75.4	131.4	39.9	4.6	1.2	
1098	156.5	-27.4	267.3	25.3	4.6	1.2	
1099	258.6	77.0	109.0	31.8	4.6	-0.0	
1100	150.9	53.1	161.3	49.7	4.6	0.1	
1101	62.7	14.9	178.2	-25.9	4.6	0.0	
1102	221.1	-5.2	347.4	47.7	4.6	1.5	
1103	315.6	18.9	66.2	-18.0	4.6	-0.9	
1104	113.7	39.5	179.5	24.8	4.6	1.5	
1105	119.9	39.1	181.3	29.4	4.6	0.6	
1106	20.0	-14.9	152.7	-76.1	4.6	1.3	
1107	359.8	10.0	102.4	-50.8	4.6	1.1	
1108	126.3	51.6	167.2	35.2	4.6	0.5	
1109	127.1	27.6	195.9	32.3	4.6	0.7	
1110	144.4	12.2	221.3	42.3	4.6	0.1	
1111	348.3	38.4	102.6	-20.5	4.6	1.2	
1112	200.7	3.7	322.1	65.4	4.6	0.6	
1113	5.3	-28.6	18.4	-83.1	4.6	1.4	
1114	174.0	31.6	193.2	73.0	4.6	-0.8	
1115	339.5	-6.3	60.2	-52.1	4.6	0.9	
1116	211.8	9.2	351.4	64.6	4.6	1.2	
1117	158.5	73.7	134.9	40.1	4.6	-0.2	
1118	343.3	11.0	82.1	-42.3	4.6	-0.6	
1119	157.5	9.4	234.2	52.2	4.6	0.6	
1120	184.6	39.3	150.3	76.0	4.6	1.4	
1121	257.8	-2.8	18.3	20.8	4.6	-0.4	
1122	98.0	50.5	164.7	17.7	4.6	0.7	
1123	208.2	23.9	23.3	75.8	4.6	-0.1	
1124	119.3	16.8	204.6	21.9	4.6	0.6	
1125	174.1	75.6	129.0	40.6	4.6	0.3	
1126	136.8	-1.2	231.2	29.2	4.6	1.1	
1127	139.7	45.6	174.5	44.4	4.6	0.3	
1128	63.1	14.9	178.5	-25.7	4.6	1.2	
1129	72.2	-9.9	207.8	-31.7	4.6	1.4	
1130	208.3	-26.3	319.7	34.5	4.6	0.0	
1131	164.6	17.7	226.9	62.3	4.6	1.5	
1132	178.3	35.6	175.1	75.0	4.6	1.2	
1133	108.1	59.5	157.0	25.7	4.6	0.6	
1134	219.1	28.6	42.8	66.8	4.6	1.5	
1135	2.0	39.2	113.8	-22.9	4.6	0.4	
1136	6.0	11.8	112.4	-50.5	4.6	1.1	
1137	119.0	28.8	192.3	25.9	4.6	0.2	
1138	173.2	29.0	202.1	72.6	4.6	0.5	
1139	63.6	22.3	172.8	-20.4	4.6	0.0	
1140	207.3	-5.2	328.5	54.8	4.6	0.7	
1141	185.6	48.7	135.7	67.7	4.6	1.0	
1142	14.2	9.5	125.2	-53.3	4.6	0.7	
1143	240.7	56.1	86.9	45.4	4.6	1.0	
1144	169.5	24.2	215.6	68.8	4.6	1.1	
1145	151.9	-12.1	252.2	34.2	4.6	0.5	
1146	342.1	30.5	93.8	-25.3	4.6	0.7	
1147	268.7	33.2	58.9	25.6	4.6	-0.4	
1148	355.9	22.9	103.2	-37.4	4.6	1.1	

Continue to next page. . .

Table A.1 - Continued

ID	RA	Dec	l	b	SN_{Stars}	SN_{Gals}	Name
1149	12.0	-19.7	116.6	-82.6	4.6	-0.3	
1150	149.4	47.7	169.7	50.5	4.6	0.5	
1151	233.5	55.8	88.9	49.1	4.6	1.0	
1152	194.8	-1.5	306.9	61.3	4.6	0.9	
1153	73.2	16.5	183.6	-17.1	4.6	-0.1	
1154	121.6	69.8	145.6	31.8	4.6	1.2	
1155	325.6	25.9	78.2	-20.1	4.6	-0.7	
1156	357.2	-10.9	77.6	-68.1	4.6	1.3	
1157	26.8	30.6	136.9	-30.8	4.6	0.7	
1158	128.5	55.2	162.7	36.4	4.6	1.1	
1159	185.8	0.9	287.3	62.9	4.6	-0.8	
1160	242.1	35.1	56.3	47.5	4.6	0.4	
1161	43.5	18.0	159.7	-36.0	4.6	-0.1	
1162	101.5	54.1	161.9	20.9	4.6	0.9	
1163	40.4	41.1	144.3	-17.1	4.6	0.8	
1164	134.7	-0.9	229.7	27.5	4.6	0.7	
1165	104.9	55.7	160.7	23.2	4.6	0.4	
1166	4.3	36.7	115.3	-25.7	4.6	0.4	
1167	189.4	36.4	139.8	80.3	4.6	0.5	
1168	133.9	56.2	161.0	39.4	4.6	0.2	
1169	349.3	17.3	93.0	-40.0	4.6	-0.0	
1170	355.7	-11.9	73.0	-67.8	4.6	1.3	
1171	348.9	2.5	81.3	-52.4	4.5	-0.4	
1172	225.6	7.3	6.4	53.2	4.5	1.1	
1173	284.2	46.1	76.0	18.3	4.5	0.5	
1174	212.0	35.6	65.1	71.6	4.5	0.7	
1175	190.1	21.8	277.1	84.1	4.5	0.5	
1176	179.6	-15.8	284.7	45.2	4.5	1.0	
1177	115.6	48.1	170.5	28.1	4.5	0.1	
1178	29.9	-22.9	201.3	-74.0	4.5	1.2	
1179	172.6	42.7	164.3	67.4	4.5	1.5	
1180	133.9	30.7	194.0	38.9	4.5	1.1	
1181	161.6	32.2	194.7	62.5	4.5	0.6	
1182	143.5	10.1	223.2	40.6	4.5	1.1	
1183	242.9	24.7	41.6	45.2	4.5	1.4	
1184	75.7	7.4	192.9	-20.1	4.5	-0.3	
1185	204.0	60.0	112.9	56.3	4.5	1.4	
1186	48.3	-5.0	186.1	-49.7	4.5	0.2	
1187	12.7	-21.9	121.7	-84.8	4.5	0.8	
1188	235.2	41.6	66.9	52.7	4.5	1.0	
1189	359.9	10.0	102.5	-50.8	4.5	1.1	
1190	138.4	41.0	181.0	43.6	4.5	0.4	
1191	189.5	23.5	262.4	85.2	4.5	0.8	
1192	81.6	7.6	196.0	-15.0	4.5	0.5	
1193	164.2	-16.9	267.3	37.9	4.5	1.5	
1194	153.5	17.8	218.9	52.6	4.5	1.5	
1195	138.5	50.8	167.4	42.9	4.5	1.3	
1196	140.3	34.4	190.2	44.7	4.5	0.8	
1197	139.9	42.2	179.2	44.7	4.5	1.1	
1198	12.5	-20.5	120.3	-83.4	4.5	1.2	
1199	63.2	14.9	178.5	-25.5	4.5	0.2	
1200	17.6	53.5	125.8	-9.3	4.5	1.4	
1201	17.5	32.1	127.5	-30.6	4.5	0.4	
1202	198.0	32.6	84.9	83.0	4.5	0.9	
1203	123.6	24.8	198.0	28.5	4.5	0.3	
1204	146.7	48.3	169.5	48.6	4.5	0.2	
1205	94.8	64.4	150.2	20.9	4.5	0.5	
1206	141.3	43.8	176.9	45.6	4.5	-0.4	
1207	25.5	-6.0	154.8	-65.7	4.5	-0.3	
1208	358.7	42.5	111.9	-19.2	4.5	-0.1	
1209	217.0	29.9	46.0	68.7	4.5	0.8	
1210	201.3	49.5	109.0	66.7	4.5	1.3	
1211	184.3	35.3	162.7	79.0	4.5	1.4	
1212	3.7	45.3	116.2	-17.1	4.5	0.7	
1213	317.6	30.3	76.4	-12.0	4.5	-0.8	

Continue to next page. . .

Table A.1 - Continued

ID	RA	Dec	l	b	SN_{Stars}	SN_{Gals}	Name
1214	156.7	-12.8	257.0	36.8	4.5	-0.1	
1215	295.0	41.7	75.2	9.4	4.5	-0.0	
1216	162.7	19.1	222.6	61.3	4.5	1.3	
1217	66.6	-21.9	219.2	-41.2	4.5	-0.9	
1218	42.2	20.9	156.6	-34.2	4.5	0.9	
1219	199.8	81.9	121.7	35.2	4.5	1.2	
1220	179.4	47.1	147.2	67.4	4.5	0.5	
1221	202.8	-24.0	314.5	38.0	4.5	-0.4	
1222	7.1	70.8	121.0	8.0	4.5	-0.0	
1223	140.9	29.1	197.7	44.5	4.5	0.0	
1224	255.2	64.2	94.4	36.2	4.5	0.9	
1225	155.9	51.4	161.6	53.1	4.5	-0.1	
1226	326.1	27.6	79.7	-19.2	4.5	1.4	
1227	59.3	-8.0	198.3	-42.1	4.5	1.5	
1228	238.5	16.7	28.8	46.7	4.5	0.9	
1229	111.2	51.9	165.7	26.0	4.5	0.9	
1230	174.8	29.1	201.5	74.0	4.5	-1.0	
1231	125.3	61.9	154.7	34.2	4.5	1.0	
1232	50.3	-8.1	191.8	-49.8	4.5	0.5	
1233	333.1	16.8	77.0	-31.6	4.5	1.3	
1234	33.3	34.1	141.7	-25.8	4.5	0.4	
1235	297.2	8.3	47.0	-8.8	4.5	-0.5	
1236	184.3	37.1	156.7	77.7	4.5	0.4	
1237	65.3	10.1	184.1	-27.0	4.5	0.1	
1238	152.8	78.8	131.8	35.4	4.5	0.6	
1239	344.1	49.3	104.4	-9.4	4.5	-0.0	
1240	328.2	-11.5	44.4	-45.3	4.5	-0.3	
1241	89.4	-6.7	212.9	-15.0	4.5	1.2	
1242	329.4	-9.7	47.5	-45.5	4.5	0.4	
1243	172.8	30.7	196.6	72.1	4.5	-0.8	
1244	174.5	30.4	197.3	73.6	4.5	1.4	
1245	208.4	-5.8	329.8	53.8	4.5	0.6	
1246	70.4	-9.7	206.7	-33.2	4.5	1.2	
1247	0.3	20.9	107.5	-40.4	4.5	1.5	
1248	139.0	-0.4	231.7	31.5	4.5	0.9	
1249	145.1	-29.5	260.5	17.2	4.5	1.0	

Appendix B

Recovery rate for satellite galaxies over the entire PS1 sky

B.1 Low–latitude

B.1.1 Northern hemisphere

This section of the appendix contains the satellite recovery fraction for low latitude patches in the Northern and Southern hemisphere.

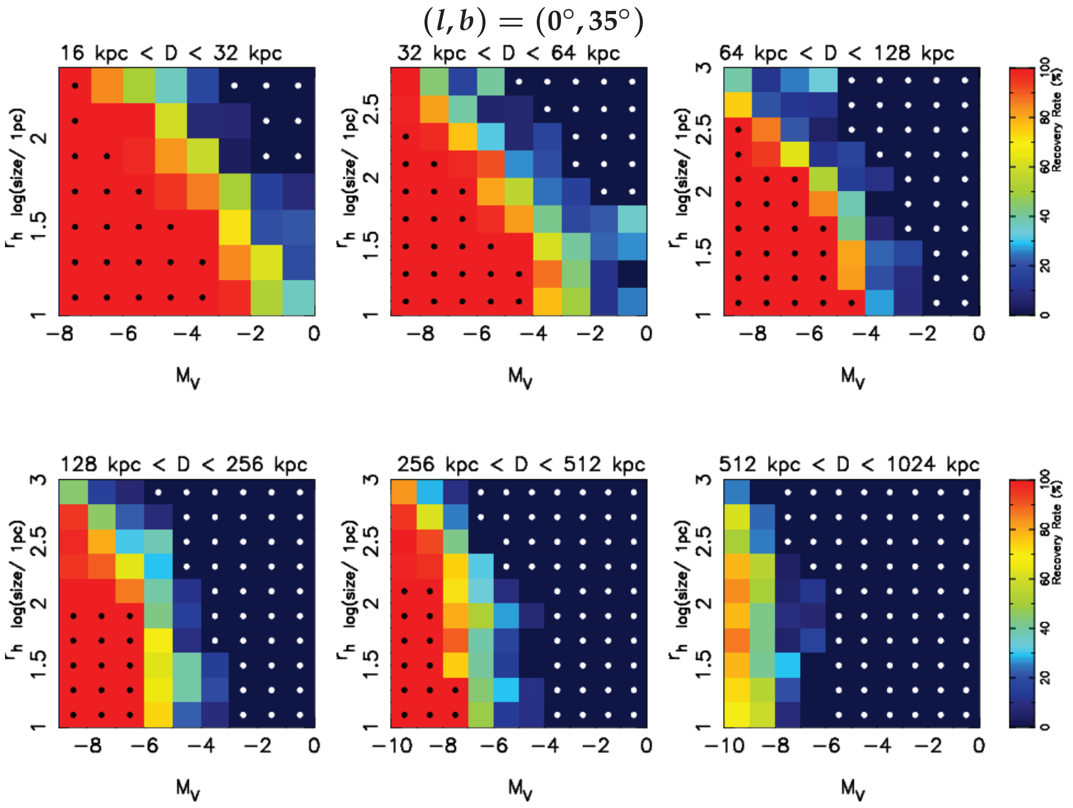

Figure B.1 - Satellite recovery fraction for $(l,b) = (0°,35°)$

$(l, b) = (35^\circ, 35^\circ)$

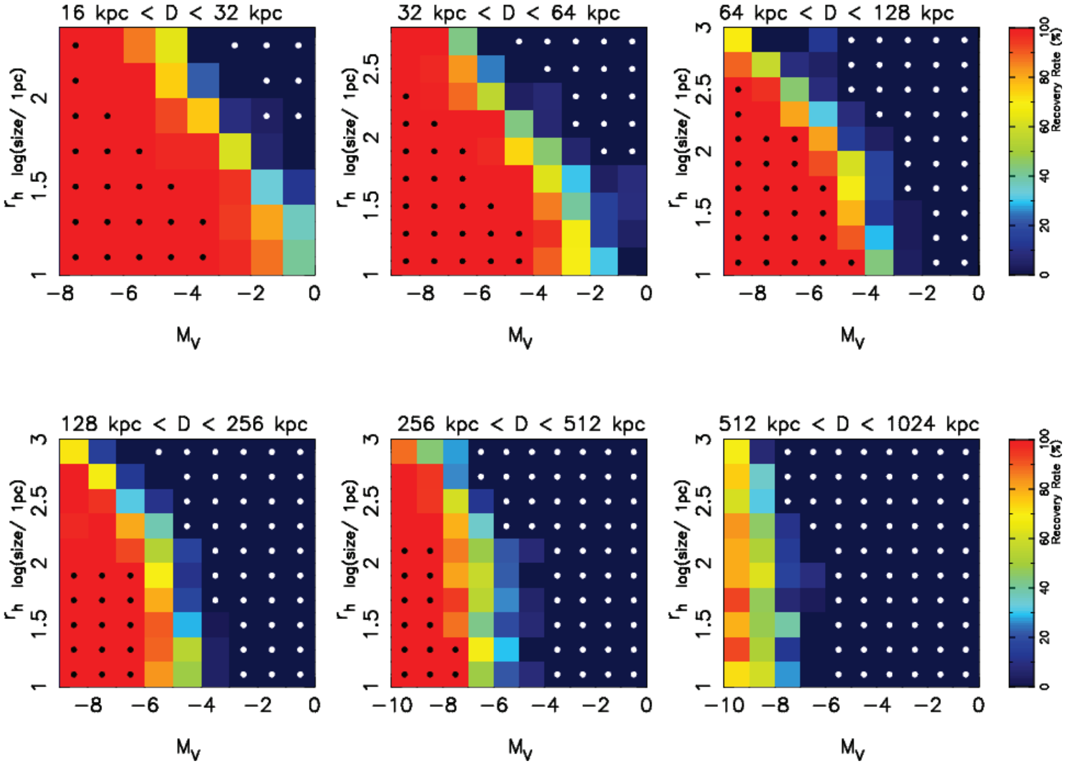

$(l, b) = (60^\circ, 35^\circ)$

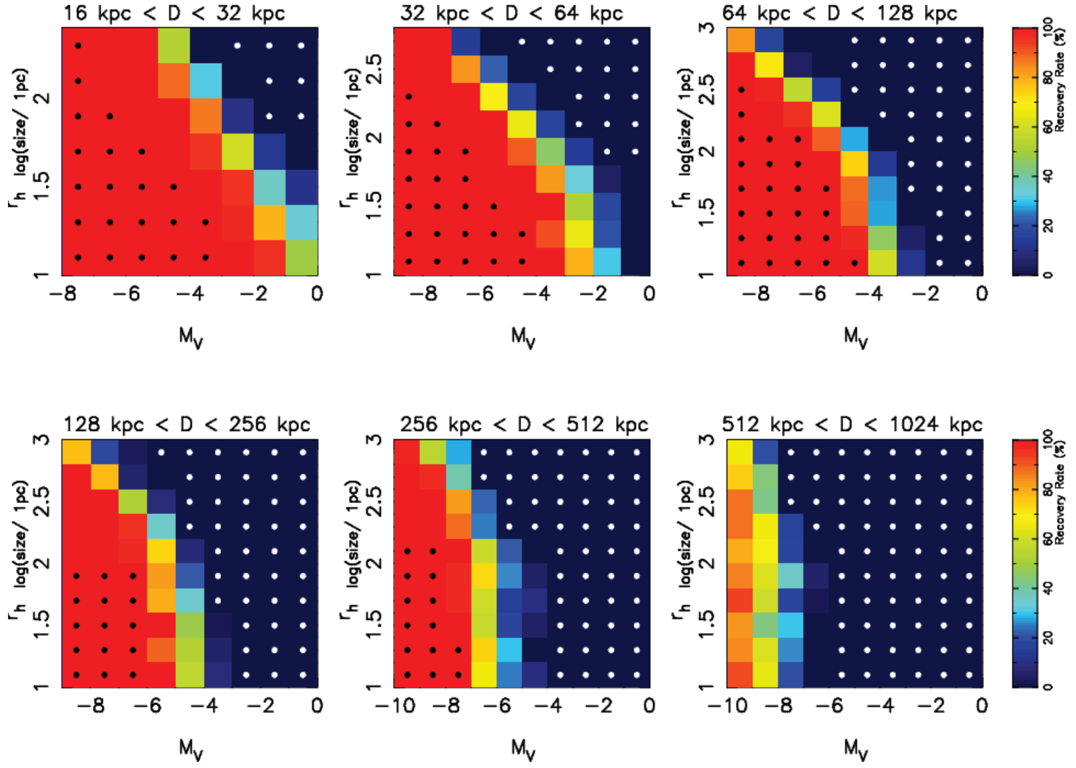

Figure B.2 - Satellite recovery fraction for $(l, b) = (30^\circ, 35^\circ)$ and $(l, b) = (60^\circ, 35^\circ)$

$(l, b) = (90^\circ, 35^\circ)$

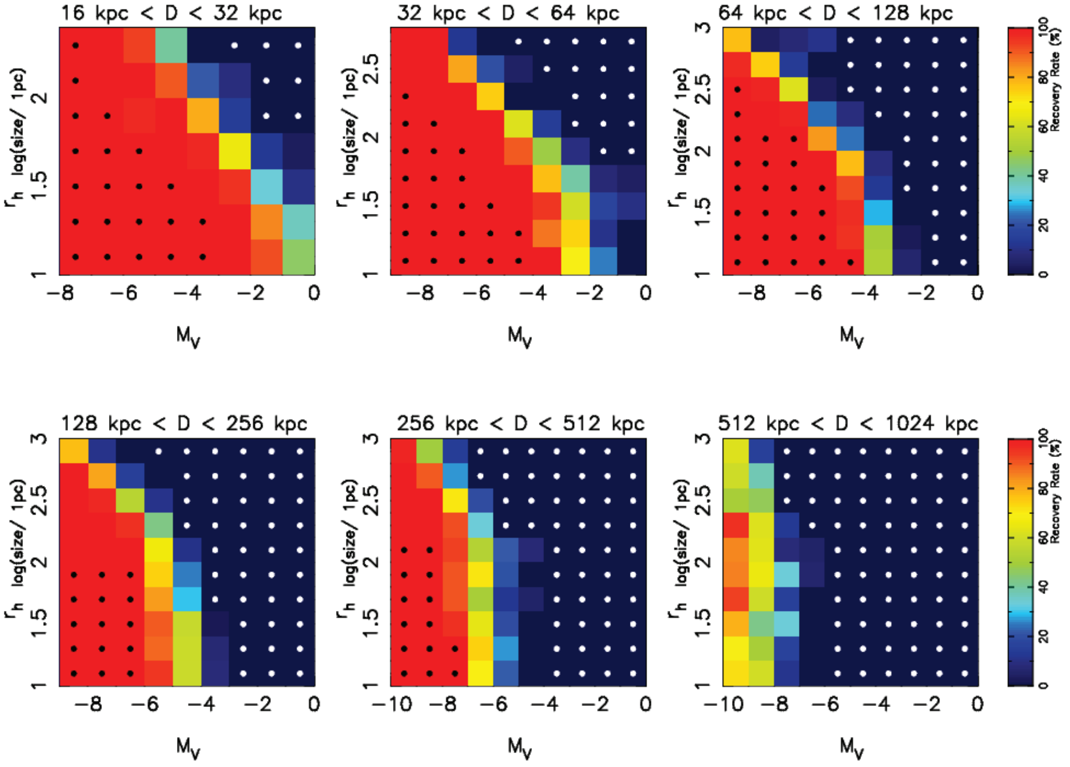

$(l, b) = (120^\circ, 35^\circ)$

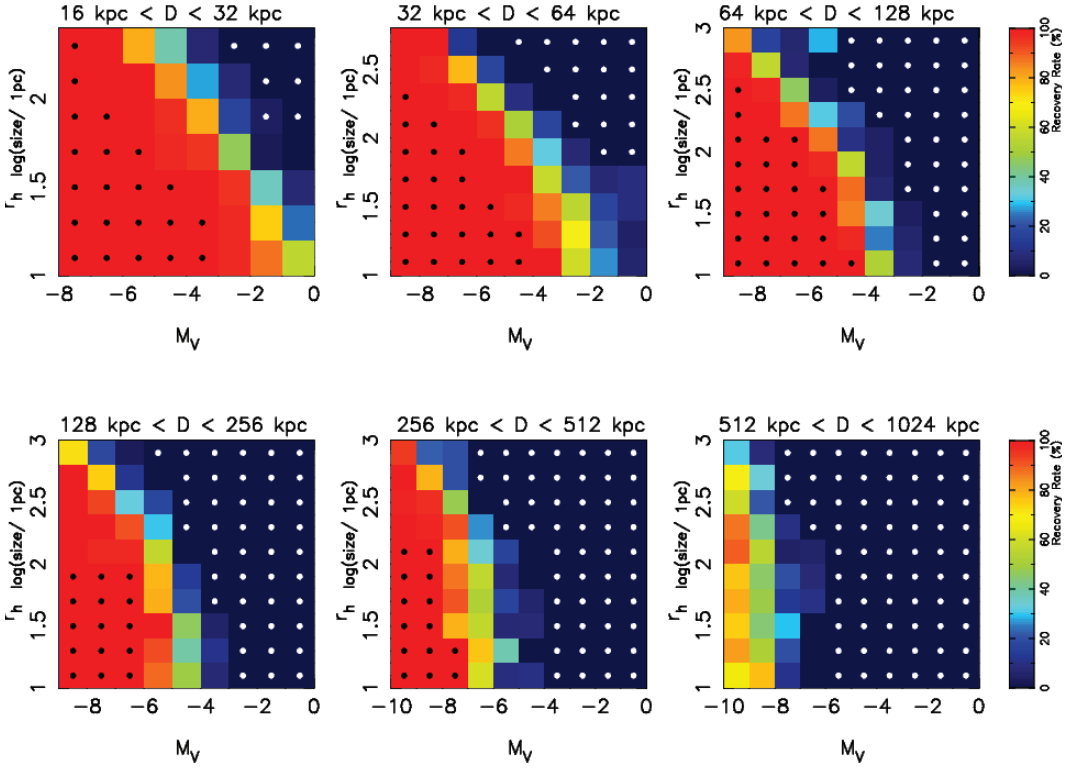

Figure B.3 - Satellite recovery fraction for $(l, b) = (90^\circ, 35^\circ)$ and $(l, b) = (120^\circ, 35^\circ)$

$(l, b) = (150^\circ, 35^\circ)$

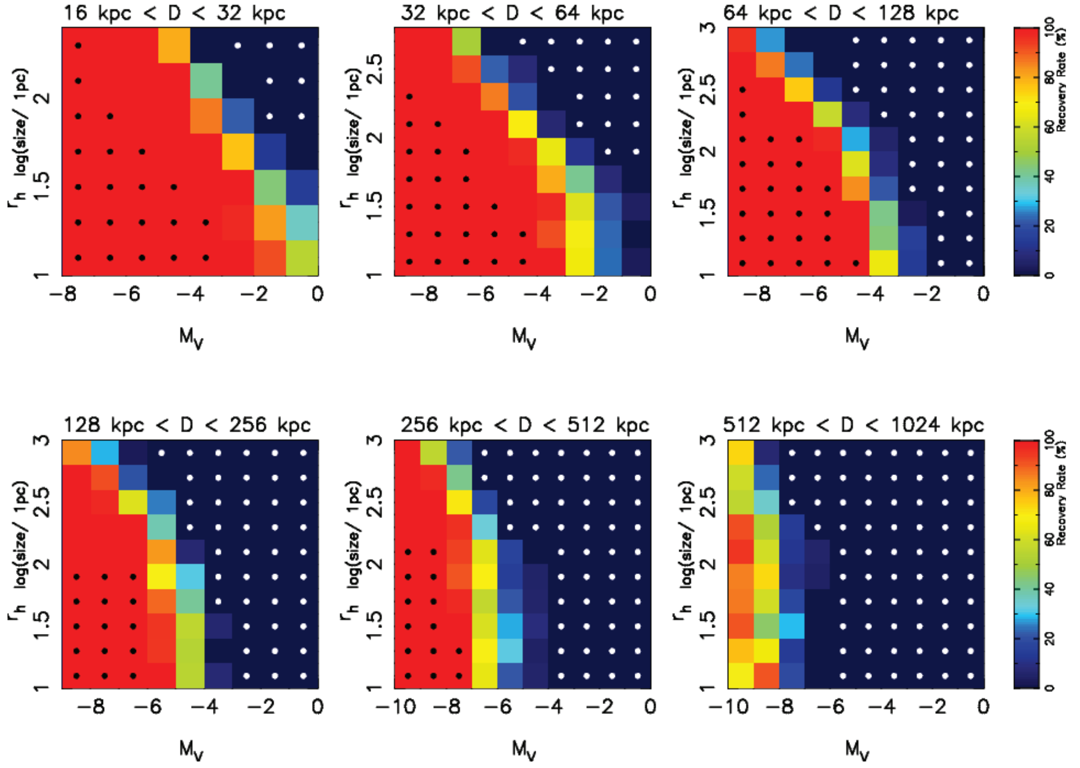

$(l, b) = (180^\circ, 35^\circ)$

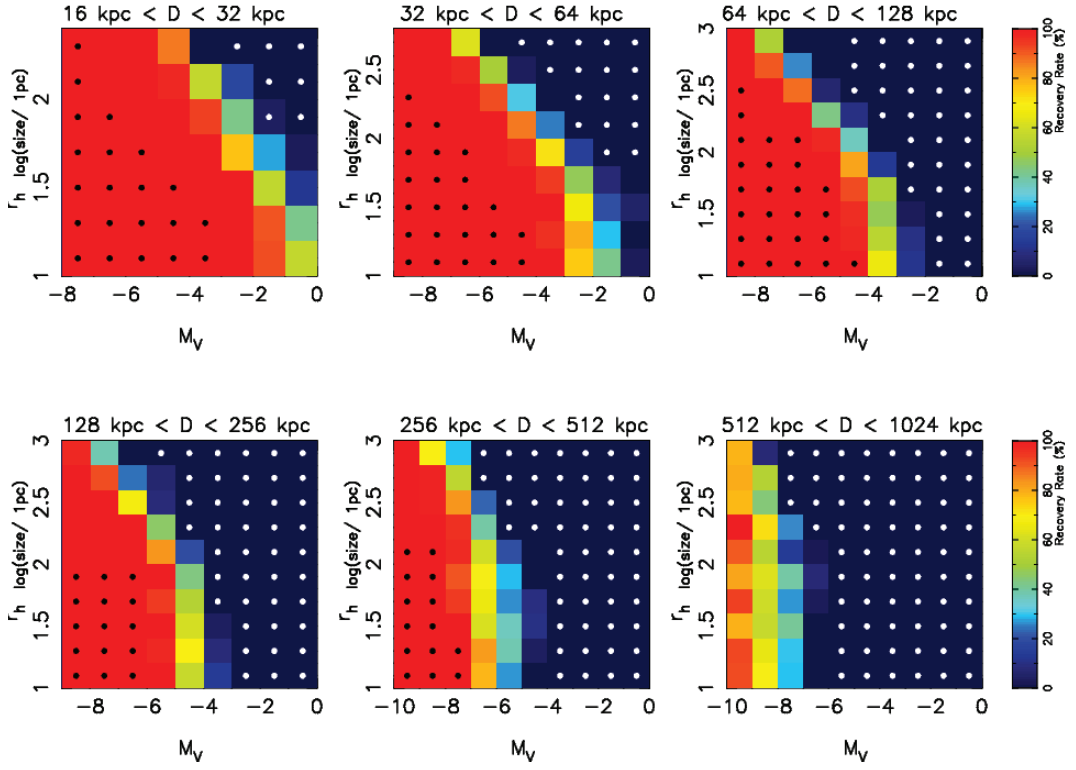

Figure B.4 - Satellite recovery fraction for $(l, b) = (150^\circ, 35^\circ)$ and $(l, b) = (180^\circ, 35^\circ)$

$(l, b) = (210°, 35°)$

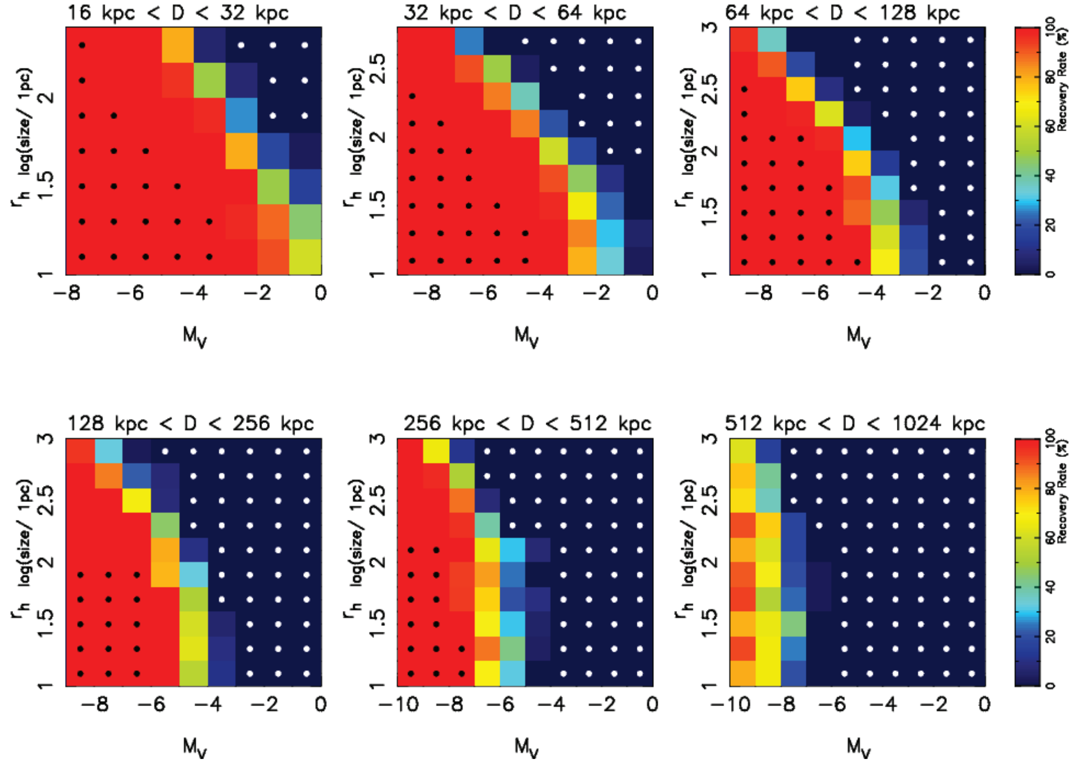

$(l, b) = (240°, 35°)$

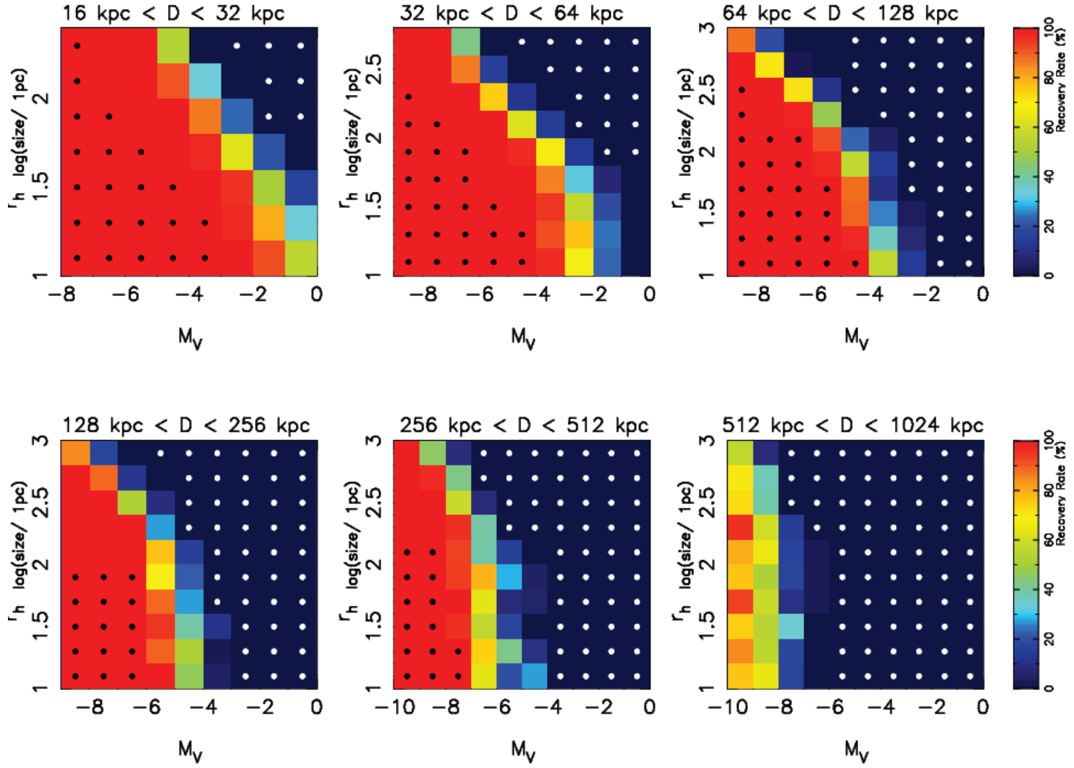

Figure B.5 - Satellite recovery fraction for $(l, b) = (210°, 35°)$ and $(l, b) = (240°, 35°)$

$(l, b) = (270^\circ, 35^\circ)$

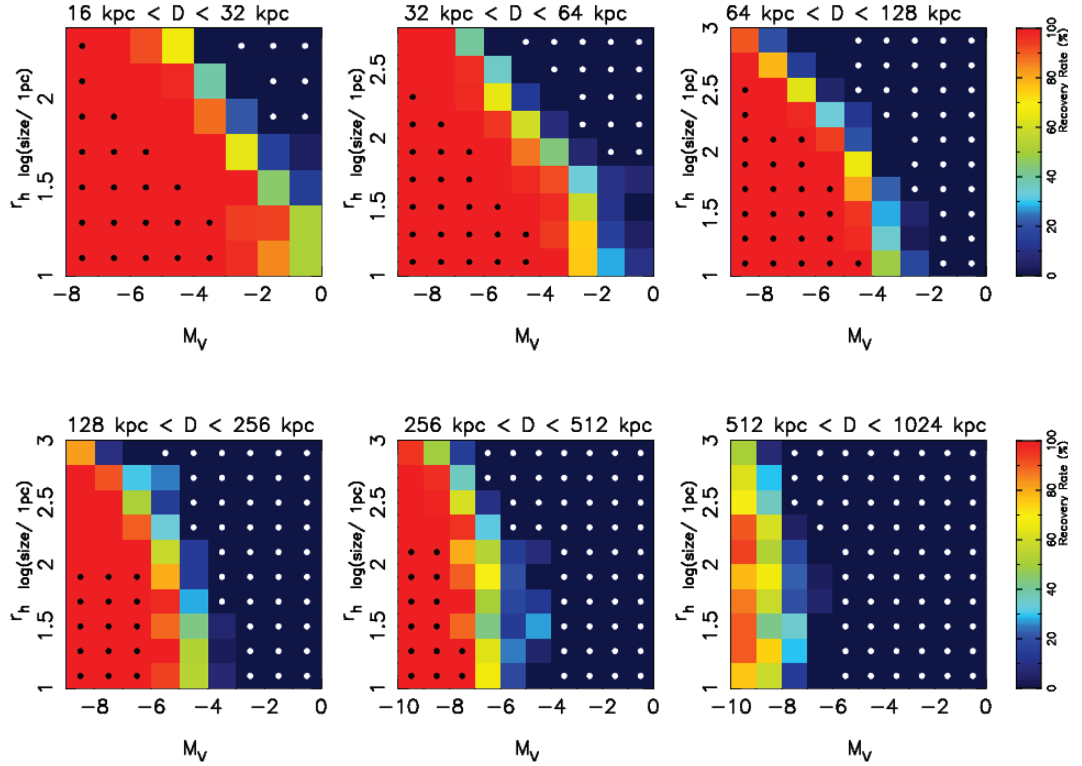

$(l, b) = (300^\circ, 35^\circ)$

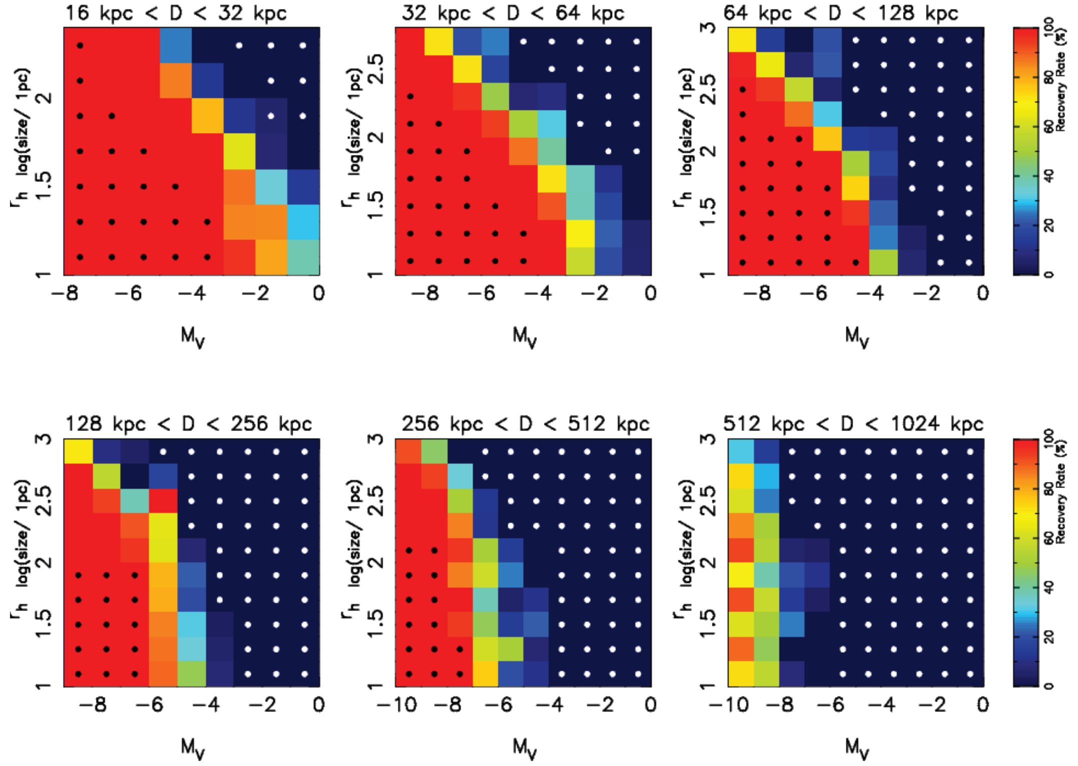

Figure B.6 - Satellite recovery fraction for $(l, b) = (270^\circ, 35^\circ)$ and $(l, b) = (300^\circ, 35^\circ)$

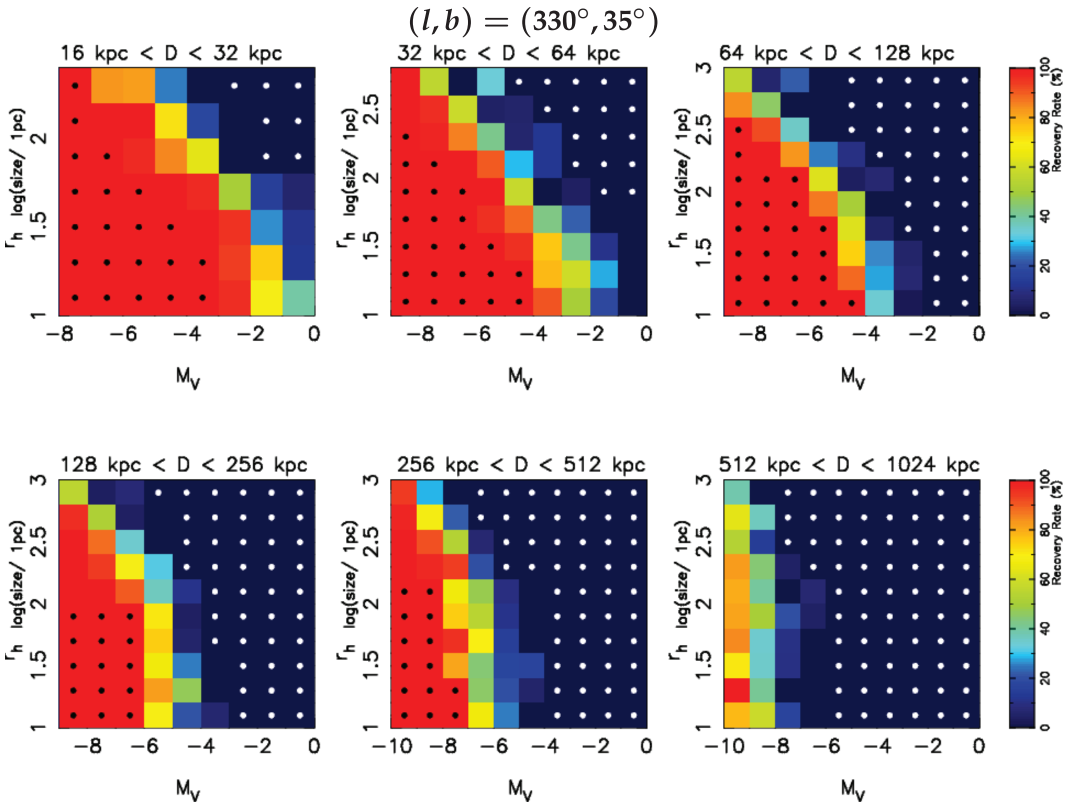

Figure B.7 - Satellite recovery fraction for $(l,b) = (330°,35°)$

B.1.2 Southern hemisphere

$(l, b) = (30^\circ, -35^\circ)$

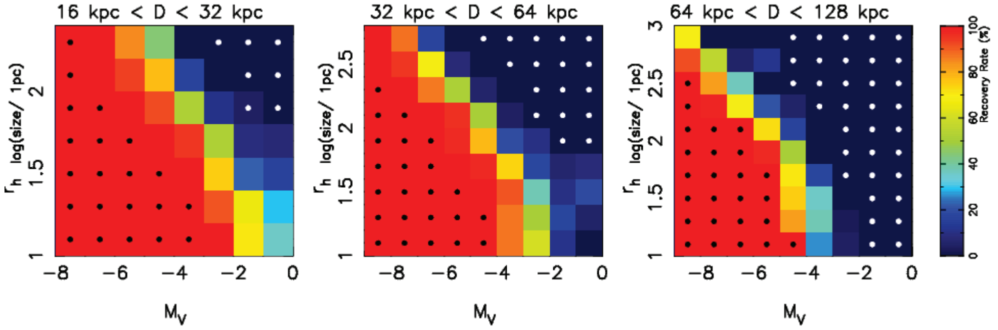

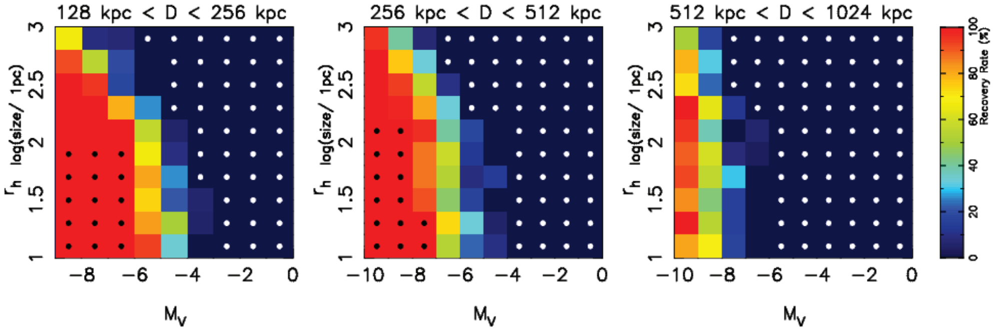

$(l, b) = (60^\circ, -35^\circ)$

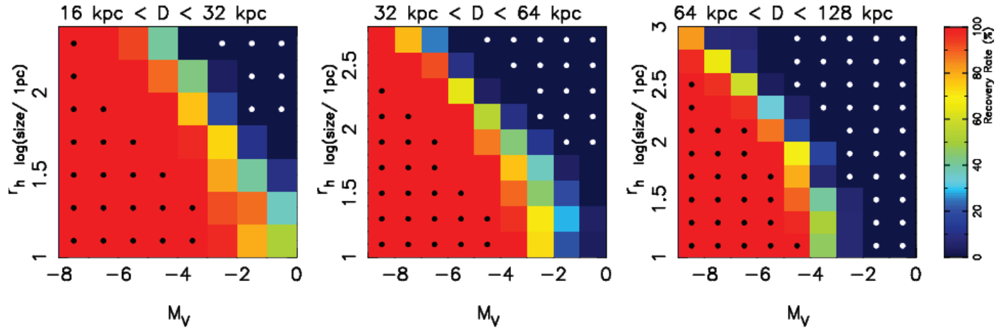

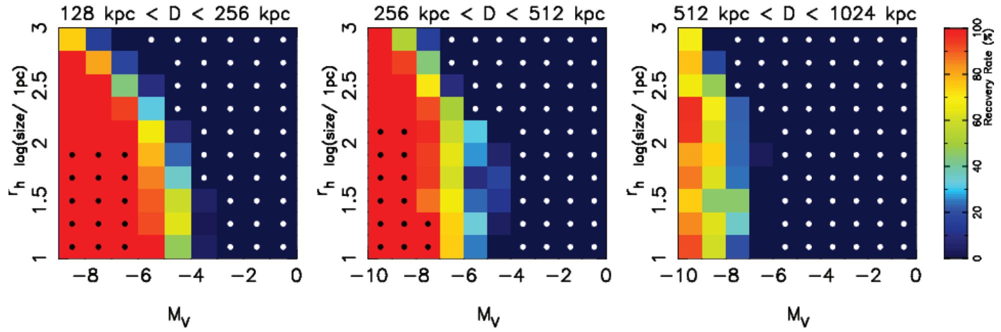

Figure B.8 - Satellite recovery fraction for $(l, b) = (30^\circ, -35^\circ)$ and $(l, b) = (60^\circ, -35^\circ)$

$(l, b) = (90^\circ, -35^\circ)$

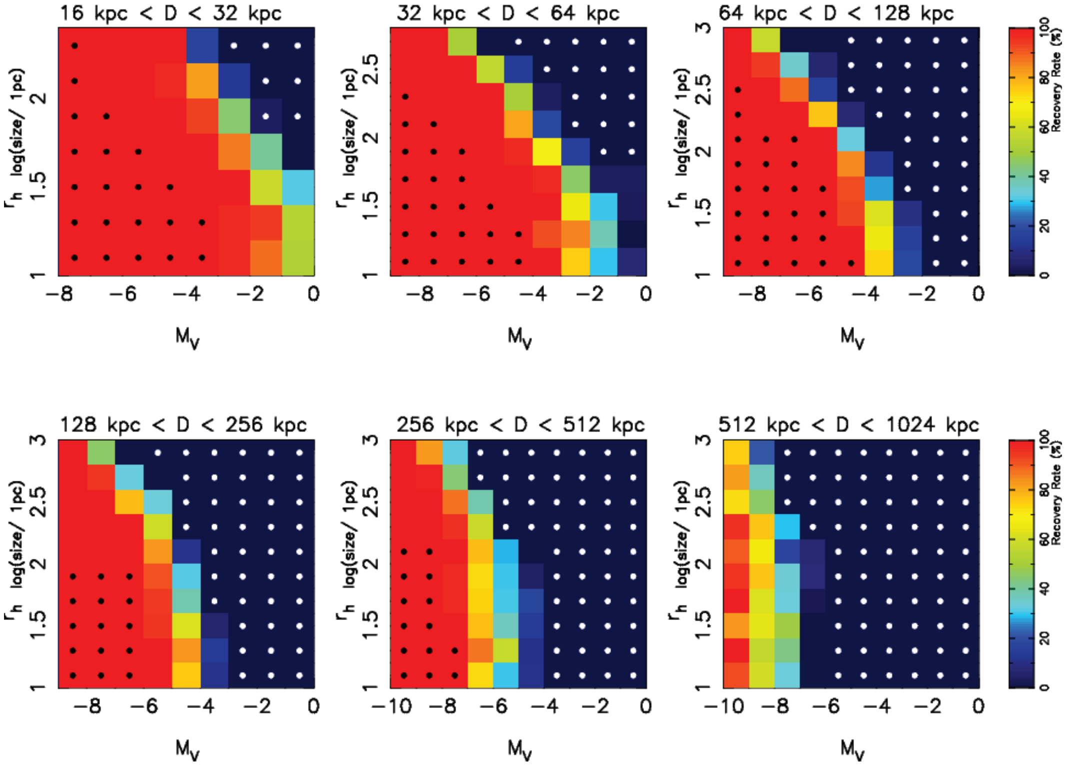

$(l, b) = (120^\circ, -35^\circ)$

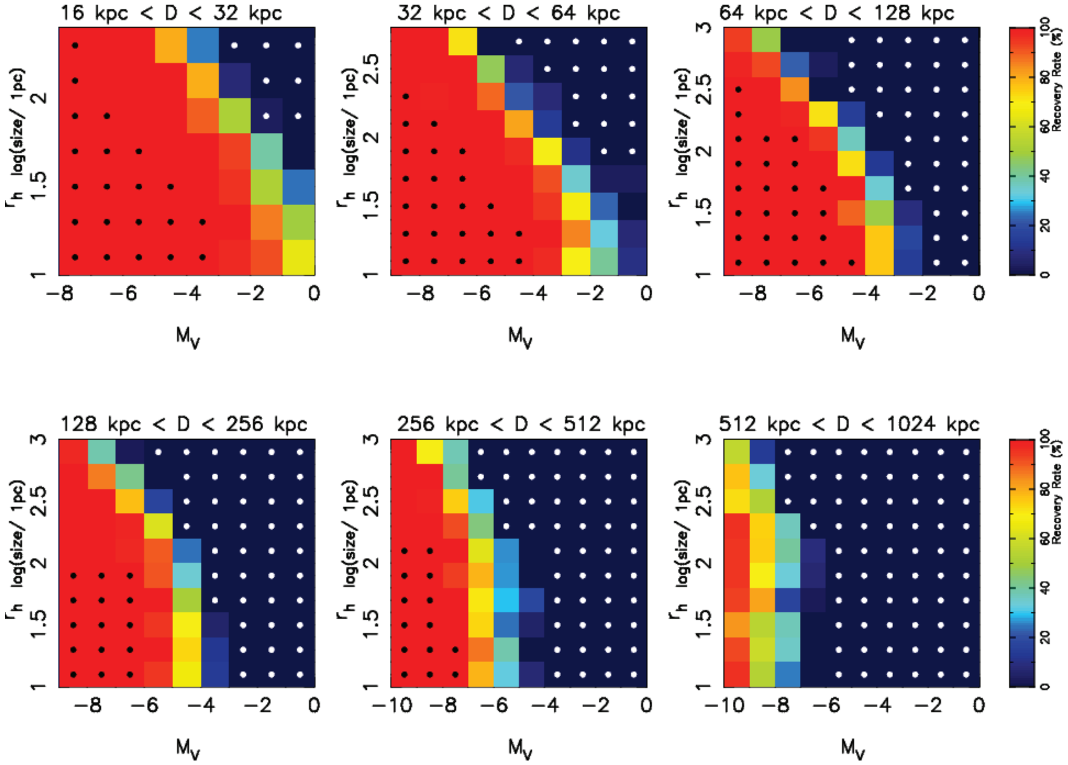

Figure B.9 - Satellite recovery fraction for $(l, b) = (90^\circ, -35^\circ)$ and $(l, b) = (120^\circ, -35^\circ)$

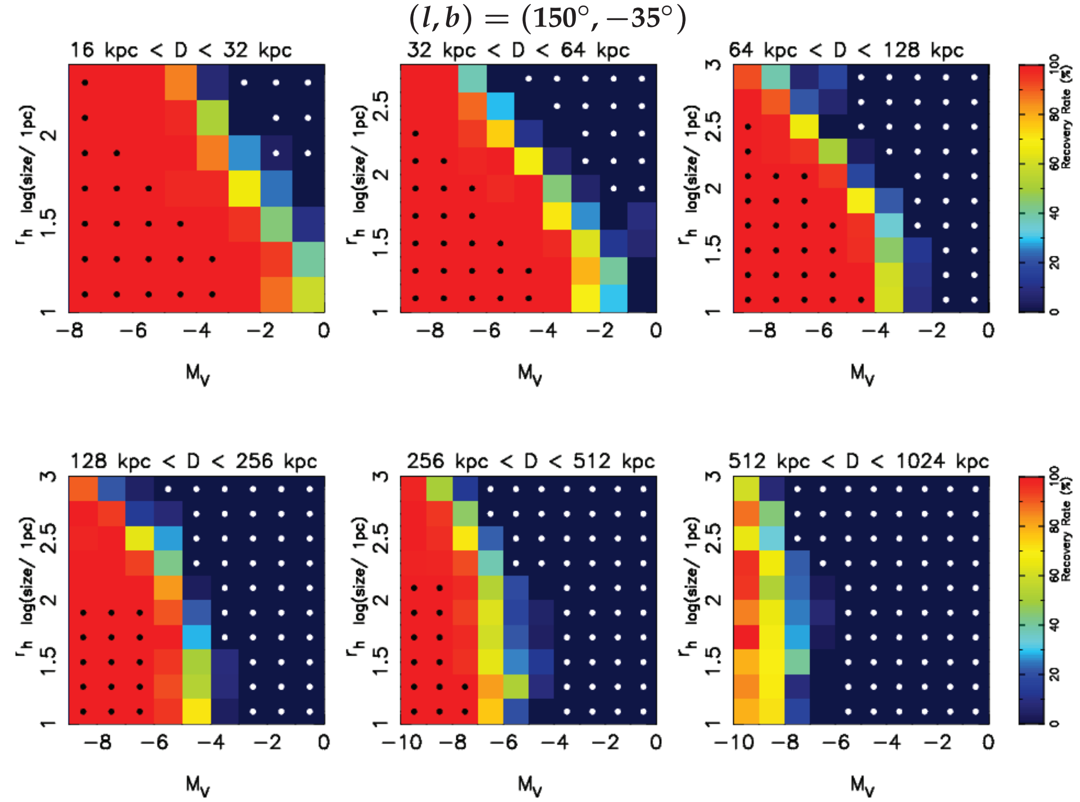
$(l, b) = (150^\circ, -35^\circ)$

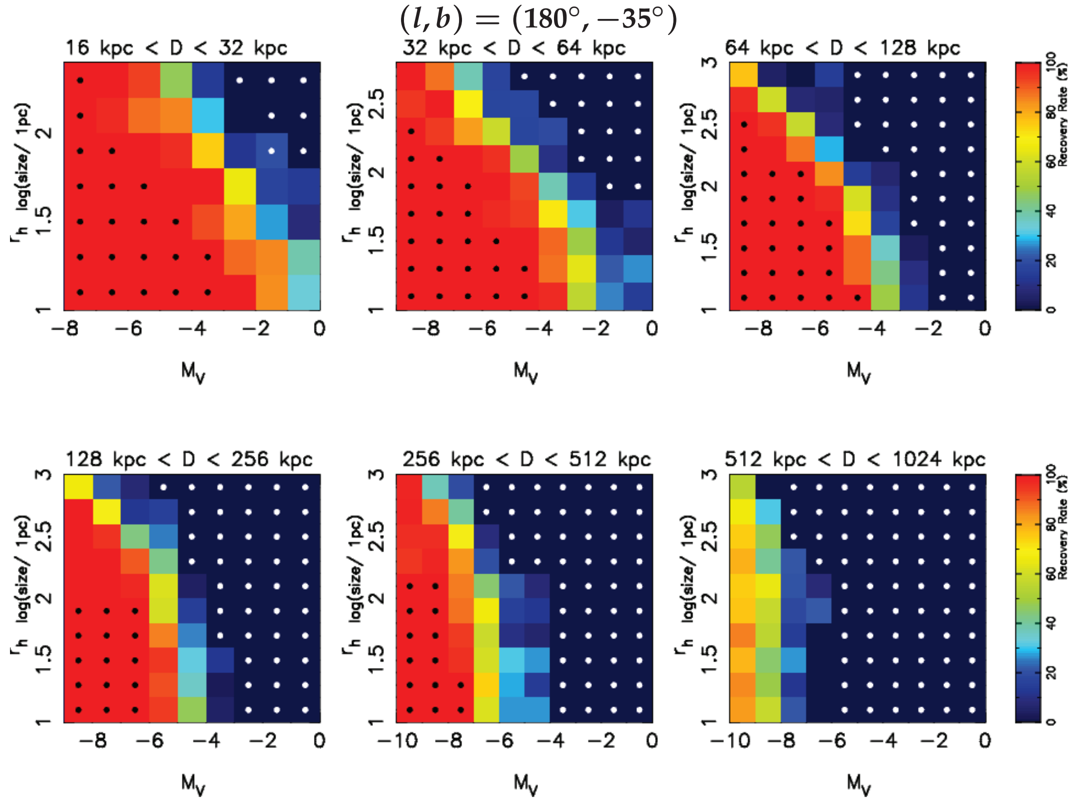
$(l, b) = (180^\circ, -35^\circ)$

Figure B.10 - Satellite recovery fraction for $(l, b) = (150^\circ, -35^\circ)$ and $(l, b) = (180^\circ, -35^\circ)$

$(l, b) = (210^\circ, -35^\circ)$

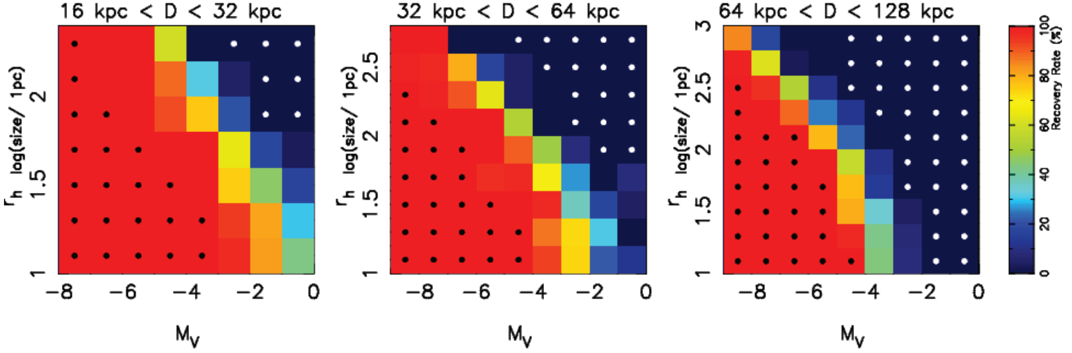

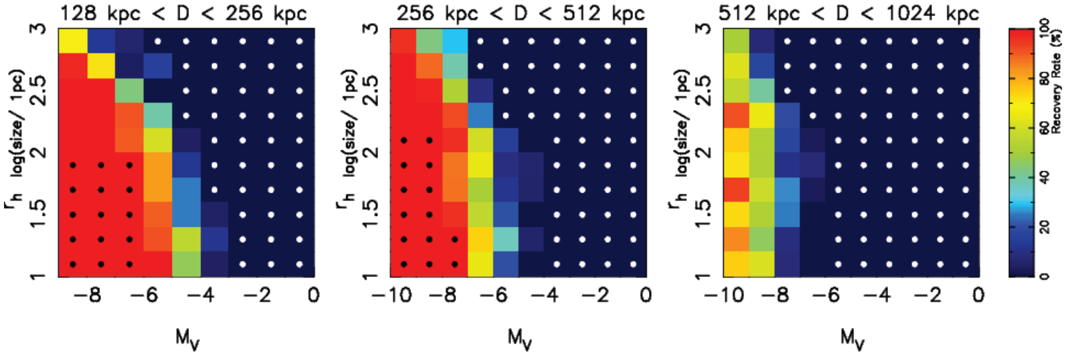

$(l, b) = (240^\circ, -35^\circ)$

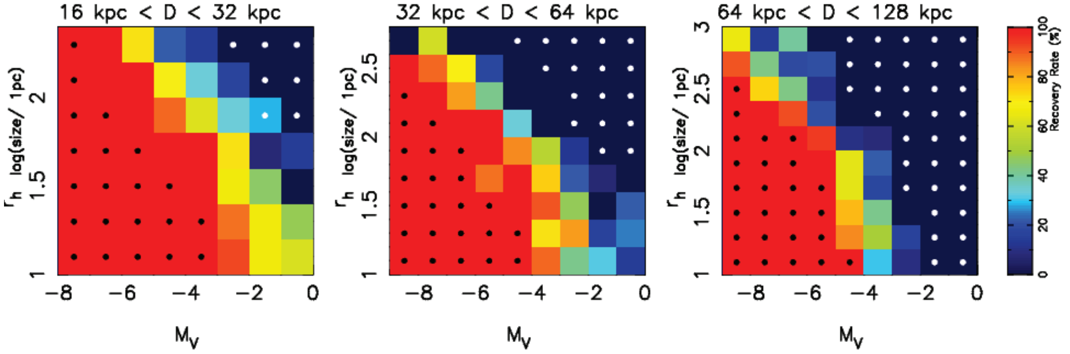

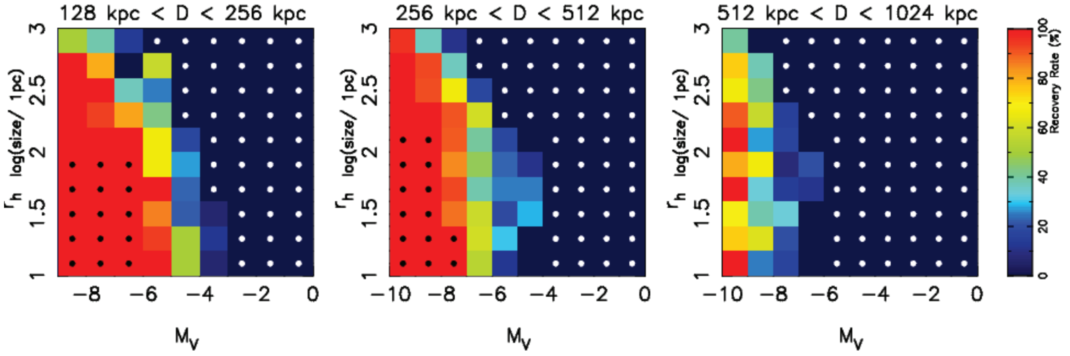

Figure B.11 - Satellite recovery fraction for $(l, b) = (210^\circ, -35^\circ)$ and $(l, b) = (240^\circ, -35^\circ)$

B.2 High–latitude

This section of the appendix contains the satellite recovery fraction for high latitude patches in the Northern and Southern hemisphere.

B.2.1 Northern hemisphere

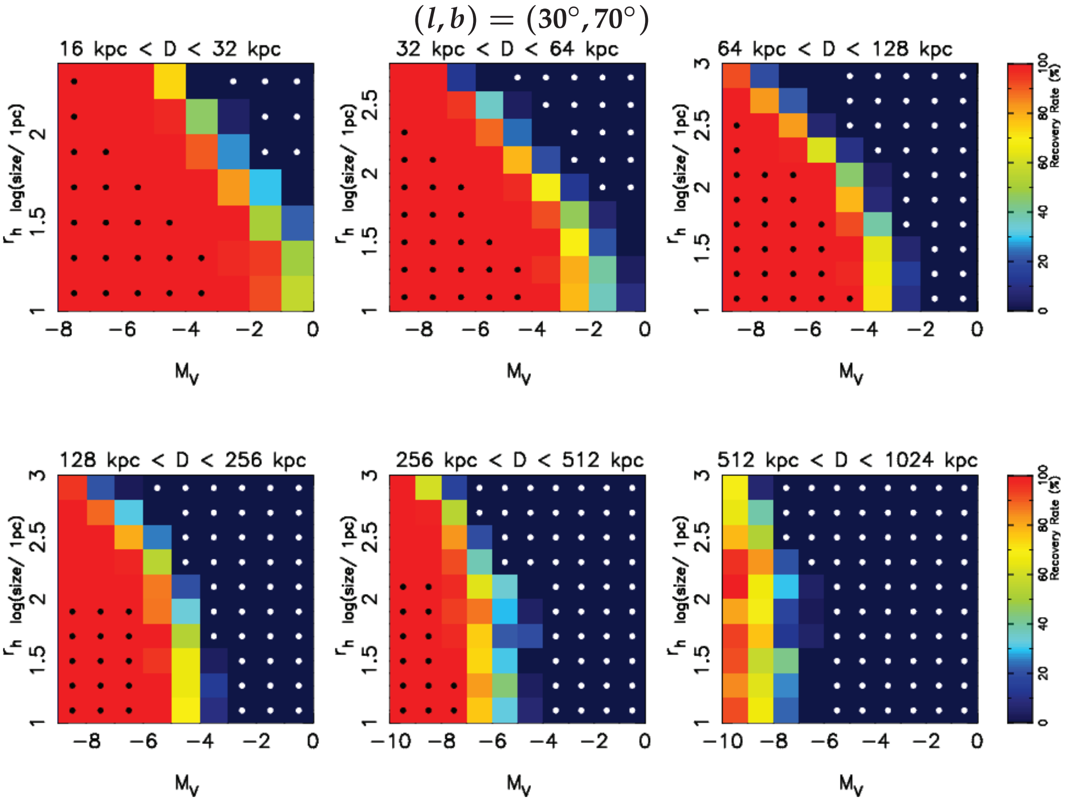

Figure B.12 - Satellite recovery fraction for $(l,b) = (30°,70°)$

$(l, b) = (90^\circ, 70^\circ)$

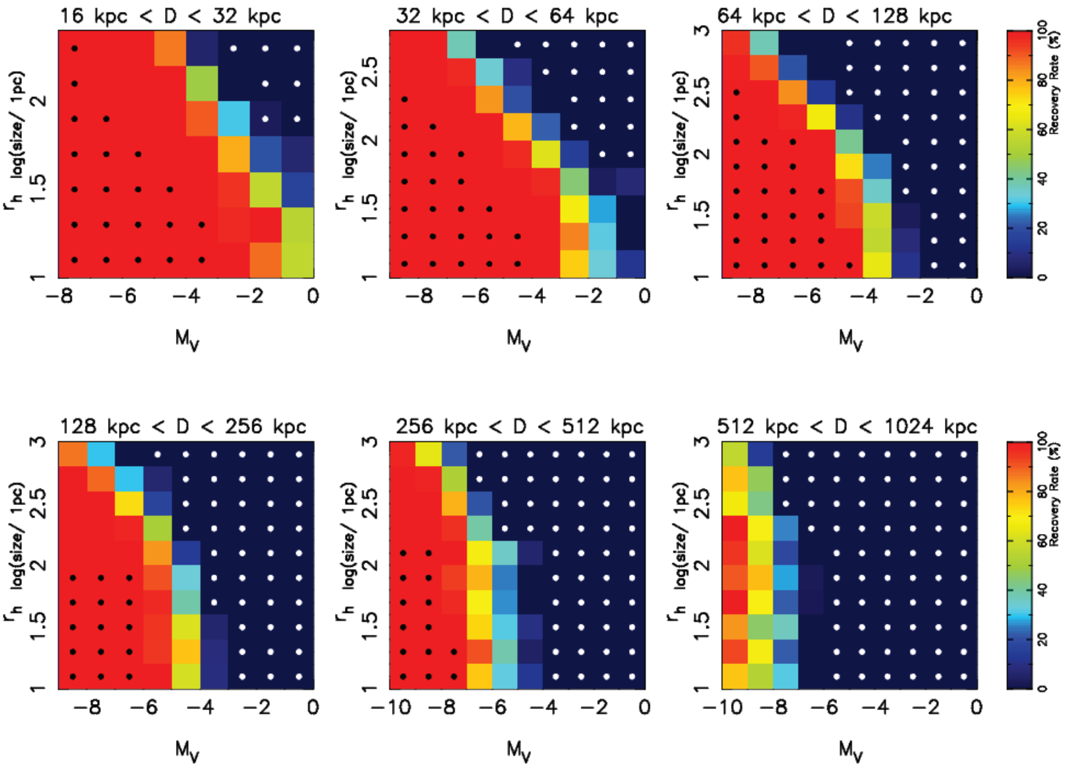

$(l, b) = (150^\circ, 70^\circ)$

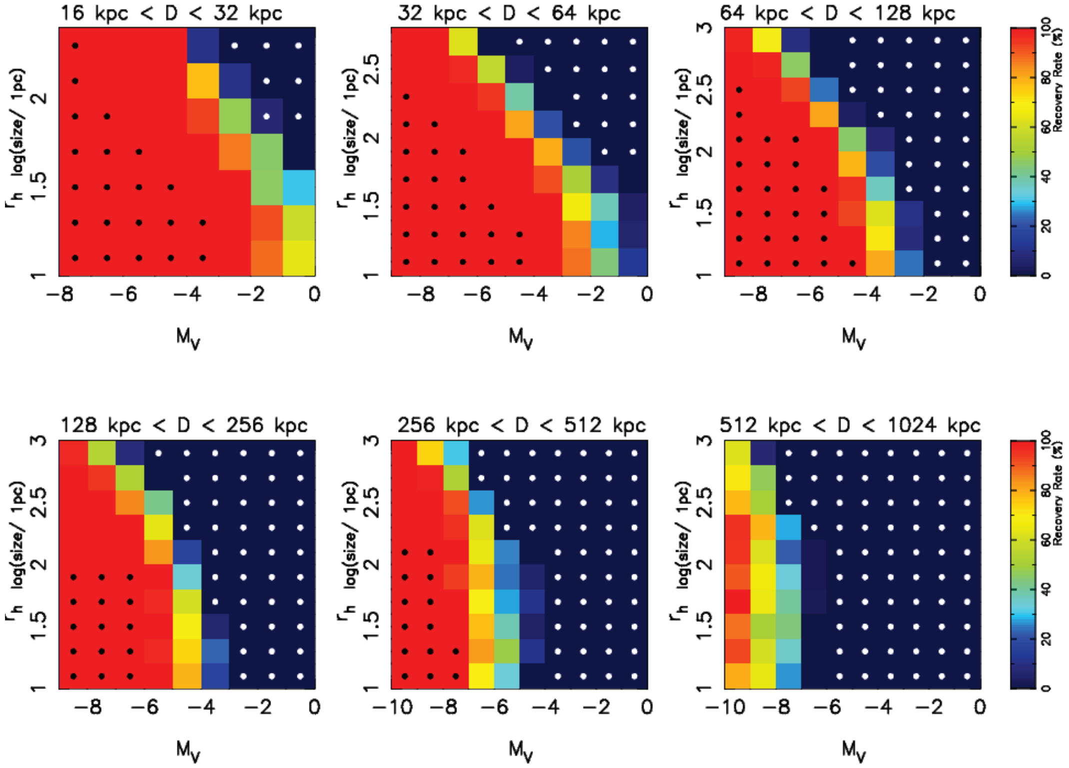

Figure B.13 - Satellite recovery fraction for $(l, b) = (90^\circ, 70^\circ)$ and $(l, b) = (150^\circ, 70^\circ)$

$(l, b) = (210°, 70°)$

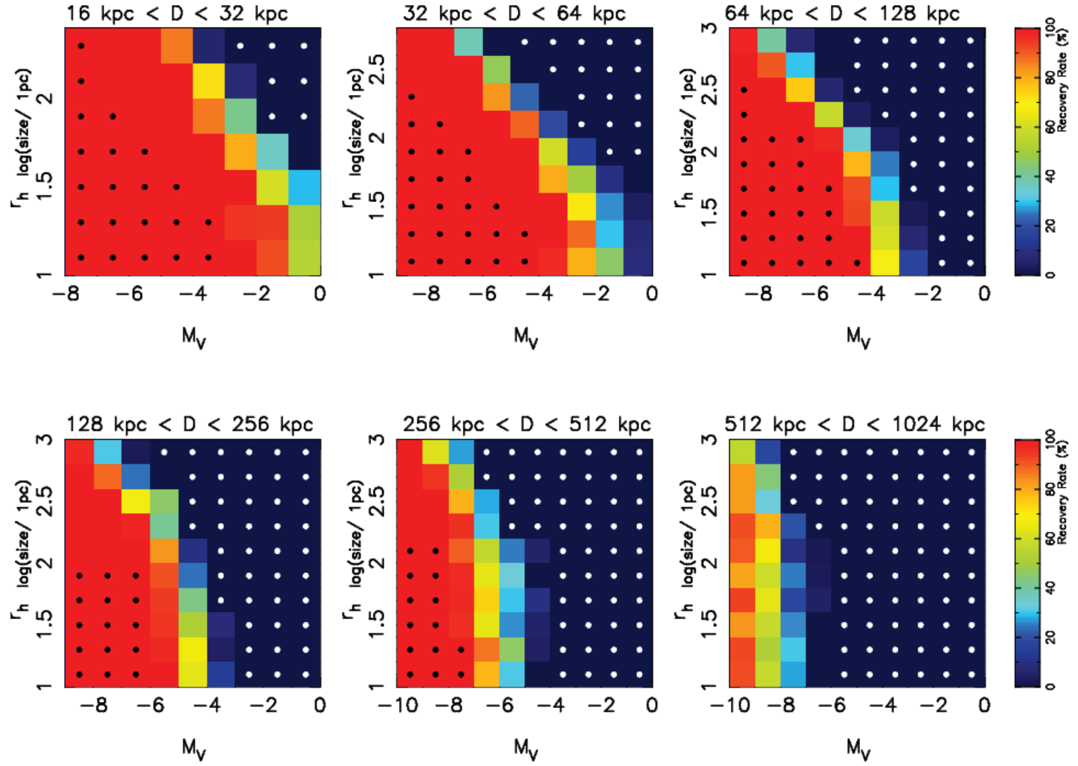

$(l, b) = (270°, 70°)$

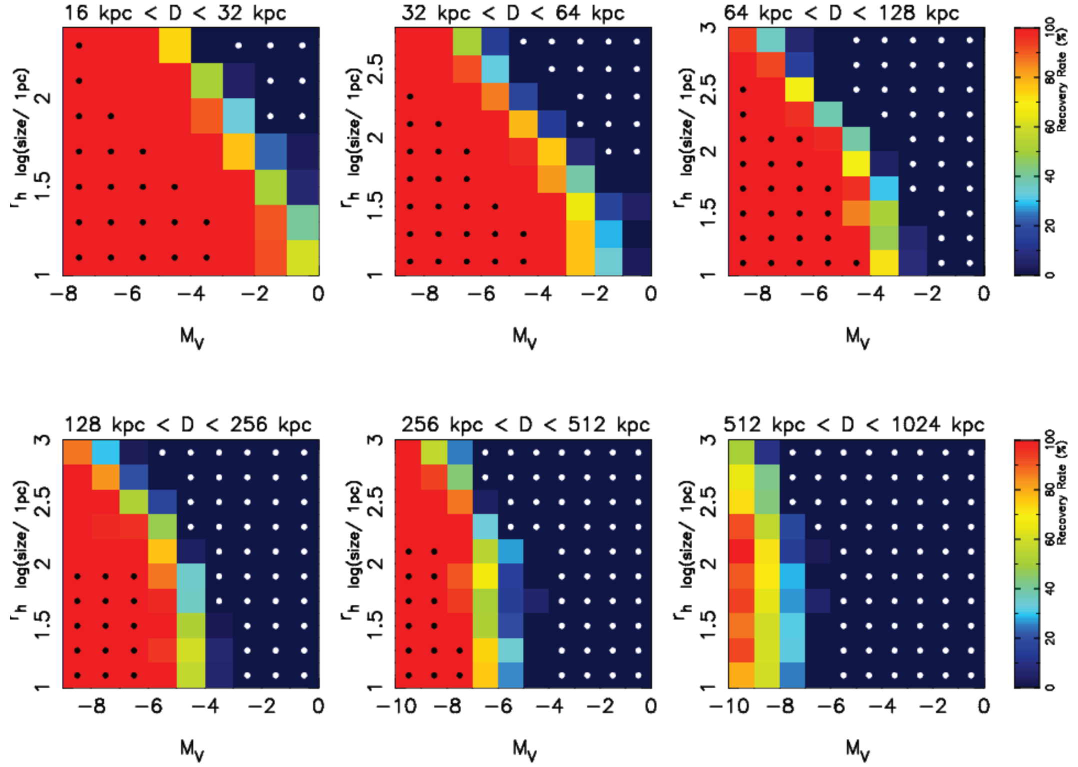

Figure B.14 - Satellite recovery fraction for $(l, b) = (210°, 70°)$ and $(l, b) = (270°, 70°)$

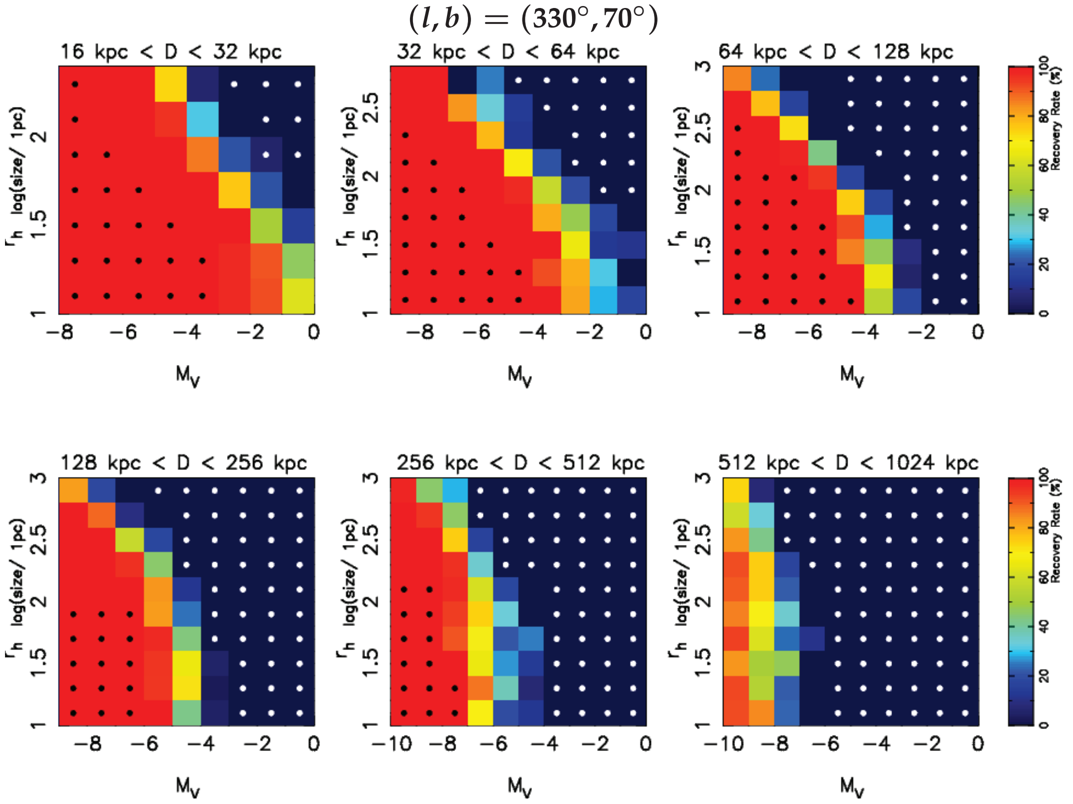

Figure B.15 - Satellite recovery fraction for $(l, b) = (330°, 70°)$

B.2.2 Southern hemisphere

$(l, b) = (30°, -70°)$

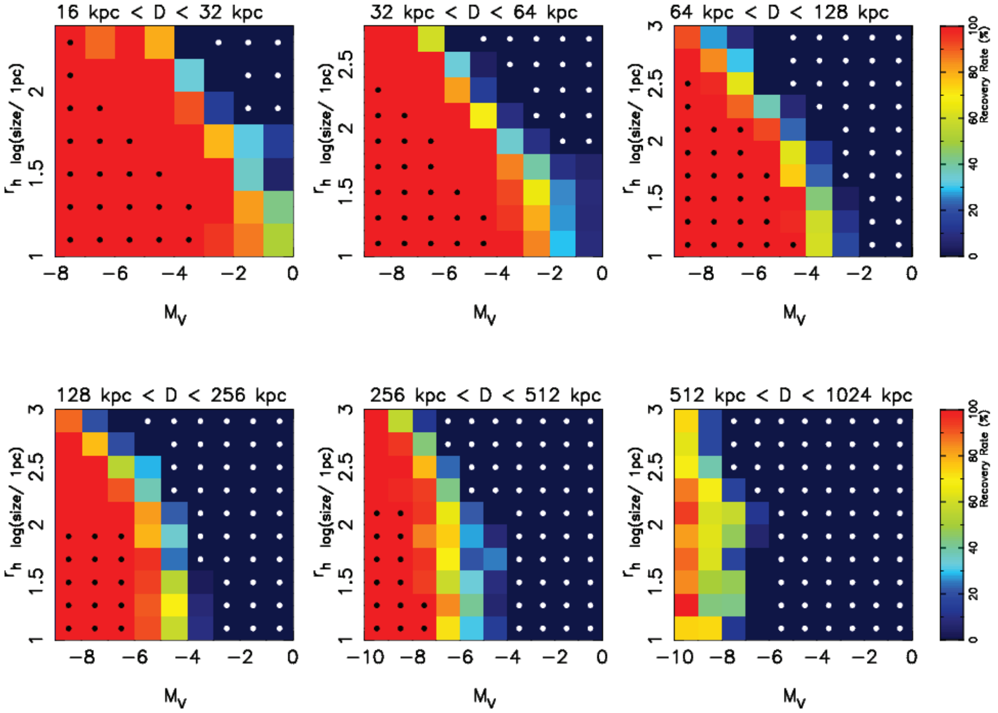

$(l, b) = (90°, -70°)$

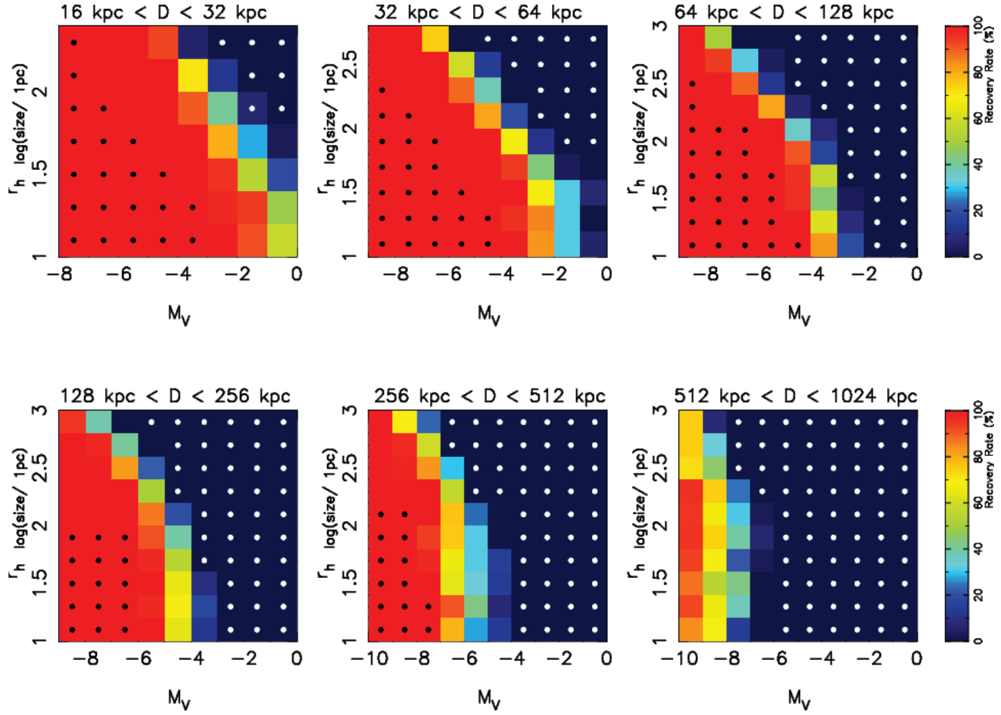

Figure B.16 - Satellite recovery fraction for $(l, b) = (30°, -70°)$ and $(l, b) = (90°, -70°)$

$(l, b) = (150°, -70°)$

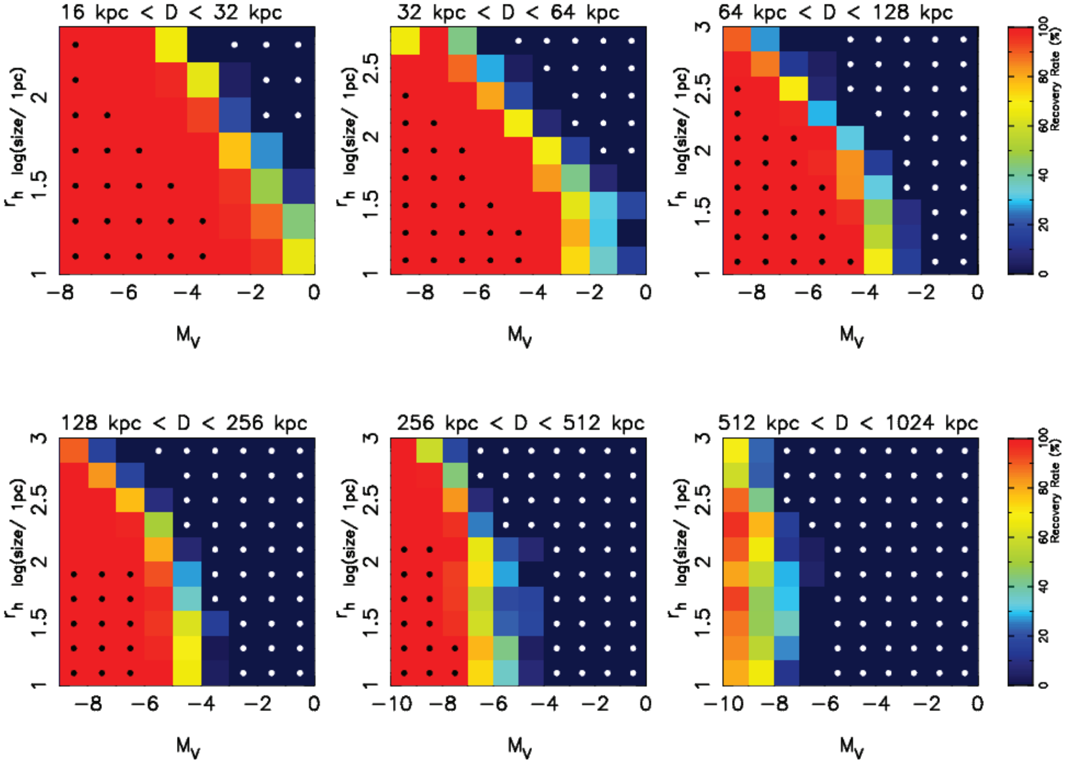

$(l, b) = (210°, -70°)$

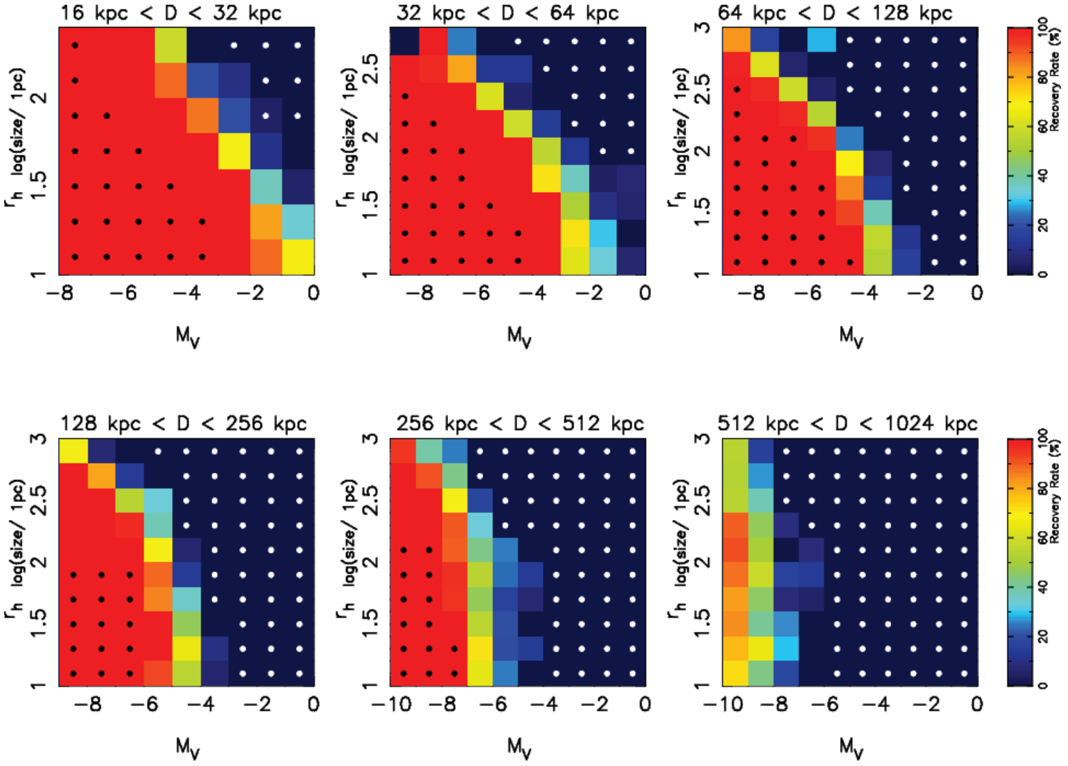

Figure B.17 - Satellite recovery fraction for $(l, b) = (150°, -70°)$ and $(l, b) = (210°, -70°)$

Résumé de Thèse

À la recherche et la caractérisation des galaxies plus sombres dans le groupe local avec le relevé Pan-STARRS 1

1 Introduction

1.1 La formation de galaxies dans le modèle ΛCDM

ΛCDM, le modèle cosmologique actuellement privilégié, décrivant l'évolution et la structure actuelle de l'Univers, se compose de deux éléments principaux: une constante cosmologique (Λ) et la Matière Noire Froide (*Cold Dark Matter* ; CDM). Le premier élément représente les effets de l'énergie sombre, qui représente l'expansion de l'espace contre la force attractive de la gravité. Le deuxième élément est une forme de matière; froide, car elle se déplace plus lentement que la vitesse de la lumière et est obscure, car elle est invisible, n'émettant pas de rayonnement (Binney & Tremaine, 2008). Cette matière est invoquée afin d'expliquer de nombreuses observations telles que la dynamique des galaxies et le regroupement de galaxies dans l'univers (Springel et al., 2005). Toute la masse visible dans l'univers ne peut expliquer les deux observations mentionnées ci-dessus. Les courbes de rotation d'étoiles dans les galaxies sont plattes, c'est à dire, la vitesse d'étoiles ne diminue pas avec la croissance du rayon de la galaxie, comme prévu à partir des lois de Newton (Sellwood & Sanders, 1988). De même, la masse visible dans l'univers ne peut pas expliquer pourquoi les galaxies sont regroupées ensemble et attirées dans des groupes tels que le Groupe Local dont la Voie Lactée, Andromède (M31) et de nombreuses autres galaxies plus petites (naines) sont ses principaux constituants. Par conséquent, une grande quantité de matière doit être présent, mais pas visible aux télescopes actuels, pour tenir compte de ces effets (Komatsu et al., 2009).

Il est dans ce contexte que les galaxies naines du Groupe Local sont devenues très intéressantes. Ces galaxies sont parmi les plus faibles en luminosité, les plus vieilles et les plus petites connues. Ces galaxies sont la plus petite échelle sur laquelle la matière noire se manifeste, contenant si peu de baryons que l'effet baryonique sur la matière noire n'est pas considéré comme très important. Ces galaxies sont donc parmi les objets les plus fortement dominées par la matière noire, que nous connaissons. Dans le modèle de ΛCDM, où les galaxies sont nées dans des halos de matière noire, elles sont proposées comme étant les constituants qui ont contribué à l'accumulation de grandes galaxies comme la Voie Lactée à travers une variété de mécanismes de fusion (collisions) et d'événements d'accrétion sur leur hôte. Plus spécifiquement, la matière noire s'effonds pour former des halos, qui au fil du temps se fondent pour produire de plus grands halos. Le gaz qui se réduit au centre de ces halos et refroidit, instigue la naissance d'une galaxie (White & Rees, 1978). La population actuelle de galaxies naines a survécu ces événements de fusion et accrétion. Avec les observations des galaxies naines actuelles nous pouvons en déduire les propriétés des constituants les plus anciens de l'univers. Puisque les étoiles sont des producteurs d'éléments chimiques, les observations de leurs abondances chimiques fournissent des contraintes sur la manière dont les étoiles se sont formées et quand la production d'étoiles a commencé et terminé. Les propriétés de ces satellites tels que leurs luminosités et tailles, ainsi que leurs contenus de matière noire, peuvent donner de fortes contraintes quant à la gamme des paramètres que ces satellites survivants peuvent prendre (Mateo, 1998;. Grebel et al., 2003; Gilmore et al, 2007). Par exemple, quelles propriétés déterminent que ces satellites se font accrétées par leur galaxie hôte? Quelles galaxies peuvent survivre ces interactions et dans quelle mesure? Quels éléments déterminent où ces satellites se situent par rapport à leur hôte?

1.2 Les Amas Globulaires

Appart les galaxies naines, une deuxième sorte de satellite existe. Les amas globulaires sont de petites concentrations d'étoiles anciennes et pauvres en métaux, résidant dans le halo d'une galaxie, assez massive pour accueillir ces satellites. Les scénarios de formation d'amas globulaires ne sont actuellement pas encore clairs, mais de façon générale, ces vieux satellites sont supposés d'être formé comme une partie de leur galaxie mère: la production d'étoiles est éteinte rapidement après la première génération d'étoiles est née. Il est pour cette raison que chaque une de ces amas globulaires ne sont pas considérés comme faisant partie de leur propre halo de matière noire. En fait, ils sont présentés comme des systèmes baryoniques, avec la plupart de leur masse visible étant la masse totale. Leurs puits de potentiel ne sont pas assez profonds et sont responsables pour le fait de ne pas pouvoir retenir le gaz, qui conduirait à des générations suivantes d'étoiles. Ces systèmes ne montrent donc pas d'écarts en métallicités. Leurs formations dans la galaxie mère expliquerait leurs emplacements préférentiels dans les parties intérieures de la Galaxie ($<$ 50 kpc). La gravité puissante qui lie ces objets explique leurs petites tailles (van den Bergh, 2008) ainsi que leurs formes sphériques ou globulaires. Dans les mêmes scénarios de formation, les amas globulaires qui sont observés dans les parties extérieures du halo de la Voie Lactée ($>$ 50 kpc) sont proposés comme étant les restants de galaxies naines plus massives, qui ont été détruites quand elles ont été accrété par la Voie Lactée.

1.3 Défis du modèle ΛCDM

Bien que ΛCDM ait largement réussi à reproduire l'univers dans sa structure actuelle, et notamment sur une grande échelle, en ce qui concerne la dynamique des galaxies et le regroupement des galaxies (Spergel et al., 2003;. Komatsu et al, 2011), le modèle ne survive pas à un scrutin rigoureux sur les plus petites échelles galactiques, celles des galaxies naines. Trois problèmes du modèle se sont présentés à la suite d'observations qui sont faites dans le groupe local et la Voie Lactée en particulier. Tout d'abord ΛCDM ne précise pas de préférence pour la façon dont ces satellites devraient être distribués autour de leur plus grande galaxie hôte (Starkenburg et al., 2013). Au lieu d'une distribution isotrope, cependant, un regroupement de ces satellites dans un plan est actuellement observé et proposé (Lynden-Bell, 1976; Pawlowski et al, 2012;. Ibata et al, 2013). Figure 1 montre la distribution actuelle des galaxies naines autour de la Voie Lactée. Deuxièmement, les simulations cosmologiques indiquent que des centaines de galaxies satellites ont dû survivre jusqu'aujourd'hui. Les observations actuelles montrent la densité de nombre de satellites étant un ordre de grandeur inférieur au nombre prévu : La Voie Lactée et M31 contiennent environ 70 satellites au total (Klypin et al., 1999). Figure 2 montre une multitude d'halos de matière noire (bleu) dans les simulations cosmologiques. Enfin, la distinction classique entre les galaxies naines et les amas globulaires est devenue tendancieuse (Gilmore et al., 2007). Bien que ce dernier point ne soit pas directement lié aux résultats du modèle de ΛCDM, ces distinctions font partie d'une théorie plus globale sur la formation des galaxies en supposant des rôles différent pour les plus petits constituants.

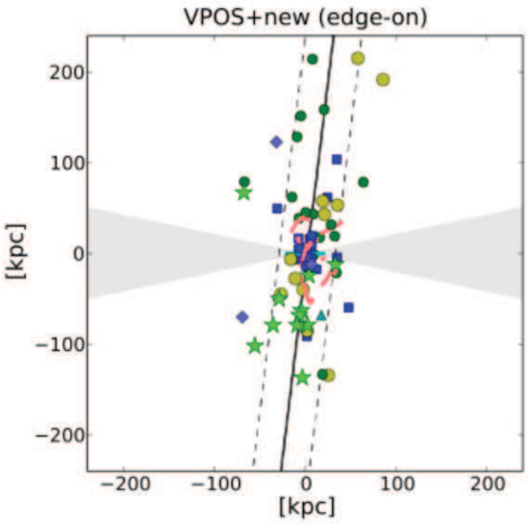

Figure 1: Le plan de satellites autour de la Voie Lactée (image de Pawlowski et al. 2015)

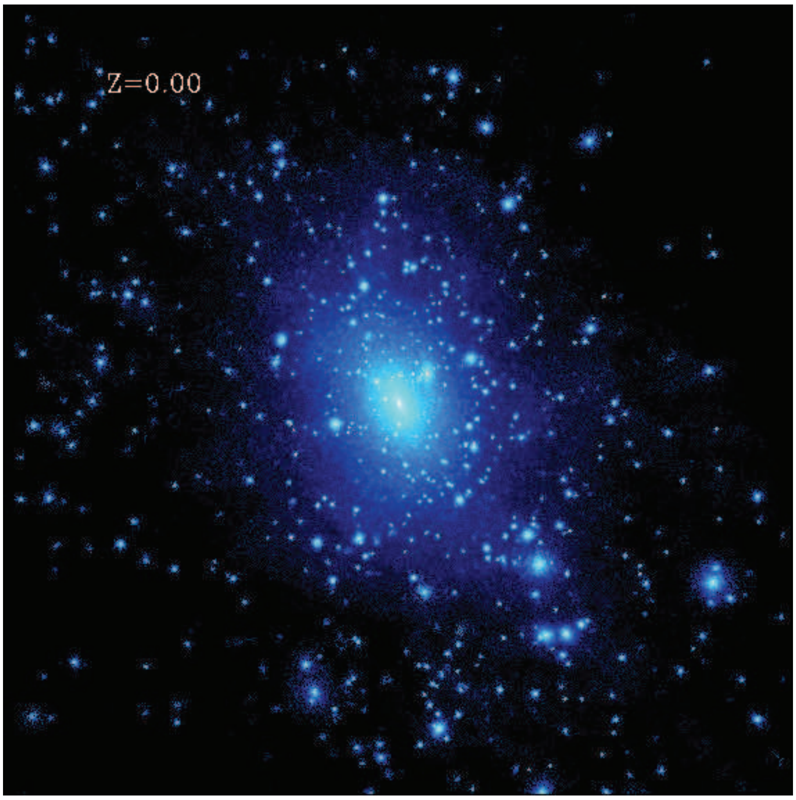

Figure 2: Simulation cosmologique qui montre une vue sur la Voie Lactée et ses environs aujourd'hui. Tous les points bleus représentent des halos de matière noire où les galaxies naines sont nées. La distribution est isotropique avec une centainde d'halos, ce qui est en tension avec les observations actuelles (Image: O. Gnedin).

1.4 Le relevé Pan-STARRS 1

Ayant expliqué les défis et les enjeus du modèle actuel du ΛCDM, ainsi que l'importance de comprendre les galaxies naines, je passerai maintenant à donner plus d'informations sur le relevé du *Panoramic Survey Telescope and Rapid Response System* ; Pan-STARRS 1 ou PS1, puisque ce relevé a été la principale ressource tout au long de la thèse pour chercher de nouvelles galaxies naines, un des buts principales de la thèse.

Le relevé PS1 a fait sa première observation en Juin 2006. Le télescope avec une taille de 1,8 m est situé sur Haleakala, Maui, Hawaii et a observé tout le ciel de nuit visible ($\delta > -30$). PS1 est panoramique *Panoramic* car les trois quarts du ciel sont observés. Le *Rapid Response* ou réponse rapide consiste en la capacité de détecter rapidement un événement astronomique intéressant, comme un astéroïde qui approche la terre. Le télescope a un appareil photo de 1.4 Giga pixels et un champ de vision de 3 degrés, équivalente à six fois la largeur de la pleine lune. PS1 a observé le ciel pendant 3.5 ans recueillant jusqu'à 4 expositions par ans dans chacune des 5 filtres optiques ($g_{P1}r_{P1}i_{P1}z_{P1}y_{P1}$; Tonry et al 2012). Une fois que les images individuelles ont été prises lors du sommet, elles sont téléchargées et traitées par le *Imaging Processing Pipeline* (Magnier, 2006, 2007;. Magnier et al, 2008).

1.5 Objectifs de thèse

Un bon nombre d'objectifs de cette thèse peuvent être vu dans le contexte des défis actuels du modèle ΛCDM. Nous avons vu dans les sections précédentes de l'introduction qu'il semblerait être une distribution anistrope, ou un plan des galaxies naines autour de la Voie Lactée. Cette idée souffre l'inconvénient que les parties du ciel sondées jusqu'à présent se retrouvent largement dans les endroits du plan. C'est pour cette raison que le relevé PS1 peut vraiment contribuer à cette discussion, puisque c'est le premier relevé qui couvre les trois quarts du ciel et peut donc faire des déclarations quantitatifs sur cette anistropie en cherchant des satellites en dehors du plan. La thèse a donc consisté de deux objectifs principaux. Le premier était la recherche de nouveaux galaxies naines autour de la Voie Lactée. Le deuxième objectif a été d'évaluer le taux de récupération de satellites simulés, à partir du quel l'anisotropie peut être quantifiée.

Dans le chapitre 2, je développe l'algorithme de recherche dans PS1, permettant la détection de nouvelles surdensités d'étoiles correspondant à de nouvelles galaxies naines. Ayant expliqué ceci, je passe à comparer l'efficacité de mon algorithme de recherche en la comparaissant avec le *Sloan Digital Sky Survey*.

Le chapitre 3 décrit les découvertes de nouveaux satellites de la Voie Lactée qui ont résulté suite à l'implémentation de l'algorithme de recherche. Ce chapitre fournit plus d'informations concernant les chapitres 4, 5 et 6.

Les chapitres 4, 5 et 6 contiennent un résumé des trois papiers qui ont résulté de mon travail de thèse détaillant la découverte et la caractérisation de cinq nouveaux satellite.

Dans le chapitre 7, les limites de détection de PS1 sont quantifiés. Plus spécifiquement, ce chapitre vise à répondre dans quelle mesure certains galaxies satellites de différents propriétés peuvent être recouverts, si ils sont simulés et injectés dans les données PS1.

Enfin, le chapitre 8 conclut avec un résumé des travaux de thèse. Ici, je conclurai avec un point de vue général du futur de ce champs d'astrophysique.

2 À La Recherche de Nouvelles Structures Stellaires Dans le Groupe Local

Dans ce chapitre, le lecteur est fourni avec les concepts généraux de l'algorithme de recherche. La nature des galaxies naines a déjà été établi dans l'introduction: elles sont parmi les galaxies les plus anciennes et les plus pauvres en métaux dans l'Univers. Puisque les étoiles vieilles et pauvres en métaux sont les principaux constituants de ces galaxies, une première étape logique serait d'isoler ces étoiles dans les données de PS1, en utilisant des isochrones. Le prochain aspect qui peut être représenté est la distance à laquelle une telle galaxie peut se trouver: ces galaxies peuvent se situer dans le voisinage de la Voie Lactée ou M31, les deux galaxies le relevé PS1 peut sonder en détail. De même, PS1 serait en mesure de trouver de galaxies naines isolés dans le Groupe Local aussi. Découvertes précédentes de galaxies naines montrent les distances variées à lesquelles ces galaxies naines peuvent se retrouver. La distance est donc pris en compte par le décalage de ces isochrones à plusieurs modules de distance de telle sorte que les étoiles qui se trouvent sur ces isochrones à la distance correspondante peuvent être isolés. Enfin, je peux tenir compte de la taille typique d'une galaxies naines en convoluant la densité d'étoiles isolées (avec les isochrones) avec des fonctions gaussiennes, qui ont des dispersions de l'ordre de la taille typique d'une galaxies naine, tout en soustrayant une convolution de la densité d'étoiles avec une gaussienne beaucoup plus grande pour tenir compte du fond galactique qui varie lentement. Cette opération produit des cartes de sur et sous densités, qui peuvent être convertis en cartes de probabilité. En tenant compte des galaxies et amas de galaxies beaucoup plus lointains et les systèmes stellaires déjà connus dans le Groupe Local, une liste de détections importantes peuvent être déterminées. Pour chaque position significative, le diagramme couleur-magnitude peut être inspecté ainsi que la distribution spatiale d'étoile afin de déterminer si une nouvelle galaxie satellite est trouvée. Dans cette analyse, l'empreinte complexe du relevé est prise en compte: certaines régions du relevé auront été mieux observé que d'autres pour des raisons météorologiques. Ces effets, ainsi que le développement de l'algorithme de recherche sur des tailles de données gérables est pris en compte pour l'algorithme de recherche de nouvelles structures stellaires.

Trois éléments supplémentaires doivent être prises en compte lors de l'exécution de cette analyse. Le premier est l'application de cette technique à des tailles de données gérables. Il est impossible d'exécuter une technique de recherche en une seule fois sur l'ensemble du catalogue de PS1. Non seulement, cela serait très confondant pour garder une trace de l'ensemble de l'opération, les problèmes de mémoire seraient énormes. Par conséquent, l'opération est réalisée sur des champs de 1600 degrés^2, en utilisant des coordonnées locales tangentiellement projetés, centrées sur b = +/-5, +/-35, +/-70. La deuxième question qui est prise en charge est la séparation d'étoiles de galaxies. Une combinaison d'un signal PS1 (stellaire) et la soustraction des magnitudes psf et aperture (galaxies) a été utilisée pour isoler les étoiles et les galaxies. Enfin, j'ai tenu compte de l'hétérogénéité spatiale, suite au mauvais temps, les trous entre les puces CCD etc. lors de l'exécution de la technique de convolution. Plus précisément, des facteurs de normalisation pour les régions du ciel qui n'ont pas été observé aussi profondément que d'autres parties. Avant l'analyse, toutes les magnitudes ont été dérougi pour tenir compte de la poussière.

Afin d'évaluer l'efficacité de l'algorithme de recherche développe, j'ai pu comparer les résultats de mon algorithme avec des algorithmes précédents développés pour le *Sloan Digital Sky Survey*; SDSS. Ce relevé a été responsable pour la découverte de nombreuses nouvelles galaxies naines. Puisque le relevé PS1 contient tout le ciel observé par le SDSS, je peux aller à tous les endroits où le SDSS a trouvé une nouvelle galaxie naine afin d'évaluer si l'endroit montre une surdensité significative suite à l'implémentation de l'algorithme. Dans la pluparts des cas une surdensité significative a été trouvée, renforçant ma confiance dans l'algorithme développé. Les probabilités de retrouvaille de ces galaxies naines du SDSS peuvent être vues dans tableau 1. Ayant constaté que l'algorithme marche, j'ai utilisé les valeurs de probabilité de ces galaxies naines pour déterminer à quelle valeur σ les données peuvent être coupées. Le but de ceci est de déterminer une limite réaliste, au-dessus duquel je peux investiguer les détections significatives. En coupant les données à 4.5σ, 1249 détections significatives ont été trouvées et investigués plus profondément.

Table 1: Significance de galaxies naines du SDSS en PS1

Galaxies Naines	$SN_{étoiles}$	$SN_{galaxies}$	Satellite	SN_{Stars}	SN_{Gals}
Leo I	97.5	27.1	Pisces II	6.7	-0.5
Leo II	89.6	11.5	Ursa Major II	6.4	2.0
Draco	47.7	5.8	Canes Venatici II	6.2	-1.2
Canes Venatici I	31.2	0.0	Segue 2	4.9	0.5
Ursa Minor	27.3	3.1	Ursa Major I	4.7	0.8
Bootes I	11.6	-0.1	Leo V	4.1	0.9
Sextans	11.2	0.1	Hercules	3.9	0.4
Willman 1	10.6	0.5	Pegasus III	3.7	-0.2
Coma Berenices	8.6	2.7	Bootes II	3.4	-0.8
Segue 1	7.3	-0.7	Leo IV	1.7	-0.1

3 Découvertes dans le relevé Pan-STARRS 1

Ce chapitre détaille les différents efforts qui ont été entrepris pour la recherche de nouveaux satellites. Suite à la découverte de nombreuses détections significatives, j'ai passé beaucoup de temps à obtenir des données plus profondes pour plusieurs détections. Dans la plupart des cas, il ne suffit pas de regarder les endroits significatives dans les données PS1 pour déterminer si une détection est 100% réelle. La qualité de données PS1 n'est pas toujours idéale et il est souvent désirable d'obtenir des données plus profondes avec d'autres télescopes afin de déterminer si la détection est réelle ou simplement une fluctuation (bruit) dans les données. Un peu moins de 100 heures de temps télescopique ont été consacrées à l'observation de candidats galaxies naines de la Voie Lactée. Une grande partie de la nouvelle couverture spatiale de PS1, comparé au relevé précédent responsable pour de nombreuses découvertes: le SDSS est dans le Sud. Nos efforts se concentrèrent davantage sur l'hémisphère Sud. Par conséquent, nous avons reçu 70 heures de recherche sur le Wide Field Imager sur le télescope 2.2m du MPG à La Silla. Cette campagne d'observations n'a abouti à aucunes nouvelles découvertes. Cet instrument a toutefois été utilisé pour confirmer la présence de notre première découverte de l'amas globulaire le plus lointain de la Voie Lactée: Laevens 1/Crater. Nous avons également reçu 20 heures de temps sur l'instrument BUSCA sur le télescope 2.2 m de l'Observatoire de Calar Alto en Espagne. Les données de cette recherche n'ont toujours pas été réduites à ce jour. Bien que je ne sache pas ce que ces images contiennent, je pense que les chances sont faibles que cette campagne révèlent de nouvelles galaxies, car la même version préliminaire des données de PS1 a été utilisé pour Calar Alto et La Silla. J'ai également été accordé 3 heures d'observations au *Large Binocular Telescope*; (LBT) et ai reçu encore quatre heures supplémentaires pour la (non-)confirmation de nouvelles galaxies naines.

4 Découverte de l'amas globulaire plus lointain de la Voie Lactée

Ce chapitre décris la découverte et surtout la caractérisation d'un nouvel amas globulaire à l'extrémité du halo la Voie Lactée. Situé à une distance héliocentrique de 145^{+17}_{-17}kpc, ce système est plutôt faible ($M_V = -4.3^{+0.2}_{-0.2}$), compact ($r_h = 20^{+2}_{-2}$ pc), rond ($\epsilon = 0.0^{+0.1}_{-0.0}$), plus jeunes que les plus anciens amas globulaires (∼8 Gyr), et assez pauvre en métaux ([Fe / H] ∼ -1.9). Bien que PSO J174.0675-10.8774 (le nom de l'amas globulaires) soit un peu plus éloigné que d'autres amas globulaires connus de la Voie Lactée, toutes les autres propriétés de ce système sont similaires à ceux des systèmes de amas globulaires dans la partie extérieure de la Voie Lactée (par exemple, Mackey Gilmore 2004; Mackey van den Bergh 2005). En particulier, la taille et la rondeur du système différencient l'amas globulaires des galaxies naines de la même luminosité, qui sont tous plus grands et ont au moins rh = 60 pc et ont tendance à favoriser les profils elliptiques de densité radiale (Martin et al 2008;. Sable et al. 2012). En outre, l'âge et la métallicité que nous déterminons de la comparaison avec isochrones sont assez typique des amas globulaires jeunes du halo externe.

Au-delà de notre environnement local, ce nouveau système stellaire est également semblable à la population de amas globulaires étendus, récemment trouvés dans les environs de M31, dont beaucoup se trouvent sur des courants d'étoiles, faibles en luminosité (Huxor et al 2005;. Mackey et al., 2010). Ces systèmes sont également ronds, mais compact pour les DG, et peuvent également présenter des branches horizontales rouges (par exemple, Mackey et al 2006, 2013;.. Huxor et al 2011). La découverte de cet amas globulaires le plus lointain de la Voie Lactée soutient l'idée que des amas globulaires éloignés sont une caractéristique commune des grandes galaxies spirales comme cela a été démontré dans M31 (Huxor et al., 2011), dans M33 (Cockcroft et al., 2011) et M81 (Jang et al. 2012). Une recherche plus détaillée dans les environs de cet nouvel objet serait intéressant dans le contexte des courants stellaires et leurs associations avec amas globulaires.

Après que cet amas globulaire avait été trouvé, nous avons appris de la découverte indépendante de cet objet par Belokurov et al. (2014) dans le relevé VST ATLAS. Leur détermination des propriétés du système sont compatibles avec les nôtres, même si ils déduisent une distance et taille légèrement plus grande ($\sim$ 170 kpc), ($r_h \sim 0.6' = 30$ pc à leur distance). Leur interprétation de la nature du système diffère néanmoins de la nôtre car ils favorisent un scénario dans lequel le système est une galaxie naine. Leur conclusion est en partie motivée par la plus grande taille qu'ils mesurent, mais aussi par leur interprétation d'une poignée d'étoiles bleues étant, qu'ils proposent en étant d'étoiles dans la phase de boucle bleue, ce qui serait indicatif d'une formation récente d'étoiles. Nous trouvons également ces étoiles dans nos données. Cependant, nous sommes prudents quant à leur interprétation. Notre analyse des paramètres structurels sur ces étoiles bleues donne une détection d'une surdensité avec une probabilité de $\sim 2\sigma - 3\sigma$. En outre, si ces étoiles étaient vraiment dans la phase de boucle bleue, on s'attendrait à la présence d'un nombre plus élevé de leurs analogues de mass faibles à des magnitudes plus faibles et couleurs plus bleues, ce que nous n'observons pas dans notre diagramme de couleur magnitude. Enfin, il ne peut pas être exclu que les deux étoiles bleues résidant à peine au-dessus de la branche horizontal pourraient en fait être des étoiles de la branche des géantes asymptotiques. Nous soulignons que cette conclusion doit être confirmée ou infirmée avec des vitesses radiales. Figure 3 montre un diagramme couleur magnitude de l'amas globulaire.

5 Découverte d'un nouveau système stellaire dans la constellation de Triangulum

Ce chapitre décris la découverte et la caractérisation de Laevens 2/Triangulum II (Lae 2/Tri II), dans les données de la PS1 et ensuite confirmé par le *Large Binocular Cameras* avec des données plus profondes. Situé à une distance héliocentrique de 30^{+2}_{-2} kpc, ce système est très faible ($M_V = -1.8^{+0.5}_{-0.5}$), vieille (~13 Gyr), pauvre en métaux ([Fe / H] $\sim$ -2.2), petite (34^{+9}_{-8} pc), et légèrement elliptique ($\epsilon = 0.21^{+0.17}_{-0.21}$). La magnitude et taille de ce nouveau système sont très similaires aux propriétés des satellites faibles Segue 1, Segue 2, Wilman 1 et Boötes II, qui ont tous été découverts récemment dans le SDSS. En fin de compte, des données spectroscopiques de haute qualité seront nécessaires pour une évaluation de la dynamique des étoiles de Lae 2/Tri II pour confirmer la nature de ce nouveau satellite. Cependant, la similitude de la distance, la taille, la magnitude absolue, l'âge et la métallicité à ceux de Wilman 1, Segue 1, Boötes II et Segue 2, que tous ont des dispersion de vitesse

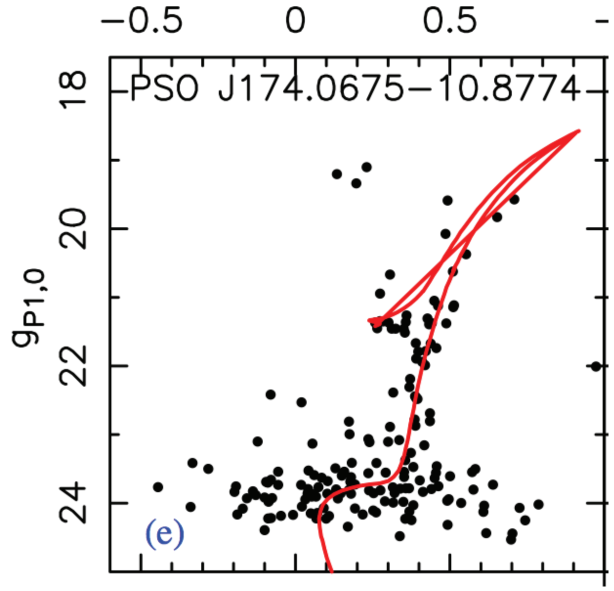

Figure 3: Diagramme Couleur Magnitude de Laevens 1/Crater. Une Branche de géantes rouges et une branche horizontale rouge est très clairement visible. L'isochrone démontre l'âge et métallicité préféré de 8 ans gigas et [Fe/H]=-1.9.

plus grandes que leur masse stellaire minuscule impliquerait (Martin et al 2007;. Simon et al., 2011; Willman et al 2011;. Kirby et al 2013) soupçonne que Lae 2/Tri II pourrait être une cinquième addition à ces types d'objets, peuplant la partie faible du domaine de galaxies. Figure 4 montre le diagramme couleur magnitude de Lae 2/Tri II

Il est également intéressant de noter que la position de Lae 2 / Tri II, $(l, b) = (141.4, -23.4)$, 20 ° à l'est de M31, place l'objet proche dans les environs de la structure du Triangle-Andromeda (TriAnd; Majewski et al 2004; Rocha Pinto et al-2004;. Sheffield et al 2014). Bien que cette surdensité stellaire de la Voie Lactée soit très complexe, avec des preuves pour plusieurs structures (Bonaca et al 2012; Martin et al 2013; Martin et al 2014), elle couvre une large gamme de distances pour englober Lae 2 / Tri II (∼15-35kpc). Une étude spectroscopique récente des étoiles au sein de TriAnd par Deason et al. (2014) a confirmé que, comme initialement proposé par Belokurov et al. (2009), que Segue 2 fait probablement partie de TriAnd, démontrant une tendance systématique de ces satellites faibles faisant partie de courants d'étoiles de la Voie Lactée. Segue 1 a été proposé d'être lié au *Orphan Stream* (Newberg et al., 2010), néanmoins des différences en abondances chimiques ont été observé entre les deux (Vargas et al 2013;.. Casey et al 2014). De même, la distance de Boötes II et la vitesse radiale sont compatibles avec le courant stellaire de Sagittaire (Koch et al., 2009), cependant des mesures d'abondances chimiques à haute résolution pour Boötes II questionnent cette association (Koch Rich 2014). Il reste possible, cependant, que les petits systèmes stellaires étaient des satellites de satellites plus grands, les progénitures de ces courant stellaires, atténuant ainsi la nécessité pour ces deux de partager des abondances similaires. Dans ce contexte, il est particulièrement intéressant de noter que Lae 2 / Tri II est situé sur l'extrapolation linéaire de l'Archaeological Survey Andromeda Pan (PAndAS) courant stellaire de la Voie Lactée (Martin et al. 2014), 10 ° au-delà de l'empreinte PAndAS où cette satellite a été découvert. Le courant et le satellite ne sont pas alignés; cependant, les incertitudes sur l'angle de position et ellipticité ne sont pas concluants en excluant une connexion entre les deux. Ici aussi, la spectroscopie est nécessaire pour obtenir la vitesse systémique de Lae 2 / Tri II pour confirmer qu'elle est compatible avec le mouvement global de Triangulum-Andromeda et, en particulier, avec la vitesse du courant PAndAS de la Voie Lactée. Ceci contribuera à renforcer ou infirmer cette hypothèse.

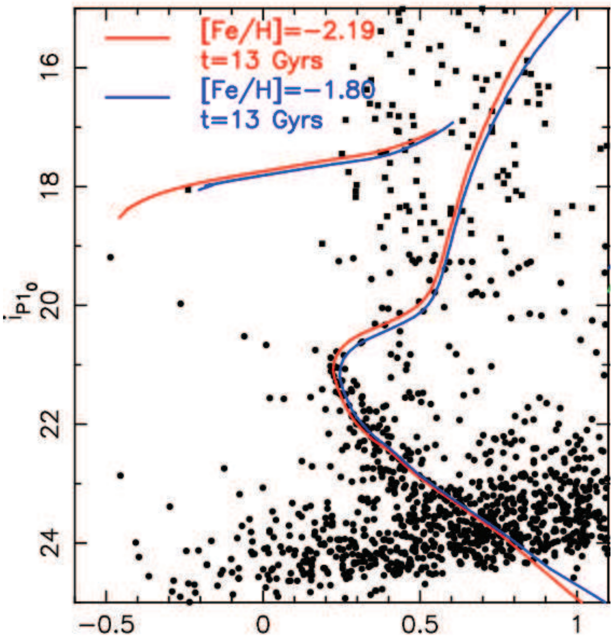

Figure 4: Diagramme Couleur Magnitude de Lae 2/Tri II. La seule caractéristique de l'évolution stellaire de ce système est la séquence principale. Des isochrones vieux et pauvres en métaux montre la population typique de cette galaxie naine.

6 Trois nouveaux satellites dans Sagittaire, Dragon et Dauphin

Ce chapitre décrit la découverte de trois nouveaux satellites: Sagittarius II (Sgr II), Draco II (Dra II) et Laevens 3 (Lae 3). Sgr II a une taille et luminosité intéressante relative à d'autres galaxies naines et amas globulaires. Bien que d'autres satellites de la Voie Lactée soient connues avec des magnitudes absolues semblables, Sgr II est plus petite que Coma Berenices ($r_h = 74^{+4}_{-4}$pc; Munoz et al. 2010, PiscesII ($r_h = 58^{+10}_{-10}$pc; Sand et al 2012), Hydra II ($r_h = 68^{+11}_{-11}$ pc; Martin et al 2015), ou les plus grands satellites comme Leo IV et Leo V ($r_h = 205^{+36}_{-36}$pc and $r_h = 133^{+31}_{-31}$ pc; de Jong et al. 2010), ou Ursa Major I ($r_h = 318^{+45}_{-45}$ pc;

Martin et al. 2008) D'autre part, Sgr II est plus grand que le plus grand amas globulaire, PAL 14 ($r_h \sim 25$pc; Hilker et al. 2006). Il convient toutefois de noter que, récemment, de M31 satellites présumés d'être d'amas globulaires ont été découverts avec des tailles similaires (Huxor et al. 2014), bien que la nature de certains de ces systèmes est également ambigu (Mackey et al. 2013). En fin de compte, la spectroscopie sera nécessaire pour mésurer la dispersion de la vitesse du satellite pour confirmer pleinement la nature de ce satellite et si il est dominé par la matière sombre.La position de Sgr II est intéressant car cet objet se trouve 15 degrés de Sgr dSph et à la position attendue de l'extrapolation de courant d'étoiles de Sagittarius, ce qui peut pointer vers une association entre le courant et l'objet. Le fait que Sgr II se trouve 40-45 kpc derrière Sgr dSph exclut un lien direct entre les deux satellites, mais une comparaison avec le modèle N-corps de Law and Majewski (2010b) pour le courant d'étoiles de Sgr révèle que Sgr II est situé à la distance prévue de ces particules du modèle. Il est donc probable que Sgr II a été introduit dans le halo de la voie Lactée avec cette partie du courant, de façon similaire à de nombreux autres amas globulaires dans le halo de la Voie Lactée (par exemple Law Majewski 2010a). La découverte de Sgr II et son association avec le courant pourrait ajouter des contraintes sur la modélisation du courant d'étoiles de Sagittarius si l'association se confirme à la base de vitesses radiales.

Draco II a également un caractère ambigu, mais ceci est principalement lié aux grandes incertitudes sur ses paramètres structurels et la distance, dûs à la nature faible de l'objet dans les données PS1. Avec la photométrie actuelle, le satellite semble partager les propriétés de Kim 2 ou Eridanus III, qui sont supposés d'être des amas globulaires (Kim et al 2015b;. Bechtol et al 2015; Koposov et al 2015). D'autre part, ses propriétés incertaines sont également totalement compatible avec ceux de Wilman , favorisée comme étant une galaxie naine (Willman et al., 2011). Ici aussi, la photométrie et / ou spectroscopie profonde sont nécessaires pour classer ce système. En tenant compte du lien commun entre systèmes stellaires faibles et les courants stellaires, j'ai étudié une possible association entre l'object et les courants stellaires déjà connus dans la Voie Lactée. Le courant le plus proche de Dra II est le courant GD-1 (Grill- Mair Dionatos 2006). L'extrapolation de l'orbite du courant à la position de Dra II montre que celui-ci se trouve seulement 5-6 degrés du satellite (Koposov et al. 2010). Toutefois, la distance extrapolée du courant atteint seulement 12 kpc, contrairement à la distance de 20kpc de Dra II. Par conséquent, si le courant GD-1 ne dévie pas de façon significative de cette extrapoltion (Koposov et al. 2010), la distance actuelle de Dra II apparaît trop élevé pour une association directe.

La petite taille de Lae 3 (7+/-2 pc) met cet object bien dans le régime des amas globulaires. Avec un âge relativement jeune (∼9 Gyr) et les populations stellaires qui ne sont pas très pauvres en métaux ([Fe / H] ∼ -1.9), il serait naturel de classer Lae 3 comme un amas globulaire, jeune dans la région extérieure du halo de la Voie Lactée (Mackey et van den Bergh, 2005). Toutefois, certaines réserves sont à noter: l'ajustement de isochrone repose sur la photométrie actuellement disponibles (Figure 5, qui souffre de surpopulation. La présence d'une étoile RR Lyra pourrait être en contradiction avec une jeune scénario de halo puisque sa présence rappelle à un système qui est âgé d'au moins 10 Gyrs. Aucune connexion possible a été trouvé entre ce nouveau système et des courants stellaires connus dans le halo de la Voie Lactée. Les diagrammes couleur–magnitude des trois systèmes stellaires peuvent être vu dans Figure 5.

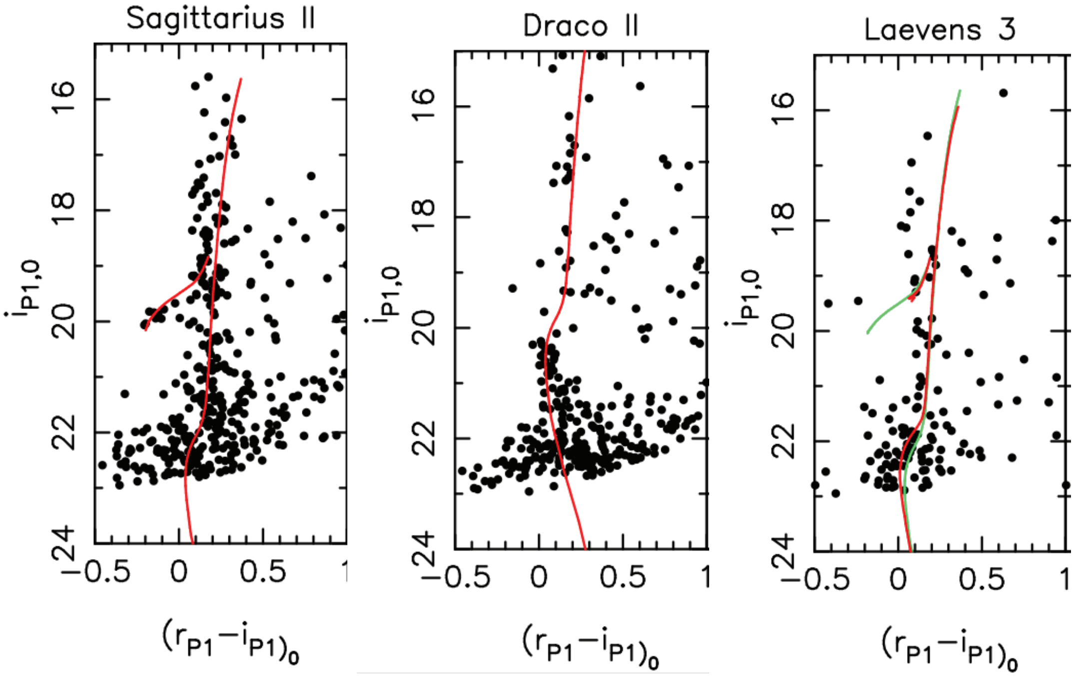

Figure 5: Diagrammes Couleur Magnitude de Sgr II, Dra II et Lae 3. Des isochrones vieux et pauvres en métaux montre la population typique de ces objects.

7 Quantifier les limites de détection du relevé Pan-STARRS 1

Déterminer les limites de détection du relevé PS1 est un exercice important, car il permettra d'évaluer deux aspects différents: la qualité des données de PS1 et l'analyse de l'efficacité de la technique de recherche développé. Avant de se lancer sur ce point, une idée générale peut déjà être théorisé concernant les résultats que telle entreprise peut donner. Tout d'abord, le relevé de PS1 est très similaire au SDSS en termes de profondeur, donc on pourrait s'attendre à ce que les résultats pour PS1 soient semblables aux tentatifs précédents des scientifiques qui ont quantifier les limites de détections du SDSS (en supposant une technique de recherche efficace). Deuxièmement, les résultats de chapitre 2 ont déjà donné une indication globale sur les propriétés de sous-structure qui peuvent être retrouvés. Si la photométrie et la distinction entre étoiles et galaxies est optimisée, les résultats suite à l'implémentation de l'algorithme de recherche sont similaires à ceux du SDSS, avec la récupération convaincante de la plupart des galaxies naines et amas globulaires du SDSS. À ce jour seulement cinq nouveaux satellites ont été trouvés, ce qui est un nombre relativement faible, lorsque l'on considère que le volume de recherche PS1 est 1,5 - 2 fois ceux du SDSS, qui dans l'ensemble a révélé 16 galaxies naines de la Voie Lactée et 5 amas globulaires de la Voie Lactée. Encore plus frappant, lors d'une inspection plus profonde concernant la nature de ces découvertes, est que pas un seul d'entre eux est un galaxies naines sans ambiguïté comme par exemple Bootes I ou Pisces II: deux des nouveaux satellites sont des amas globulaires (Laevens 1/Crater et Laevens 3), ensuite Triangulum II montre des caractéristiques similaires à ceux de Segue 1, avec les deux derniers découvertes plus récents, affichant des propriétés entre galaxies naines et amas globulaires (Sagittaire II, Draco II). Le nombre bas de découvertes illustre la nécessité de quantifier les limites de détection. Cet effort peut à son tour conduire à la quantification de la (an)isotropie de la distribution d'amas globulaires de la Voie Lactée.

Le but de ce chapitre est donc de quantifier la réponse à la question suivante: Si x-nombre de galaxies sont insérés dans le relevé PS1 avec Y-paramètres en z-position, quelle est la probabilité d'observer la galaxie i avec le paramètre y_i à position z_i". Laissez-nous rapporter cela au cas spécifique de deux galaxies naines du SDSS: Bootes I ($M_V = -6.3$, $r_h = 242$pc et $d = 67$kpc) et Segue 1 ($M_V = -1.5$, $r_h = 29$ pc et $d = 23$ kpc). Dans le premier cas on peut être assez confiant de récupérer cette galaxie (à cette distance) dans la plupart des endroits dans le ciel, à cause de ses propriétés (lumineuse, grande et assez proche). Segue 1, d'autre part, est si faible que la récupération réussie d'une telle galaxie sera très sensible à la position où la galaxie est insérée. Par exemple, en plaçant cette galaxies naines un peu plus près du disque de la Voie Lactée, pourrait signifier que ses 30-40 étoiles bleues ne sont pas très significatives par rapport à ses régions voisines. En d'autres mots, cet exercice sera très intéressant pour sonder la limite de luminosité de surface.

La quantification des limites de détection dépend de deux phases principales. Premièrement des galaxies artificielles sont simulées. Deuxièment ces galaxies sont insérées ou cachées dans les données PS1 et l'algorithme de recherche est ensuite ré-exécuté pour déterminer la récupération fractionnaire de satellites de propriétés diverses à différents endroits dans PS1. Pour simuler les galaxies, trois étapes principales sont nécessaires. Premièrement photométrie est généré pour les différentes galaxies simulées (voir Figure 6). Des incertitudes photométriques en fonction de magnitude sont prises en compte par la dispersion des étoiles dans l'espace couleur-magnitude. Deuxièmement la complétude du relevé est prise en compte : Les étoiles non observables sont éliminés à partir des échantillons simulés. Enfin, les étoiles, qui sont gardées après cette opération, sont assignés des positions, générées, utilisant la fonction Plummer (voir Figure 7). Ainsi, dans tout le ciel couvert par PS1, 250 000 galaxies naines artificielles sont insérées.

Les résultats ont montré que l'efficacité de la recherche fonctionne bien (voir Figure 8). Le taux de recouvrement est plus élevé pour les galaxies insérées aux latitudes plus élevés, où la contamination stellaire de la Voie Lactée est réduite. Les taux de récupération en fonction de la position ont été étudiés pour quatres galaxies naines artificielles différentes dont les propriétés correspondent à celles de Segue 1, Bootes I, Leo IV et Andromeda IX. En faisant varier leurs paramètres structurels en échantillonnant les incertitudes, les

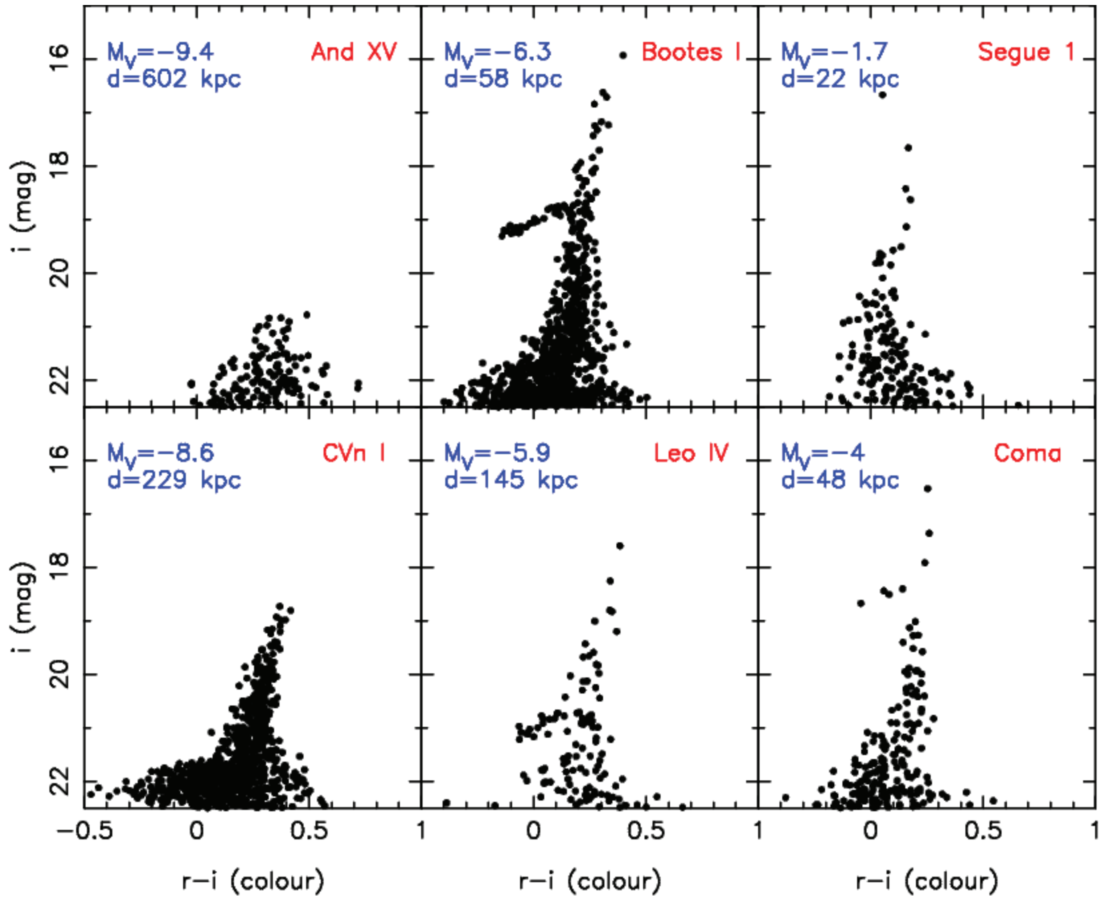

Figure 6: Diagrammes couleur-magnitude de galaxies naines simulées avec des propriétés quio resemble celles de six galaxies naines connues: Andromeda XV, Boötes I, Segue 1, Canes Venatici I, Leo IV and Coma Berenices. Les magnitude et distances citées sont celles des galaxies naines simulées.

taux de récupération pour ces satellites se sont montrés globalement conformes aux taux de récupération du SDSS (Koposov et al., 2008) en tenant compte des différences de méthodologie suivie. Le taux de récupération peut être utilisé comme un tremplin pour recalculer la fonction de luminosité des galaxies naines de la Voie Lactée sur tout le ciel après que la distribution des galaxies naines de la Voie Lactée fût étudiée. Des preuves provisoires montrent que cette distribution est anisotrope.

8 Conclusion et perspectives pour le futur

8.1 Conclusion

Un algorithme de recherche a été développé afin de trouver de nouvelles galaxies naines de la Voie Lactée. En tenant compte de la distance, la taille, la metallicité et l'âge d'une

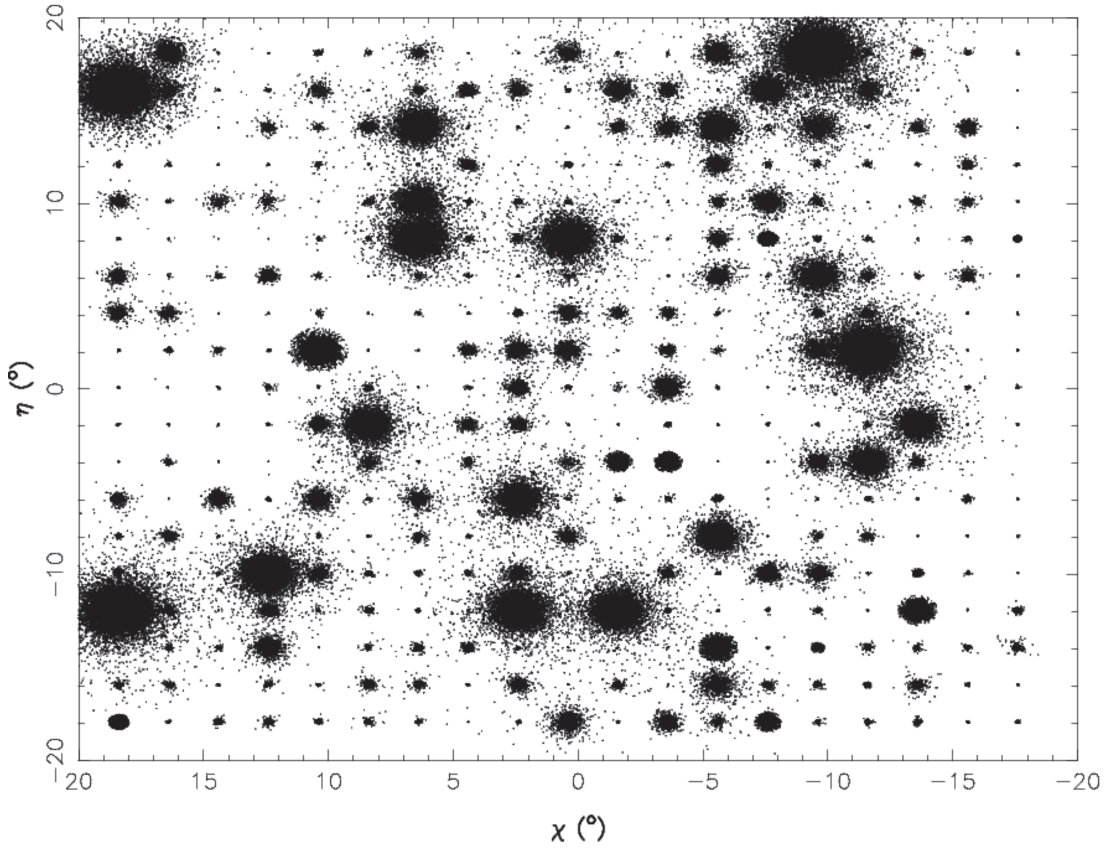

Figure 7: Distribution spatiale de 361 galaxies naines simulées. Ces galaxies démontrent les différentes sortes de galaxies naines qui peuvent être créées

probable galaxie naine nouvelle, un algorithme de convolution est développé pour tout le ciel de Pan-STARRS 1. Cette opération produit des cartes de densité qui sont convertis en des cartes de probabilités. Cette opération tien compte de la poussière galactique, la séparation d'étoiles de galaxies et la grande taille des données. L'efficacité de l'algorithme de recherche a été analysé en regardant si la plupart de galaxies naines trouvées dans le grand relevé précèdent: SDSS, responsable pour la découverte de beaucoup de nouvelles galaxies naines, sont retrouvées. La plupart de galaxies naines sont retrouvées, confirmant que l'algorithme marche bien. Investigation de nouvelles détections, conduit à la découverte de cinq nouveaux satellites dont deux amas globulaires (Laevens 1 et Laevens 3) et trois galaxies naines probables (Triangulum II, Draco II et Sagittarius II).

Les limites de détection du relevé PS1 ont été quantifiées en simulant de galaxies naines à la base de photométrie et constituants spatiales. Ces galaxies naines ont été insérées dans les données PS1. L'algorithme de recherche a été retourne sur l'ensemble de données (avec l'addition des galaxies simulées). Le taux de récupération sont similaires à ceux du SDSS, ce que montre que l'algorithme marche bien. Ces résultats peuvent être utilisés pour montre la distribution anisotrope des galaxies naines de la Voie Lactée.

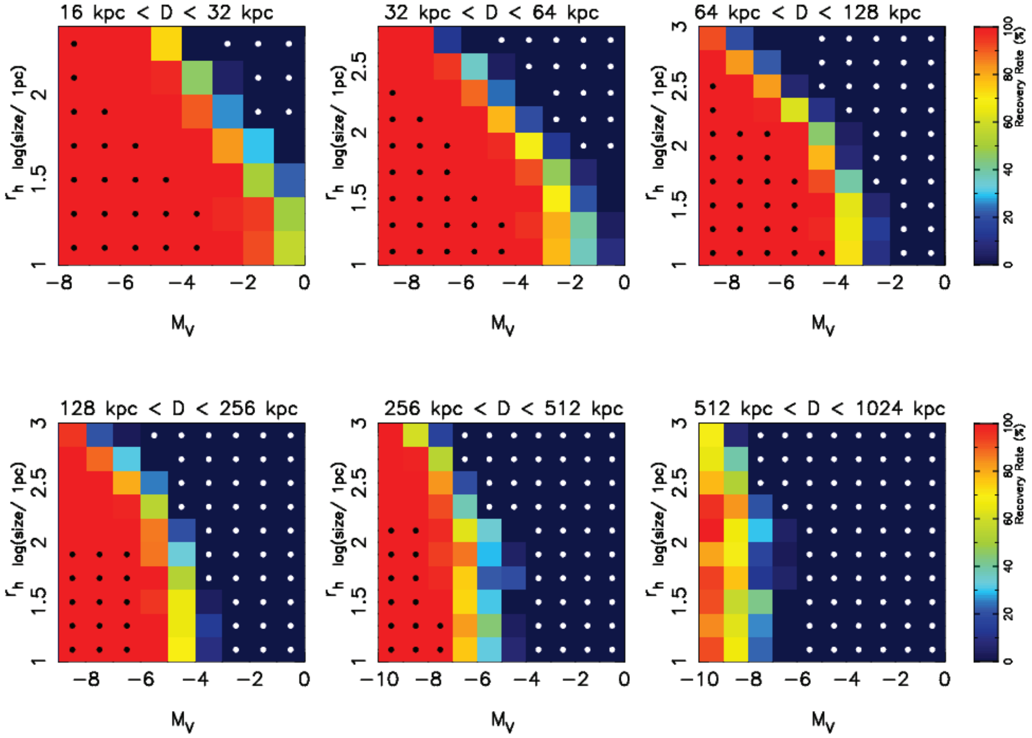

Figure 8: Taux de récupération de galaxies naines simulées pour une partie du ciel de PS1. Les six paneaux indiquent les six différents bins de distance. Chaque paneau contient le taux de récupération pour le bin de sitance pour un bin de taille et magnitude spécifique. Les points noirs et blancs représentent les bins qui n'ont pas été simulés, puisque pour ces paramètres le taux de récupération est déjà connu: 100% (noir) our 0% (blanc)

8.2 Perspectives pour le futur

Un des principaux défis pour l'avenir sera de mieux comprendre la population de galaxies naines de la Voie Lactée. Plus précisément, nous devons comprendre comment les amas globulaires, les galaxies naines et les systèmes stellaires qui montrent des caractéristiques entre ces deux types sont formés dans le contexte de formation de galaxies. Il est utile de rappeler comment les choses ont évolué en trois ans. En 2012, parmi toutes les galaxies naines que nous connaissions, seulement quatre d'entre eux montraient des propriétés entre amas globulaires et galaxies naines. À peine trois ans plus tard, environ 40% de la population galaxies naines se compose de ces objets. Une attente naturelle pour l'avenir est que beaucoup plus de ces satellites seront trouvées, car la plupart de galaxies naines doivent déjà être trouvées. Nous sommes venus au point où les recherches de galaxies naines sont devenues un peu moins intéressantes puisque il semblerait en avoir beaucoup. La prochaine étape naturelle est donc d'essayer d'utiliser les informations de ces satellites pour les comprendre d'une meilleure façon dans le contexte des simulations de ΛCDM. L'échantillon de galaxies naines dans ce zone de transition est désormais si important que nous avons déjà un échantillon statistiquement significatif de ces objets. Nous avons besoin de passer autant de temps possible à collecter de nouvelles données pour ces satellites sur les plus grands télescopes du monde entier. Nous devons mesurer avec grande précision le contenu de matière noire, des dispersions de vitesse et métallicités. Il y a beaucoup d'ambiguïté dans ces systèmes à l'heure actuelle parce que des différents groupes d'astrophysiciens mesurent des différentes propriétés de ces galaxies naines suite à la taille d'échantillons qui sont petits. Nous devons revenir à ces objets tout au long de plusieurs années pour vérifier que leurs propriétés mesurées n'ont pas changé. La deuxième question à laquelle il faut répondre est : Sont ces objets les subhalos de matière noire dans les simulations de ΛCDM? Sont-ils les halos de sub-subhalos, dont nous savons très peu à l'heure actuelle? Est-ce que ces objets sont associés à des courants d'étoiles et donc les restants d'une entité plus large? Le gros problème est que les recherches photométriques pour ces objets faibles sont en avance sur les moyens spectroscopiques. Avec les télescopes actuels, il est déjà incroyablement difficile d'obtenir une mesure précise et exacte pour ces objets faibles et seulement à 40 kpc. Beaucoup de défis ne seront résolus si nous attendre la prochaine génération de télescopes.